Dry, bi-, and oxidative CO_2 reforming of CH_4 in an atmospheric pressure glow discharge reactor: an experimental study

Bart Wanten

Supervisor **Prof. Dr. Annemie Bogaerts**

Thesis submitted for the degree of Doctor of Science: Chemistry
Faculty of Science | Department of Chemstry | University of Antwerp, 2024

University
of Antwerp

Faculty of Science
Department of Chemistry

Dry, bi-, and oxidative CO_2 reforming of CH_4 in an atmospheric pressure glow discharge reactor: an experimental study

PhD thesis submitted for the degree of Doctor in Science at the University of Antwerp to be defended by Bart Wanten

Supervisor:
Prof. Dr. Annemie Bogaerts

Antwerp, 2024

Members of the jury

Internal jury members

Prof. Dr. Vera Meynen (Chair, member of individual doctoral commission (IDC))

Laboratory of Adsorption and Catalysis, University of Antwerp

Prof. Dr. Annemie Bogaerts (Promotor, member of IDC)

Plasma Lab for Applications in Sustainability and Medicine – Antwerp, University of Antwerp

Prof. Dr. Patrice Perreault (member of IDC)

ElectrifHY, University of Antwerp

Dr. Georgi Trenchev

Plasma Lab for Applications in Sustainability and Medicine – Antwerp, University of Antwerp and D-CRBN

External jury members

Dr. Anton Nikiforov

Research Unit Plasma Technology, University of Ghent

Dr. Nuno Pinhão

Institute for Plasma Research and Nuclear Fusion, Technical University of Lisbon

Dr. Ramses Snoeckx

EMPA, Swiss Federal Laboratories for Materials Science and Technology

Acknowledgements

While I am writing this section, it has been more than 10 years since for me, chemistry simply was a very interesting course I had in high school, given by a very good teacher who was able to spark my interest in the fascinating world of atoms, molecules, reaction mechanisms, experiments, lab techniques, etc. What I could not predict at that time, was that this interest in chemistry would eventually form the basis for my bachelor and master degree, all the way up to the point where we are today, where I am writing this PhD thesis. On the front of this thesis, you can only find my name (and the name of my promotor), but over the span of 10 years, there are of course multiple people that have contributed to this thesis one way or another. In fact, this work would simply not have been possible at all without the everlasting and unconditional support of a select group of people, who I explicitly want to thank in this section.

Let's start with my promotor, Annemie. I remember that when we had to choose a topic for our bachelor thesis, we had to provide a top 3 from all the available options, which was needed to distribute the different students among the groups, as at that time, the 3rd bachelor year was a relatively large group. I was very interested in the topic of experimental research at PLASMANT, but so were a lot of people. Eventually Annemie had allowed me to still do my bachelor's thesis within PLASMANT with her as promotor, despite many others who were already assigned to her. This is the first of many examples where she truly showed her belief in me, and I cannot express how grateful I am for this. During my PhD, Annemie made such a difference by just being her enthusiastic self, by showing understanding and support during difficult times (which are frequent during any PhD, and for me this was no exception), by always communicating in a positive way (for example, through a number of smileys in an e-mail), and by being very approachable for just a regular conversation about literally anything.

Furthermore, I should not forget my colleagues. Overall, I truly appreciated all experimentalists, modelers and ATP that I have had the chance to work with and that have helped and supported me during my time at PLASMANT. Since I count over 80 (ex-) colleagues in total, I will not mention everyone explicitly here, but a few colleagues do deserve some special recognition.

First, I want to express my thanks to all co-authors who have contributed to the publications linked to this doctoral thesis. My thanks towards Stein, Christine, Joachim and

Georgi, for their contribution leading to my very first research paper (see Chapter 3). I want to thank Rani and Robin as well, for the major contribution to our review paper discussing the correct performance metrics for plasma-based CO_2 conversion (part of it is presented in Chapter 2). I often receive positive reactions related to this paper, both from within and outside our research group, and this is a true testament of our hard work together. Likewise, I want to thank Stein, Robin, Morgane and Senne, for their contribution to the work which I discuss in Chapter 4. Special thanks are in place for Stein, who developed the fluid dynamics model from which we obtained valuable insights, and Robin, for the electron microscopy analysis of the carbon deposits. Someone who also deserves recognition is Yury, specifically for his extensive help with the experiments involving H_2O addition, leading to the paper on which Chapter 5 is based. Finally, I want to explicitly thank Dr. Marc Escribà-Gelonch and Dr. Jose Osorio-Tejada, for their impressive work on the life cycle assessment and techno-economic analysis they carried out based on our experimental data, with help from Dr. Le Yu and under the supervision and great support of Prof. Dr. Volker Hessel. I am very grateful that I can include this work as final chapter of this thesis (i.e., Chapter 6), to be able to answer the final, yet very relevant research questions addressed in this thesis.

Special credit should also be given towards Marleen, Maryam, Georgi and Joachim, who supervised me during either my bachelor- or master thesis period within the group, through which it all started. Joachim was also a fellow PhD student during my entire PhD, and I can call him a true friend at this point. Next, I should thank Fanny, Sean and Yury, who were the experimental post-docs in the group during the start of my PhD. Because of the minor issue of a world-wide pandemic, they were among the only colleagues I had the chance to work closely with for quite some time, and all of them fulfilled the role of mentor to me at some point during my PhD. Finally, I want to thank Hamid, Karen, Shangkun, Callie, Robin and Elizabeth for their direct and indirect support during the last months and weeks of my PhD while I was writing this thesis.

Fortunately, a PhD is not only about work, and for this reason I want to thank the PLASMANT event committee explicitly for organizing the very fun teambuilding activities. I am 100 % certain that for many years to come, the game they thought out that took place in the city center of Antwerp will be considered as the best PLASMANT team building activity ever. I am also very happy I had the chance to supervise Christine, Morgane and Amira during their bachelor’s thesis and Stein during his master’s thesis. This never felt as an obligated task and each time I really enjoyed interacting with them.

Next, all my fellow students during my years as bachelor and master also deserve some special recognition. In particular, I want to thank Dries and Roel for the very nice restaurant visits, the long political discussions and the possibility to collectively complain entire evenings about the life as a PhD student. For the same reason, I also want to thank my best friends Pieterjan, Thomas and Tim, who I know by now for at least 15 years. You cannot imagine how good it felt these past years, specifically during the more difficult times of my PhD, to be able to meet you, laugh together and forget all worries for a while.

Finally, I have to thank my family for their endless support. Words cannot describe how grateful I am for everything my parents have given me, from the very first years of my life until now. Without their support, I would not have been able to start nor finish my PhD. I also want to thank my sisters, brother-in-law, aunt, grandparents and also my 3-year old niece, for being who they are and for being part of my life. From the bottom of my heart, thank you.

Summary

Since the industrial revolution in the eighteenth century, the concentration of greenhouse gases in the Earth's atmosphere has increased substantially, leading to global warming and rapid environmental changes. With increasing knowledge over the past decades about the impact of this phenomenon, it is clear that mankind must make a transition where chemical processes are operated in a more sustainable way.

This, of course, is not a straightforward task. Several established processes (e.g., the industrial steam reforming of methane, SRM) lead to a significant amount of CO_2 emissions due to the use of fossil fuels, for example to deliver the required heat for the reaction to proceed, but also because it is often an inevitable by-product formed during (certain stages of) the specific reaction process. Any of these processes faces a significant cost to capture and store CO_2, required to avoid its emission. Therefore, both from an economic as well as an environmental point of view, it would be ideal if a process could avoid the use of fossil fuels by becoming electricity driven, coupled to a renewable energy source, while also providing a pathway to valorise CO_2 and other greenhouse gases, turning them from a waste gas into a valuable chemical feedstock.

A possible candidate to achieve this goal, is plasma technology. It is electricity driven, it allows for a high flexibility and modularity and it can provide the required conditions for the conversion of relatively stable molecules, like CO_2. Indeed, a plasma is typically generated by applying a high voltage between two electrodes, leading to a cocktail of reactive species (radicals, ions, electrons, electronically and vibrationally excited molecules, etc.) and the gas temperature can reach temperatures above 1000 K very fast. In this thesis, I focus on the combined conversion of CO_2 and CH_4 by means of a plasma reactor, in particular a confined atmospheric pressure glow discharge (cAPGD). Specifically, I conducted experiments for a wide range of conditions and additive gases, with the goal to find the optimal reaction conditions with this specific plasma reactor, that leads to the formation of syngas, a mixture of CO and H_2. Syngas can be further processed into a variety of liquid fuels, such as methanol and various long-chain hydrocarbons, depending on the relative amount of CO and H_2.

After introducing this topic in Chapter 1 and defining the performance metrics to evaluate the experiments in Chapter 2, I discuss the dry reforming of methane (DRM) carried out by means of the cAPGD in Chapter 3. Here, an excellent performance compared to the state-

of-the-art is achieved. Specifically, a CO_2 and CH_4 conversion of 64 % and 94 % is reached, respectively, at an energy cost of 3.2-4 eV/molecule (ca. 310-380 kJ/mol). The confinement in the plasma is assumed to play a crucial role with regards to these excellent results. Unfortunately, the product output's value remains limited, as soot formation limits the use of sufficiently high amounts of CH_4 with this setup, necessary to achieve a syngas ratio (H_2/CO) that is high enough for further processing towards methanol or towards liquid fuels in the Fischer-Tropsch (FT) process.

A potential solution for this issue is the addition of other gases next to CO_2 and CH_4 that can avoid the formation of soot particles to some extent. In Chapter 4, a small fraction of O_2 is added, leading to the so-called "oxidative CO_2 reforming of methane" (OCRM). The best performance is obtained for a 42.5-42.5-15 vol% CO_2-CH_4-O_2 mixture, leading to a CO_2 and CH_4 conversion of 50 and 74 %, respectively, and an energy cost as low as 2 eV/molecule (or 190 kJ/mol). The syngas ratio, however, is only slightly improved, being close to 1, but solid carbon deposition still negatively affects the overall stability of the plasma, avoiding a further increase in the syngas ratio. Additionally, the deposited carbon material is analysed by means of electron microscopy, showing the structure and impurities present in this solid fraction. Finally, a multidimensional model designed by a fellow colleague and applied to these experiments, grants us more insight in the exact mechanisms at play at specific positions in the reactor setup.

In Chapter 5, the experiments with H_2O added instead of O_2 are presented, describing the "bi-reforming of methane" (BRM). Compared to the other reaction processes, the addition of H_2O effectively helps in counteracting soot formation. A mixture of 14–41-45 vol% CO_2-CH_4-H_2O leads to the overall best results in terms of stable plasma and performance metrics, i.e., a CO_2 and CH_4 conversion of 49 % and 74 %, respectively, at an energy cost of 4 eV/molecule (or 390 kJ/mol). Moreover, we reach CO and H_2 yields of 59 % and 49 %, respectively, and a syngas ratio of 2, which is ideal for further methanol synthesis.

A comparison of these processes with one another and the current state-of-the-art, in terms of environmental impact and economic potential, is given in Chapter 6. Through a techno-economic analysis (TEA) and cradle-to-gate life cycle assessment (LCA), performed by external collaborators (Dr. M. Escribà-Gelonch, Dr. J. Osorio-Tejada, Dr. L. Yu, L. and Prof. Dr. V. Hessel) based on our input data, the OCRM process is found to be the most promising on a small scale in terms of competitiveness and environmental impact, with a score twice as high as for the BRM process on almost all environmental parameters considered. On a large scale, the BRM process appears to be the most competitive. Compared with current classical SRM technologies and plasma-based DRM processes (carried out through a dielectric barrier discharge (DBD), microwave (MW) and pulsed plasma reactor) all three plasma processes lead to an improved environmental performance overall and achieve a medium-high circularity.

Finally, I present an overall conclusion in Chapter 7, while also providing a future outlook on CO_2 and CH_4 conversion by means of a cAPGD and plasma reactor technology in general.

Samenvatting (Dutch Summary)

Sinds de industriële revolutie in de 18de eeuw, is de concentratie aan broeikasgassen in de atmosfeer sterk toegenomen, wat leidt tot de opwarming van de aarde, met als resultaat zeer snelle veranderingen in onze omgeving. Door een toename aan kennis afgelopen decennia omtrent de impact van deze fenomenen, is het duidelijk dat de mensheid een transitie moet ondergaan waarbij chemische processen opereren op een meer duurzame manier.

Dit is natuurlijk geen simpele opdracht. Verschillende gevestigde processen (bv., de industriële "*steam reforming of methane*", SRM) leiden tot een significante hoeveelheid aan CO_2 uitstoot omwille van het gebruik van fossiele brandstoffen, bijvoorbeeld om de warmte te leveren die nodig is om de reactie te laten doorgaan, maar ook omdat het vaak als onvermijdelijk bijproduct wordt gevormd tijdens (specifieke stadia van) het reactieproces. Elk van deze processen kijkt aan tegen een significante kost om CO_2 op te vangen en op te slaan, noodzakelijk om de uitstoot te vermijden. Daarom, zowel vanuit een economisch als een ecologisch perspectief, zou het ideaal zijn indien een proces het gebruik van fossiele brandstoffen kan vermijden door aangedreven te worden via elektriciteit, gekoppeld met een hernieuwbare energiebron, terwijl het ook een pad aanlevert om CO_2 en andere broeikasgassen te valoriseren, en zo een afvalgas omzet in een waardevolle chemische bouwsteen.

Een mogelijke kandidaat om dit doel te bereiken, is plasmatechnologie. Het wordt aangedreven via elektriciteit, laat een hoge flexibiliteit en modulariteit toe en het levert de noodzakelijke condities om relatief stabiele moleculen, zoals CO_2, om te zetten. Een plasma wordt inderdaad typisch opgewekt via het aanleggen van een hoogspanning tussen twee elektroden, wat leidt tot een cocktail aan reactieve deeltjes (radicalen, ionen, elektronen, elektronisch en vibrationeel geëxciteerde moleculen, enz.) en het gas kan zeer snel temperaturen boven 1000 K bereiken. In deze thesis, focus ik op het omzetten van zowel CO_2 als CH_4 door middel van een plasmareactor, in dit geval een "*confined atmospheric pressure glow discharge*" (cAPGD). Specifiek voerde ik experimenten uit voor een brede waaier aan condities en toegevoegde gassen, met als doel het vinden van de optimale procescondities met deze specifieke plasmareactor, dat leidt tot de vorming van syngas, een mengsel van CO en H_2. Syngas kan verder verwerkt worden in verschillende vloeibare brandstoffen, zoals bijvoorbeeld methanol en verschillende lange-keten koolwaterstoffen, afhankelijk van de relatieve hoeveelheid aan CO en H_2.

Na het introduceren van dit onderwerp in Hoofdstuk 1 en het definiëren van de prestatieparameters voor het evalueren van de experimenten in Hoofdstuk 2, bespreek ik de "*dry reforming of methane*" (DRM) uitgevoerd met behulp van de cAPGD in Hoofdstuk 3. Hier wordt aangetoond dat een excellente prestatie wordt behaald in vergelijking met de "*state-of-the-art*". Specifiek, een CO_2 en CH_4 conversie van respectievelijk 64 % en 94 % bij een energiekost van 3.2-4 eV/molecule (ca. 310-380 kJ/mol) wordt bekomen. Het omsluiten van het plasma speelt wellicht een belangrijke rol bij het behalen van deze excellente resultaten. Helaas blijft de waarde van de product output beperkt, omdat de vorming van roet zorgt voor een limitatie op vlak van de hoeveelheid aan CH_4 die kan gebruikt worden met deze opstelling, en hogere hoeveelheden zijn nodig om een voldoende hoge syngas verhouding (H_2/CO) te bekomen voor verdere omzetting naar methanol of vloeibare koolwaterstoffen in het Fischer-Tropsch (FT) proces.

Een mogelijke oplossing voor dit probleem is het toevoegen van andere gassen naast CO_2 en CH_4 die de vorming van roet deeltjes kunnen vermijden tot op zekere hoogte. In Hoofdstuk 4 leidt een kleine fractie aan O_2 tot de zogenaamde "*oxidative CO_2 reforming of CH_4*" (OCRM). De beste prestatie wordt bekomen bij een 42.5-42.5-15 vol% CO_2-CH_4-O_2 mengsel en leidt tot een CO_2 en CH_4 conversie van respectievelijk 50 en 74 %, en een energie kost zo laag als 2 eV/molecule (of 190 kJ/mol). De syngas verhouding is enkel lichtjes verbeterd, zijnde dicht tegen 1, maar depositie van het vaste koolstof-materiaal beïnvloedt nog steeds de algemene stabiliteit van het plasma op een negatieve manier, waardoor een verdere verbetering in syngas verhouding niet mogelijk is. Daarnaast is het afgezette koolstof-materiaal geanalyseerd via elektronenmicroscopie, wat de structuur en de onzuiverheden in de vaste fractie aan het licht brengt. Tot slot, een multidimensionaal model ontworpen door een collega, wordt toegepast op deze experimenten, en bezorgt ons meer inzicht in de exacte mechanismen die plaatsvinden op specifieke plaatsen in de reactoropstelling.

In Hoofdstuk 5 worden de experimenten met H_2O in plaats van O_2 gepresenteerd, waarbij de "*bi-reforming of methane*" (BRM) wordt beschreven. In vergelijking met de andere reactie-processen helpt de toevoeging van H_2O effectief in het tegengaan van de roetvorming. Een mengsel van 14–41-45 vol% CO_2-CH_4-H_2O leidt tot de beste resultaten in termen van plasmastabiliteit en prestatie-parameters, d.w.z. een CO_2 en CH_4 conversie van respectievelijk 49 % en 74 %, bij een energiekost van 4 eV/molecule (of 390 kJ/mol). Daarbij wordt ook een CO en H_2 opbrengst van respectievelijk 59 % en 49 % en een syngas verhouding van 2 bekomen, wat ideaal is voor verdere synthese van methanol.

Een vergelijking van deze processen onderling en met de huidige "*state-of-the-art*", op vlak van impact op de omgeving en economisch potentieel, wordt behandeld in Hoofdstuk 6. Via een techno-economische analyse (TEA) en "*cradle-to-gate*" levenscyclus beoordeling ("*life cycle assessment*", LCA), uitgevoerd door externe medewerkers (Dr. M. Escribà-Gelonch, Dr. J. Osorio-Tejada, Dr. L. Yu, L. and Prof. Dr. V. Hessel), en op basis van onze inputdata, wordt duidelijk dat het OCRM proces op kleine schaal het meest veelbelovend is op vlak van competitiviteit en ecologische impact, met een dubbel zo hoge score als voor BRM op bijna alle beschouwde omgevingsparameters. Op grote schaal lijkt het BRM proces het meest competitief. In vergelijking met de huidige klassieke SRM technologieën en plasma-gebaseerde DRM processen (uitgevoerd met behulp van een "*dielectric barrier discharge*" (DBD), "*microwave*" (MW) en gepulseerd-plasma reactor) leiden alle drie deze plasmaprocessen tot een verbetering qua ecologische impact in het algemeen, en behalen ze een middelhoge circulariteit.

Tot slot presenteer ik een algemene conclusie in Hoofdstuk 7, waarbij ik ook vooruitblik op de toekomst van CO_2 en CH_4 conversie door middel van een cAPGD en plasma reactor technologie in het algemeen.

Table of contents

List of abbreviations

Abbreviation	Meaning	Abbreviation	Meaning
0D	Zero-dimensional	**HPLC**	High-performance liquid chromatography
2D	Two-dimensional	**HT((n)c)**	Human toxicity (including (non-) carcinogenic)
3D	Three-dimensional	**LCA**	Life cycle assessment
AC	Alternating current	**LFI**	Linear flow index
ACC	Annualized capital cost	**LHV**	Lower heating value
AP	Acidification potential	**LTE**	Local thermal equilibrium
APOS	Allocation at the point of substitution	**MCI**	Material circularity indicator
BF	Bright-field	**MFC**	Mass flow controller
BRM	Bi-reforming of methane	**MW**	Microwave
BSE	Backscattered electron	**OES**	Optical emission spectroscopy
CAPEX	Capital expenditure	**OCRM**	Oxidative CO_2 reforming of methane
(c)APGD	(Confined) atmospheric pressure glow discharge	**ODP**	Ozone depletion potential
CCS	Carbon capture and storage	**OPEX**	Operating expenditure

CCU	Carbon capture and utilization	**PAH**	Polycyclic aromatic hydrocarbons
CED(f/m)	Cumulative energy demand (fossils/materials)	**PEM**	Proton exchange membrane
CEPCI	Chemical engineering plant cost indices	**Ph**	Photochemical ozone formation
CTU(e/h)	Cumulative toxicity unit (environment/humans)	**POM**	Partial oxidation of methane
DBD	Dielectric barrier discharge	**PPC**	Post-plasma catalysis
DC	Direct current	**PSA**	Pressure swing adsorption
DRM	Dry reforming of methane	**PSU**	Power supply unit
EDX	Energy dispersive X-ray	**PV**	Photovoltaic
EIO	Economic input-output	**RE**	Respiratory effects
EP(t/w)	(Terrestrial/Freshwater) eutrophication	**(r-)WGS**	(Reverse) water-gas shift
EMAF	Ellen MacArthur Foundation	**SE**	Secondary electron
(F)ET	(Freshwater) ecotoxicity	**SEI**	Specific energy input
FT	Fischer-Tropsch	**SEM**	Scanning electron microscopy
GA(P)	Gliding arc (plasmatron)	**SRM**	Steam reforming of methane
GC	Gas chromatography	**TEA**	Techno-economic analysis

GWP	Global warming potential	**TEM**	Transmission electron microscopy
HACA	H-abstraction C_2H_2-addition	**TRL**	Technology readiness level
HHV	Higher heating value	**UCOP**	Unitary cost of production

Chapter 1 Introduction

1.1 Environment and energy

Environmental changes have always had a major impact on human development. Following the last ice age, humans were able to move successfully into every part of the world by adapting to the environment and using it intelligently.[1] From the period when humans were hunter-gatherers to an agricultural-based society, all the way up to our modern post-industrial society: every major part in our timeline is defined by how we use the environment to our benefit, and how we respond to environmental changes. At the same time, every subsequent era was not predictable by its predecessors, and at the height of each era, it was simply expected that the current "way of life" would go on forever.[2]

In our current time-period, there is an increased concern about rapid environmental changes. Since the industrial revolution in the eighteenth century, the concentration of greenhouse gases in the Earth's atmosphere has increased, leading to an enhanced greenhouse effect and, consequently, an exponential rise in temperature of the atmosphere.[3] Because of this, the world is experiencing floods, severe droughts, heat waves, forest fires, … more frequently and more intense. These phenomena endanger the existence of entire eco-systems, and in many ways also our current way of life.[4] As a result, once again humans must adapt and transition into a new era, to tackle the threat of global warming.

Anthropogenic emissions of CO_2 and CH_4 are currently the main contributors to global warming. Different methods to capture e.g. CO_2 exist (so-called carbon capture and storage, CCS), and have been well reviewed by Spigarelli and Kawatra.[5] However, capture and storage alone still represents a significant and costly endeavor for industry.[6] The creation of a neutral carbon cycle through the utilization of captured CO_2 and CH_4, in contrast to only storage, has the highest potential to provide a permanent solution against continuing global warming (so-called carbon capture and utilization, CCU).[7] In this way, specifically CO_2 is no longer treated as waste product, but as a "renewable carbon source", of which more valuable products can be derived. However, CO_2 is thermodynamically a highly stable molecule (i.e., a standard Gibbs free energy of formation of -394.4 kJ/mol)[8], which means that a large amount of energy is required to convert it.[7] The energy source used to carry out this conversion should not be fossil fuels, as it would undo any effort. Indeed, three-quarters of global greenhouse gas emissions result from the burning of fossil fuels for energy.[9] Thus, renewable energy sources with a much lower environmental impact are required. Fortunately, over the past decades the amount of renewable energy generated through various sources has increased substantially, as seen in Figure 1. Today, approximately one-seventh of the world's primary energy is sourced from renewable technology, and when looking only at the global electricity mix, one-third of our electricity comes from renewables.[9]

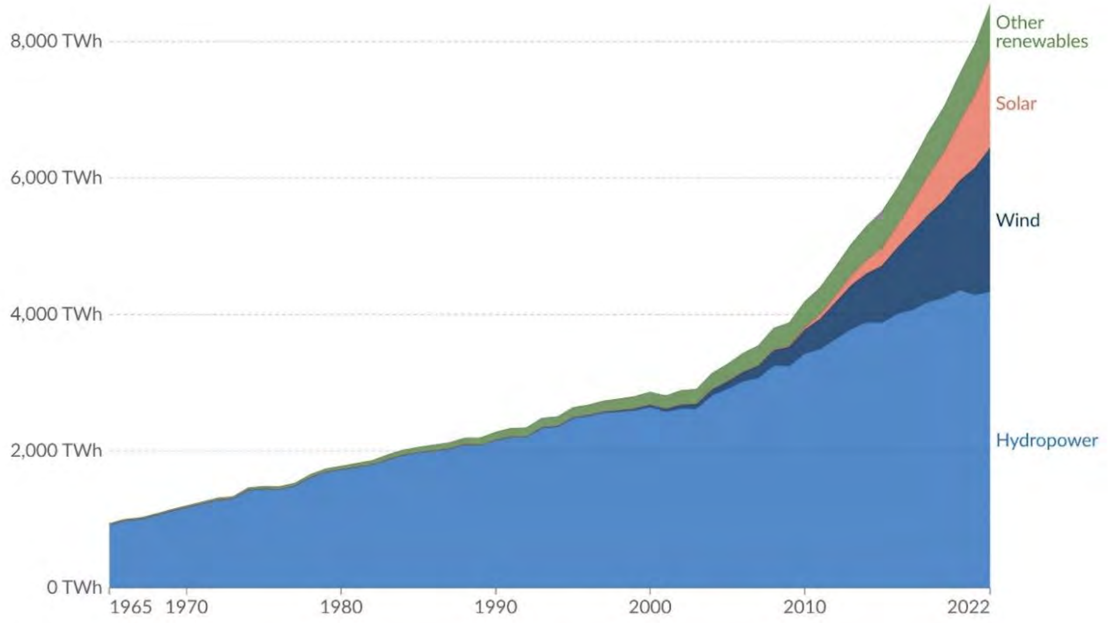

Figure 1: Renewable electricity generation across the globe, expressed in TWh, from 1965 to 2022. 'Other renewables' refers to renewable sources including geothermal, biomass, waste, wave and tidal. Traditional biomass is not included.[9]

However, many renewable energy sources (especially wind and solar) have an intermittent character. Therefore, the CO_2 conversion technology should be able to follow an irregular supply of electrical energy.[10] This means that a long start-up procedure, i.e. to reach a certain temperature and pressure, followed by a continuous operation and eventually a long shut-down procedure, is unwanted. Rather, a process is required that can immediately be switched on/off, and thus which can immediately deliver the high amount of energy necessary for CO_2 conversion. This high operational flexibility, while making use of renewable electricity, can mainly be found in electrochemical reactors and plasma reactors.[10–12]

1.2 Plasma technology

Enter the concept “plasma”, also often called “the fourth state of matter”.[7,10,12] Indeed, when heating up any substance, it will transition from the gas phase to the plasma phase at some point. For example, in a fusion reactor, extremely high temperatures are applied, leading to full ionization of the molecules and the generation of a plasma inside the reactor. However, a more appropriate term would be a “fully or partially ionized gas”. Indeed, not all plasmas require full ionization to be defined as such, in fact, many plasma reactors operate at conditions where the majority of the species remain as gaseous, neutral molecules.[10,12]

“Gas discharge reactors”, for example, are another type of plasma reactors which, in their simplest form, apply an electric field between two electrodes while a gas is flowing in between. The electric field leads to the generation of free electrons attracted by the positively charged electrode (anode), and simultaneously the ions are attracted by the negatively charged electrode (cathode). However, most of the gas remains present as neutral molecules. Through collisions with the charged species, these molecules can ionize, excite or dissociate into other species. New electrons, created through ionization or secondary electron emission at the cathode, give rise to further ionization collisions, and so the plasma is self-sustained.

Plasmas are involved in many applications because of their very specific characteristics. For example, neon lights are essentially neon gas discharge tubes, where the emission of photons leads to the typical bright red-orange color that is observed.[13] The highly reactive species generated in a plasma can also be used for coating deposition, or the treatment of surfaces, through etching, sputtering, etc., with a well-known example being the etching to develop patterns on silicon wafers for microelectronic devices.[14] Furthermore, the dissociation collisions taking place will create radicals, which can easily react into new components. Overall, radicals and highly energetic electrons provide a way toward otherwise impossible reaction pathways, which makes a plasma reactor an interesting tool for the conversion of thermodynamically stable molecules, creating the basis for plasma-based gas conversion.[12,15]

When this process takes place at a gas temperature near room temperature, the plasma is defined as a non-thermal plasma, given by the fact that not thermal heat, but the energetic electrons (which have a temperature of around 10 000 K), are the driving force for the conversion mechanism. As demonstrated by Slaets et al.[16] for several CO_2-CH_4 mixtures and a gas residence time in the ms-range, there is a clear conversion by the plasma, through electron impact reactions, at gas temperatures below 2000 K. Compared to pure thermal conditions, this conversion would be much lower. Above 2000 K, this is no longer the case, i.e. conversion through collisions between heavy species starts to dominate to an extent that electron-impact reactions only have a negligible effect towards the conversion.[16] This is the case with so-called “warm plasmas”, where the typical gas temperature is between 2000 and 4000 K, and the overall better energy efficiency of the process is also due to these high temperatures, accelerating the conversion.[12,16]

In this thesis, the performance of a cAPGD will be investigated and this can be categorized as a warm plasma reactor. It is important to note that the high gas temperatures obtained in these warm plasmas are present in less than a second, upon ignition, and most plasma reactors can operate at atmospheric pressure.[10,12] In addition, the scale at which plasma technology is applied can vary from watt to megawatt, and from a few mL/min to 1000 L/min (and more, in upscaled reactors). This high flexibility and modularity are key advantages of plasma reactor technology, and as described earlier, these are necessities for any technology applied towards CCU.[10–12]

We should add that, as mentioned earlier, electrochemical reactors also have this high flexibility and modularity, and the technology is in general already much more commercialized, e.g. to generate H_2 from H_2O.[12] The technology readiness level (TRL) for its application to various processes is also considered to be higher[11], and as such, electrochemical reactors are generally seen as the closest competitors for plasma reactors.[10,12] However, especially towards the field of CO_2 conversion, electrochemical reactors still face significant challenges, most importantly moving away from the use of rare-earth metals to earth-abundant metals, to make the process economically feasible.[17] In general, plasma reactors do not require rare-earth materials, which is a critical advantage over electrochemical reactors.

1.3 Pathways to close the carbon loop

As mentioned earlier, CCU is considered to have the highest potential to provide a permanent solution against continuing global warming.[7] There are several technologies to capture CO_2 and/or CH_4 from flue gas, for example through chemical absorption, physical adsorption, membrane separation, etc.[18–20]. A mixture of CO_2 and CH_4 (along with several impurities) can also be obtained from several types of agricultural and organic waste, in which case it is labeled as biogas.[21–23] The latter often undergoes several purification steps to obtain biomethane, which is considered as a more environmental friendly alternative for natural gas and is used as fuel for electricity, heat and transport.[21,23]

To effectively close the carbon loop, CO_2 and/or CH_4 should be further converted into valuable chemicals after their capture. Plasma reactor technology has the potential to be used for this purpose, while also being coupled to a renewable energy source. In this section, we will discuss some important aspects regarding various reactions involving CO_2 and/or CH_4, specifically the conversion of each pure gas individually (i.e., CO_2 splitting and CH_4 pyrolysis) as well as the combined conversion of CO_2 and CH_4, the DRM.

1.3.1 CO_2 splitting

The most straightforward pathway to convert CO_2 is CO_2 splitting into CO and O_2, presented as reaction (R1):

$$CO_2\ (g) \rightleftharpoons CO\ (g) + \frac{1}{2} O_2\ (g) \qquad \Delta H° = +283\ kJ/mol \qquad \text{(R1)}$$

Because of the high stability of CO_2, this is a highly endothermic reaction, with a reaction enthalpy of +283 kJ/mol CO_2. Therefore, relatively high temperatures are required to reach a significant level of conversion. In Figure 2, the theoretical conversion and energy efficiency as function of temperature, when purely thermal energy is used, is presented. As can be seen, the temperature required to reach full conversion for CO_2 splitting is well above 3000 K, and the maximum energy efficiency is also reached at approximately 3000 K.[12]

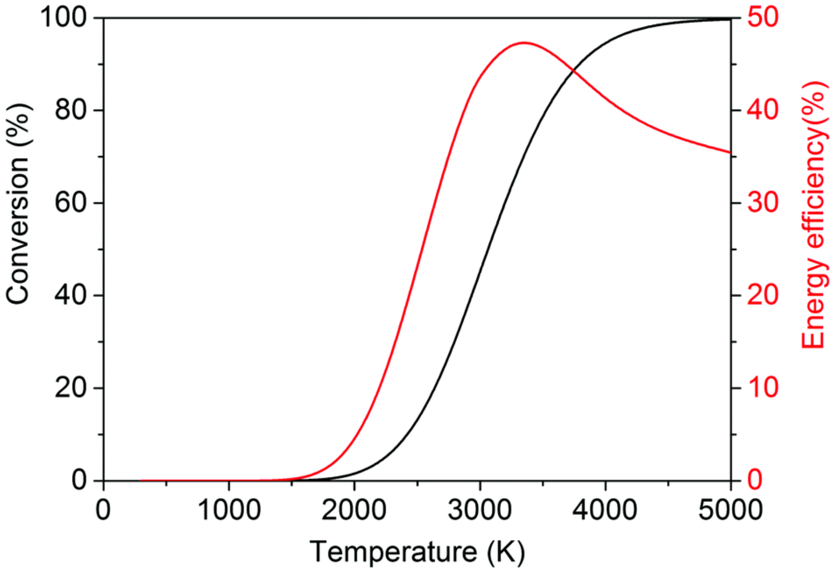

Figure 2: Calculated theoretical thermal conversion (left axis) and corresponding energy efficiency (right axis) as a function of temperature for the pure splitting of CO_2 into CO and O_2.[12]

However, even when this temperature is reached, there are several issues that prevent this reaction process to become effective. When CO_2 first splits into CO and O, the latter will recombine with other O radicals to form O_2. In order to directly use the exhaust gas in industrial applications like, e.g., the FT process, an O_2-free output stream needs to be obtained from CO_2 splitting.[24] Without the use of additional reactants such as solid carbon[24,25], or the use of oxygen separation membrane technology[26], the downstream separation costs of the gas mixture (e.g., through pressure swing adsorption, PSA) will be significantly higher and the overall energy efficiency will decrease.

Another issue is that Figure 2 only represent the conversion at thermodynamic equilibrium for each temperature, without taking into account the kinetics involved.[12] Indeed, even when e.g. 50 % conversion is thermodynamically favored at a temperature slightly above 3000 K, the actual reaction time that is obtained in practice might not be sufficient to reach this value of 50 %. At this temperature, longer reaction times might be needed, but this also means more energy spent per mole CO_2, increasing the energy cost. On the other hand, when bringing the gas temperature back to lower levels (necessary for several downstream processes), the thermodynamic equilibrium will dictate an increased recombination rate of CO and O/O_2 into CO_2. This will again lower the conversion of CO_2 and the overall energy efficiency, and this can only be avoided by either again introducing ways to remove O/O_2 prior to this step[24] or by extremely fast cooling (i.e., quenching) of the gas mixture.[27]

Due to these issues, thermal CO_2 splitting is not economically interesting at this point, thus it is not yet applied on an industrial scale. On the other hand, plasma-based CO_2 splitting has great potential, also for industrial applications, as demonstrated by D-CRBN, PLASMANT's spinoff company. Furthermore, additional changes to limit the recombination reactions and/or avoid the presence of O_2 in the output stream, can make this process profitable. Currently, the potential of (i) the use of nozzles to quench the output streams[27], (ii) the use of oxygen separation membranes[26] and (iii) the use of a carbon bed[24,25,28] near the output stream, in combination with a plasma reactor, is being actively investigated and shows a lot of potential.

1.3.2 CH_4 pyrolysis

Utilization of H_2 has been given great attention as carbon-free fuel used in e.g. automotive industry, energy production, etc.[29] Of course, the production of H_2 must avoid additional CO_2 emissions in order to be a truly sustainable fuel. This is in contrast with "grey" H_2 produced through the SRM, which emits approx. 10 kg of CO_2 for every kg of H_2 produced[30], yet is still the most developed and cheapest method for H_2 production.[31] To obtain "green"

H_2, water electrolysis is carried out while coupled to a renewable energy source.[29,31] However, with a reaction enthalpy of +285.8 kJ/mol H_2 there is, just as for CO_2 splitting, a large amount of energy required for the reaction to proceed. For this reason, CH_4 pyrolysis has received increased attention in the last decades as an alternative pathway for H_2 production (leading to so-called “turquoise” H_2).[29,31] This is presented as reaction (R2):

$$CH_4\ (g) \rightleftharpoons C(s) + 2\ H_2\ (g) \qquad\qquad \Delta H^\circ = +74.9\ kJ/mol \qquad \text{(R2)}$$

As can be seen, the reaction enthalpy of +74.9 kJ/mol CH_4 (or 37.4 kJ/mol H_2) is 248.4 kJ/mol H_2 lower than for water splitting. Simultaneously, it does not produce additional CO_2. Important to mention regarding environmental impact is that the source of CH_4 does not need to be natural gas, but can also come from landfill gas or biogas. These will still be produced even in a scenario where fossil fuels are completely abandoned, and overall this approach can even lead to negative CO_2 emissions.[29]

Plasma technology is already commercially used by many companies for CH_4 pyrolysis[32,33]. An example is Monolith[34], which produces carbon black next to H_2. However, based on numbers from 2017, the global annual demand for H_2 was 60 million ton. Yet, producing this amount through CH_4 pyrolysis would lead to 180 million ton of carbon black, while the global annual demand for carbon black was only estimated at 15-20 million ton. The imbalance between these two demands will likely continue to grow in the (near) future, especially as the H_2 demand is expected to increase sharply.[29] It should be noted though that (i) carbon black is not the only possible carbon material, hence the commercial value of it can vary[32] and (ii) there are usually a lot of intermediate steps before only H_2 and solid carbon remains, as presented by the Kassel mechanism.[29,35,36] The intermediate products are mainly C_2 olefins, which have a much higher global annual demand (range of hundreds of millions of tons). As a result, a lot of investigation is done towards so-called “non-oxidative coupling of CH_4” into C_2’s, and plasma technology is promising for this purpose.[29,30,35,37–39]

However, the performance varies extensively between different plasma reactor setups and process conditions, and overall it remains challenging to achieve a high selectivity towards (one of) these olefins together with a high CH_4 conversion. Moreover, the stability of several plasma reactors is influenced by the extent with which soot particles are formed. Specifically, it can lead to erosion of electrodes, problems with plasma ignition and stability, and (if present) catalyst deactivation.[29,30] For this reason, often plasma-based CH_4 pyrolysis is carried out in the presence of an inert gas such as Ar, or in the presence of additional H_2, to limit the rate of soot formation and deposition.[29,30,35]

1.3.3 Dry reforming of methane (DRM)

The combined conversion of CO_2 and CH_4 or the DRM, is presented as reaction (R3):

$$CO_2\ (g) + CH_4\ (g) \rightleftharpoons 2\ CO(g) + 2\ H_2\ (g) \qquad \Delta H^\circ = +247\ kJ/mol \quad \textit{(R3)}$$

There are several advantages compared to the pure CO_2 splitting and CH_4 pyrolysis discussed earlier. First, though this is still a highly endothermic reaction, the reaction enthalpy is decreased with 36 kJ/mol CO_2 compared to CO_2 splitting, decreasing the required temperature needed for the reaction to proceed. Second, the main product is a mixture of CO and H_2, also called syngas. This is considered as a precursor for the production of several highly valuable chemicals, as will be discussed in section 1.3.4. Finally, the fact that a mixture of CO_2 and CH_4 is required allows for the use of a biogas mixture, which mainly consists of CO_2 and CH_4, and removes the need to separate CO_2.[10,12,22,40]

Nevertheless, on an industrial level, DRM is not widely used. Though the amount of unwanted solid carbon with CH_4 pyrolysis is diminished, soot is usually not completely avoided. For traditional thermal catalysis, this often leads to catalyst poisoning.[12] Hence, during last decades a lot of research focusses on applying alternative methods for DRM, including plasma technology. In 2017, Snoeckx and Bogaerts presented a review on plasma-based DRM[12], indicating that the performance in terms of conversion and energy cost varies heavily between plasma types. Figure 3 shows the combination of energy cost and total conversion based on several literature data, as it is presented in the work of Snoeckx and Bogaerts. Note that the definition of the performance metrics such as "total conversion" will be discussed in detail in Chapter 2.

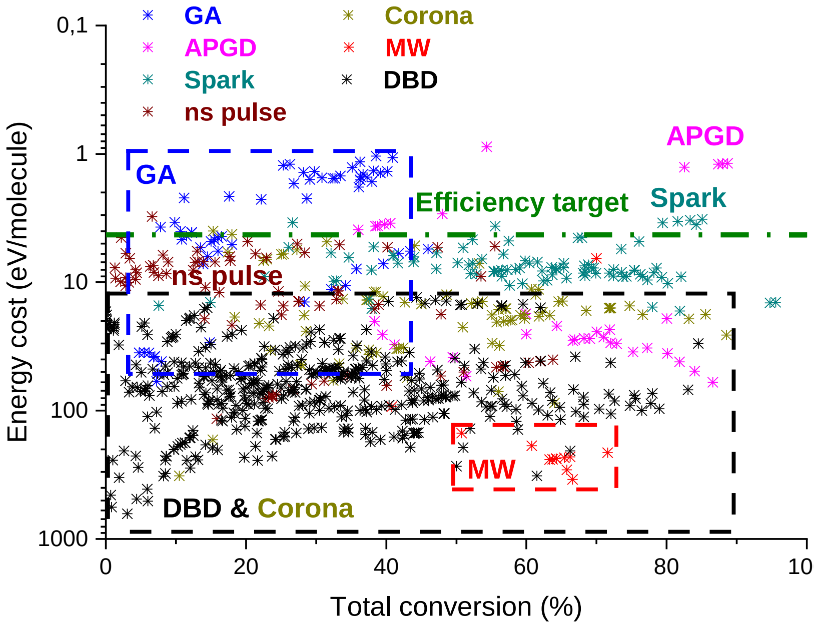

Figure 3: Comparison of data collected from literature by Snoeckx and Bogaerts.[12] *The graph plots energy cost (eV/molecule) as function of total conversion (%) while indicating the corresponding plasma reactor type. Note that the y-axis has a logarithmic scale and is reversed, meaning the lowest (= best) energy costs are found at the top of the graph. The indicated energy cost/efficiency target corresponds to 4.27 eV/molecule or 60 % energy efficiency.*

We will discuss some of the different plasma types mentioned in Figure 3 in more detail in section 1.4. Note that the efficiency target indicated corresponds to a value of 4.27 eV/molecule (corresponding to an energy efficiency of 60 %), which Snoeckx and Bogaerts defined as the maximum energy cost that should be reached in order for plasma technology to be competitive with other existing/emerging technologies, such as electrolysis.[12] Indeed, Buttler and Spliethoff report the energy efficiency of electrolysis for energy storage of green hydrogen to be between 60 and 80 %, which is a direct competition for the industrialization of plasma-based DRM.[41] Hence, optimization of the reactor design, plasma conditions and experimental mixtures is needed to compete with the industry standard. On the other hand, DRM has the advantage that the produced gas is immediately accessible for further chemical processes, such as the FT process, without the need of supplying additional CO or CO_2 similar to producing syngas with electrolysis.[42]

An important sidenote is that specifically for non-thermal plasmas, syngas may not be the main focus, but the direct formation of oxygenates like methanol, formic acid, etc. In this case, the energy cost target can be higher, as direct formation of these components means the step required to process syngas further into these components is not needed, which reduces the overall energy cost.[12] However, even then the overall energy cost remains quite high, and these components are often not obtained with high selectivity, greatly diminishing their commercial viability.[12,43]

1.3.4 Processing of syngas into valuable chemicals

While syngas can be used on its own, for example for heating or power generation through combustion in gas turbine engines, its main value comes from its function as building block for all products normally produced from crude oil or natural gas.[44] The most industrially relevant processes for the conversion of syngas into valuable liquid chemicals are the FT synthesis and syngas-to-methanol conversion.[45]

FT involves a polymerization reaction by means of a catalyst (which can be Co, Fe, Ru, …) at various conditions in terms of temperature and pressure, leading to saturated and unsaturated long-chain hydrocarbons as well as oxygenates.[46–48] Next to temperature and pressure, the type and the composition of the catalyst, an important parameter determining the product composition is the so-called syngas ratio (i.e., molar or volumetric H_2/CO ratio).[44,45,48–50] For example, when targeting alkanes, a syngas ratio of 2n+1/n is required, while a ratio of 2 is required for the production of olefins and alcohols.[48,50] Furthermore, the ideal syngas ratio to obtain a certain product can also vary depending on whether e.g. a fraction of CO_2 is still present next to H_2 and CO[49], or depending on the type of catalyst used. For example, a syngas ratio of 2 (or at least between 1.7 and 2.15)[51] is optimal when using a cobalt catalyst[52], but when using an iron catalyst, lower syngas ratios (around 1) are also suitable.[49]

Methanol synthesis from syngas is mainly done through reaction with a Cu-Zn-Al_2O_3 catalyst at pressures of 50-100 bar and temperatures of 200-300 °C.[48,53,54] Specifically, methanol would be an ideal end product for plasma-based CO_2 and CH_4 conversion. It can serve as a convenient energy storage medium, an easily transportable fuel used by the automotive and shipping industry, a solvent and a building block for several other value-added chemicals, like formaldehyde, acetic acid, dimethyl ether, etc.[53,55,56] With currently a global annual demand above 100 million tons, renewable methanol is both from an environmental and economic point of view a highly attractive chemical.[55,57,58]

Also for methanol synthesis, a syngas ratio of 2 is ideal.[48,54] Hence, for plasma-based DRM, not only the conversion and energy cost is important, but the obtained syngas ratio should also be evaluated in light of the possible end products that can be derived.

1.4 Plasma reactor types

In Figure 3 many types of plasma reactors are indicated. A typical text-book example is a simple setup with two electrodes (i.e., a cathode and anode) at low pressure, where the relation between voltage and current (so-called current-voltage characteristics) are displayed. This is presented in Figure 4.[59] When a direct current (DC) discharge is generated by means of an "external agent" (for example through rays leading to photo-emission of electrons from the cathode), a very low current will be present at a high voltage, but the discharge will not emit visible light – at this stage it is called a "dark discharge". Further increase of the voltage will increase the current, and at some point the "breakdown voltage" is reached. This means there is an electron avalanche, which is strong enough to self-sustain the plasma. A sheath is formed at the cathode, leading to secondary electron emission upon impact of ions attracted by the cathode. This is also accompanied by a significant decrease in voltage and a characteristic glow – hence the name "glow discharge". For an increasing current, the voltage will stay stable for a while and then will start to rise, until there is a sharp drop. At this point, thermionic field emission starts to dominate over secondary electron emission, in which case an "arc discharge" is formed.[60] Hence, even for one relatively simple setup, the properties of the plasma generated can differ significantly.

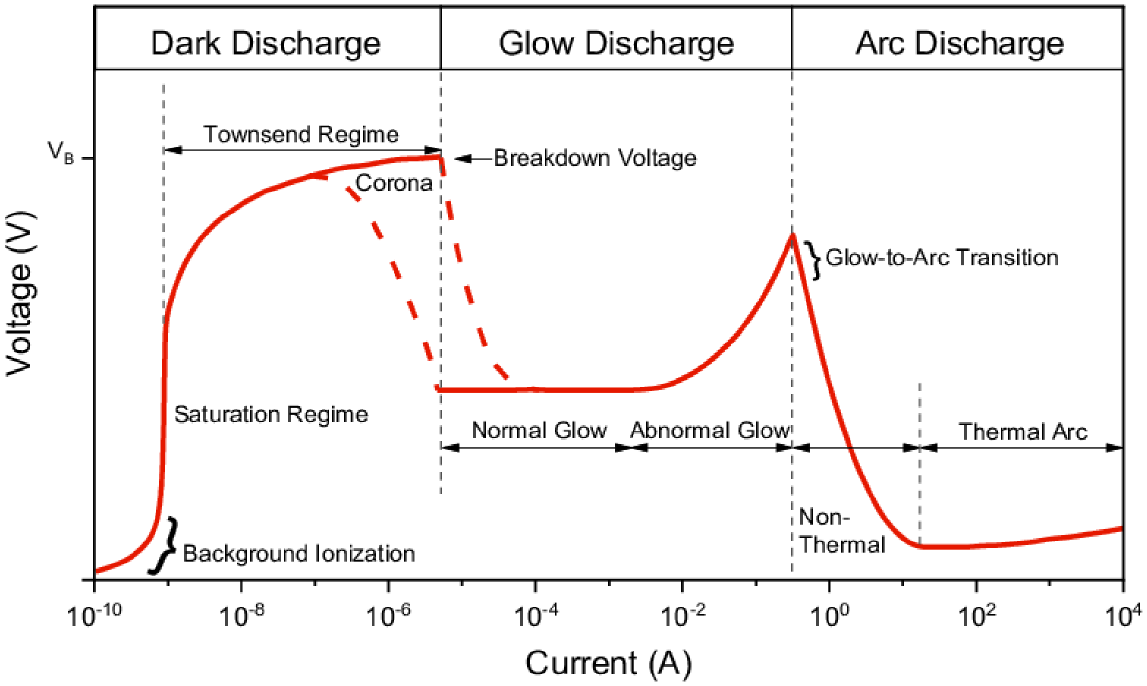

Figure 4: V-I curve for a low-pressure DC gas discharge, showing the different stages (dark discharge, glow discharge and arc discharge) and the transitions between them.[59]

Although Figure 4 corresponds to plasmas at reduced pressure, the same discharge types (dark, glow and arc discharges) exist at atmospheric pressure as well. For example, one of the most common plasma reactor types used for gas conversion is a gliding arc (GA) discharge, which is typically operated at atmospheric pressure. In its classical configuration, a gas flows between two diverging flat electrodes on which a potential difference is applied, leading to the formation of an arc discharge at the shortest interelectrode distance. The arc is carried with the gas flow, increasing in length due to the diverging electrodes, until the delivered power becomes insufficient to sustain the arc. At this point, the arc extinguishes and simultaneously a new arc is formed at the shortest interelectrode distance, after which the entire process repeats itself.[12] Figure 5 shows a picture of this type of GA discharge. Multiple different configurations exist for GA reactors[28,61–70], such as a gliding arc plasmatron (GAP) where the arc is stabilized in the center by a reverse vortex flow, increasing both the residence time as well as the fraction of gas transforming into plasma.[63,65] Nevertheless, the main principle of operation remains the same for all GA reactors.

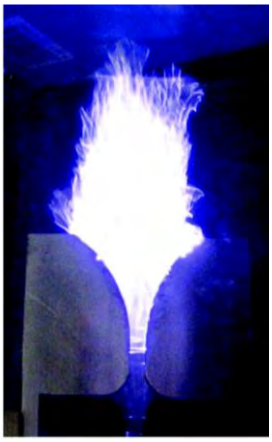

Figure 5: Picture of a GA plasma in a classic configuration.[12]

As mentioned, glow discharges can also be generated for relatively simple setups at atmospheric pressure. A typical configuration for an APGD consists of a cathode pin facing an anode plate, with gas flowing axially with respect to the pin[71–78], though some alternative configurations are also reported[79–82]. The applied current is usually in the order of 10^{-2} A, and to prevent glow-to-arc transition, the current is often limited by the use of a large external ballast resistor.[60,71–73,82] Figure 6 shows a picture of a typical glow discharge.

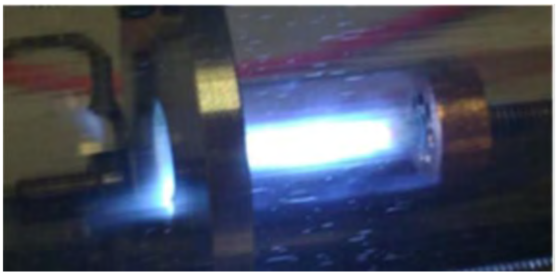

Figure 6: Picture of an APGD in a vortex flow configuration, with CO_2 as discharge gas.[71]

Both plasma types have been studied for CO_2 and CH_4 conversion, as is shown in Figure 3. Generally, GA reactors yield very good efficiencies, easily reaching the efficiency target, yet the total conversion so far seems to be limited to ca. 40 %.[12] It is assumed that one of the main reasons for this limited conversion is the limited fraction of gas flowing through the active plasma region, as deduced from a multidimensional model of a GAP used for CO_2 splitting, even though it is already improved compared to a traditional GA configuration due to the reverse vortex flow.[65] On the contrary, some data points corresponding to an APGD reactor present a total conversion between 80 and 90 %, with efficiencies similar to the ones obtained for GA reactors.[12] Nevertheless, these specific data points originate from one paper only[74], and have not been reproduced since then. Hence, more research is clearly needed to evaluate the true potential of APGD reactors.

The other plasma reactor types indicated in Figure 3 are briefly described as follows:

- A dielectric barrier discharge (DBD) reactor consists of two electrodes and has at least one dielectric barrier between them. Typically, these reactors operate at temperatures close to room temperature and therefore they are often combined with a catalytic packing, in contact with the plasma.[12,43,83–85]
- A corona discharge occurs for a sufficiently large electric field near thin wires, sharp points or edges. These are always non-uniform and have a luminosity close to the sharp electrode, while the charged particles are dragged to the other electrode by weak electric fields.[12,86,87]
- In spark discharge reactors, a streamer connects two electrodes but the power provided is constricted, such that it cannot evolve into a stationary arc. As a result, an initiation of streamers develop into highly energetic spark channels, which extinguish and reignite periodically, similar to what happens in nature with lightning.[12,88–90]
- Nanosecond pulsed discharges rely on repetitively pulsed excitation through a ns scale pulse rise time and duration, allowing relatively low power consumption,

while still obtaining a highly non-local thermal equilibrium (LTE) state with very high plasma densities.[12,91,92]

- Finally, a plasma can also be generated without any electrodes, but by applying the electrical power as microwaves (i.e. electromagnetic radiation in the frequency range of 300 MHz to 10 GHz). These reactors are categorized as microwave (MW) plasma reactors, and are also often used for gas conversion applications.[12,27,93–96]

1.5 Confined atmospheric pressure glow discharge (cAPGD)

In 2019, Trenchev et al.[71] presented several reactor configurations for an APGD, tested towards CO_2 splitting. A “basic APGD” involved the typical configuration discussed earlier, i.e., a cathode pin facing an anode plate, with the gas flowing axially with respect to the cathode, through a hole in the center of the anode plate further downstream. A quartz tube surrounds the plasma and the electrodes, which are made from Therma 310S stainless steel, and the cathode also has a tip made from tungsten. This configuration yielded only a limited CO_2 conversion (3.5 – 4.5 %), mainly because the interelectrode distance (and thus the power input) was limited in order to avoid melting of the cathode tip. A “vortex-flow APGD” already led to an improved conversion (max. 8.3 %), as it both increased the residence time of the gas in the active plasma region, as well as the fraction of gas flowing through the same region, while simultaneously decreasing the gas temperature due to the increased turbulence, allowing a larger power input.

The best performance, however, was obtained with a cAPGD. As mentioned, a main limitation for the GAP reactor seems to be the limited gas fraction flowing through the active plasma region[65], and the same is true for both the basic and vortex-flow APGD. Therefore, a high-temperature resistant ceramic tube is used to encapsulate the plasma zone as much as possible, maximizing the fraction of gas treated by the plasma. The cathode is now a stainless steel grooved pin, where the gas flows through the grooves with a high velocity. This again allows a higher power input compared to the basic APGD, as the high gas velocity leads to very efficient cooling of the cathode. A schematic representation of the plasma, ceramic tube and electrodes is given in Figure 7, with the direction of the gas flow indicated.

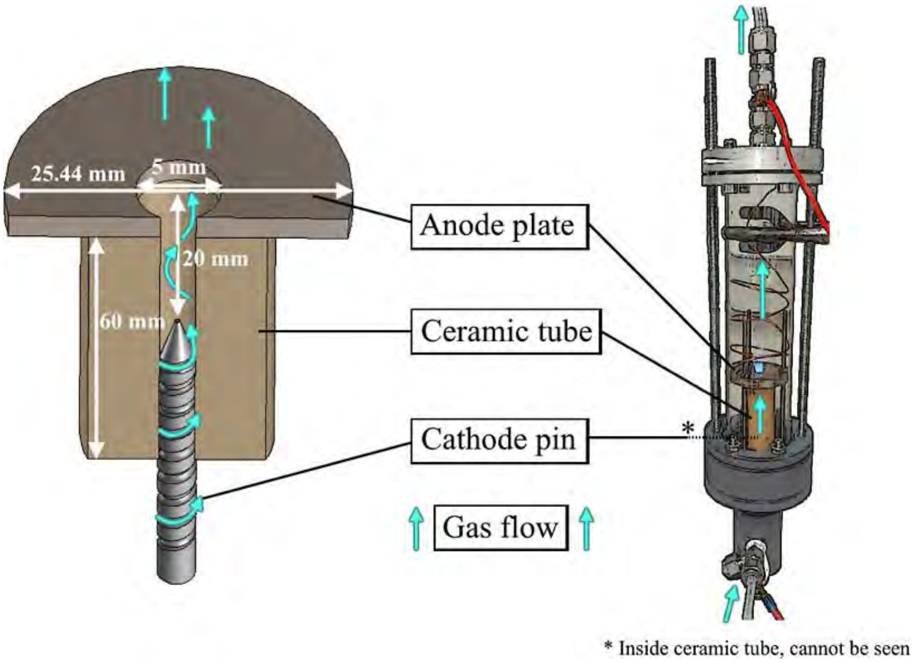

Figure 7: Schematic representation of the cAPGD, with indication of the position of cathode, anode and ceramic tube, the characteristic dimensions, and the direction of the gas flow (turquoise arrows).[97]

As a result, a conversion up to 12.5 % is obtained, which is up to a factor 3 higher than for the other configurations. It should be noted that the energy efficiency is somewhat worse (24 % for the confined design vs ca. 30 % for the basic and vortex-flow design), which is unavoidable in this configuration, as a fraction of energy will be deposited in the ceramic wall, heating it to above 100 °C. Simultaneously, the SEI in this configuration is higher, which is often accompanied by a lower energy efficiency. Nevertheless, the enhancement in conversion compensates for this drop in energy efficiency, and together with its very simple design, the cAPGD is evaluated as the most promising configuration overall.[71]

1.6 Aim of this thesis

In section 1.3, it is shown that DRM has several advantages over the individual CO_2 splitting and CH_4 pyrolysis. Plasma-based DRM has received increasing interest over the past decades, and as a result, several literature values for conversion and energy cost exist, linked to different plasma reactor types. Among these types, the best overall data points from the ones collected by Snoeckx and Bogaerts[12] are obtained with an APGD reactor, although originating from only one paper[74]. Simultaneously, different configurations of an APGD reactor were investigated by Trenchev et al.[71] in terms of their performance towards CO_2 splitting. It was found that a cAPGD holds great potential due to its significantly improved conversion, while still maintaining a relatively high energy efficiency.

Because there is a clear need to investigate the potential of an APGD reactor used for DRM in general, and specifically the confined configuration seems to hold a lot of potential, a logical first research question is:

- *How does the cAPGD setup perform when applied for DRM?*

First, in order to answer this research question, a clear overview needs to be presented on which performance metrics need to be considered and how they are correctly defined, in order to be able to evaluate the performance of any plasma reactor properly. This overview will be presented and discussed in Chapter 2. Afterwards, the research question above will be addressed in detail in Chapter 3, discussing the obtained results and observed trends for DRM experiments carried out with the cAPGD reactor.

A second major topic will be how soot formation affects the performance. Indeed, for DRM performed by thermal catalysis, this is a major obstacle as it leads to catalyst deactivation. In section 1.3.2, we already mentioned how for plasma-based CH_4 pyrolysis soot formation leads to several issues.[29,30] Serious carbon deposition, with associated stability issues, is also observed for DRM carried out with other plasma types, such as MW reactors[98], but also for the APGD.[74,77] When this is problematic, often another reactant is added that can help reduce the rate of soot formation, leading to our second research question:

- *How do additional reactants next to CO_2 and CH_4 change the performance of the cAPGD?*

Often N_2 or noble gases such as He or Ar are added to reduce soot formation and stabilize the plasma.[30,35] While at some conditions their addition can have a beneficial effect on the performance overall, this is not always the case.[30,35,51,99] In addition, these gases remain present in the product stream, and therefore the process always requires a separation stage further downstream. Other gases that can be added, while being able to reach a certain level of conversion, are O_2 and H_2O. Both are known to be effective reactants when it comes to reducing soot formation[42,77,100–104] and their effect on DRM in a cAPGD will be investigated in this thesis. In Chapter 4, experiments carried out when a small fraction of O_2 is added (so-called oxy-CO_2 reforming of methane, OCRM) are discussed in terms of their performance, while also analyzing the carbon deposition in more detail. Simultaneously, a multi-dimensional model, constructed within the research group PLASMANT, is applied to these experiments to provide more insight in the underlying chemistry. In Chapter 5, the addition of H_2O (BRM) is investigated, while the performance is compared with the available literature on plasma-based BRM, as well as the previously discussed DRM and OCRM carried out with the cAPGD reactor.

We started the introduction by explaining the need for CCU, and how in this regard plasma-based CO_2 and CH_4 conversion can play a role. Therefore, it is important to also address the following final research question:

- *How do DRM, OCRM and BRM in a cAPGD compare to each other in terms of environmental and economic impact?*

This topic is addressed in Chapter 6, based on an LCA and TEA, performed by our external collaborators but using our data, applied to the overall best results for each of these three reactions. These three processes are not only compared to one another, but also with the current state-of-the-art, to evaluate the overall potential of plasma-based syngas production. Finally, a conclusion is provided based on these research questions in Chapter 7, as well as a future outlook.

Chapter 2 Performance metrics for plasma-based CO_2 and CH_4 conversion[1]

2.1 Introduction

A performance metric can be described as a measure to evaluate the efficiency, effectiveness, and quality of a system, process, or entity[105]. For plasma-based gas conversion, performance metrics specifically indicate how (un)successful a plasma reactor is regarding the applied reaction, and serve as objective parameters that can be used to compare different reactors or different reactions with each other. In this chapter, we will define the main performance metrics for DRM, i.e., the reactant conversion, the product selectivity and yield, the energy cost and the energy efficiency. Each of these metrics will be used throughout this thesis. Some performance metrics, such as energy efficiency, can be defined in various ways, which is also addressed in this chapter. Finally, note that the syngas ratio (i.e. H_2/CO) is also an important performance metric for DRM, but will not be discussed here in detail, as this is already done in section 1.3.4.

2.2 Reactant conversion

The first performance metric that we discuss is the reactant conversion. The closer this value gets to 1 (or 100 %), the better the performance, as it means more reactant has reacted away. The definition for the conversion of an individual reactant i, χ_i, is given as:[12]

$$\chi_i = \frac{\dot{n}_i^{in} - \dot{n}_i^{out}}{\dot{n}_i^{in}} \tag{1}$$

---

[1] This chapter includes section 4 and 5 of the following paper:
Plasma-based CO_2 conversion: How to correctly analyze the performance?
B. Wanten*, R. Vertongen*, R. De Meyer, A. Bogaerts
Journal of Energy Chemistry, 86, 180–196 (2023).
https://doi.org/10.1016/j.jechem.2023.07.005
*Shared first author

In equation (1), $\dot{n}_i$ stands for the molar flow rate of reactant i. The superscripts in and out indicate whether it concerns the value at the reactor inlet (before the reaction takes place) or the reactor outlet (after the reaction has taken place).[12]

Two general aspects should be considered in order to solve this equation. First, since multiple gases are present in the output gas mixture upon conversion of CO_2 and CH_4, analysis of the gas composition throughout this thesis is done via gas chromatography (GC) measurements. Indeed, GC allows proper separation and accurate quantification of all components.[106,107] Through calibration curves, a linear relationship between the measured peak areas and the volumetric or molar fraction (i.e., expressed in vol% or mol%) of each component in the mixture is obtained. Note that indeed because the GC samples at constant temperature and pressure, volumetric fractions can be considered equal to molar fractions. However, fractions are not the same as the individual flow rates of each species. Expressing equation (1) in terms of fractions leads to equation (2):

$$\chi_i = \frac{\frac{\dot{n}_i^{in}}{\dot{n}_{tot}^{in}} - \frac{\dot{n}_{tot}^{out}}{\dot{n}_{tot}^{in}} \cdot \frac{\dot{n}_i^{out}}{\dot{n}_{tot}^{out}}}{\frac{\dot{n}_i^{in}}{\dot{n}_{tot}^{in}}} = \frac{y_i^{in} - \frac{\dot{n}_{tot}^{out}}{\dot{n}_{tot}^{in}} \cdot y_i^{out}}{y_i^{in}} \tag{2}$$

With y_i the molar or volumetric fraction of reactant i (which are obtained through GC measurements) and $\dot{n}_{tot}$ the sum of the molar flow rates of all species, i.e., both reactants and products. A second general aspect that needs to be considered is that, as can be seen, solving equation (2) requires not only knowledge on the fractions of the reactants, but also the output-to-input ratio of the total molar flow rates (or volumetric flow rates at constant temperature and pressure), also called the flux ratio.[108] Typically this value is above 1 for DRM, as the stoichiometry in reaction (R3) shows that the total amount of molecules (thus, the molar or volumetric flow rate) rises upon conversion. This ratio can be obtained through various methods, specifically the addition of a standard component in the output gas stream, the use of a volumetric flow meter, or (when certain conditions are met) through the mass- and/or atom balances. When this is done, the general definition for reactant conversion becomes:[108]

$$\chi_i = \frac{y_i^{in} - \alpha \cdot y_i^{out}}{y_i^{in}} \tag{3}$$

With α representing the flux ratio. Finally, note that in Figure 3 the x-axis represents “total” conversion. This is a weighted average of all reactant conversions, with the input fraction of the reactants acting as weighing factor. This value provides the conversion of the gas mixture as a whole, without specifying the individual conversion of each reactant separately. The definition for total conversion is given by equation (4):

$$\chi_{tot} = \sum_{i} \left(y_i^{in} \cdot \chi_i\right) \tag{4}$$

It is important to note that other scientific fields do not use the concept of total conversion. Nevertheless, this parameter is quite commonly used within the plasma-based gas conversion community, and the formulas in which it is used are carefully checked for their validity.

2.3 Product selectivity and yield

Aside from conversion, product selectivity and yield are two other critical performance metrics. Product selectivity expresses how much of one specific product is formed, relative to all other products. The product yield is the combination of conversion and product selectivity, and shows how much a particular product is formed, relative to the theoretical maximum amount that could have been formed. When there are no significant side reactions, as in pure CO_2 splitting, expressing a selectivity or yield is not necessary. For (R1), all CO_2 is converted into CO and O_2 (with negligible amounts of other products, such as O_3), and thus, there is a fixed selectivity towards CO and O_2. The yield of CO or O_2 is not fixed, but it gives no extra information compared to the conversion. For DRM, on the other hand, by-products can be formed. Therefore, it is more interesting to report values that express the degree to which a desired product is produced, and even necessary when comparing conditions in one setup or comparing setups with each other. The atom-based (A-based, in this case either the carbon-, hydrogen- or oxygen-based) selectivity for product j, S_j^A, is defined as:

$$S_j^A = \frac{\mu_j^A \cdot \alpha \cdot y_j^{out}}{\sum_i \left(\mu_i^A \cdot \left(y_i^{in} - \alpha \cdot y_j^{out}\right)\right)} \tag{5}$$

With μ^A the stoichiometric coefficients (i.e., the number of atoms A per molecule). The sum of the selectivities for the same base-atoms should be 100 % when all products are considered, because it represents the distribution of the atoms among the products that are formed.

The atom-based yield of product j, Y_j^A, is defined as:

$$Y_j^A = \frac{\mu_j^A \cdot \alpha \cdot y_j^{out}}{\sum_i(\mu_i^A \cdot y_i^{in})} \tag{6}$$

In this case, the sum of the yields for the same base-atom should be equal to the conversion of the reactants containing the same base-atom, when all products are considered. Indeed, product yield expresses the actual amount of a product relative to the theoretical maximum amount that can be formed of that same product. Mathematically, it can be considered as the product of conversion and selectivity for the same base-atom:

$$Y_j^A = S_j^A \cdot \chi_i^A = \frac{\mu_j^A \cdot \alpha \cdot y_j^{out}}{\sum_i\left(\mu_i^A \cdot \left(y_i^{in} - \alpha \cdot y_j^{out}\right)\right)} \cdot \frac{\sum_i\left(\mu_i^A \cdot \left(y_i^{in} - \alpha \cdot y_j^{out}\right)\right)}{\sum_i(\mu_i^A \cdot y_i^{in})} \tag{7}$$

We should address that until this point, we considered all products to remain in the output gas stream. However, this is not the case. With the experiments performed, a cold trap was always used to condense the liquid product fraction, which mainly consisted of H_2O. Additionally, solid carbon deposition is often observed to some extent. A selectivity and yield for these products can be defined, but a distinction needs to be made between the flux ratio before and after condensation/deposition, as the total number of molecules in the gas flow decreases upon condensation/deposition of products. A relationship between the flux ratio before and after condensation/deposition (α^{init} and α^{fin}, respectively) is given by equation (8):

$$\alpha^{init} = \frac{\alpha^{fin}}{1 - \sum_k y_k^{out}} \tag{8}$$

With $\sum_k y_k^{out}$ representing the sum of all fractions corresponding to the liquid and solid products, when taking into account all gaseous, liquid and solid products (i.e., the fraction of these products when they were still in the gas stream). The selectivity and yield corresponding to these products can then be calculated through equation (5) and (6), on the condition that $\alpha^{fin} \cdot y_j^{out}$ is replaced by $\alpha^{init} \cdot y_k^{out}$. Of course, y_k^{out} can be difficult or impossible to derive, unless it concerns one well defined product. As we will discuss in the next chapters, the liquid fraction mainly consisted of H_2O, while other liquid products and the solid fraction were only present in significantly lower amounts. Because of this, the fraction (as well as selectivity and yield) of H_2O can be derived through atom or mass balance equations, since it becomes the only unknown.

2.4 Energy cost

The energy cost expresses the amount of energy consumed by the reaction, relative to the amount of reactants converted or, alternatively, the amount of desired products formed. In general, this comes down to two general equations representing a "conversion-based" (equation (9)) and a "production-based" energy cost (equation (10)):

$$EC_{conv} = \frac{P}{\sum_i \dot{n}_i^{conv}} \tag{9}$$

$$EC_{prod} = \frac{P}{\sum_j \dot{n}_j^{out}} \tag{10}$$

With $\dot{n}_i^{conv}$ the amount of moles i converted per unit of time. The unit with which the energy cost is expressed can vary, depending on the unit with which power and flow rate are defined, but usually it is expressed in kJ/mol or (as is done in Figure 3) eV/molecule. Often kJ/L is used as well, but this requires that the reference temperature and pressure at which the flow rate is defined should be indicated. In this thesis, we apply the definition used by Bronkhorst[109], i.e., we use normal liter (Ln) per unit of time when it represents the volumetric gas flow rate at 0 °C and 1 atm, and standard liter (Ls) when it corresponds to 20 °C and 1 atm. Also note that for the power P, we have to distinguish between the actual power deposited in the plasma (i.e., the plasma power), the power delivered by the power supply unit (PSU) and the overall consumed power by the PSU (i.e., the plug power). All three can be obtained, but unless mentioned otherwise, we always consider plasma power.

Transforming equations (9) and (10) to express them in terms of fractions instead of flow rates, results in the following:

$$EC_{conv} = \frac{SEI}{\chi_{tot}} \tag{11}$$

$$EC_{prod} = \frac{SEI}{\alpha \cdot \sum_j y_j^{out}} \tag{12}$$

With SEI standing for "specific energy input", which is the ratio of power over the total input flow rate.[12] In the case of DRM, the products considered in equation (12) are often only CO and H_2. Therefore, in the following chapters we will rather use the term "syngas-based energy cost", due to it representing the amount of energy consumed relative to the amount of syngas formed, excluding any by-products. Finally, it should be noted that Pinhão et al.[108] correctly stated that the SEI does not take into account the change in molar flow rate across the reactor, and thus despite what the name suggests, it only provides an approximate indication of the energy density deposited in the gas. However, since the ratio of applied power over input flow rate is a common factor in many equations and is often described as SEI in literature as well, we always write it like this.

2.5 Energy efficiency

In general, energy efficiency can be described as a measure on how efficiently the required energy to run a certain reaction or process is provided. A common definition to express the energy efficiency η for a chemical reaction is presented as follows:[12]

$$\eta = \frac{\chi_{tot} \cdot \Delta H^\circ}{SEI} \tag{13}$$

With ΔH° the standard reaction enthalpy (note that the GC measurements take place downstream of the reactor, at the same temperature and pressure, for both input and output mixtures). For an endothermic reaction (i.e., a positive reaction enthalpy), this ratio is indeed a correct representation of the energy efficiency, as it equals 0 when there is no conversion, and 1 (or 100 %) when all applied energy is used to carry out the reaction and stored as chemical energy in the product output. However, special attention should be given to the "units" for which the standard reaction enthalpy is defined. In this case, as we are using the total conversion (representing the amount of reactants converted), the reaction enthalpy should also be defined in kJ per mol reactant, to make this equation valid. Specifically for DRM, often the reaction enthalpy of 247.3 kJ/mol is used, as given by reaction (R3). However, this value is expressed per mole CO_2 or per mole CH_4. Therefore, specifically for the DRM reaction a factor 2 should be added in the denominator.

Of course, the formation of by-products will alter the value for the overall reaction enthalpy. Hence, one has to include all products and reactants to determine a reaction enthalpy correctly. To account for this aspect, we transform this equation such that individual formation enthalpies H^f are used, given that a reaction enthalpy can be deconstructed into them as given by Hess's law. This leads to equation (14):

$$\eta = \frac{\alpha \cdot \sum_j \left(y_j^{out} \cdot H_j^f \right) - \sum_i \left(y_i^{in} \cdot \chi_i \cdot H_i^f \right)}{SEI} \tag{14}$$

Both equation (13) and (14) are also sometimes called the "chemical energy efficiency". However, in some situations these definitions are not ideal to obtain an energy efficiency. For example, a consequence of having to include all products means that also all the liquid products (in non-negligible amounts) need to be taken into account. As already mentioned in section 0, the molar fraction of these products (before condensation, in the original gas stream) can be very difficult or impossible to measure or derive. In that case, equation (14) cannot be solved. Ignoring, e.g., the formation of H_2O can also lead to a significant overestimation of the energy efficiency, as it has a highly negative reaction enthalpy.

For this reason, an alternative definition exist, which is also called the "fuel (production)" energy efficiency, and exists in two general forms:

$$\eta = \frac{\alpha \cdot \sum_j \left(y_j^{out} \cdot HHV_j \right)}{SEI + \sum_i \left(\left(y_i^{in} - \alpha \cdot y_i^{out} \right) \cdot HHV_i \right)} \tag{15}$$

$$\eta = \frac{\alpha \cdot \sum_j \left(y_j^{out} \cdot HHV_j \right)}{SEI + \sum_i \left(y_i^{in} \cdot HHV_i \right)} \tag{16}$$

In equation (15) and (16), HHV stands for "higher heating value" of a species, which is a measure for the energy that is released upon full oxidation of the corresponding species. More specifically, it is (in terms of absolute value) equal to the reaction enthalpy upon conversion of the species with O_2 into their most thermodynamically stable products. In this case, these products are CO_2 and/or H_2O, which by definition have a HHV equal to 0 kJ/mol, together with O_2. Essentially, HHV's and formation enthalpies only differ in terms of these two zero-reference points (CO_2 and H_2O (liquid) instead of C (graphite) and H_2). Note that HHV describe the reaction enthalpy with the produced H_2O considered to be fully condensed into the liquid phase. When considering H_2O in the gas phase, and thus not taking into account the additional energy released upon condensation, lower heating values (LHV) for the different components are used instead.

The fuel energy efficiencies are structured such that the applied energy and the heat of combustion (i.e., the energy that would come free upon full oxidation) that can be attributed to the reactants are both in the denominator, with only the heat of combustion that can be attributed to the products in the numerator. Together with the fact that the

HHV's cannot be negative (since the most thermodynamically stable components are the zero-reference), the energy efficiency value will at all times be between 0 and 1. As such, this definition is still a valid way to express energy efficiency, even though it is expressed differently compared to equation (14).

Nevertheless, even for this type of definitions, there are various slightly different forms. Equation (15) and (16) differ in terms of whether they include only the converted amount of reactants, or the initial amount of reactants. This difference is important as, when all products are included, the former represents the fraction of "transformed" energy that is not lost as heat or radiation, but stored as chemical energy in the products. In other words, equation (15) gives a (theoretical) value of 1 when the reaction proceeds without heat losses, independent of how much reactant is converted. Because equation (16) includes the initial amount of reactants, it will only reach a value of 1 when the reaction proceeds without heat losses, but also only when the reactant is fully converted. With this definition, the heat of combustion attributed to unconverted reactants is considered as another form of "lost" energy.

Finally, in literature often only the desired products (e.g., syngas for DRM) are considered for these definitions and not all products, even when by-products are present in significant amounts. In contrast to equation (13) and (14), where the reaction enthalpy should correspond to the overall reaction process (involving all side-reactions), this does not make equation (15) and (16) invalid. Rather, the heat of combustion that can be attributed to the by-products is simply considered as another form of "lost" energy. This, of course, provides another practical advantage over the chemical energy efficiency, as despite the fact that it can be difficult to measure all products accurately, a fuel energy efficiency can still be obtained. To summarize, an energy efficiency of 1 (or 100 %) would mean for:

- Equation (15), incl. all products: a reaction that proceeds without heat losses.
- Equation (16), incl. all products: a reaction that proceeds without heat losses and 100 % conversion of all reactants.
- Equation (15), incl. only the desired products: a reaction that proceeds without heat losses and 100 % selectivity towards the desired products.
- Equation (16), incl. only the desired products: a reaction that proceeds without heat losses and 100 % yield of the desired products.

To conclude this section, we present a numerical example to illustrate the variety in results for energy efficiency depending on the definition used, which we plot in Figure 8. The various definitions are applied to a DRM dataset, given in Table 1.

Table 1: Numerical example for DRM in a warm plasma with a SEI of 240.6 kJ/mol; flow rates of gases at the inlet, and unreacted gases and products at the outlet.

Flow rate (mLs/min)	**CO_2**	**CH_4**	**H_2**	**CO**	**C_2H_2**	**C_2H_4**	**C_2H_6**	**H_2O**
In	650	350	0	0	0	0	0	0
Out	300	90	375	575	15	2	0.4	125

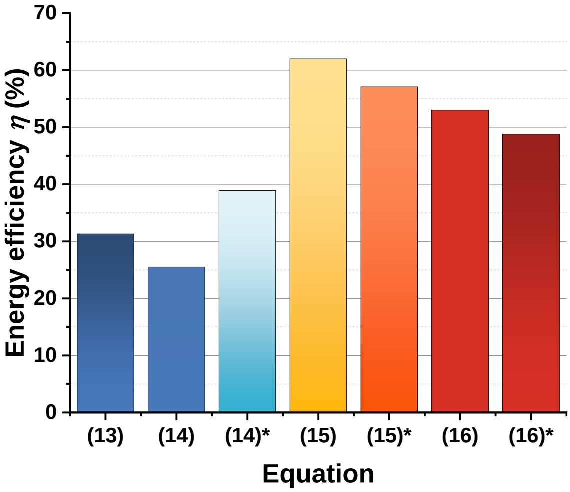

*Figure 8: Numerical example of the energy efficiency calculated according to the various definitions for DRM. * indicates that only syngas is taken into account as product (i.e., H_2O and C_2H_X are ignored). For eq. (13), the "ideal" stoichiometry is used (described by reaction (R3) for DRM) with the reaction enthalpy of 247 kJ/mol divided by 2.*

As can be seen, the values can differ significantly. As a result, we consider energy cost as a more objective parameter, hence this will mainly be used throughout this thesis to evaluate the performance of the reactor. Only in Chapter 5 we will use energy efficiency values, specifically based on equation (15), and when comparing our values with energy efficiencies from literature, the latter will be re-calculated through equation (15), to allow a fair comparison.

Chapter 3 Dry reforming of methane in an atmospheric pressure glow discharge: confining the plasma to expand the performance[2]

Abstract

In this chapter, we present a cAPGD reactor, applied towards the DRM. An excellent performance is achieved, i.e., a CO_2 and CH_4 conversion of 64 % and 94 %, respectively, at an energy cost of 3.5–4 eV/molecule (or 310–380 kJ/mol). The confinement of the plasma, such that the dimensions of the gas pathway are similar to the dimensions of the active plasma region, maximizes the fraction of gas passing through this region. In addition, the close proximity of the high-temperature resistant ceramic tube to the plasma could facilitate a wall-stabilization effect, and the confined configuration allows applying a relatively high SEI, leading to the high overall conversion. An extensive literature comparison makes clear that these results are among the best reported for all types of plasma reactors in literature. The main product formed is syngas, with H_2O and C_2H_2 as by-products. Despite these promising aspects, the syngas ratio remains limited to maximum 0.64, which limits the value of the potential products that can be derived in a later stage.

---

[2] This chapter is based on:
Dry reforming of methane in an atmospheric pressure glow discharge: Confining the plasma to expand the performance
B. Wanten, S. Maerivoet, C. Vantomme, J. Slaets, G. Trenchev, A. Bogaerts
Journal of CO_2 utilization, 56, 101869 (2022)
https://doi.org/10.1016/j.jcou.2021.101869

3.1 Introduction

Since CO_2 and CH_4 are the two main greenhouse gases, their conversion into valuable products is one of the most important subjects in current catalysis, energy and environmental research.[110] As discussed in section 1.3.3, DRM involves the conversion of CO_2 and CH_4 into syngas (CO and H_2), which can be used as building block for several value-added chemicals, including methanol and long-chain hydrocarbons.[50,110–112]

DRM is seen as an attractive alternative for the SRM, which converts CH_4 together with H_2O. The latter is carried out at high temperatures (1023–1223 K) and elevated pressures (14–20 atm), typically on a Ni/Al_2O_3-catalyst bed due to its low cost and selectivity.[113] In addition, it produces syngas with a H_2/CO ratio of 3, or even higher due to the water-gas shift (WGS) reaction taking place simultaneously[113], which is higher than what is needed for the synthesis of these value-added chemicals.[50,110–112] Therefore, a lot of research has been and is being performed on DRM, also due to its large potential as future process to produce syngas from biogas in a more sustainable way. However, DRM through thermal catalysis is not yet being applied on a large scale, as regular catalyst deactivation (due to solid carbon formation) severely limits its potential.[50,110,111]

As discussed in Chapter 1, using plasma technology for DRM seems to be an attractive route.[12] A plasma reactor can easily reach the required temperatures for the DRM reaction, it only requires electricity and it can be turned on and off fast, so it can handle the intermittent character of renewable energy sources.[10,12] Indeed, when excess energy is available, it can be used by plasma reactors to create value-added chemicals. Therefore, plasma creates an ideal pathway for chemical energy storage, providing an attractive alternative for large batteries.[97] Overall, it provides a high flexibility and modularity[11], and the use of several types of plasma reactors for DRM has already been reported extensively in recent decades.[10,12]

Nevertheless, Figure 3 (see section 1.3.3) shows that many plasma reactors still suffer from limitations, leading to either a limited conversion (as is the case for many GA plasma reactors[12,40,51]) or an energy cost that is too high (which is a common problem for DBD's[12,66,69,114]). Only a spark discharge[89] and especially an APGD[74] were able to combine energy costs below the target set by Snoeckx and Bogaerts with relatively high conversions. In section 1.4, we briefly discussed the different plasma reactor types, incl. glow discharges, which display a tendency towards field emission rather than thermionic cathode emission and typically combine a low current (a few to a few tens of mA) with a high voltage (a few to a few tens of kV).[71] While the exceptionally good results presented by Li et al.[74] make

APGDs appear very promising for DRM, they have not been studied to a large extent.[12,74,77,115,116] In addition, a new promising APGD reactor design was recently presented by Trenchev et al.[71], showing a clear improvement in terms of CO_2 conversion when encapsulating the plasma zone by a high-temperature resistant ceramic material. This cAPGD design has not been tested yet for DRM.

Therefore, in this chapter, we present a study of the performance of a cAPGD towards DRM where its potential is investigated. Experiments were performed for a wide range of currents, flow rates and CO_2/CH_4 ratios and the reactor and different conditions are evaluated in terms of conversion, energy cost and product output. In addition, we provide an updated version of Figure 3 to better highlight our own results with respect to the current state-of-the-art.

3.2 Experimental setup

The APGD plasma reactor under study (Figure 9) consists of a cathode pin and anode plate, both made from stainless steel (Therma 310S). The cathode and the discharge region are fully surrounded by a tube made of MACOR® machinable ceramic, which is sufficiently heat resistant against the nearby plasma.[117] The inner radius of the ceramic tube is 2.5 mm. The cathode contains a groove of ± 1 mm deep, through which the gas can enter the discharge zone. This provides a vortex flow and a high gas velocity close to the cathode, to effectively cool the latter, as well as the ceramic tube inner walls. The anode plate is positioned at the end of the ceramic tube, at a distance of 22 mm from the cathode tip, and contains an opening in the center through which the gas can exit the reactor.

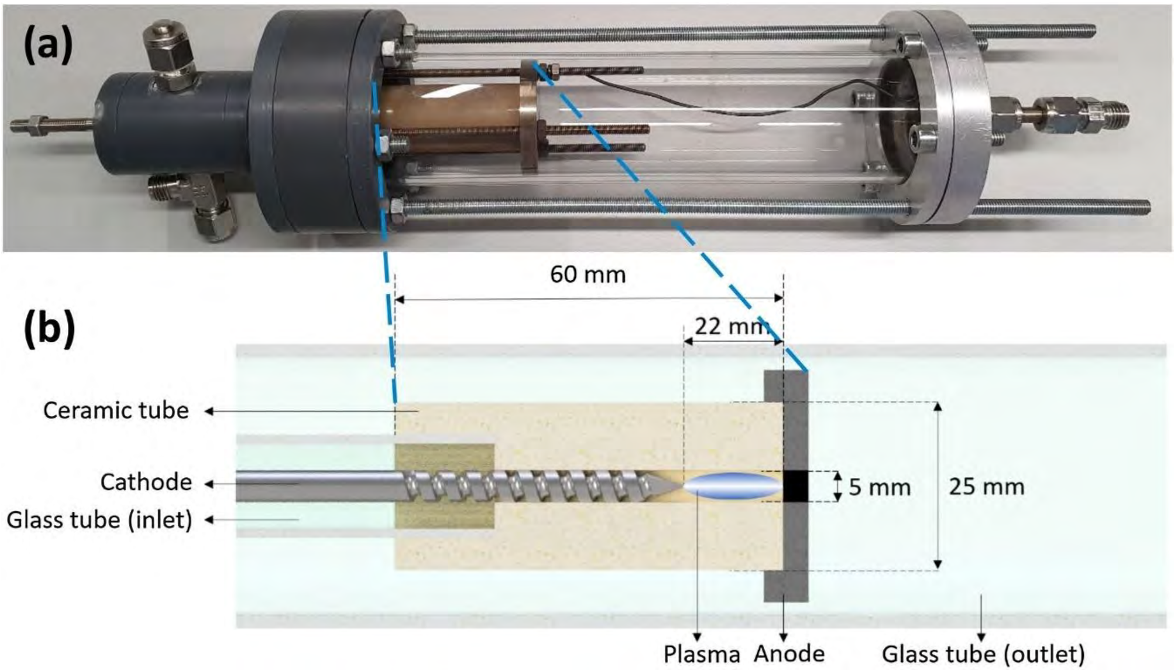

Figure 9: Photograph (a) of the cAPGD plasma reactor and schematic representation (b) with important parts and dimensions indicated.

The entire experimental set-up is presented in Figure 10. The flow rate of all feed gases is regulated by Bronkhorst mass flow controllers (MFCs), and the flow rates are expressed in Ln/min. The gas mixture flowing out of the reactor first goes through a liquid trap to remove any liquid products. The liquid trap is cooled by ice, keeping the temperature locally to ca. 10 °C. The remaining gas mixture is analyzed by means of a Thermo Scientific Trace 1310 GC. For every condition, a blank measurement is performed next to three plasma measurements. N_2 is used as internal standard to account for the effects of gas expansion and of condensation of liquid products on the measured concentrations (i.e., it acts as a measure for the change in total number of moles, specifically in the gas stream), and is added to the gas mixture after the reactor and liquid trap (see supporting information in section 8.1.1). The main performance metrics, presented in Chapter 2, are calculated for each measurement and their weighted averages are presented in the following sections. The error bars on the experimental results are obtained according to the theory of linear propagation of uncertainties.[118,119] Also the liquid fraction is analyzed by means of GC and high-performance liquid chromatography (HPLC) (see details in section 8.1.1).

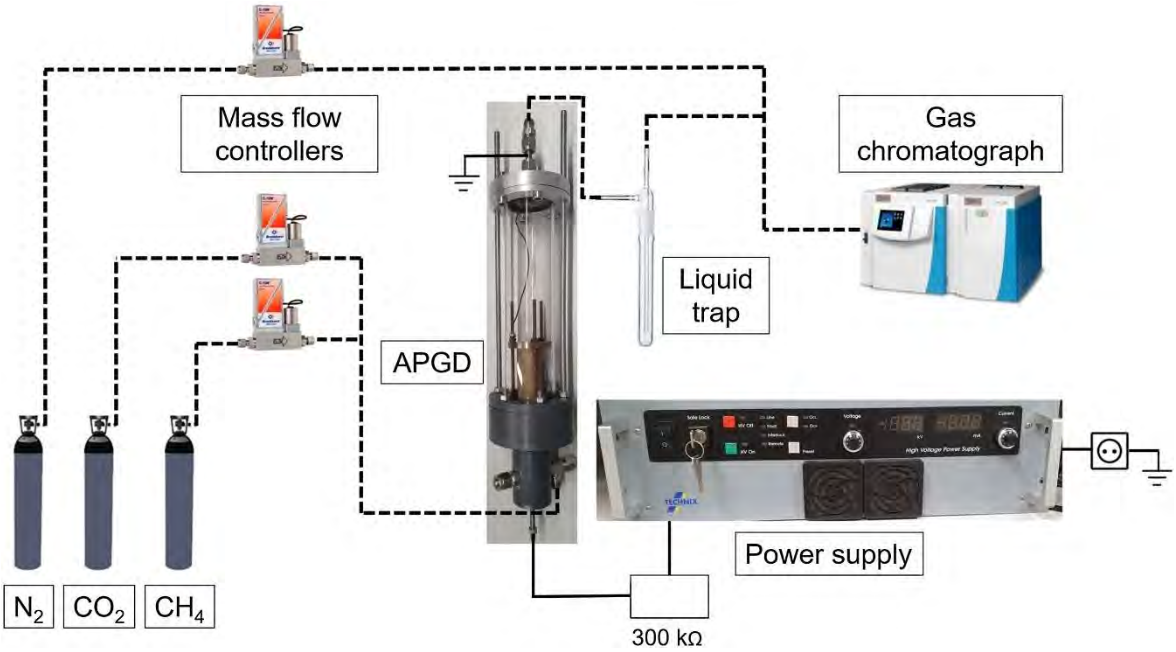

Figure 10: Schematic overview of the experimental set-up. Electrical connections are represented by full lines, gas connections by dashed lines.

The reactor and overall electrical setup described by Trenchev et al.[71] for CO_2 splitting is kept the same for our DRM experiments. A current-controlled high voltage Technix DC power supply capable of supplying up to 30 kV and 40 mA is used to deliver the power to the plasma. The initial voltage has been pre-set each time to 30 kV, after which it drops once the plasma is ignited to a value that can be read directly from the power supply (around 10−15 kV, depending on the applied conditions). The interelectrode distance was kept at 22 mm, and the plasma is sustained in the glow regime by means of three ballast resistors connected in series, with each a resistance of 100 kΩ, a tolerance of 5 % and a temperature coefficient of ± 260 ppm/°C.[120] Specifically, the ballast resistors ensure that the current remains sufficiently low and stable at all times. The plasma voltage as function of the fixed current is presented in Figure 11. The voltage remains fairly high, with only a slight drop at an increased current. This profile closely resembles the profile observed earlier for CO_2 splitting in the cAPGD[71], therefore, together with the stable current obtained, we can consider the plasma to remain in the glow regime upon addition of CH_4. However, as stated by Trenchev et al.[71], a glow-to-arc transition would be indicated by a significant and rapid drop in voltage. As we will show further in this thesis, in particular in Chapter 5, such a drop was sometimes observed at sufficiently high CH_4 input fractions, most likely because of the disturbing effect of deposited solid carbon particles.

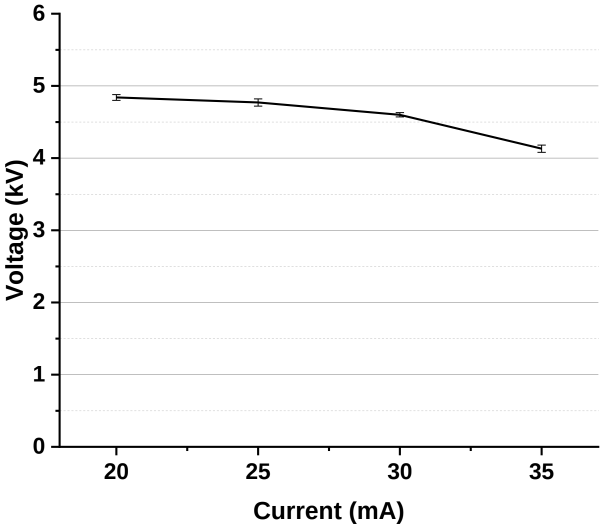

Figure 11: V-I (voltage vs current) characteristic of the cAPGD, at an interelectrode distance of 22 mm for a CO_2-CH_4 mixture with a 75/25 input ratio.

Following the approach by Trenchev et al.[71], the plasma power P_{plasma} can be determined by subtracting the resistor power from the total power, as defined by equation (17).[71,97]

$$P_{plasma} = V_{tot} \cdot I - R_{ballast} \cdot I^2 \tag{17}$$

Here, the ballast resistance $R_{ballast}$ is known, i.e. 300 ± 9 kΩ (error based on the tolerance), and the current I and total voltage V_{tot} can be read from the PSU display. In addition, this approach was validated through initial measurements of the plasma current and voltage by means of a high voltage probe connected to the live electrode (i.e., the reactor's cathode) and a shunt resistor connected to the ground electrode (i.e., the reactor body), both connected to an oscilloscope. The obtained plasma power through both methods only differed by ca. 5 W, which is well within the experimental error margin. As mentioned in Chapter 2, the plasma power and not the overall applied power will be used in the energy cost calculations.

3.3 Results and discussion

First we present the obtained conversions and energy costs as a function of electrical current, gas flow rate and CH_4 fraction in the mixture. Subsequently, we compare our results with the current state-of-the-art on plasma-based DRM through an updated version of Figure 3. Finally, we analyze the product output in terms of syngas ratio, selectivity and yield for the various conditions, and discuss the overall performance and limitations.

3.3.1 Conversion

The CO_2, CH_4 and total conversion are presented in Figure 12, for different currents (a) and flow rates (b), at a CH_4 fraction of 25 %, as well as for different CH_4 fractions, at 35 mA and 1 Ln/min (c), and at 25 mA and 0.5 Ln/min (d).

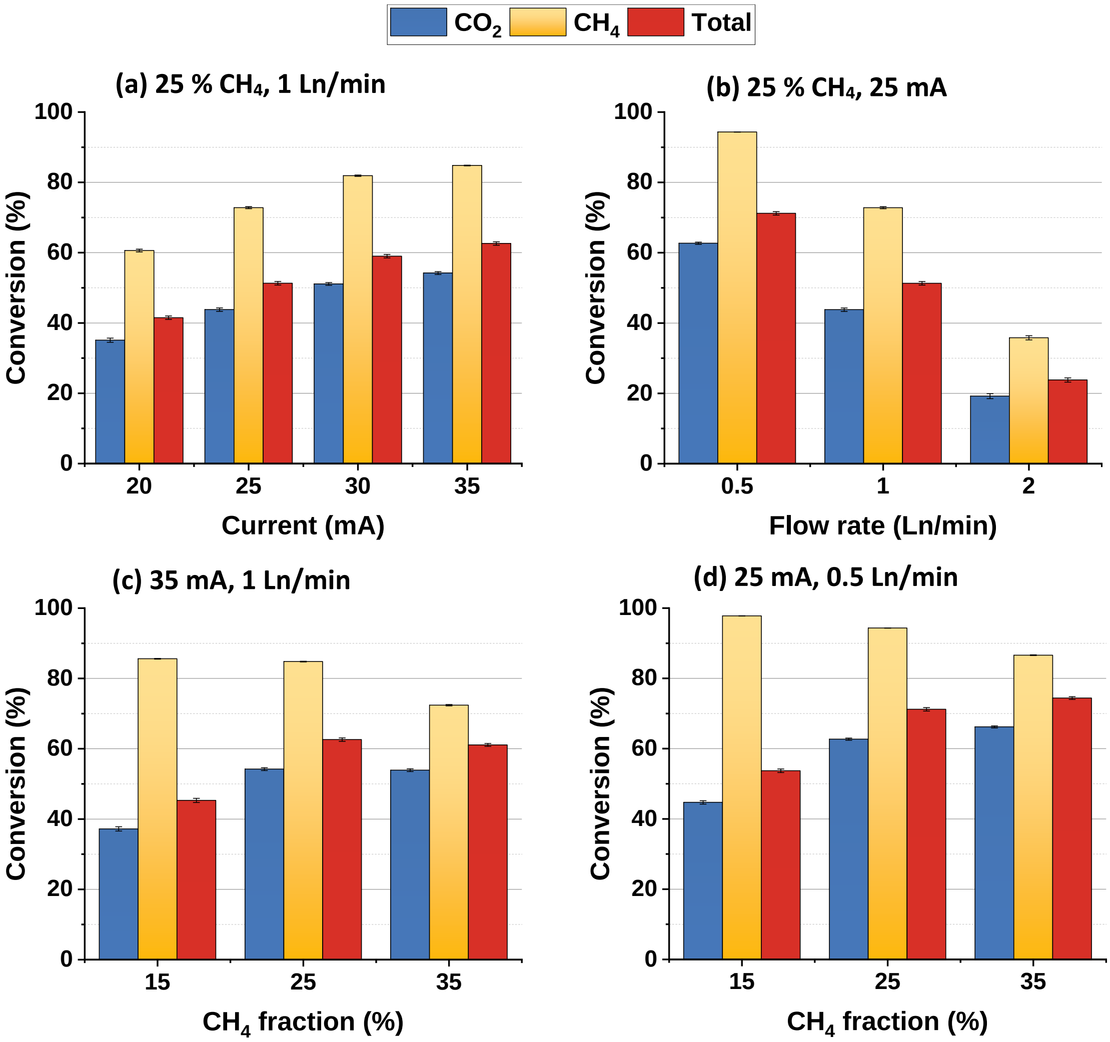

Figure 12: CO_2 and CH_4 conversion, as well as total conversion, for different currents (a), flow rates (b) and CH_4 fractions (c, d). The other conditions (CH_4 fraction, current, flow rate) that are kept constant, are indicated in the figure. Error bars are added, but are often too small to be visible.

It is clear that the CH_4 conversion is much higher than the CO_2 conversion, which makes sense, as the bond breaking energy for a single CH bond (4.48 eV) is much lower than for a double CO bond (5.52 eV).[12,40] Furthermore, a higher current or lower flow rate yields a higher conversion, due to a higher SEI. Note that we could not (much) further increase the current, due to the limits of the power supply and ballast resistors, while decreasing the flow rate further would result in overheating and damage of the ceramic tube and electrodes.

In addition, upon rising the CH_4 fraction in the mixture, the CO_2 conversion clearly rises, while the CH_4 conversion slightly drops. This corresponds to the trends observed in literature.[12,40] According to the chemical kinetics model developed by Cleiren et al.[40], an increasing fraction of CH_4 in the input mixture will give rise to an increased amount of H radicals, which aid in the conversion of CO_2. Simultaneously, by decreasing the CO_2 input fraction the amount of OH radicals decreases as well, which play an important role in CH_4 conversion, explaining the decrease in conversion. As a result of these trends, the total conversion increases significantly from 15 to 25 % CH_4, but remains more or less constant upon further increasing to 35 % CH_4. The latter is attributed to two aspects: the drop in CH_4 conversion will affect the total conversion the most at 35 % CH_4 (as it is simply a larger fraction of the input gas mixture), and at 35 % CH_4, solid carbon formation starts to affect the plasma stability. Indeed, upon increasing the CH_4 fraction, voltage (and thus also power) fluctuations could not be avoided, leading to a clear negative effect on the conversion and the reactor's performance in general. For this reason, we could not obtain reproducible data at CH_4 fractions higher than 35 %.

The above trends as a function of current (or power), flow rate and gas mixing ratio correspond well with other reports in literature – both a higher current and a lower flow rate lead to an increased temperature, favoring the conversion of the highly endothermic DRM.[12] More important, however, is the level of conversion that is reached here. For instance, at 0.5 Ln/min, 25 mA and 25 % CH_4, the CO_2 and CH_4 conversion reach 63.7 ± 0.4 % and 94.28 ± 0.07 %, respectively, leading to a total conversion of 71 ± 3 %. These values are higher than what is typically reported in literature for plasma-based DRM[12] (see also section 3.3.3 below). We can assume that this is a direct effect of confining the glow discharge by the ceramic tube[71]. Indeed, earlier plasma fluid dynamics simulations revealed that the glow discharge plasma exhibits a width of approximately 4 mm, and does not fill the entire reactor if the latter is much wider, which was the case for the basic APGD reactor, studied by Trenchev et al.[71] The same issue also occurs in typical GA plasmas, where the plasma arc is located in the center, and a large fraction of gas passes through the reactor without passing through the active plasma region, as reported in literature multiple times.[40,51,63,68,121] Hence, by inserting a ceramic tube with an inner diameter comparable to the plasma width, we ensure that the plasma fills most of the reactor, and the fraction of gas passing through the active plasma region is maximized. Simultaneously, Trenchev et al.[71] showed that the SEI that can be achieved in this configuration is higher than for other APGD configurations, which benefits the conversion. Finally, the ceramic tube could also facilitate a certain “wall stabilization” effect.[122] Due to the direct contact of the plasma with the ceramic walls, the temperature gradient of the discharge in the radial direction is flattened, i.e. the plasma itself is additionally cooled, while the surrounding gas is additionally heated. This leads to lesser contraction of the plasma (i.e., the plasma stabilizes or “sticks” to the constricting walls), leading to a larger zone where the conditions for CO_2 and CH_4 conversion are fulfilled, in contrast to a non-confined set up. The full effect of wall-stabilized plasmas in general is still under investigation[123], but regardless, confinement of the plasma certainly causes an increase in conversion.

3.3.2 Energy cost

Figure 13 presents the energy cost as a function of current (a), flow rate (b), both again for 25 % CH_4, and as a function of CH_4 fraction, for 35 mA and 1 Ln/min (c), and 25 mA and 0.5 Ln/min (d). We also plot the SEI (black curves, right y-axis).

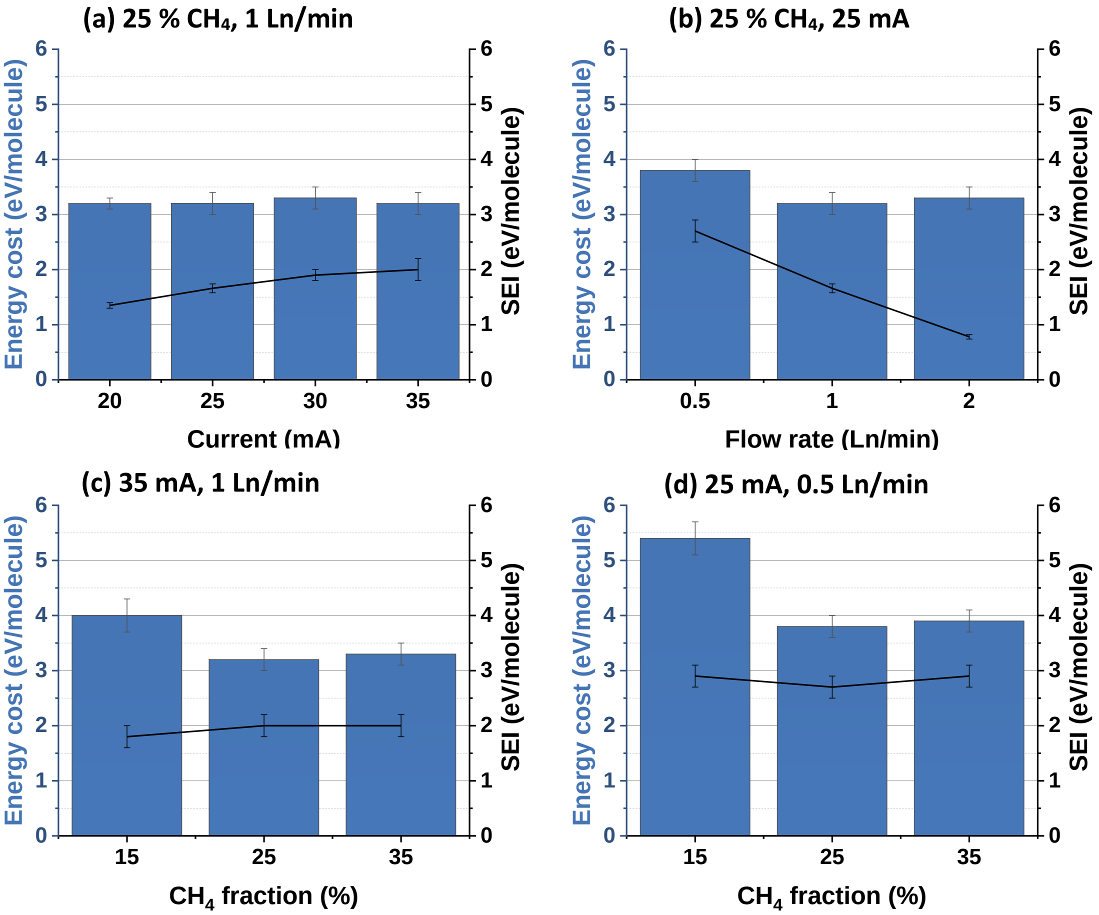

Figure 13: Energy cost as a function of current (a), flow rate (b) and CH_4 fraction (c, d). The other conditions that are kept constant are indicated in the figure. Error bars are added, but are often too small to be visible. The energy cost is calculated from the total conversion and SEI, and therefore, the latter is also plotted for all conditions (black curves, right y-axis).

The energy cost is typically in the order of 3.2−4 eV/molecule, or 310−380 kJ/mol, for all conditions investigated (except at a 15 % CH_4 fraction, where it is a bit higher). Indeed, it remains overall constant as a function of current, and varying the flow rate also has no significant effect (certainly not between 1 and 2 Ln/min), which indicates that the rise in conversion (upon higher current and lower flow rate) is proportional to the rise in SEI. Note that in literature often a higher energy cost is observed for a higher SEI, because the conversion often levels off upon rising SEI.[12] This shows another advantage of the cAPGD reactor: because a high level of conversion can be reached for DRM, it allows for a proportional rise in conversion with respect to the SEI, at least up to a certain level. Indeed, for 0.5 Ln/min the energy cost is slightly higher, probably due to more heat loss towards the walls of the ceramic tube. Of course, when confining the plasma, heat losses to the walls are unavoidable, but we use a material that is relatively non-conductive towards heat, so most of the energy would still be kept inside the discharge zone.

The SEI stays almost constant for different CH_4 fractions, so when comparing the energy cost for the different CH_4 fractions, we observe the opposite trend as for the total conversion. This is logical, because the energy cost is inversely proportional to the total conversion. Indeed, the energy cost drops upon increasing the CH_4 fraction from 15 to 25 %, while it stays more or less constant from 25 to 35 %.

3.3.3 Comparison with state-of-the-art

We can conclude that our best results are obtained at 35 % CH_4, 25 mA and 0.5 Ln/min (highest total conversion, i.e., 74.4 ± 0.4 %, with an energy cost of 3.9 ± 0.2 eV/molecule) and at 25 % CH_4, 35 mA and 1 Ln/min (lowest energy cost of 3.2 ± 0.2 eV/molecule, for still a relatively high total conversion of 62.6 ± 0.5 %). We have now added this data to the literature overview figure presented in section 1.3.3, and updated this overview with additional data points, based on more recent literature.[42,51,84,90,91,95,103,124–127] This is presented in Figure 14, indicating that our results are among the best results reported up to now for plasma-based DRM.

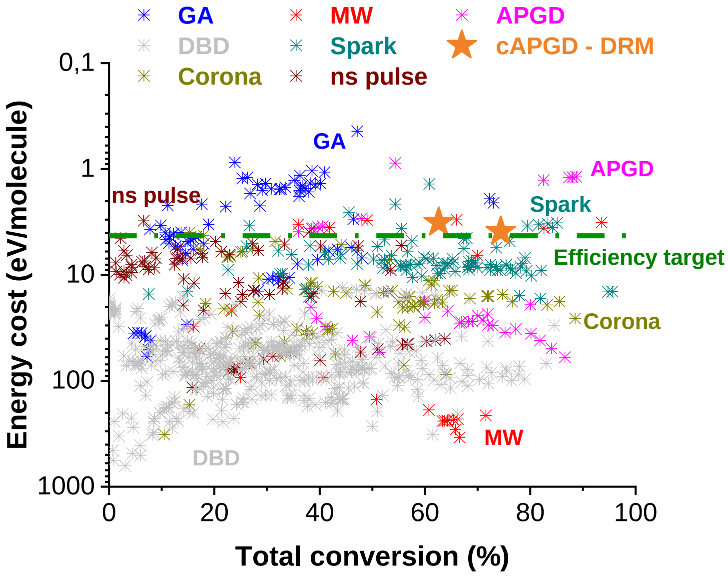

Figure 14: Comparison of literature data collected by Snoeckx and Bogaerts[12], updated by us with additional data points, based on more recent literature[42,51,84,90,91,95,103,124–127]. Our own best results (at 25 % CH_4, 35 mA and 1 Ln/min, and 35 % CH_4, 25 mA and 0.5 Ln/min) are added as orange stars.

The best results obtained with our cAPGD are added as orange stars to this overview (see upper right corner). As we can see, our own results reach a fairly high conversion, at an energy cost better than the efficiency target determined by Snoeckx and Bogaerts.[12] We can link this good performance to the confinement of the plasma by the ceramic tube. It was already demonstrated for CO_2-splitting that this confinement leads to a significant improvement in conversion[71], and our results confirm that the same is true for DRM. Results from many GA reactors stay well below our best results in terms of the combination of total conversion and energy cost.[12,40,51,63,68,121]

There are however a few data points, although originating from only five papers, with still a higher conversion and a lower energy cost combined.[42,74,89,95,126] A spark discharge[89] and another APGD set-up[74] were already mentioned in the introduction, and by updating the overview with more recent literature data, a GA set-up[42] and two MW plasma reactors[95,126] also appear to lead to better results. However, the better results with the spark discharge from Chung et al.[89] and the GA from Li et al.[42] were obtained in combination with catalysts, which typically leads to a higher conversion. Additionally, Li et al.[42] added a small fraction of O_2 to increase the conversion. The addition of O_2 will be discussed in Chapter 4.

As for the MW plasma reactors from Sun et al.[95] and Chun et al.[126], both show through photographs that a significant volume of the reactor is filled by the plasma, mainly due to the significantly higher plasma deposited power (i.e., a few kW), as both works state it increases linearly with SEI. Indeed, due to the fact that these reactors are electrode-free, gas temperatures well above 5000 K can be obtained without causing significant damage. This provides both a high gas fraction treated by the plasma as well as a sufficiently high temperature to reach a very high level of conversion for both CO_2 and CH_4. While their conversion is a bit higher, their energy cost remains comparable to the one obtained with our experiments.

Still, no literature values are better than the ones obtained with the other APGD set-up from Li et al.[74] Nevertheless, it is clear that our cAPGD plasma reactor is very promising for DRM as well, also due to its very simple, inexpensive design and easy operation.

3.3.4 Product output

As stated in sections 1.3.3 and 1.3.4, the goal of DRM is to produce syngas, which can be further converted into methanol, or other valuable chemicals such as olefins and hydrocarbons in the FT process. Therefore, it is important to assess the current performance of our APGD reactor towards syngas formation in its desired ratio. Figure 15 presents the H_2/CO ratio for different currents (a) and flow rates (b) at a CH_4 fraction of 25 %, as well as for different CH_4 fractions at (c) 35 mA and 1 Ln/min and (d) 25 mA and 0.5 Ln/min.

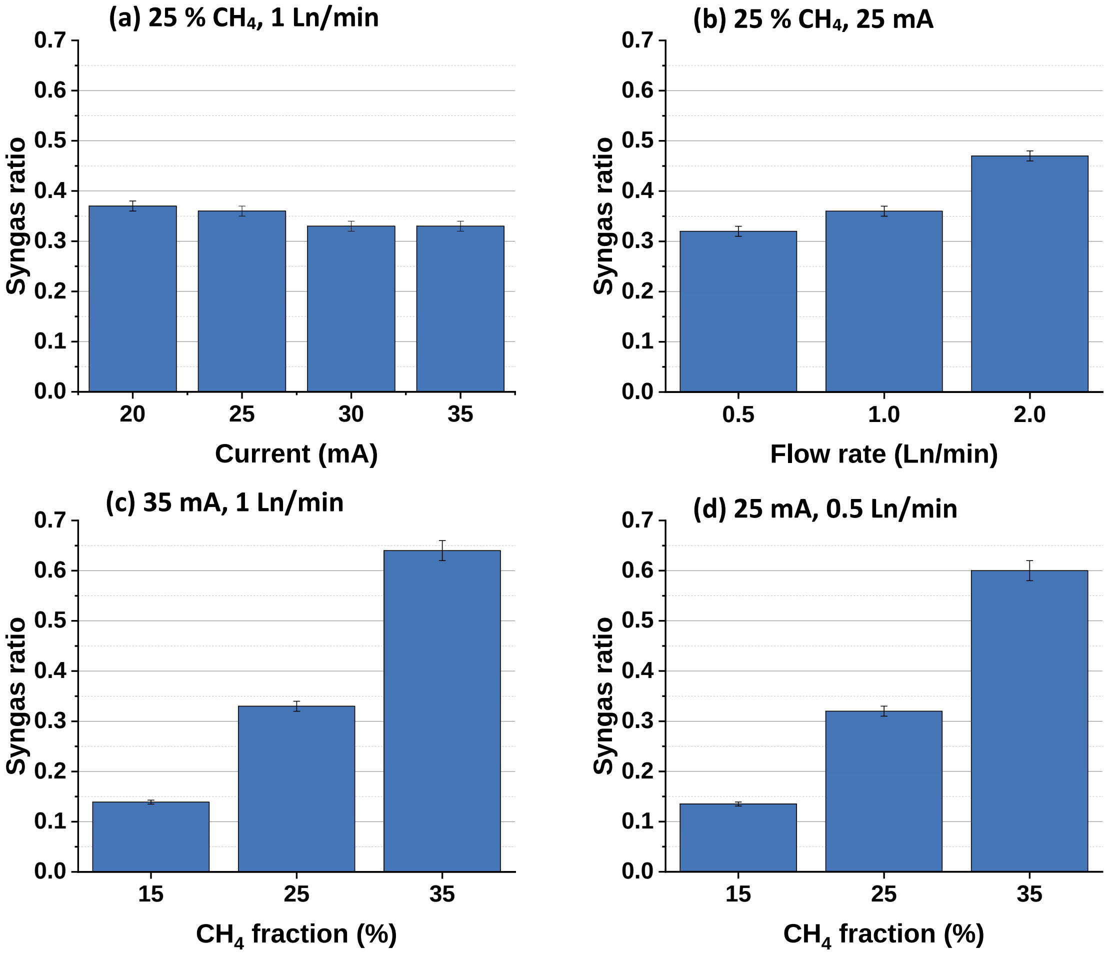

Figure 15: Syngas ratio as a function of current (a), flow rate (b) and CH_4 fraction (c, d). The other conditions that are kept constant are indicated in the figure. Error bars are added, but are often too small to be visible.

Because we are limited in increasing the CH_4 fraction, we cannot reach the ideal ratio of 2, and even a ratio of 1 is not reached. Indeed, the highest H_2/CO ratio obtained at 35 % CH_4 is equal to 0.64 ± 0.02 (a) and 0.60 ± 0.01 (b). This indicates that the current set up, despite the excellent conversion and energy cost obtained, cannot provide a high-value syngas stream at this point. Nevertheless, we believe that additional adjustments can be made to both the set up and the reaction process to increase the H_2/CO ratio, and the product output in general. Indeed, it is for example shown in literature that the addition of fractions of O_2 or H_2O, allow for increased amounts of CH_4 in the inlet gas mixture, and therefore a higher H_2/CO ratio.[42,127,128] Additionally, a power supply capable of delivering higher powers could also help with stabilizing the discharge.[30] Furthermore, it is also shown that a catalyst bed and a second inlet downstream to add additional amounts of CH_4, can increase the H_2/CO ratio above 1.[42,124,125] Therefore, with the excellent performance of our reactor for DRM in terms of conversion and energy cost demonstrated already at this point, we expect that such adjustments will further improve the reactor's potential.

In terms of trends, the H_2/CO ratio clearly rises upon higher CH_4 fractions, which is logical, since H_2 can only be formed out of CH_4. For different currents and flow rates the differences are smaller, although there is a clear increase at lower currents and higher flow rates. This is due to the fact that, since CH_4 is more easily converted than CO_2, a lower SEI has a larger negative effect on the CO_2 conversion. For example, at 25 mA and 2 Ln/min there is almost a factor 2 difference between the CO_2 and CH_4 conversion, and therefore more H_2 and less CO is formed compared to other conditions.

Next to syngas, other gases are formed at all conditions, like C_2H_2, C_2H_4 and C_2H_6, but the sum of their concentrations often doesn't exceed 1 %. Among these C_2-components, C_2H_2 is always the most abundant (between 50–90 %), followed by C_2H_4 (10–35 %) and C_2H_6 (1−10 %). In addition, some solid carbon is deposited during the experiments, and although it leads to voltage fluctuations from 35 % CH_4 onwards, its overall concentration in the mixture is relatively low. This can be deduced from the obtained carbon balance: as deposited carbon is not included in the calculations, the number that is missing to obtain a carbon balance equal to 1 can be roughly linked to the amount of deposited carbon. However, the carbon balance is always very close to 1, within the experimental error margin.

Finally, a liquid fraction is formed, consisting of water and small amounts of oxygenated components. One liquid fraction, collected under the conditions of 25 % CH_4, 20 mA and 1 Ln/min, was analyzed by means of GC and HPLC (see details in section 8.1.1). Next to water, the only components that were detected were formaldehyde (204 ± 2 ppm), acetic acid (115 ± 2 ppm) and methanol (24 ± 1 ppm). This corresponds with other observations throughout literature.[12,108,129] Note that although it was possible to quantify the concentration of these components in the collected liquid fraction, the exact amount produced over time is difficult to determine since a lot of liquid product was lost as well, through condensation at the reactor walls or between the reactor and the liquid trap. The condition of the liquid sample that was analyzed was chosen because of the lower SEI, because based on literature[129], the concentration of oxygenated components does not rise with higher SEI, nor are any new products formed in significant amounts. As function of CH_4 fraction, we expect no differences in terms of order of magnitude of the concentration of the liquid components, due to the small range investigated. The fact that the liquid fraction consists of quasi pure H_2O also allows us to estimate the fraction of gases that are dissolved and left behind in the cold trap. Specifically for CO_2, this is important to take into account as it has the highest solubility in water of all gas components that were detected. At ca. 10 °C, the solubility of CO_2 in water is ca. 2.5 g per kg H_2O.[130] When applying this to the data we obtained, this would mean an underestimation of the CO_2 output flow rate by 0.01-0.07 %, thus sufficiently small across all conditions.

A better overview of the quantities of the main products formed can be obtained by looking at the (C-, H- and O-based) selectivities and yields. These are presented in Figure 16, at 25 mA and 0.5 Ln/min, and 15 % (a), 25 % (b) and 35 % (c) CH_4. The results towards selectivity are quite similar for the other currents and flow rates (as illustrated in section 8.1.2).

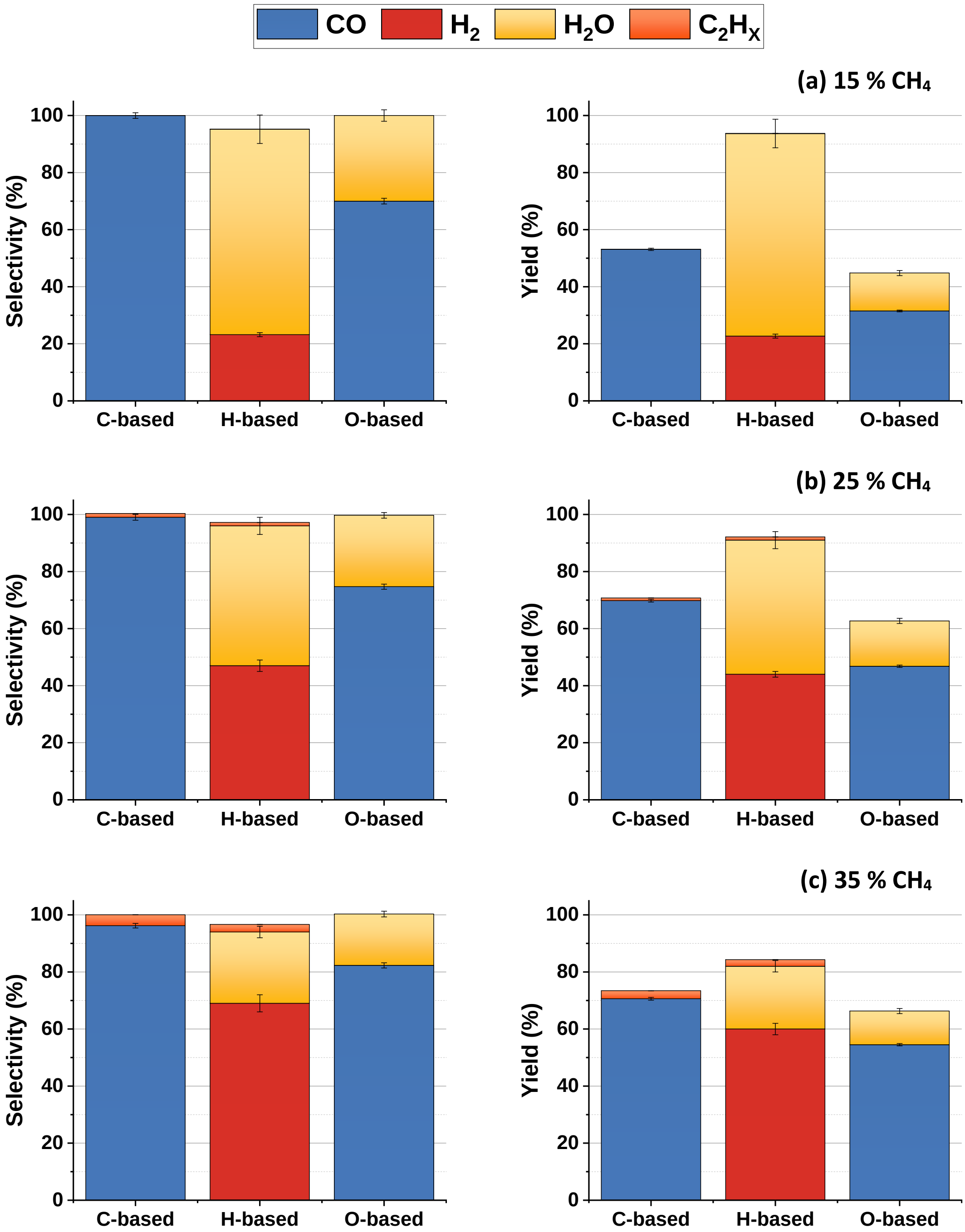

Figure 16: C-, H- and O-based selectivities (left) and yields (right) for 15 (a), 25 (b) and 35 % (c) CH_4 at 25 mA and 0.5 Ln/min. C_2H_2, C_2H_4 and C_2H_6 are grouped together as "C_2H_X" but C_2H_2 is the major component (~54 (a), 79 (b) and 86 % (c) of the total C_2H_X-fraction). The selectivity and yield for H_2O is calculated based on the approach described by Pinhão et al.[108] *Error bars are added, but are often too small to be visible.*

By definition, the sum of all selectivities (being either C-, H- or O-based) should be 100 %, when all reaction products are included. Likewise, the sum of all (C-, H- or O-based) yields should be equal to the conversion of the reactants that contain that atom, weighted over the number of atoms and the initial concentration for each reactant. Both are indeed the case in our measurements, as the sum of all selectivities is always very close to 100 % and the sum of all yields is always very close to the CO_2, CH_4 or total conversion (in case of O-, H- and C-based yields, respectively). As H_2O could not be measured with our GC, its selectivity and yield was determined through the O-balance, as suggested by Pinhão et al.[108] (see detailed explanation in section 8.1.3). As a consequence of this method, the error bars for H_2O can be larger than for the other components, which were measured directly.

The C-based selectivity towards CO is very high for all conditions, in the range of 95–100 % for all CH_4 fractions. The C_2H_X-components reach a maximum selectivity of 3.75 ± 0.04 % at 35 % CH_4, and are not visible in Figure 16 at 15 % CH_4 (< 0.02 %). The same relative differences are observed for the yields, as these are equal to the product of selectivity and conversion. Overall, this clearly shows that only a small amount of carbon atoms are "lost", and the vast majority is involved in the desired CO (and thus syngas) production.

From the H-based selectivities, we see that either H_2O or H_2 has the highest value. The fact that H_2O is a major by-product is detrimental, as the formation of H_2O over H_2 is an economic loss. Upon increasing the CH_4 fraction, the H_2O selectivity drops from 71 ± 6 % to 26 ± 2 %, while the H_2 selectivity rises from 23.7 ± 0.3 % to 69 ± 1 %. As a consequence, the highest yield for syngas is obtained at this condition. Figure 16 is also in line with Figure 15, as the H_2 yield strongly increases for higher CH_4 fractions, while the CO yield does not rise to the same extent. The H-based selectivity for the C_2H_X-components is similar as observed for the C-based selectivities (i.e. < 3 %), with again a small increase towards higher CH_4 fractions. Knowing that acetylene is a common pre-cursor for forming poly-cyclic aromatic hydrocarbons, involved in soot formation[30,36], it also explains why the latter is observed the most at the highest CH_4 input fraction.

Finally, the O-based selectivity towards CO is always in the range of 70–80 %, with the highest value at 35 % CH_4, while the remaining fraction is mostly H_2O (see above). It should be mentioned that a very small fraction of O_2 (i.e., 0.01-0.09 %) was also detected, but due to its low concentration at all conditions it was not plotted in Figure 16. When comparing all different currents and flow rates (see section 8.1.2), the selectivities remain relatively constant, but as a general trend, the C_2-components become somewhat more important upon lower SEI, although their C- and H-based selectivity is never above 5 and 4.5 %, respectively.

3.4 Conclusion

In this chapter, we investigated the performance of a cAPGD plasma reactor applied towards DRM. A total conversion up to 74.4 % is reached, with an energy cost generally staying below 4.27 eV/molecule, which is the efficiency target defined by Snoeckx and Bogaerts.[12] By adding this data to an updated version of Figure 3, it is clear that this performance is among the best compared to the current state-of-the-art for plasma-based DRM for all types of plasma reactors reported in literature. The excellent performance can mainly be linked to the relatively high SEI and the confinement of the reactor, similar to the size of the plasma width. In this way, a larger gas fraction passes through the active plasma region, and potentially it also leads to a wall-stabilization effect.

Syngas is the major product, but the presence of H_2O, small hydrocarbons and soot particles is also confirmed, while valuable liquid products like methanol are only formed at ppm levels. Despite syngas being the main product, the syngas ratio remains below 1. This is due to the fact that we were limited to a CH_4 fraction up to 35 %, as higher CH_4 fractions gave rise to more soot deposition on the electrodes, leading to voltage fluctuations and thus an unstable plasma behavior. Essentially, direct processing of the produced syngas into methanol is not possible because of the low syngas ratio, which is a major limitation.

Overall, the current challenge involves combining this excellent conversion and energy cost with a more valuable product output. For this, suppression of soot formation will be needed. As discussed briefly in section 3.3.4, there are various ways to achieve this. One of the available options is the addition of an extra reactant, such as O_2, that can help counteract the soot deposition, while syngas remains the main product. Therefore, next chapter will investigate the effect of the addition of small fractions of O_2, i.e., OCRM, carried out with the cAPGD reactor.

Chapter 4 Effect of O_2 on dry reforming of methane in an atmospheric pressure glow discharge: revealing the optimal gas composition[3]

Abstract

In this chapter, we study the effect of O_2 addition to the combined conversion of CO_2 and CH_4 (so-called OCRM) in the cAPGD reactor. Specifically, the optimal gas mixing ratio is determined through evaluating conversion, energy cost, product output and plasma stability. A mixing ratio of 42.5-42.5-15 CO_2-CH_4-O_2 yields the best performance, with a CO_2 and CH_4 conversion of 50 and 74 %, respectively, and an energy cost as low as 2 eV/molecule (corresponding to 190 kJ/mol), i.e., clearly below the target defined to be competitive with other technologies. The syngas components are the most important products, with the highest syngas ratio obtained being around 1, only slightly better than what was obtained for DRM. Nevertheless, plasma destabilization at high CH_4 fractions due to solid carbon deposition remains a limiting factor for further improving this syngas ratio. In addition to determining the optimal gas composition, analysis of the solid carbon material is carried out through electron microscopy measurements. The material is categorized as turbostratic carbon and is found to be contaminated with steel particles, pointing at electrode erosion and rendering it unappealing as a side product. Besides the experiments, a two-dimensional (2D) axisymmetric fluid dynamics model developed by S. Maerivoet was able to successfully predict the experimental trends, while providing unique insights in the conversion and formation mechanisms.

---

[3] This chapter is based on:
Effect of O_2 on Plasma-Based Dry Reforming of Methane: Revealing the Optimal Gas Composition via Experiments and Modeling of an Atmospheric Pressure Glow Discharge
S. Maerivoet*, B. Wanten*, R. De Meyer, M. Van Hove, S. Van Alphen, A. Bogaerts
ACS Sustainable Chemistry and Engineering, 12, 11419 – 11434 (2024)
https://doi.org/10.1021/acssuschemeng.4c04283
*Shared first author

4.1 Introduction

The conclusion of Chapter 3, describing the DRM carried out with the cAPGD, was twofold. On one hand, an excellent performance was achieved in terms of conversion and energy cost (i.e., 64 % of CO_2 and 94 % of CH_4, at an energy cost of 3.5–4 eV/molecule).[131] On the other hand, the value of the product output was limited. Indeed, at low CH_4 input fractions, other reaction pathways lead to H_2O being a significant by-product, diminishing the amount of the more desired H_2 and thereby decreasing the syngas ratio. This is a consequence of side-reactions like, for example, the reaction of CO_2 with H_2, known as the reverse water–gas-shift reaction (rWGS)[132], presented as reaction (R4).

$$CO_2\ (g) + H_2\ (g) \rightleftharpoons CO(g) + H_2O\ (g) \qquad \Delta H^\circ = +41.1\ kJ/mol \tag{R4}$$

On the other hand, increasing the CH_4 input fraction leads to an increased syngas ratio and less H_2O, but then solid carbon formation is observed. Black particles are deposited on the electrodes, as well as on the walls of the ceramic and the glass of the reactor. Furthermore, the formation of solid carbon particles severely influences the plasma dynamics and stability. Indeed, it is known that these particles can act as macroscopic charge carriers, typically acquiring a negative charge due to the high mobility of the electrons, reducing the electron density.[98] This also explains why we observe difficulties with sustaining the plasma at high CH_4 fractions, as well as why most of the soot is deposited at the (positively charged) anode.

In addition, the carbon material may accumulate over time, potentially leading to blockages and contamination of the downstream system, posing significant challenges to long-term operations. The formation of solid carbon could be due to other possible side-reactions described as the Kassel mechanism[133], where CH_4 is converted into small hydrocarbons (which are also present as by-products) and subsequently decomposed into H_2 and solid carbon.[30,35]

$$2\ CH_4\ (g) \rightleftharpoons C_2H_6(g) + H_2\ (g) \qquad \Delta H^\circ = +64.9\ kJ/mol \tag{R5}$$

$$C_2H_6\ (g) \rightleftharpoons C_2H_4(g) + H_2\ (g) \qquad \Delta H^\circ = +137.0\ kJ/mol \tag{R6}$$

$$C_2H_4(g) \rightleftharpoons C_2H_2(g) + H_2\ (g) \qquad \Delta H^\circ = +174.5\ kJ/mol \tag{R7}$$

$$C_2H_2(g) \rightleftharpoons 2\ C(s) + H_2\ (g) \qquad \Delta H^\circ = -226.7\ kJ/mol \tag{R8}$$

Another possible pathway for the formation of soot (which is the common term to address carbon particles observed during incomplete combustion of hydrocarbons), is through C_2H_2 serving as a pre-cursor to benzene and higher aromatics. Eventually, these evolve into polycyclic aromatic hydrocarbons (PAH's), which then agglomerate into visible particles, mainly through the H-abstraction-C_2H_2-addition (HACA) mechanism.[30,100,134]

It is clear that the rate of solid carbon formation highly depends on the CH_4/CO_2 ratio, which therefore has to be limited for the reactor to operate without excessive solid carbon deposition. This limits the reachable syngas ratio of the plasma system, voiding the advantage of immediately using the plasma products as reagents for other chemical processes, like the FT process. A potential solution for this might be adding O_2 to the gas mixture, allowing the following reactions to take place:[135,136]

$$2\ C\ (s) + O_2(g) \rightleftharpoons 2\ CO\ (g) \qquad \Delta H^\circ = -221.0\ kJ/mol \qquad \textit{(R9)}$$

$$C\ (s) + O_2(g) \rightleftharpoons CO_2\ (g) \qquad \Delta H^\circ = -393.5\ kJ/mol \qquad \textit{(R10)}$$

$$2\ CH_4(g) + O_2(g) \rightleftharpoons 2\ CO\ (g) + 4\ H_2\ (g) \qquad \Delta H^\circ = -71.4\ kJ/mol \qquad \textit{(R11)}$$

$$CH_4(g) + 2\ O_2\ (g) \rightleftharpoons CO_2(g) + 2\ H_2O\ (g) \qquad \Delta H^\circ = -802.3\ kJ/mol \qquad \textit{(R12)}$$

Reaction (R9) and (R10) show solid carbon reacting away through O_2 into either CO or CO_2. Therefore, we hypothesize that adding O_2 can positively affect the syngas ratio, because it may allow to use a higher CH_4 fraction without destabilizing the plasma. In addition, O_2 will also react with CH_4 directly through reaction (R11) or reaction (R12). While (R12) would be an unwanted reaction (i.e., it would lead to a decrease in CO_2 conversion), reaction (R11) opens up a new pathway to form syngas. This reaction is also known as the partial oxidation of methane (POM). The combination of the DRM and the POM is essentially OCRM[137], which is the reaction that we will investigate in this chapter through experiments with the cAPGD plasma reactor.

Despite our main goal is to diminish solid carbon formation, the exact structure and value remains unknown, other than it being clusters of carbon atoms. This, of course, hardly narrows it down, as carbon clusters can exist as fullerenes, nanoparticles and -tubes, fibers, graphene, graphite, etc.[138] Therefore, in this chapter we provide an analysis of the structure and composition of the solid carbon material by means of electron microscopy measurements. This can provide us with more insight in the economic value as side-product. Indeed, the properties and applicability of a carbon material (and thus, its economic value) is strongly governed by its structural characteristics, surface chemistry, and porosity.[138]

Finally, to better understand the underlying physics and chemistry, we also applied a fluid dynamics model, which was developed by a fellow PhD student at PLASMANT, and described in more detail in Maerivoet et al.[139] , to our experimental dataset. Specifically, in this 2D axisymmetric model the temperature profile and gas flow behavior in the reactor is calculated, while self-consistently coupled with the plasma chemistry. Since the temperature in this APGD reactor is above 2000 K, and many plasma species are very reactive and short-lived, measurements of species densities or core temperatures in an optically blocked plasma reactor (due to the ceramic piece) is very complicated. Therefore, a model can provide us with unique insights into the physics and chemistry, such as the underlying reaction pathways.

4.2 Methods

4.2.1 Experimental setup

Figure 17 schematically illustrates the entire experimental setup. The electrical circuit (cfr. thick dark red lines) and gas flow circuit (cfr. thin black lines) leading up to the reactor are the same as presented in Figure 10, with the only difference being one additional gas cylinder (also from © Air Liquide) to deliver O_2 with 99.9 % purity. After exiting the plasma and leaving the reactor, the resulting gas mixture again enters an ice-filled cold trap, condensing all products with low boiling points to liquid form. This is now even more important as we use an Agilent micro GC, for which the entrance of any liquid samples needs to be avoided, since it would cause severe damage to the injection system. The gas exiting the cold trap is further led toward the GC as a homogeneous mixture. For each measurement, either plasma or blank, the GC has a sample period of 30 s, extracting gas flow from the setup, after which it is injected onto the column. As H_2O cannot be detected in the GC, its concentration formed in the plasma is based on the O atom-balance, as also explained in Chapter 3 (and section 8.1.3). Details on the gas and liquid analysis are given as supporting information (see section 8.2.1).

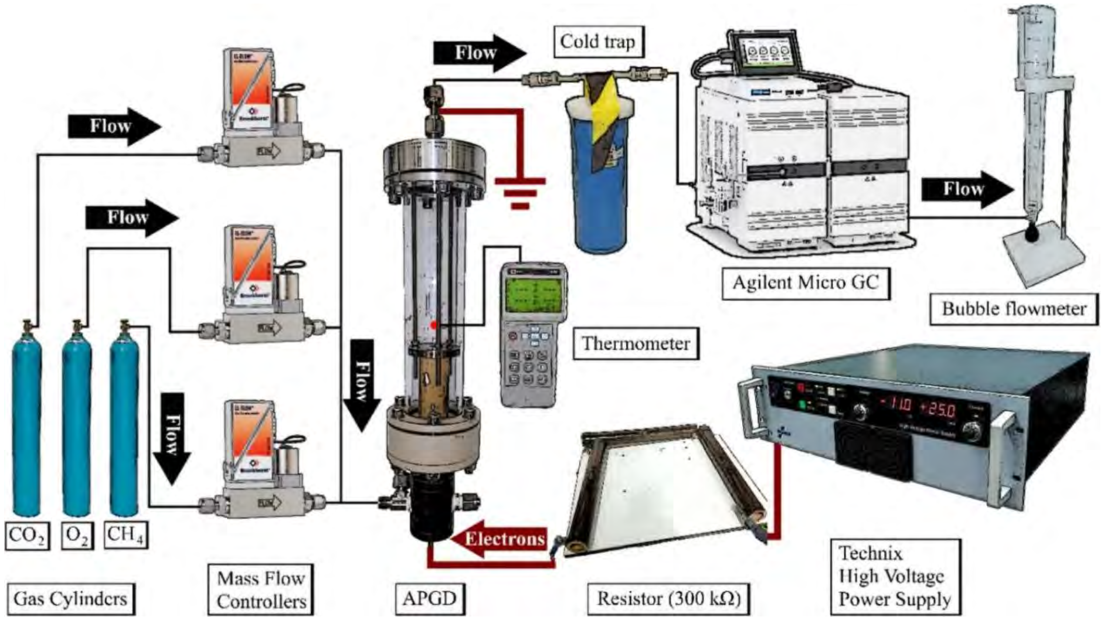

Figure 17: Schematic representation of the entire experimental setup. Black thin lines depict gas flow; red thick lines depict electrical current.

After a gas sample is injected onto the GC columns, the gas passes through without any flow loss and the exact flow rate is measured using a soap-film ("bubble") flow meter, which now replaces the standard component used in Chapter 3. The flow rate measured during a blank measurement is equal to the flow rate at the inlet of the reactor during a plasma measurement. As such, the flux ratio is directly obtained through equation (18) and is used together with the concentrations to calculate the performance metrics described in Chapter 2.

$$\alpha = \frac{\dot{V}_{tot}^{out}}{\dot{V}_{tot}^{in}} \tag{18}$$

Another difference compared to the setup presented in Figure 10 is that we now use thermocouples and a cylindrical glass casing with an extra opening, which allows us to measure the temperature at different locations, i.e., outside the ceramic tube, in the plasma afterglow and close to the reactor outlet. Most interesting is the temperature measured in the afterglow, because it yields measurable differences at different conditions; its position is also indicated in Figure 17, i.e., the thermocouple tip is placed approximately 1 cm above the anode. Note that measuring the temperature inside the plasma was not possible due to the hindrance by the ceramic tube, a too high temperature for the thermocouples and interference with the plasma itself.

4.2.2 Experimental conditions investigated

We investigated two experimental series, called A and B. In series A, we increase the O_2 fraction up to 15 %, keeping the CO_2/CH_4 ratio fixed. The 15 % O_2 fraction is determined as the upper limit, to keep all experiments safe and well below the explosion limit; see more details in section 8.2.2. In series B, we increase the CH_4 fraction, while the CO_2 fraction drops and the O_2 fraction is kept constant at 15 %. The exact experimental conditions are listed in Table 2.

Table 2: Overview of all the experimental conditions.

Series A						
CO_2-CH_4-O_2 (%-%-%)	65-35-0	62-34-3	61-33-6	59-32-9	57-31-12	55-30-15
Plasma power (W)	85 ± 6	97 ± 5	97 ± 5	97 ± 5	95 ± 5	93 ± 5
Input flow rate (Ls/min)	1.04 ± 0.01	1.07 ± 0.02	1.04 ± 0.01	1.05 ± 0.01	1.04 ± 0.01	1.04 ± 0.01

Series B				
CO_2-CH_4-O_2 (%-%-%)	55-30-15	49-36-15	42.5-42.5-15	36-49-15
Plasma power (W)	93 ± 5	95 ± 5	94 ± 5	75 ± 6
Input flow rate (Ls/min)	1.04 ± 0.01	1.04 ± 0.01	1.06 ± 0.02	1.05 ± 0.01

The plasma power fluctuates slightly, depending on the initial gas mixture. Indeed, at a constant current and interelectrode distance (20 mm), the gas composition (as well as solid particle formation and deposition) has the largest impact on the voltage, which results in some variation in terms of power over the series of experiments. The total gas inlet flow rate was set at 1 Ls/min (i.e., at 20°C and 1 atm) for all gas mixing ratios. The measured flow rates listed in Table 2 are not exactly 1 Ls/min though, due to a small but systematic error on the MFCs. However, the deviations between the values are small, just like the error margins on the measured values, indicating that no significant error is introduced when determining the flux ratio.

4.2.3 Analyses of solid carbon deposits

In order to understand the structure of the formed carbon material, and to investigate whether it may be a valuable side product, a fellow PhD student (Robin De Meyer) analyzed this material by scanning electron microscopy (SEM) and transmission electron microscopy (TEM). For the SEM analyses, he employed a Thermo Fisher Scientific Quanta FEG 250, which was additionally equipped with an Oxford Instruments energy dispersive X-ray (EDX) detector, enabling spectroscopic analyses to determine the elemental composition of the samples. The TEM measurements were performed using a Thermo Fisher Scientific Tecnai Osiris G20, operated at 200 kV in bright-field (BF) TEM imaging mode. For the SEM analyses, he placed the collected material directly on a double-sided conductive carbon tape. Prior to TEM analyses, the sample was suspended in acetone by sonication and vortexing, after which a few drops of the suspension were placed on a holey carbon TEM grid that was left to dry under ambient conditions.

In addition to the characterization of the formed carbon particulates, we also investigated whether O_2 addition affects the properties of the formed solid carbon material, by analyzing two samples. Each sample was collected at the anode of the APGD reactor after operating the plasma for 1 h in a 36-49-15 CO_2-CH_4-O_2 mixing ratio for the “with O_2” sample, and a 65-35-0 mixing ratio for the “without O_2” sample.

4.2.4 Description of the fluid dynamics model

The model used in this Chapter was developed by a fellow PhD student (Stein Maerivoet), and explained in detail in Maerivoet et al.[139], but applied here to many more experimental conditions (see Table 2), compared to the five conditions studied in the original model paper. A combination of a three-dimensional (3D) gas fluid dynamics model and a 2D coupled gas flow + plasma model is required to obtain realistic results. Specifically, the 3D gas fluid dynamics model feeds an inflow velocity field to the 2D axisymmetric coupled model, since the geometry of the cathode does not allow for an axisymmetric inflow below the cathode. The 3D model only solves the gas flow equations, i.e., the Reynolds-averaged Navier–Stokes Shear Stress Transport equations, while the 2D axisymmetric coupled model also includes heat balance equations, chemistry and transport of species. Important to mention is that a heat source is used to describe the plasma, instead of solving equations for the current conservation and the Poisson equation, to save computation costs. This approximation is valid, as the chemistry in the APGD is quasi-thermal, based on the expected temperature range of the plasma. For example, an earlier study showed that a DC APGD operating in dry air gave rise to a gas temperature of ca. 3000 K[73], and Slaets et al.[16] showed that for CO_2-CH_4 mixtures at these temperatures, thermal chemistry is dominant. Imaging of the APGD plasma by Trenchev et al.[71] is used to obtain a realistic heat source shape.

Note that we use the model only to obtain more insights in the underlying chemistry, but the model itself is not the main focus, as it was developed by Stein Maerivoet. For a detailed description of the modeling equations, geometry and boundary conditions, as well as an overview of all reactions included in the model, we refer to the paper by Maerivoet et al.[139]

4.3 Results and discussion

4.3.1 Measured conversion, energy cost, product output

4.3.1.1 Conversion

In Figure 18a we plot the conversion of CO_2, CH_4 and O_2, as well as the total conversion, describing the converted fraction of the gas mixture as a whole, as a function of the O_2 fraction in the input mixture (i.e., series A, cf. section 4.2.2 above). Every condition is measured in three successive experiments, consisting each of three samples, leading to consistent values and thus small error bars, as shown in Figure 18a.

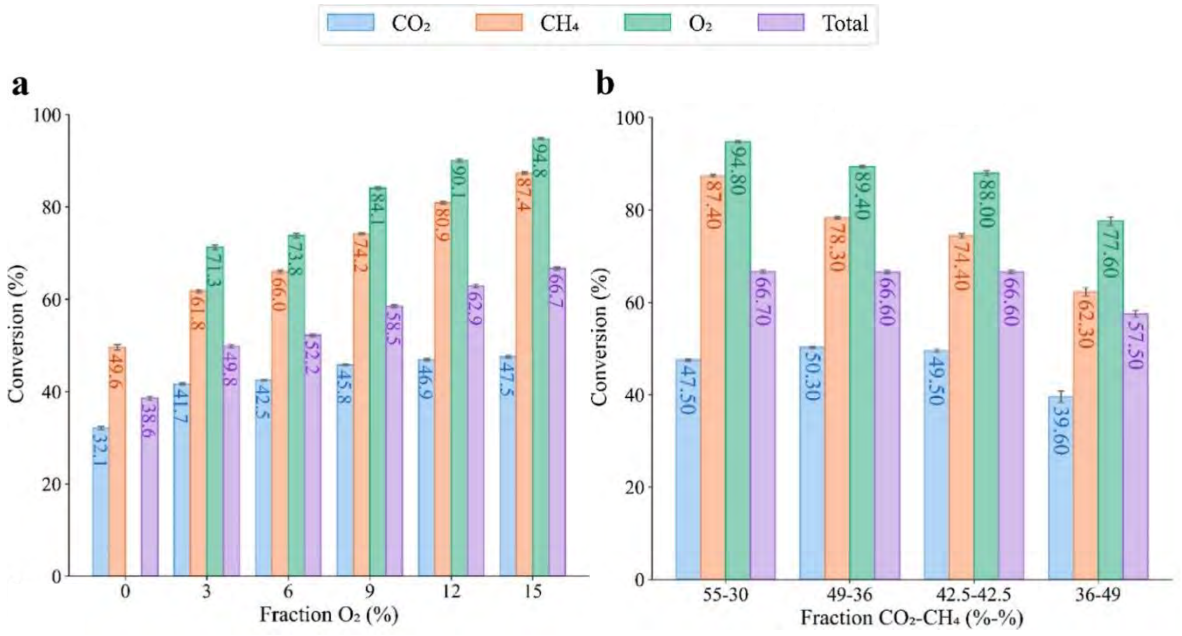

Figure 18: Conversion of CO_2, CH_4 and O_2, as well as the total conversion, as a function of O_2 fraction [(a) series A], and CO_2-CH_4 fraction [(b) series B]. The error bars are based on three successive experiments.

The conversion of all three molecules increases with rising O_2 fraction, and thus the total conversion rises as well. The higher CH_4 conversion upon rising O_2 fraction can be explained by the POM (reaction (R11)), which means an additional conversion pathway besides DRM, as well as by a higher gas temperature (see section 4.3.4.3 below). The rising CO_2 conversion is a bit less intuitive. A higher O_2 fraction opens a pathway toward full oxidation of CH_4 into CO_2 (reaction (R12)), which would lead to a net drop of CO_2 conversion. However, O_2 addition leads to a higher gas temperature (see section 4.3.4.3 below), because of the energy released by the POM; indeed, reaction (R11) is an exothermic reaction. This will lead to a higher conversion in general (as the chemistry is mainly driven by thermal reactions at these high temperatures), and thus also the CO_2 conversion. The net effect of these phenomena is a slight increase of CO_2 conversion upon rising O_2 fraction. This trend is more extensively described in the paper by Maerivoet et al.[139]

Figure 18b illustrates the conversion of CO_2, CH_4 and O_2, as well as the total conversion, as a function of CO_2-CH_4 fraction in the mixture, at fixed O_2 fraction of 15 % (i.e., series B, cf. section 4.2.2 above). At the applied current and flow rate, a CH_4 fraction above 49 % was not possible, due to a significant decrease in voltage and plasma power over time as a result of the formation of too many solid carbon particles, which are further discussed in section 4.3.2. The evolution toward an unstable plasma can be observed from the (slightly) increasing error margin at higher CH_4 fractions as well. The conversions of CH_4 and O_2 both drop upon higher CH_4 fractions. Since the conversion of CO_2 increases slightly upon increasing CH_4 fraction up to the 42.5-42.5-15 CO_2-CH_4-O_2 mixture, the total conversion remains around 67 % until this mixing ratio, followed by a drop at a higher CH_4 fraction.

Hence, we define the 42.5-42.5-15 CO_2-CH_4-O_2 mixture as the best condition (also in combination with the results below), yielding a total conversion of 66.6 ± 0.4 %, and corresponding CO_2 and CH_4 conversions of 49.5 ± 0.3 and 74.4 ± 0.5 %, respectively. This condition does not coincide with the highest CO_2 conversion, which is reached for the 49-36-15 mixture, i.e., 50.3 ± 0.2 %.

4.3.1.2 Energy cost

Figure 19a depicts the energy cost of series A, as well as the corresponding plasma power used at each condition. The 65-35-0 CO_2-CH_4-O_2 condition operates at a lower overall power due to the formation of solid carbon at the anode and in the plasma, increasing the plasma conductivity over time and therefore lowering the power. Since the power remains constant over the rest of the conditions within this series, while the total conversion increases, the energy cost drops. Just like for the conversion, the plasma stability at each condition is again reflected by the magnitude of the error bar. The largest error on the plasma power (for the 65-35-0 condition) represents a change in plasma power over the duration of the experiment. This change is attributed to the formation, destruction and removal by the gas flow of carbon deposits.

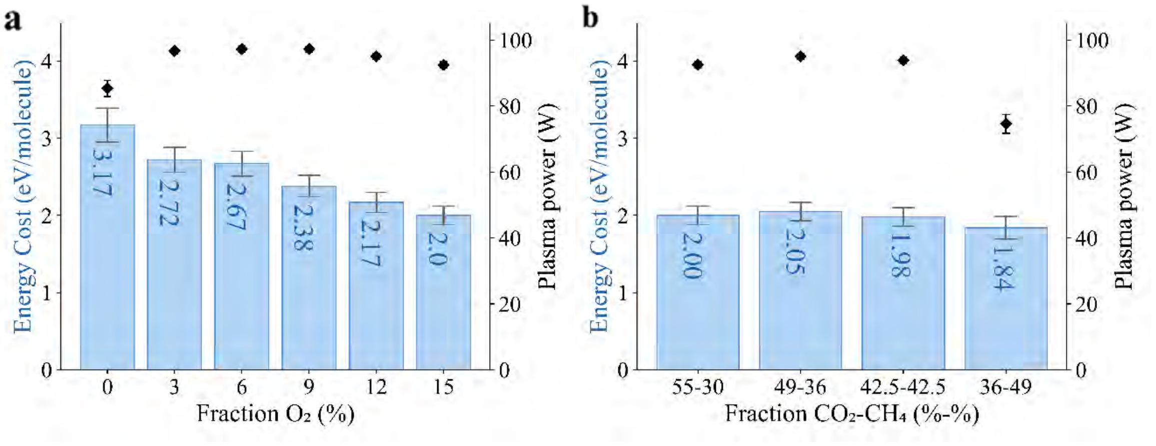

Figure 19: Energy cost in eV/molecule, as well as plasma power (right y-axis), as a function of O_2 fraction [(a) series A], and CO_2-CH_4 fraction [(b) series B]. Error bars are based on three successive experiments.

The energy cost of series B, shown in Figure 19b, is stable across the series. The lowest energy cost of both series is reached at the 42.5-42.5-15 mixture, yielding 1.98 ± 0.12 eV/molecule, which corresponds to 190 ± 10 kJ/mol. The energy cost at the 36-49-15 mixing ratio is even slightly lower (1.84 ± 0.15 eV/molecule), but this is attributed to the instability of the condition, resulting in a lower measured plasma power. However, this unstable condition also reduces the reproducibility, and therefore we believe the 42.5-42.5-15 mixing ratio is more favorable.

Note that the energy cost plotted in Figure 19 represents the energy cost per converted molecule. The energy cost per produced molecule, i.e., the syngas-based energy cost, can be found in section 8.2.3. The minimum energy cost of syngas production is also found at condition 36-49-15, reaching 1.28 eV/molecule of syngas at a 1.07 syngas ratio (see section 4.3.1.3 below). This is due to the drop in the formation of H_2O in series B, while the conversion at this condition is still high (57.5 % total conversion).

4.3.1.3 Syngas ratio

As illustrated in Figure 20a, the syngas (or H_2/CO) ratio drops upon increasing O_2 fraction. Indeed, the formation of H_2O from CH_4 and O_2 reduces the availability of H for H_2 formation. Note that the trend of how the syngas ratio changes over series A matches the reverse trend of CH_4 conversion in Figure 18a. Indeed, a higher CH_4 fraction in the mixture enhances the H_2/CO ratio, as illustrated in Figure 20b. The best syngas ratio (1.066 ± 0.022) is reached at the 36-49-15 mixing ratio, but the latter has a lower reproducibility (cf. the larger error bar) and also suffers from excessive carbon deposition. Therefore, also in combination with the conversion and energy cost data shown above, we believe the 42.5-42.5-15 mixing ratio is more beneficial, in terms of long-term stability due to limited carbon deposition, although it yields a syngas ratio of only 0.784 ± 0.008. This value is too low for most syngas applications (requiring a ratio of 2), although the FT process with an iron catalyst operates at syngas ratios around 1, making our current results more suitable already.[49]

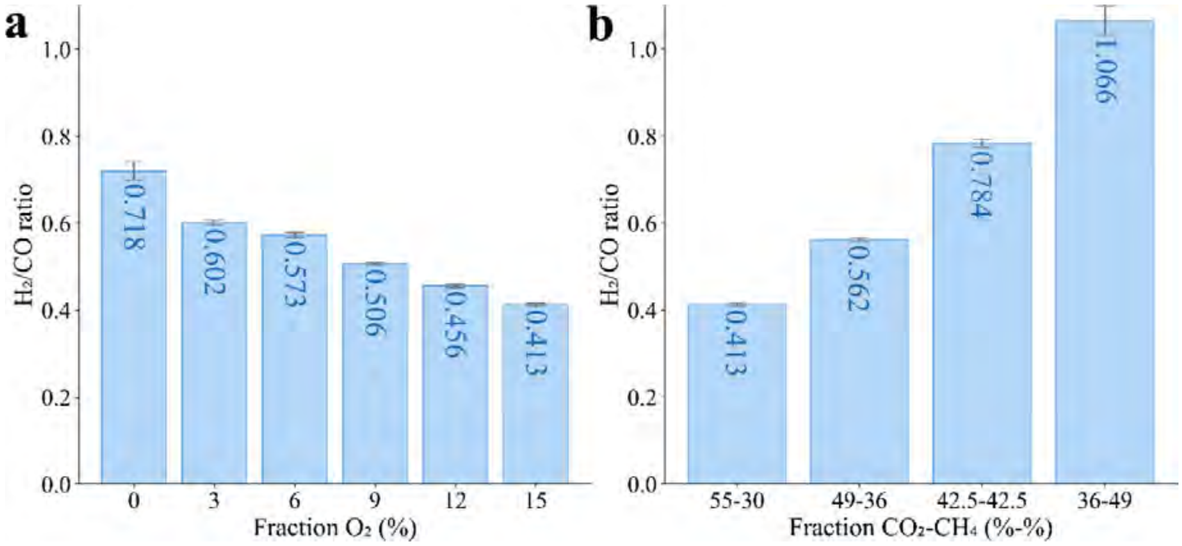

Figure 20: Syngas ratio as a function of O_2 fraction [(a) series A], and CO_2-CH_4 fraction [(b) series B]. Error bars are based on three successive experiments.

4.3.1.4 C-based product selectivity

Figure 21a shows the C-based selectivity at each condition of series A, for CO and all C_2H_x molecules together, i.e., C_2H_2, C_2H_4 and C_2H_6. Upon O_2 addition, the CO selectivity rises, while the C_2H_x selectivity drops almost threefold, from 9.44 ± 0.14 % without O_2 to 3.36 ± 0.02 % at 15 % O_2 addition. Figure 21b illustrates the C-based selectivity of C_2H_x, split up in its components. The major component is C_2H_2, followed by C_2H_4 and C_2H_6. The highest loss in selectivity with increasing O_2 fraction is therefore attributed to the loss of C_2H_2 selectivity. The C-based selectivity of series B is plotted in Figure 21c. As can be expected, a higher CH_4 fraction leads to a higher C_2H_x selectivity, and the main component is again C_2H_2, as is clear from Figure 21d. Note that the sum of the selectivities is often not perfectly equal to 1, as it is derived from measured values with small inaccuracies, linked to the calibration, and the experimental error margins.

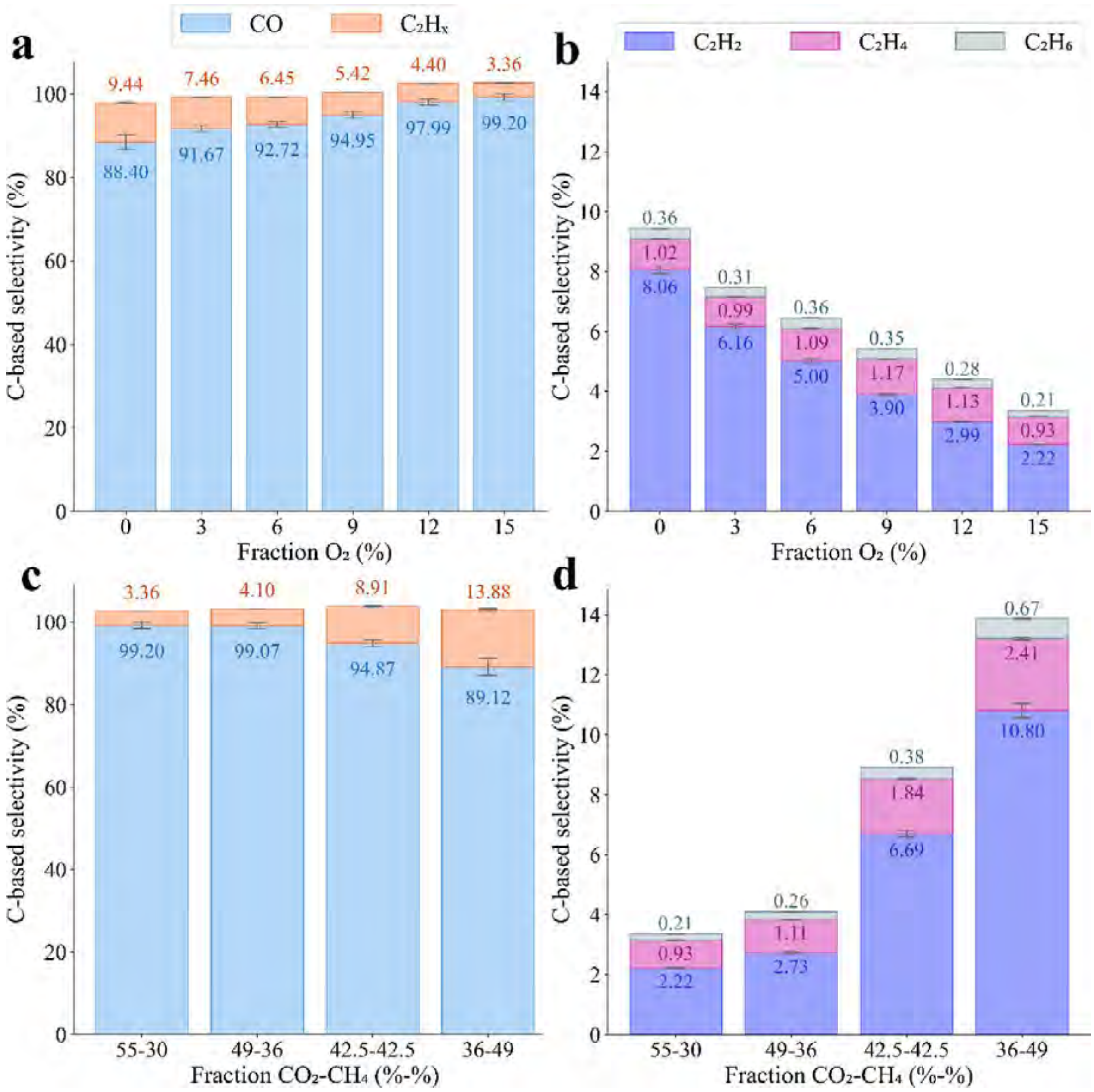

Figure 21: C-based selectivity, as a function of O_2 fraction [(a,b) series A], and CO_2-CH_4 fraction [(c,d) series B]. In (a,c) the C_2H_x compounds are combined, while in (b,d) the individual C_2H_x compounds are shown. Error bars are based on three successive experiments. As the selectivities are calculated from experimental results with small inaccuracies, the total selectivities are not perfectly equal to 1.

4.3.1.5 H-based product selectivity

The H-based selectivity of series A is plotted in Figure 22a. Most striking is the rising H_2O selectivity upon increasing O_2 fraction, because the O atoms originating from O_2 react with H from CH_4 dissociation into H_2O, at the expense of H_2 (and C_2H_x) formation. Indeed, both the C_2H_x and H_2 selectivities drop in favor of the H_2O selectivity. The overall larger error bar for the H_2O selectivity is due to the large error on the O-balance. It should be kept in mind that H_2O does not enter the GC and is condensed in a cold trap. The H_2O concentration is determined using the absence of O-atoms when comparing the inlet and outlet mixtures (see Chapter 3 and section 8.1.3). Therefore, the H_2O concentration depends on the concentration of every other component containing an O-atom, hence, its error will always be larger than any of the directly measured components at the GC. Figure 22b depicts the evolution of C_2H_x components over series A, demonstrating a drop in C_2H_2 selectivity with increasing O_2 fraction, similar to the C-based selectivities in Figure 22b. The H-based selectivity of series B (see Figure 22c) clearly indicates that a higher CH_4 fraction enhances the selectivity of H_2 and C_2H_x, and reduces the H_2O selectivity, which translates to a drop in molar H_2O formation, since the conversion of reactants is more or less constant over series B (see Figure 18b above). Figure 22d illustrates that the individual C_2H_x selectivities of series B again rise upon higher CH_4 fraction, with C_2H_2 being again the dominant component. Again, the sum of the individual selectivities is not perfectly equal to 1.

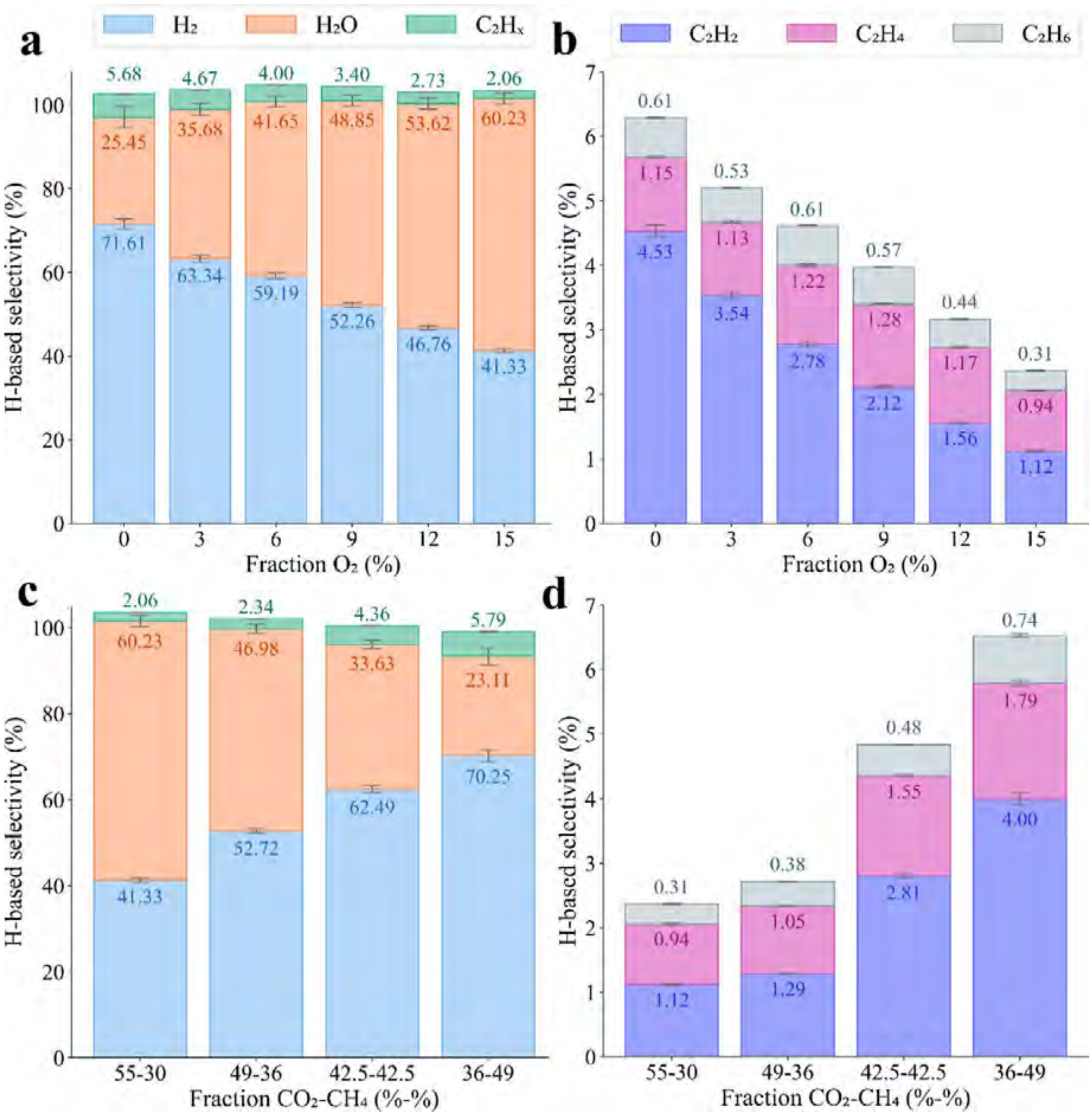

Figure 22: H-based selectivity, as a function of O_2 fraction [(a,b) series A], and CO_2-CH_4 fraction [(c,d) series B]. In (a,c) the C_2H_x compounds are combined, while in (b,d) the individual C_2H_x compounds are shown. Error bars are based on three successive experiments. As the selectivities are calculated from experimental results with small inaccuracies, the total selectivities are not perfectly equal to 1.

4.3.2 Analysis of the solid carbon deposits

The SEM, EDX, and TEM analyses of the solid carbon samples revealed no significant differences between the samples “with O_2” and “without O_2”. Therefore, we will discuss here the results of the sample “with O_2”, while corresponding data for the sample “without O_2” is presented in section 8.2.4. However, we did observe clear macroscopic differences between the two experiments and corresponding samples. Most notably, the amount of solid carbon was significantly lower for the experiment with O_2 compared to the one without O_2. This makes sense, since more of the CH_4 reacts with the added O_2, limiting the amount of CH_4 that can decompose to form the solid carbon particles (see section 4.3.4.4 below). This demonstrates that O_2 addition helps to reduce solid carbon formation, which is the main aim of our work. It is however worth noting that despite the significant effect on the plasma stability, the amount of solid carbon formed was typically rather small. We were not able to collect sufficient material in a reliable way for a bulk characterization, such as thermogravimetric analysis.

An overview of the material characterization of the "with O_2" solid carbon sample is presented in Figure 23. A backscattered electron (BSE) SEM image is shown in Figure 23a, and a secondary electron (SE) SEM image of the same area is presented in Figure 23b. The BSE signal is mostly affected by the density of the sample, i.e., heavier particles will give a higher signal. The SE signal is much less sensitive to the composition of the sample, but rather reveals structural information of the surface of the material. The BSE image (Figure 23a) shows a heavy spherical particle against a light carbon background. The solid carbon itself is mostly observed as large particles or agglomerates, ranging from a few µm up to hundreds of µm. At higher magnification, the surface of the carbon appears rough, indicating it may consist of smaller structures (Figure 23b). We investigated the composition of the heavy particle in Figure 23a using EDX spectroscopy. The EDX spectrum is presented in Figure 23c and shows that the particle consists of Fe, Cr, Ni, and a small amount of Mn. This aligns very well with the composition of the stainless steel anode in the cAPGD reactor used in our work. These heavy particles were common throughout the carbon samples, and show that there is in fact electrode erosion, which subsequently heavily contaminates the solid carbon formed by CH_4 in the plasma. Finally, a representative BF-TEM is shown in Figure 23d. The TEM image reveals that the material consists of graphene-like planar carbon structures, that do not have a significant ordering. This means that the material is not really amorphous, though it is also not crystalline, given the lack of long-range ordering. Based on these observations, the carbon material may be categorized as turbostratic carbon.[140,141]

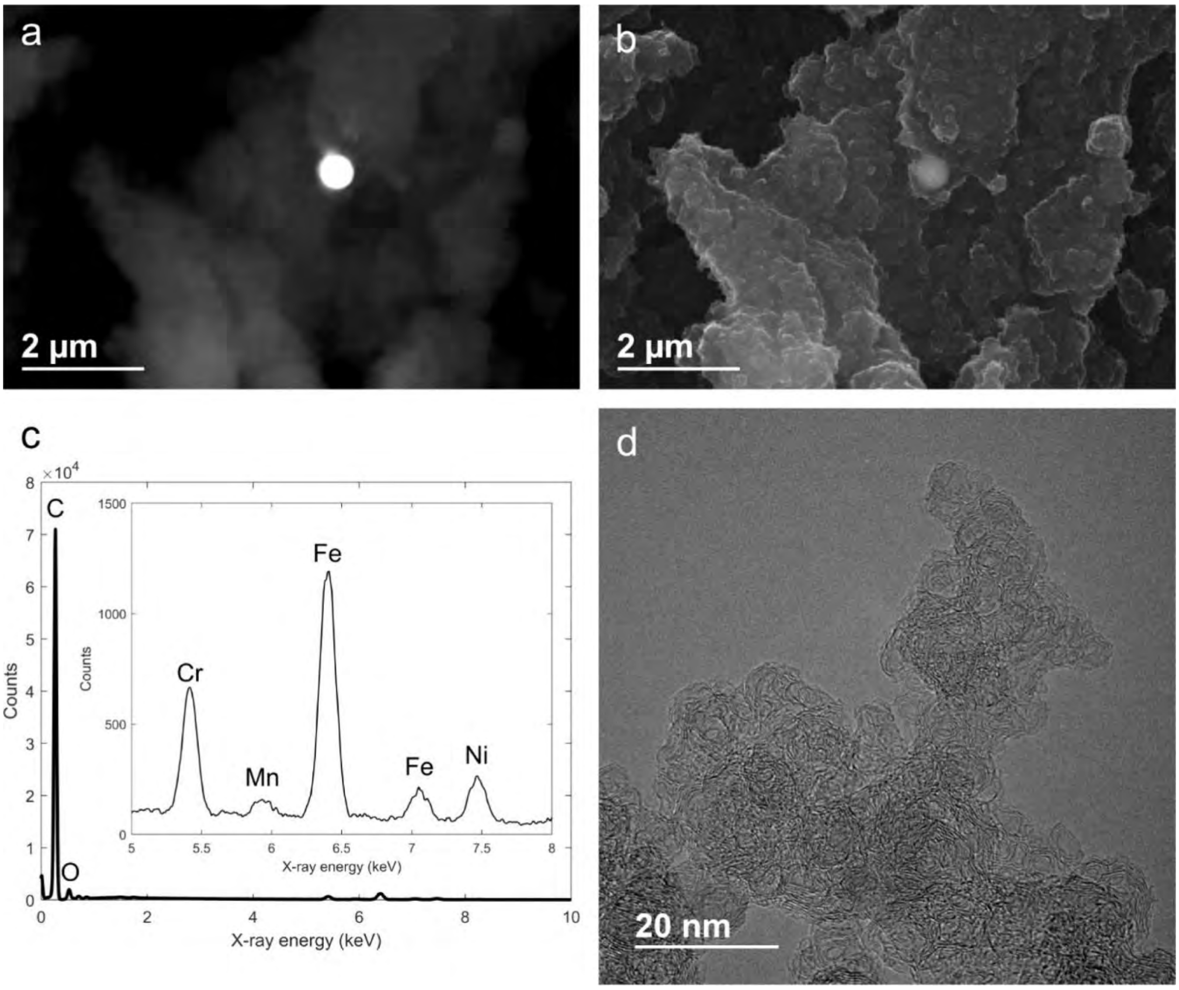

Figure 23: SEM, EDX, and TEM data for the carbon collected at the anode after an experiment with a 36-49-15 CO_2-CH_4-O_2 ratio. (a) BSE SEM image, highlighting a heavy, spherical particle. (b) SE SEM image of the same area as in (a), showing the microscopic structure of the carbon surrounding the heavy spherical particle. The carbon material appears to consist of a large agglomerate of smaller structures. (c) EDX spectrum of the heavy particle presented in (a), the inset shows the same spectrum but zoomed in on a relevant energy range, proving that the heavy particle is in fact stainless steel (containing Fe, Cr, Ni, and a small amount of Mn). (d) Representative BF-TEM image of the carbon material. The material consists of layers of graphene-like carbon that are not structured, indicating the material is not crystalline, but also not fully amorphous.

The fact that we do observe some electrode erosion at these conditions is problematic. While turbostratic carbon could be a valuable product, the significant contamination of the carbon with the electrode metal particles renders it much less appealing. Furthermore, as explained in section 4.1, the solid carbon heavily affects the plasma dynamics and it could accumulate downstream in the system during long operations, potentially causing blockages or posing a fire hazard. Therefore, this justifies the aim of our work to minimize the solid carbon formation, without sacrificing the overall performance.

4.3.3 Benchmarking with state-of-the-art literature

Some other researchers have also studied OCRM in various plasma reactors over the last decades. Table 3 compares our data with those from literature, for a spark-shade reactor[142], an alternating current (AC) pulsed GA reactor[62], a spark discharge reactor[88], a plasma-shade reactor[101], a GAP[51] and a classical GA reactor[61].

Table 3: Comparative study in terms of conversion χ (%), energy cost EC (eV/molecule) and syngas ratio of our results (cAPGD) with data for OCRM obtained with various plasma reactors in literature. Input fractions, total input flow rate $\dot{V}_{tot}^{in}$ (Ls/min) and power P (W) are also provided. Values indicated with "" could not be verbatim traced in original paper; instead it was calculated using the available data. "/" means no corresponding value was present in the paper and it could also not be calculated using the available data.*

	Input fraction (%)				**$\dot{V}_{tot}^{in}$ (Ls/min)**	**P (W)**	**χ (%)**		**EC (eV/molec.)**	**H_2/CO ratio**
	CO_2	**CH_4**	**O_2**	**N_2**			**CO_2**	**CH_4**		
cAPGD (our data)	55	30	15	/	1.04	93	47.5	87.4	1.98	0.413
	49	36	15	/	1.04	95	50.3	78.3	1.98	0.562
	42.5	42.5	15	/	1.07	94	49.5	74	1.98	0.784
Spark-shade[142]	39	38	23	/	1.36	70	25	59	1.56*	0.71
	28	45	27	/	1.36	70	30	69	1.23*	0.88
	23	48	29	/	1.36	70	28	70	1.16*	1.0
	16	53	31	/	1.36	70	24	75	1.05*	1.2
	11	56	33	/	1.36	70	16	80	0.98*	1.5
AC-pulsed GA[62]	32	48	20	/	15	280	28	52	0.60*	1.6
	31	46	23	/	15	280	25	65	0.49*	1.5
	29	44	27	/	15	280	25	77	0.42*	1.4
	28	42	30	/	15	280	33	88	0.37*	1.3

	27	40	33	/	15	280	39	95	0.35*	1.1
Spark discharge[88]	33	56	11	/	0.17*	48	58	72	6.18*	1.3
	33	56	11	/	0.17*	64	67	80	7.38*	1.2
	32	53	15	/	0.18*	48	58	74	5.71*	1.2
	32	53	15	/	0.18*	64	67	80	6.94*	1.1
	30	50	20	/	0.20*	48	57	76	5.00*	1.1
	30	50	20	/	0.20*	64	68	83	6.00*	1.1
Plasma-shade[101]	32	48	20	/	1.25*	119	36	64	2.28*	/
	31	46	23	/	1.30*	106	34	67	2.18*	/
	30	44	26	/	1.36*	98	31	75	2.01*	/
	29	42	29	/	1.40*	88	35	84	1.82*	/
GAP[51]	10	10	9	71	10	364	44	93	3.97*	0.60
	15	10	13	62	10	421	45	96	3.33*	0.68
Classical GA[61]	29	29	9	33	1	100	18	23	12.57*	1.8
	12	28	13	47	1	100	17	27	12.57*	2.0
	3	25	21	51	1	100	12	46	12.61*	2.0

The results obtained in the spark-shade reactor[142] yield somewhat lower conversions, but also slightly lower energy costs, compared to our cAPGD. The authors obtained an energy cost of 1.56 eV/molecule at a 39-38-23 CO_2-CH_4-O_2 mixing ratio, which is comparable to our value of 1.98 eV/molecule at a mixing ratio of 42.5-42.5-15 (lower O_2 fraction). The lower power and higher O_2 fraction in this reactor suggest that a larger portion of the heat of the spark-shade reactor originates from the conversion of O_2. The CO_2 and CH_4 conversions at the 39-38-23 mixing ratio are 25 and 59 %, respectively, i.e. much lower than our values of 50 and 74 % for the 42.5-42.5-15 mixing ratio. Besides the absolute values, the results follow the same trends as in our study: a higher CH_4 and O_2 fraction simultaneously results in a lower energy cost, as well as a higher CH_4 conversion and a lower CO_2 conversion. In our work, we determined the effect of O_2 and CH_4 fraction using two separate series, but it is clear that the dominant trend in energy cost in the spark-shade reactor is similar to the trend shown by our series A, hence attributed to the change in O_2 fraction.

The CO_2 conversion in the plasma-shade reactor[101] is lower than in our experiments, but the CH_4 conversion and energy cost are similar to our data, also using similar flow rate and power. However, this paper used high O_2 fractions up to 29 %, while we limited this fraction to maximum 15 % as a safety precaution (see section 8.2.2). At 20 % O_2 fraction, the authors reached a lower CH_4 conversion and a higher energy cost than in our cAPGD. No syngas ratio was mentioned in this study.

The plasma-shade and spark-shade reactor were developed by the same group and both reactors exhibit similar conversions and energy costs as in our experiments. The major difference between these reactors and our cAPGD is the voltage and current profile: the spark-shade and plasma-shade operate at AC with a frequency of 95 kHz, while our cAPGD operates at DC. In the AC configurations, the fast switching polarity between the electrodes will lead to a somewhat colder plasma, yet a more evenly distributed gas temperature.[143,144] The voltage reaches ~4 kV at the peak of the sine wave, while the voltage in our cAPGD is kept at ~10 kV. However, the AC reaches maxima of 40 mA (no root-mean-square value was provided), comparable to the 25 mA present in our cAPGD. Furthermore, the shade reactors operate using a high-voltage electrode and a rotating grounded stainless steel wire to create the desired plasma. Essentially, both these shade reactors and our cAPGD are considered to operate in the glow regime and they produce similar results with similar SEIs. We believe that the conversion in DRM in these warm plasma reactors is pre-dominantly due to the high plasma temperature and not as much due to electron reactions, as also discussed by Slaets et al.[16] and Maerivoet et al.[139] This conclusion is supported by the fact that glow regimes, although with somewhat different electrical characteristics, lead to similar experimental results.

The spark discharge[88] shows high energy costs, but also somewhat higher conversions, which may be expected due to the low flow rate (around 0.2 Ls/min) and thus longer residence time. The trends, however, are similar to our work, as the energy cost drops with rising O_2 fraction. Further, a small rise in CH_4 conversion can be noted, but the difference is too little to make any firm conclusion without knowing the error values. The AC pulsed

GA[62] reactor shows a very low energy cost. However, the conversion is typically also somewhat lower than in most other plasma types. Perhaps, the high flow rate used in this reactor (15 Ls/min) has a significant effect on the energy cost at high power when using 20–33 % of O_2. Another reason could be the (much) higher O_2 fraction in the mixture. However, exact comparison is not possible, due to the different reactor setups. The rising conversion of CH_4 and CO_2, as well as the decreasing energy cost upon increasing O_2 fraction, do however match the trends found in our cAPGD, in spite of the quite different conditions (i.e., much higher flow rate and power, and much higher O_2 fraction). The fact that this reactor operates as an arc can also yield major differences with our results. We believe further research is needed on this setup to understand the very good stated energy costs.

In earlier work from our group, a GAP[51] was investigated for CO_2 and CH_4 conversion in the presence of both O_2 and N_2. Relatively high N_2 fractions were used, to mimic industrial gas emissions, and thus the CH_4 and CO_2 fractions were quite low. The CO_2 conversion was comparable to our present study, while the CH_4 conversions was close to 100 %. The slightly higher energy cost of 3.33 eV/molecule can be explained by the low CO_2 and CH_4 fractions in the mixture, as a consequence of dilution by N_2. The effect of N_2 on the CO_2 and CH_4 conversion was further elaborated upon by Van Alphen et al.[99], who showed that addition of N_2 can increase the overall temperature and thus the conversion. Simultaneously, it could also increase the conductivity and thus reduce the power input, while also increasing the stability of the plasma. The overall effect on the performance was found to be only beneficial when the N_2 fraction is kept around 20 %. Fractions of 60-80 % would lead to an increased energy cost, which we also observe for the GAP in Table 3.

Finally, the classical GA plasma[61] also used N_2 in the gas mixture. It operates at similar flow rate and power as our cAPGD, but yields significantly lower CO_2 and CH_4 conversions, and a much higher energy cost of 12.57 eV/molecule, although it reaches a much more optimal syngas ratio. This is attributed to the higher CH_4/CO_2 ratio in the mixture, for which a stable plasma was enabled by the N_2 admixture. This paper again demonstrates the possibility of stabilizing a high CH_4/CO_2 plasma using N_2, and thus allowing a higher syngas ratio, but at the expense of a higher energy cost.

While the arc plasmas operate at vastly different flow and power regimes, their conversion resemble the same trends. As the conversion of CH_4 reaches almost 100 % for the AC Pulsed GA and the GAP, the CO_2 conversion cannot surpass 50 %, something that is possible and happens in the cAPGD and the spark discharge.

Overall, it is clear that in all plasma reactors, a syngas ratio above 1 is only feasible for a higher CH_4 fraction than CO_2 fraction in the mixture. Our cAPGD leads to a rather low syngas ratio compared to the other plasma reactors. Stabilizing the plasma at higher CH_4 fractions in the cAPGD will thus be necessary to increase the syngas ratio. As mentioned above, N_2 could assist in stabilizing the plasma, allowing for higher CH_4 fractions, albeit often with an increased energy cost. The spark-shade and AC pulsed GA operate at higher O_2 fraction, as well as a (somewhat) higher flow rate, although direct comparison is challenging, due to the different plasma types. Addition of H_2O vapor to the reactant mixture could also help to improve the syngas ratio, because in this case, H_2 can be produced not only from CH_4, but also from the H_2O vapor.

Apart from the syngas ratio, which clearly needs improvement in our case for most downstream processes (except FT with Fe catalyst), we can still conclude that our cAPGD is promising for the OCRM reaction, with a low energy cost (only slightly higher than for the spark-shade reactor, while the AC pulsed GA showed very low values, as discussed above), and with the best CO_2 conversion of all the reactors operating around 1 Ls/min.

4.3.4 Modelling results and comparison with the experiments

We use our model to compare with the experimental trends, in terms of conversion, product output and the afterglow temperature, for model validation and to gain insights in the experimental data, and especially in the underlying chemistry.

4.3.4.1 Conversion

Figure 24 compares the calculated and measured conversions. Series A is plotted in Figure 24a, where the experimental trend of increasing CH_4 conversion upon increasing O_2 fraction is indeed reproduced by our model. The calculated conversion of CH_4 reaches 99.9 %, at the condition 55-30-15 CO_2-CH_4-O_2 of series A, while the experimental conversion is 87.4 %. This could be explained by an overestimation of the plasma width (defining the heat source; see section 4.2.4 above), and while we could fit the heat source shape to better match the experimental conversion, we decided not to do this. Typically, the matching of unknown experimental parameters (temperature, residence time, cooling rate,...) is done in global models, explaining why such models can provide results that (apparently) better match the experiments. In contrast, in our multidimensional coupled model, we have calculated all these parameters self-consistently, without any adjustment for a better fit to the experimental data. While this obviously results in a non-perfect match, such multidimensional models, where the gas flow, heat transfer, chemistry and transport of species are coupled, are definitely an improvement to gain more insight in the underlying mechanisms, at least when they are able to reproduce trends. Indeed, apart from the absolute values, the trends in CH_4 conversion are well reproduced by our model, including the largest jump in CH_4 conversion, which can be observed when going from 0 to 3 % of O_2 addition for both the model and the experiment.

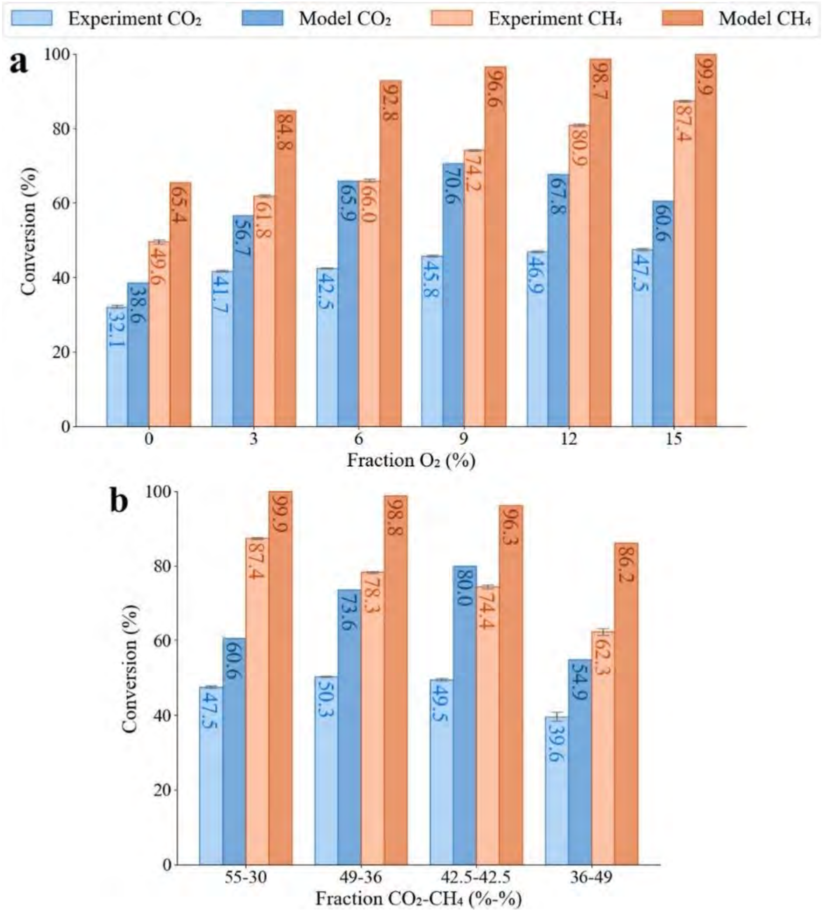

Figure 24: Experimental and modeled conversion for CO_2 and CH_4 as a function of the O_2 fraction [(a) series A] and CO_2–CH_4 fractions [(b) series B].

The trend of calculated CO_2 conversion shows somewhat weaker agreement with the experimental trend. While the experimental value gradually increases upon increasing O_2 fraction, our model shows a peak at 9 % O_2 added, followed by a small drop at higher fractions. This drop is not attributed to less conversion of CO_2 in the plasma, but rather to the presence of the water–gas shift reaction after the plasma in our model, converting CO and H_2O into H_2 and CO_2. This is due to the high afterglow temperature, which is overestimated in our model, as compared to the experiments. This is further discussed in section 4.3.4.3 below.

4.3.4.2 Product composition

A further model validation should be based on the full composition of the outlet mixture and not just on the conversion. Figure 25 depicts the molar composition of the gas measured in the GC and at the outlet of the model, for series A and series B. The trends in modeled and experimental CO_2 and CH_4 molar fractions match the trends in conversion shown in Figure 24 above. The WGS reaction reduces the calculated CO molar fraction in conditions above 9 % O_2, and it enhances the H_2 molar fraction, although the preference to form H_2O over H_2 at higher O_2 fractions results in a net decrease of the H_2 fraction upon increasing O_2 fraction, both in the model and the experiments. Furthermore, the decreasing and increasing trend of C_2H_x molar fractions in the experiments for series A and B, respectively, is somewhat exaggerated in the model. This is not only due to the approximation of the heat source (cf. above), but also due to the formation of solid C in the experiments, which could not yet be accounted for in the model. The calculated trends in CO_2, CH_4 and H_2 molar fractions in series B are similar to the experimental trends. The most important difference is the jump from condition 42.5–42.5 to 36–49 CO_2–CH_4, which can be explained by the significant power drop due to instability of the plasma, as observed in Figure 19b. The experimental trend in series B shows an increase in unconverted O_2 with increasing CH_4 fractions. We would thermodynamically expect CH_4 to exothermically react with O_2. This is not the case in the experiments, as can been seen in Figure 25b, nor is it the case in the model, where the unreacted O_2 fraction increases from 1.18×10^{-7} % at 55–30–15 (not visible in the plot as the value is too small) to 0.04 % at 36–49–15. Therefore, we will analyze the temperature data below, to better understand this behavior.

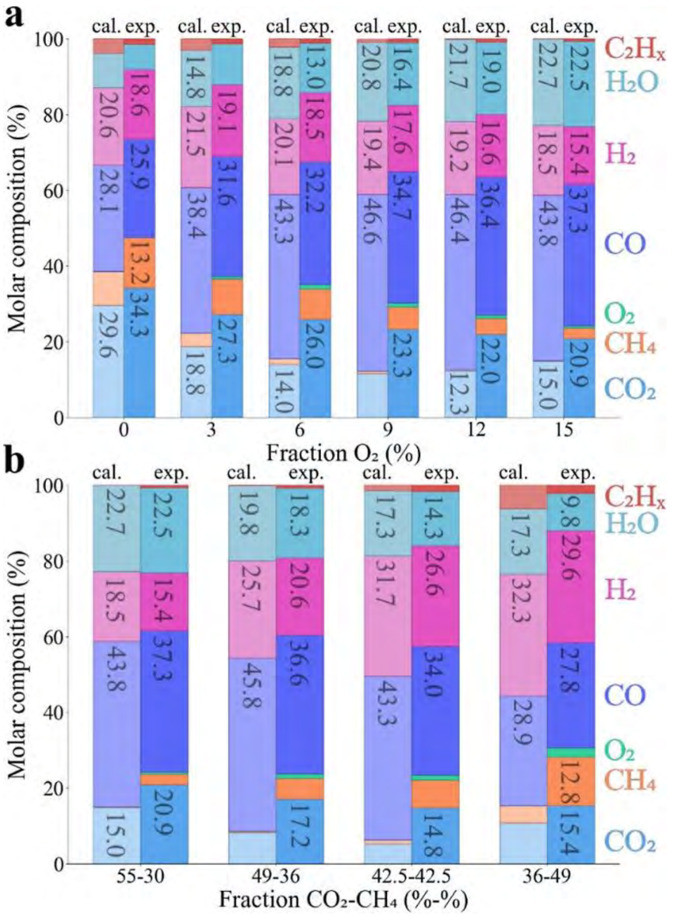

Figure 25: Molar compositions at the outlet of the experiments and the model, as a function of O_2 fraction [(a) series A] and CO_2–CH_4 fraction [(b) series B].

4.3.4.3 Afterglow temperature

As described in section 4.2.1, we measured the afterglow temperature at ca. 1 cm after the anode plate using a thermocouple. Note that optical emission spectroscopy (OES) would provide more accurate temperature information in comparison with a thermocouple, but it was not possible due to ceramic tube surrounding the plasma. The calculated temperature on the other hand is affected by the shape and position of the heat source. Given its approximate nature in the model, we will only compare trends. Figure 26a,b depict the afterglow temperature of series A and series B, respectively. The input power for all conditions (except condition 65-35-0 of series A and condition 49-36-15 of series B) is comparable, meaning that any change in temperature in the afterglow is due to a change in chemistry. Despite the difference in absolute values, the general experimental and modeled trends in series A exhibit good agreement, showing clearly that an increase in O_2 fraction leads to a higher temperature due to more exothermic reactions, as observed also in the enhanced H_2O production with increasing O_2 fraction in Figure 25a. The modeled and experimental trends of series B are also in agreement, although this cannot be explained from the thermodynamics, as mentioned before. The drop in temperature is linked to the higher H_2 formation and the lower H_2O formation. As less O is available due to the drop in CO_2, the formation of H_2O is limited to such an extent that the edges of the plasma are not hot enough to activate the reaction between O_2 and CH_4, and this is also observed in the drop in afterglow temperature, both in the model and the experiments.

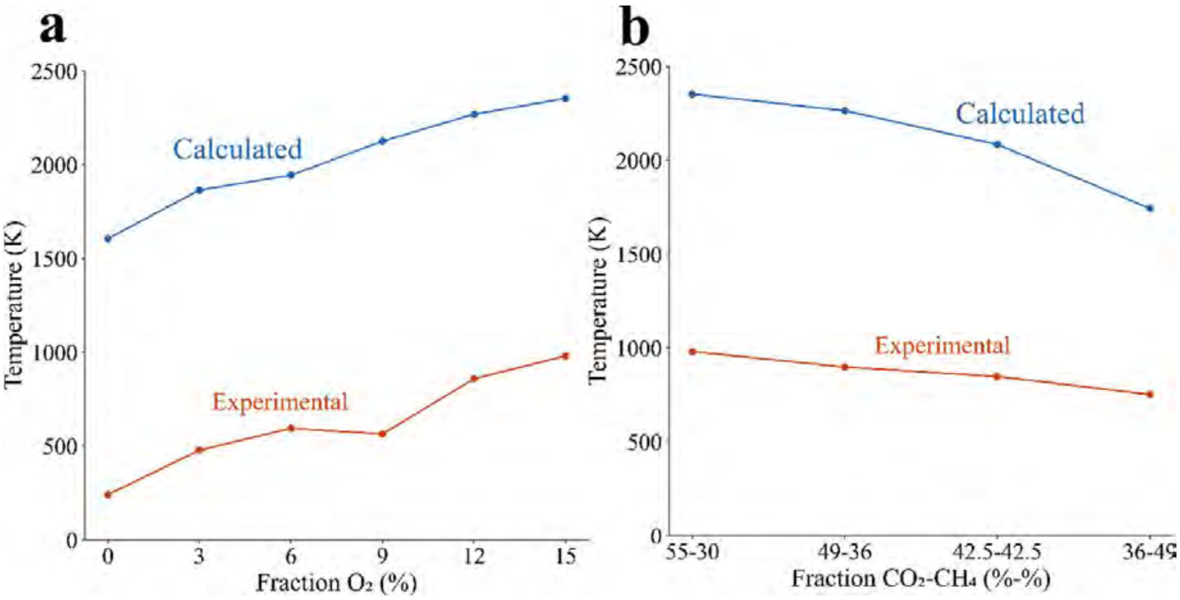

Figure 26: Experimental and modeled temperature of the afterglow, 1 cm after the anode plate, as a function of O_2 fraction [(a) series A] and CO_2–CH_4 fractions [(b) series B].

Nevertheless, even though the trends are reasonably captured, the discrepancies observed thus far in terms of absolute values indicate that some complexities in the experiment are not yet taken into account in the model.[139] We already discussed the potential influence of the estimated heat source shape, but other effects can also play a role. For example, the effect of soot particles, which act as macroscopic charge carriers and thus can severely influence the plasma dynamics[98], is not directly included in the model. Furthermore, the thermal properties of the ceramic wall reported in literature, influencing the heat losses in the reactor and therefore the (afterglow) temperature, are only determined at much lower temperatures (e.g., thermal conductivity up to max. 900 K) than the ones obtained in our model. In addition, potential surface reactions taking place at the ceramic wall, are also not included in our current model. This is another reason why we decided not to tune the shape and position of the heat source: fitting it to achieve perfect agreement with the experiments, while simultaneously ignoring other uncertain parameters, might give a false impression about the predictive capability of our model in terms of absolute values.

Rather, in order to obtain better agreement with the experimental results, a further improvement of the model is necessary. A setup which would allow more optical diagnostics could yield a more complete validation of the gas composition and temperature predicted by the model, by measuring the densities and evolution of transient species.[139] In addition, we should aim to obtain the shape of the plasma from self-consistent calculations of the current conservation and Poisson equation. This will be the subject of future research.

4.3.4.4 Multidimensional reaction analysis

The aforementioned temperature changes will impact the conversion, as more CO_2 and CH_4 will be converted when a larger part of the reactor has a sufficient temperature. However, the effect of O_2 on the DRM chemistry should not be neglected, and therefore, we performed a reaction analysis for conditions 65-35-0 CO_2-CH_4-O_2 and 55-30-15 of series A. Figure 27 shows the multidimensional reaction pathway analysis for condition 65-35-0 of series A, indicating where most of the shown species are present in the plasma, as well as the temperature profile of the plasma. Species plots in Figure 27 do not indicate how much of a species is present in a reactor, but rather where most of it resides, with the light yellow indicating a higher presence and black indicating an absence. Note that such a multidimensional reaction pathway analysis, showing not only the reaction pathways but also where in the plasma these reactions are dominant (which appears different for different reactions), is not possible with a global (zero-dimensional, 0D) model, mostly used in literature for reaction pathway analysis[92,131,145], but really requires a more-dimensional model, as used in our work.

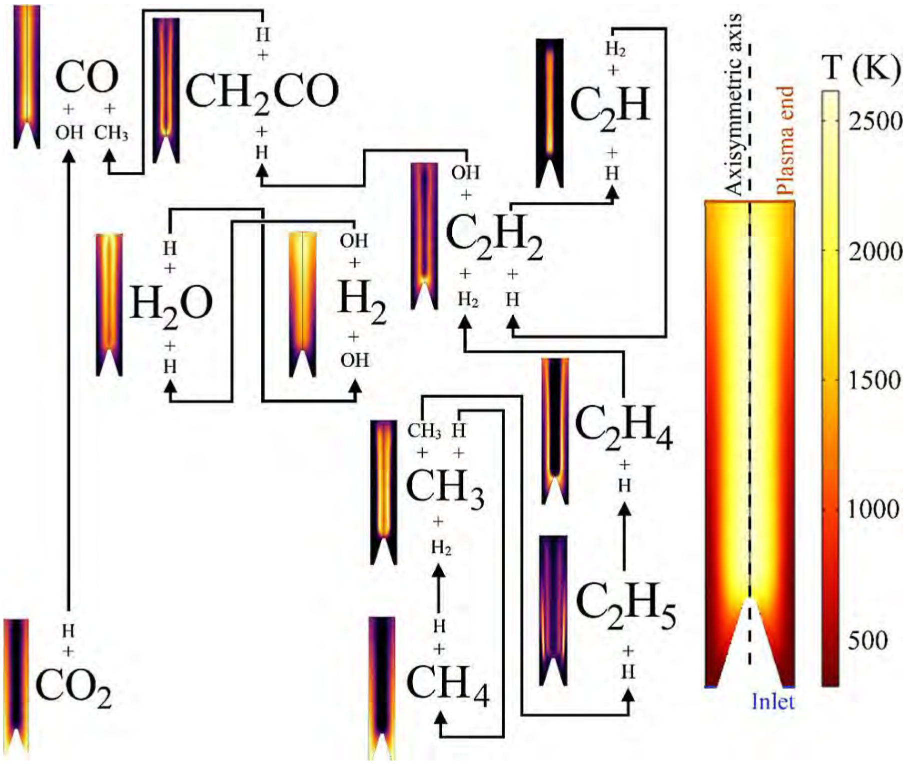

Figure 27: Multidimensional reaction pathway analysis for condition 65-35-0 CO_2-CH_4-O_2 of series A, indicating where most of the shown species are present in the plasma (left), with the temperature profile of the plasma shown at the right.

Only the species with the highest concentrations are plotted, to show a clear chemical pathway. Starting the pathway analysis from the left bottom corner, we find that almost all CO_2 conversion proceeds via reaction of CO_2 with H, to form CO and OH. The latter is an important radical for many pathways, i.e. the shift from H_2 to H_2O and vice versa (as indicated in the middle of the figure). The reaction of OH with H_2 to form H and H_2O is shown in both directions, because they are important in different regions, as indicated from the 2D species concentration profiles. The formation of H_2O from H_2 is important near the edges of the plasma, where H_2 is formed from the reaction of CH_4 and H, producing CH_3 and H_2, but it also stems from the reaction of C_2H_4 to C_2H_2 and H_2 (as also indicated in the middle-bottom part of the figure). H_2 is then again formed from H_2O in the center of the plasma. Note that the plot of H_2O shows a smaller fraction of H_2O present in the center due to this reaction. Furthermore, the production of C_2H_2 from CH_4 passes through multiple hydrocarbons. Indeed, C_2H_5 is created from CH_3, which then generates C_2H_4 closer to the center of the plasma and eventually C_2H_2 even closer to the center (see right part of the figure). We can see that additional CO is formed from reactions of C_2H_2 with, again, OH, leading to the formation of CH_2CO, which eventually decomposes with H to CH_3 and CO (left top of the figure).

Figure 28 illustrates the multidimensional reaction pathway analysis for condition 55-30-15 CO_2-CH_4-O_2 of series A, indicating where most of the depicted species are present in the plasma, and the temperature profile of the plasma.

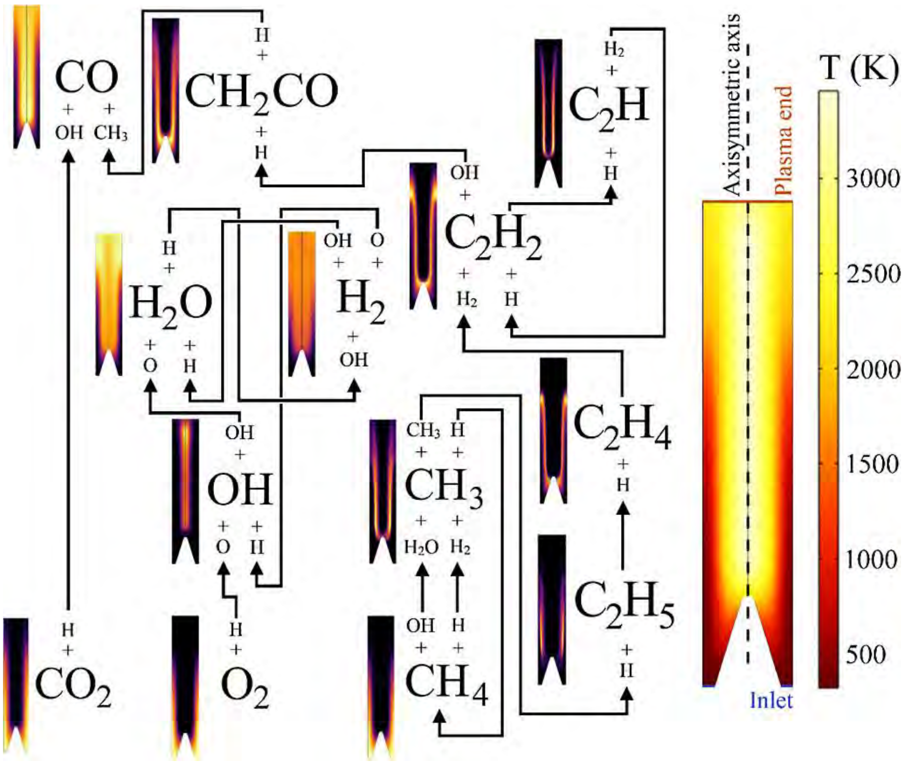

Figure 28: Multidimensional reaction pathway analysis for condition 55-30-15 CO_2-CH_4-O_2 of series A indicating where most of the shown species are present in the plasma (left), with the temperature profile of the plasma shown at the right.

The most pronounced difference in the chemistry compared to Figure 27 is the presence of O radicals provided by O_2, which allows for more reactions involving H_2 and H_2O to be present. The reaction of H_2 with O is an additional source for OH radicals, which can react with itself to form H_2O and O. These additional OH radicals allow for an additional reaction to destroy CH_4, as the latter now also reacts with OH radicals to form CH_3 and H_2O. The presence of C_xH_y species is now much more away from the plasma center compared to Figure 27. This is attributed to the higher temperature, forcing stronger temperature gradients.

These strong gradients result in a smaller space to be occupied by species that will react away at higher temperatures. This is also the reason why much less C_2H_2 can be found near the outlet of the model in the 15 % O_2 case, which is in line with the experiments. Furthermore, as mentioned in section 4.1, C_2H_2 is known as a precursor for the formation of PAH's[30,100], and also the Kassel mechanism[133] describes the formation of solid carbon from C_2H_2 and C_2H, both of which are more present in and near the edges of the plasma in Figure 27. Even though solid carbon particles are not taken directly into account in our model, the increased presence of its precursor also indicates an increased solid carbon formation in condition 65-35-0 compared to condition 55-30-15, which is in line with our experiments.

Furthermore, Figure 28 shows that the formation of H_2O from O_2 is mainly via the reaction of two OH radicals. Additionally, C_2H_2 (and thus solid carbon) will be removed by an increase of OH radicals in the plasma, as the pathway analysis shows the production of CH_2CO in this case. The presence of both pathways means that a rise in OH radical density linearly increases the removal rate of solid carbon (rate of solid carbon removal $\sim$ [OH]), but results in a quadratic increase of the production rate of H_2O (rate of H_2O production from $O_2 \sim [OH]^2$). Hence, adding O_2 has a larger effect on the (low-value) H_2O production than on the solid carbon removal, which explains why the beneficial effects of adding O_2 towards plasma stability and syngas ratio remain small.

4.4 Conclusion

We investigated the effects of O_2 addition to the plasma-based conversion of CO_2 and CH_4 into syngas, i.e., so-called OCRM, in an APGD plasma reactor, by both experiments and modeling.

At an input flow rate of 1 Ls/min and a current of 25 mA, adding O_2 results in a more stable plasma due to the enhanced oxidation of solid carbon (formed upon CH_4 decomposition), as well as in a higher conversion of all reactants, but also in a higher selectivity toward H_2O, and thus a less valuable product output. On the other hand, at an O_2 fraction of 15 %, which was the highest fraction added in our experiments for safety reasons, we could increase the CH_4 fraction beyond the value that was possible without O_2, while still having stable plasma conditions. Such higher CH_4 fractions are clearly beneficial, reaching a high conversion of all reactants, at a lower H_2O selectivity, and higher H_2 selectivity and thus a higher syngas ratio. However, too high CH_4 fractions (i.e., a CO_2-CH_4-O_2 mixing ratio of 36-49-15) again give rise to unstable plasma conditions due to excess solid carbon formation.

The solid carbon material formed in the plasma was found to be contaminated with stainless steel particles, originating from the electrode. The carbon itself consists of planar carbon structures without significant additional ordering, meaning it could be categorized as turbostratic carbon. However, given the contamination of the carbon with steel particles, the value of this side product appears minimal.

Modeling helps us to better understand the underlying physics and chemistry. We applied a 2D axisymmetric coupled fluid dynamics model, developed by a fellow PhD student (Stein Maerivoet), to calculate the conversion, product composition and gas temperature in the afterglow. This model can match most experimental trends, although the calculated afterglow temperature is overestimated, which could be explained by the shape and position of the assumed heat source in the model. This overestimated temperature leads to (an overestimation in) the water–gas shift reaction in the afterglow. We would be able to reach better agreement by tuning the heat source in the model, but we wanted to avoid overfitting of one specific parameter without any validation. In future research, we aim to perform optical measurements and implement self-consistent calculations of the current-conservation and Poisson equation, which will allow a more complete validation of the model. On the other hand, the model shows that the lower H_2O formation upon increasing the CH_4 inlet fraction at 15 % O_2 can explain the lower temperature, demonstrating the value of this type of (fluid dynamics) model compared to simpler thermodynamic calculations.

Overall, we found that a CO_2-CH_4-O_2 mixing ratio of 42.5-42.5-15 yields the best performance, when looking at conversion, energy cost, product output, as well as plasma stability. We obtained a CO_2 and CH_4 conversion of 50 and 74 %, respectively, and an energy cost of 1.98 eV/molecule (corresponding to 190 kJ/mol), which is clearly below the efficiency target determined by Snoeckx and Bogaerts to be competitive with classical DRM and other emerging technologies (i.e., 4.27 eV/molecule).[12]

Mainly syngas is formed (i.e., CO and H_2), with a H_2/CO ratio of 0.8. This value is too low for direct use in methanol or FT synthesis (except when using iron catalysts). Hence, we need to make further efforts to create a more stable plasma at higher CH_4 fractions as well, in order to reach higher H_2/CO ratios, up to the order of 2. This could be achieved by adding N_2 or a noble gas to the gas mixture, but this is often at the expense of a higher energy cost, as demonstrated in literature, while side products may also limit the usage. Another option, supported by the modeling results, could be the addition of H_2O vapor to the plasma, which opens the way for BRM. This will be described in the next Chapter.

Chapter 5 Plasma-based conversion of CO_2 and CH_4 into syngas: a dive into the effect of adding water[4]

Abstract

In this chapter, we present the experiments on BRM, producing syngas out of H_2O vapor next to CO_2 and CH_4, in the cAPGD reactor. Compared to both DRM and OCRM, the addition of H_2O helps in counteracting soot deposition, and thus avoids destabilization of the generated plasma. A mixture of 14-41-45 CO_2-CH_4-H_2O leads to the overall best results in terms of stable plasma and performance metrics. We obtain a CO_2 and CH_4 conversion of 49 % and 74 %, respectively, at a SEI of 2.2 eV/molecule. The energy cost is 4.0 eV/molecule, which is below the target defined for plasma-based syngas production to be competitive with other technologies. Moreover, we reach CO and H_2 yields of 59 % and 49 %, and a syngas ratio of 2, which is ideal for further methanol synthesis.

---

[4] This chapter is based on:
Plasma-based conversion of CO_2 and CH_4 into syngas: A dive into the effect of adding water
B. Wanten, Y. Gorbanev, A. Bogaerts
Fuel, 374, 132355 (2024)
https://doi.org/10.1016/j.fuel.2024.132355

5.1 Introduction

In Chapter 4, we have seen only a limited improvement by adding O_2 to a CO_2-CH_4 mixture, in terms of product output and plasma stability. Therefore, different ways to avoid the negative effects of solid carbon deposition need to be explored.

From literature we already know that both power and flow rate have an influence. Kelly et al.[98] noted that to achieve a stable ignition and conversion of a CO_2-CH_4 mixture (close to a 50/50 ratio) with a MW reactor, a considerable increase in SEI is required for even a small increase (e.g. 5 %) in CH_4 fraction. The mechanism behind this could very well be similar to what we observed through the model in section 4.3.4.4 when O_2 was added, i.e., a lower amount of C_2H_X species positioned further from the center, due to the higher temperature and stronger temperature gradient. Chun et al.[126] also demonstrated a MW reactor that operates in a stable way for a 50-50 CO_2-CH_4 mixture, at a significantly higher power of 3 kW and flow rate of 30 L/min. They state that carbon deposition is still observed at the inner wall of the quartz tube, as expected, but due to the high plasma temperature (ca. 5000 K), it is almost immediately burned away, or it is blown off to the plasma exit under influence of the high flow rate.

Furthermore, Biondo et al.[36] studied the effect of the flow dynamics on the formation and destruction of carbon deposits in plasma. It is clear from their research that the physical expulsion of carbon deposits highly depends on the core-periphery transport of the gas. As seen in section 3.2, a vortex flow is present in our APGD, which in turn will also result in the removal of some carbon deposits due to physical expulsion. This was also observed experimentally, and the cycle of soot growth and physical expulsion can also be assumed to lead to variations in voltage and power. Note that this does not compromise any of the conclusions presented in Chapter 4: as we keep our input flow rate constant at all conditions, we consider that any change in plasma stability is an effect of the changing chemistry, and not because of small differences in the flow regime.

It is clear that both physical and chemical effects can influence the removal of carbon deposits. However, in this chapter we will further focus on the chemical effects through additive gases. This makes sense, as the main goal would be to produce syngas with a H_2/CO ratio of 2, and it is clear that with both DRM and OCRM we are still far from this value. In Chapter 1 we stated that this value of 2 is most suitable for the further conversion towards methanol, which is one of the most valuable chemicals, since it is both a liquid fuel and a hydrogen carrier, and many other chemicals and products can be derived from it.[48]

The additive gas under study in this chapter is H_2O, for a variety of reasons. First, the conversion of CO_2, CH_4 and H_2O into syngas is also known as the BRM, and it is basically the combination of SRM and DRM. The reaction equation is given by (R13):

$$CO_2\ (g) + 2\ H_2O\ (l) + 3\ CH_4\ (g) \rightleftharpoons 4\ CO(g) + 8\ H_2\ (g) \quad \Delta H^\circ = +747.6\ kJ\ mol^{-1} \qquad \textit{(R13)}$$

In literature, BRM is already described extensively by means of thermal catalysis[22,146–149], but also for various plasma types, such as a MW[127,150,151], DBD[85] or GA[103,104] reactor, and clearly holds promise. On one hand, H_2O acts as an additional source for H_2, next to CH_4, so it is easier to obtain a syngas ratio close to 2, as is also observed through (R13).[22,103,104,127,152] This means that, when coupled to a methanol synthesis reactor further downstream, plasma-based BRM can produce methanol, in contrast to plasma-based DRM or OCRM, where an additional external supply of H_2 (from e.g. H_2O electrolysis) would be required.[42] In addition, some amount of H_2O is also present in certain raw biogas mixtures.[22]

On the other hand, the addition of H_2O seems to be an alternative and efficient way to prevent soot formation, based on the available literature.[22,85,100,103,104,150,151,153] From the chemical analysis in section 4.3.4.4, it was clear that OH radicals lead to a linear increase in the removal rate of solid carbon, but an even larger increase in the H_2O production rate – yet, when H_2O is the source for these radicals and we can achieve a net H_2O conversion, the latter is no longer an issue. Further, Wang et al.[100] discussed the reduction of carbon deposits by addition of H_2O in hydrocarbon flames. Although they acknowledge there is still a debate in literature regarding the exact mechanism, the general agreement is that the OH radicals coming from H_2O efficiently intervene in the soot nucleation step, and thus prevent the growth of PAHs into soot particles.[100,102]

For these reasons, we investigate in this chapter the performance of BRM in the cAPGD and provide a comparison with the current state-of-the-art.

5.2 Methods

5.2.1 Experimental setup

An overview of the experimental setup is presented in Figure 29, again similar to the setup presented in Figure 10 and Figure 17. A difference for the present experiments is that CO_2 and CH_4 are mixed with de-ionized water before entering the reactor. The H_2O container is heated by a silicon oil bath positioned over a hotplate stirrer (IKA RCT basic). The exact flow rate of H_2O vapor (and hence its input fraction) is regulated through keeping the oil bath at a specific temperature. The calculations for the flow rates of H_2O vapor (in mol/min) are provided as supporting information (see section 8.3.1). For each selected oil bath and H_2O vapor temperature, the stainless steel gas line between the H_2O container and the reactor inlet is heated up to a temperature approx. 10 °C higher than the oil bath temperature to avoid condensation of H_2O and to allow the introduction of a homogeneous CO_2-CH_4-H_2O gas mixture into the plasma. This is also why we refer to the H_2O input as "vapor", and not as "steam": no heterogeneous H_2O droplets (which would be the case when steam, aerosol or mist generators would be applied) enter the plasma reactor. For our purposes, where we want to focus solely on the role of H_2O on the overall chemistry and performance, a homogeneous mixture is preferred. The output gas mixture is again led into a cold trap and carbon filter before entering a heated sample gas line, connected to an Agilent two-channel 990 MicroGC.

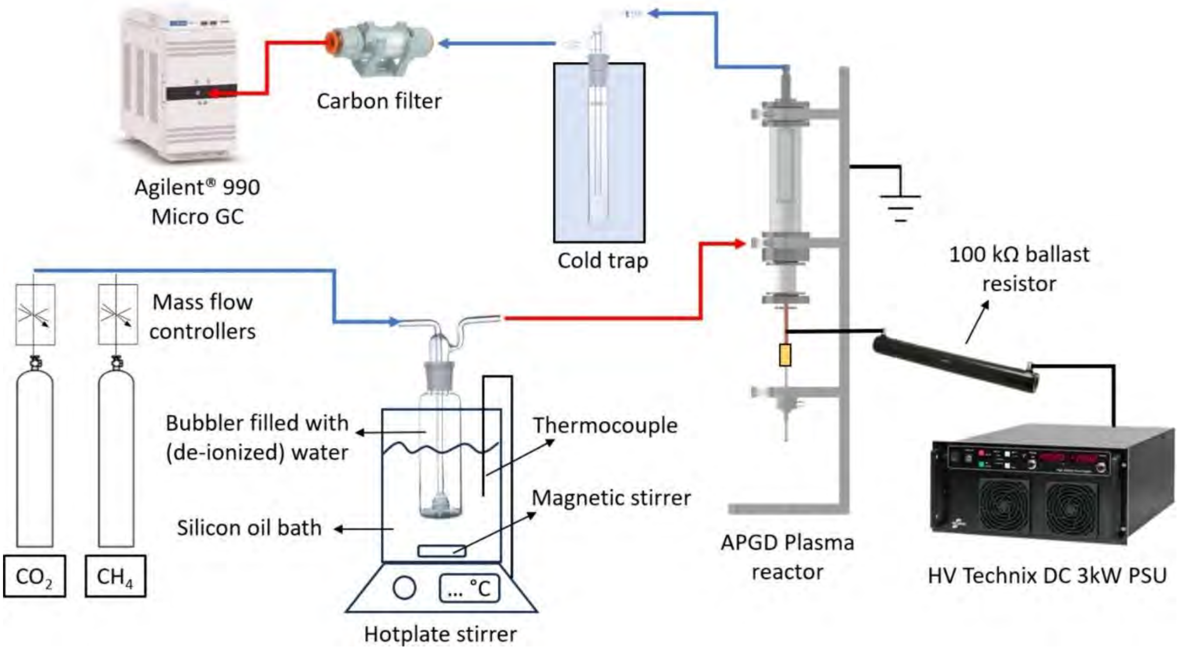

Figure 29: Overview of the experimental setup. Gas lines are represented by blue (around room temperature) and red (heated) arrows, thick black lines represent HV and ground cables.

The reactor used in this study is an upgraded version of the reactor previously described in Chapter 3 and Chapter 4, and is schematically and photographically presented in Figure 30. While the concept of the design itself is not significantly altered, there are some changes worth mentioning. First, the ceramic tube is now made of 99.7 % Al_2O_3, which provides a better thermal shock resistance compared to MACOR. In addition, the dimensions of the electrodes, ceramic tube opening and downstream reactor parts have been slightly adapted to allow larger input flow rates, theoretically up to 10-15 L/min (though the flow rate used in these experiments was kept lower to ensure sufficient mixing of the dry gas with the H_2O vapor). Additionally, the stainless steel cathode pin is now connected to a remotely controlled stepper motor, allowing the cathode to be moved in the axial direction closer to or further away from the anode plate, even while the plasma is already ignited. As a consequence, plasma ignition can take place very easily at reduced inter-electrode distances, and subsequently the electrodes can be moved further apart, to obtain a longer (desired) discharge length (and higher plasma power). Ultimately, this allows us to achieve inter-electrode distances where direct ignition of the plasma, with the gas mixture under study, would be impossible.

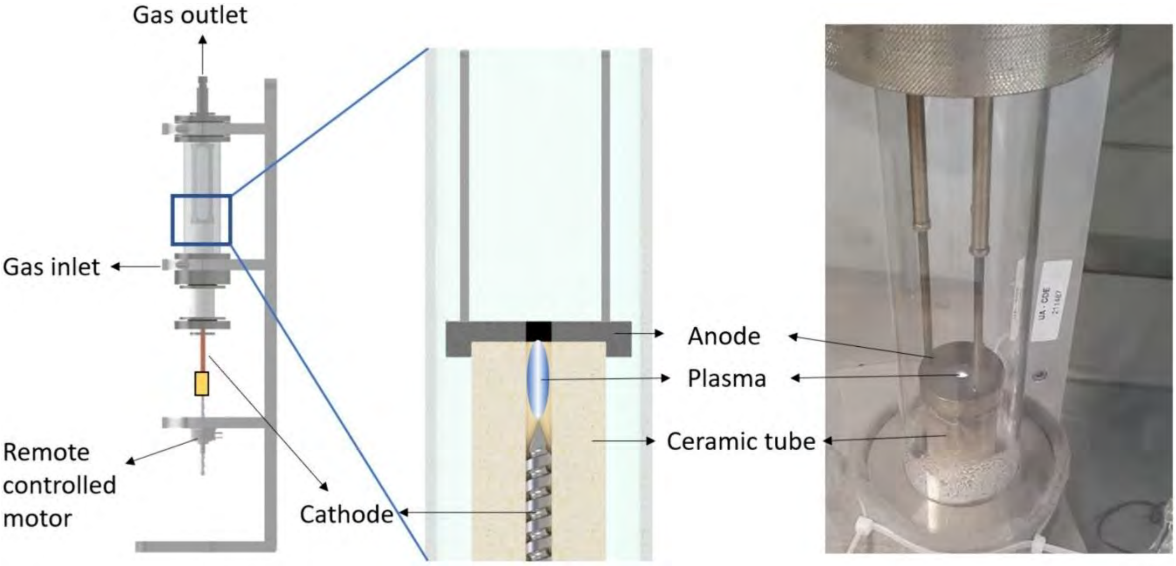

Figure 30: Schematic (left + middle) and photographic (right) representation of the APGD plasma reactor used in this study. Important reactor parts are indicated.

Also another current-controlled high voltage DC Technix PSU is used compared to the one described in Chapter 3 and Chapter 4. This one is capable of supplying max. 20 kV and 150 mA (=3 kW). Ballast resistors (with a net resistance of 100 kOhm) are still put between the HV cable and the cathode to limit and stabilize the current.

5.2.2 Experimental procedure and performance metrics

We kept the total input flow rate constant at 3 Ls/min (using the Bronkhorst definition for standard conditions, i.e., 1 atm and 20 °C) and the plasma power at 300 W. Initially the plasma is ignited for pure CO_2 and the oil bath surrounding the H_2O container is set to a temperature corresponding to a specific H_2O vapor flow rate (75, 85 and 95 °C – the relationship between temperature and H_2O vapor flow rate is derived and presented in section 8.3.1). Once this temperature is reached, CH_4 is added. At this point, the CO_2 and

CH_4 flow rates are arranged through separate MFCs to obtain various CO_2/CH_4 ratios (65/35, 50/50, 35/65 and 25/75). This leads to 12 different mixtures, presented in Table 4. For each stable condition (the stability of the mixtures will be further elaborated in section 5.3.1), four GC samples are taken, with the first sample taken 2–3 min after the input mixture, power and flow rate are set, and further after 3.5 min runtime between each sample. For each GC sample, we recorded the voltage, current and oil bath temperature. This procedure is repeated three times in total for each condition, and the results presented in section 5.3 are the weighted averages for each condition.

Table 4: Overview of 12 different mixtures tested experimentally, obtained through combining four different CO_2/CH_4 ratios and three different H_2O temperatures.

		CO_2/CH_4 ratio			
		65/35 (1.86)	50/50 (1.00)	35/65 (0.54)	25/75 (0.33)
		CO_2-CH_4-H_2O mixture (%)			
Liquid H_2O temperature (°C)	75	**47-25-28**	**36-36-28**	**25-47-28**	**18-54-28**
	85	**42-22-36**	**32-32-36**	**22-42-36**	**16-48-36**
	95	**36-19-45**	**27.5-27.5-45**	**19-36-45**	**14-41-45**

The formulas to calculate the performance metrics presented in Chapter 2 are also used in this Chapter, with specifically equation (15) to express the energy efficiency. The input molar flow rates are controlled through the MFC's for CO_2 and CH_4 and the oil bath temperature for H_2O. The output molar flow rates are derived through the molar fractions associated to each species measured through the GC samples on one hand, and the total output molar flow rate on the other hand. The latter can be derived from the carbon balance, and this approach was validated by comparison with measurements done with a soap film flow meter. More information on the derivation of the output molar flow rates of all species can be found in section 8.3.2.

The input power used in the energy cost and energy efficiency equations does not only consist of the plasma power, but also the minimum power required to fully evaporate H_2O, to afford the desired input flow rate of H_2O. This power, $P_{H_2O\ evap}$, is derived through the following equation:

$$P_{H_2O\ evap} = \frac{\dot{n}_{H_2O}^{input} \cdot HHV_{H_2O\,(g)}}{60\ s\ min^{-1}} \tag{19}$$

With $\dot{n}_{H_2O}^{input}$ the molar input flow rate of H_2O, and $HHV_{H_2O\,(g)}$ equal to the HHV of H_2O vapor, or also the latent heat of vaporization, equal to 44.2 kJ/mol[154].

5.3 Results and discussion

5.3.1 Soot formation and plasma stability

We start our results section by showing the different behavior in terms of stability, with and without additional H_2O. In Figure 31 we present the plasma power as function of time for a 55–45 CO_2-CH_4 input mixture, without any additional H_2O as a reactant, and for a 32–32–36 CO_2-CH_4-H_2O input mixture.

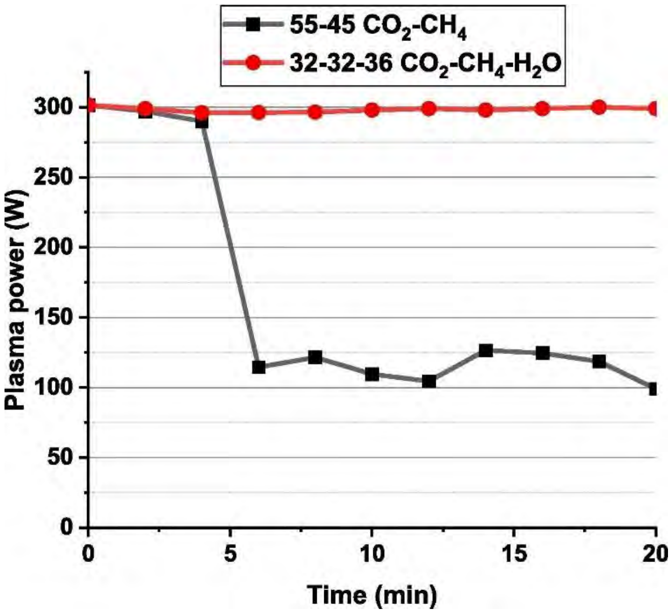

Figure 31: Plasma power as a function of time for a 55–45 CO_2-CH_4 input mixture, where the effect of soot formation on the plasma power is clearly visible and for a 32–32–36 CO_2-CH_4-H_2O input mixture, where no significant soot formation and a stable plasma power is observed. Total input flow rate and initial plasma power are 3 Ls/min and 300 W, respectively.

For a 55–45 CO_2-CH_4 input mixture, after approximately 5 min, the plasma power drops instantly to almost one third of its initial value, a behavior that could indicate a transition into an arc. As discussed before, soot deposition has a significant effect on the plasma dynamics and voltage, and consequently the plasma power. Since this drop in power leads to a lower temperature, at which soot formation is favored[22], this negative effect will only enforce itself. The slight fluctuations observed afterwards are likely due to the cycle of growing soot clusters, which at some point are physically expulsed by the gas flow, as explained in section 5.1.[97] In Figure 32 we present a picture of the reactor's glass tube after this measurement, where the glass wall of the side after the anode is covered with soot. Illustratively, at the same (initial) conditions for a 32–32–36 CO_2-CH_4-H_2O mixture, no significant soot formation was observed. In this case, the plasma power remains very stable around the initial value of 300 W.

Figure 32: Picture of APGD reactor's glass tube after the measurement, with a 55–45 CO_2-CH_4 input mixture at 3 Ls/min and 300 W. The glass wall at the side after the anode, where the gas exits the plasma, is covered with soot.

This significant change in plasma power will affect the performance metrics severely. The CO_2, CH_4 and H_2O conversion, as well as the CO and H_2 yield, are presented as a function of time for a 32–32–36 CO_2-CH_4-H_2O input mixture in Figure 33a, and for a 55–45 CO_2-CH_4 mixture in Figure 33b. The total input flow rate and (initial) plasma power are 3 Ls/min and 300 W, respectively. The GC measurements with water started three minutes after the oil bath temperature, power and flow rate were set, as described in section 5.2.2. The GC measurements without water started as soon as the plasma was ignited.

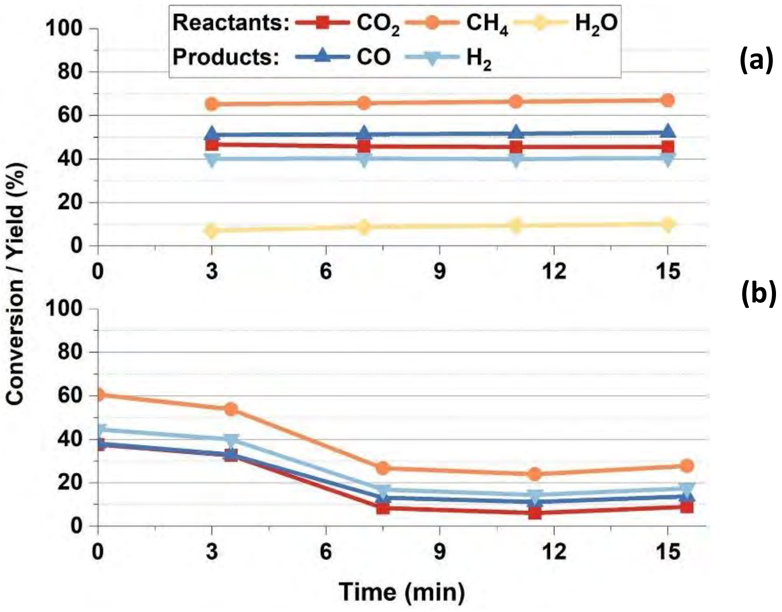

Figure 33: CO_2, CH_4 and H_2O conversion (%) and CO and H_2 yield (%) as a function of time for (a) a 32–32–36 CO_2-CH_4-H_2O input mixture and (b) a 55–45 CO_2-CH_4 input mixture. Both measurements are done at a total input flow rate of 3 Ls/min and an initial plasma power of 300 W.

Figure 33a shows a constant conversion and yield over the entire duration of the experiment. In Figure 33b, we see that the initial conversion and yields are approximately at the same level as for the condition with H_2O added, but they decay rapidly over time. Of course, this confirms our previous observations in Chapter 3 and Chapter 4 with the same APGD reactor, where we were unable to obtain a stable plasma for DRM with CH_4 fractions above 35 %.[131]

In section 5.2.1, we briefly discussed the improvements in terms of reactor design (with adjustable cathode–anode distance) and the use of a different power supply. This provides us with better control over the plasma power, and specifically for the present experiments, this also aids us in counteracting the decreasing voltage during soot deposition. Indeed, a small drop in voltage could be compensated by a slight increase in current (which was not really possible for the DRM experiments, because the current was close to the maximum limit of the PSU) or inter-electrode distance (which always remained constant during DRM and OCRM). Slightly changing the inter-electrode distance and current such that the plasma power remains equal, did not significantly change any of the performance metrics (see section 8.3.3). Likely, the fact that the overall performance remains the same for different lengths is due to compensating effects linked to the increased contact area between the plasma and the wall, different temperature distributions, an increased residence time, etc.

Nevertheless, when the rate of soot formation was too high, we observed a clear instability similar to what is shown in Figure 31 and Figure 33, which could not be circumvented.

For this reason, we categorized the 12 different mixtures presented in Table 4 into three groups based on their stability, and we indicated them through a color code in Table 5. A green color represents mixtures where no significant soot formation was observed. When only a very small fraction of soot (i.e. < 1 mg after 15 min) was collected afterwards, with a minor effect on the plasma power, easily circumvented through a slight change of the current and inter-electrode distance, the mixtures are indicated in orange. Mixtures where the rate of soot formation was too high to achieve stable performance, are indicated in red. Consequently, for the gas mixtures in red color, no reproducible experimental results could be obtained.

Table 5: Overview of different mixtures tested experimentally. Mixtures indicated in green had a stable plasma power and no soot was observed, mixtures indicated in orange required a few slight changes to the inter-electrode distance to maintain a constant plasma power, and only < 1 mg soot was collected afterwards. Mixtures indicated in red had too extensive soot formation to achieve reliable results.

		CO_2/CH_4 ratio			
		65/35 (1.86)	50/50 (1.00)	35/65 (0.54)	25/75 (0.33)
		CO_2-CH_4-H_2O mixture (%)			
Liquid H_2O temperature (°C)	75	**47-25-28**	**36-36-28**	**25-47-28**	**18-54-28**
	85	**42-22-36**	**32-32-36**	**22-42-36**	**16-48-36**
	95	**36-19-45**	**27.5-27.5-45**	**19-36-45**	**14-41-45**

Table 5 clearly indicates that at the conditions under study, a CH_4 fraction above ca. 42 % (i.e. upper right corner of Table 5) is accompanied with extensive soot formation. This is not really an improvement compared to DRM and OCRM in the previous chapters. However, at the same CH_4 input fraction, we do observe a difference in stability depending on the CO_2/H_2O ratio. For example, two mixtures in Table 5 have 36 % CH_4, yet the mixture with only 19 % CO_2 and 45 % H_2O was visibly more stable (no soot observed at reactor walls, stable plasma power), while combined with 36 % CO_2 and only 28 % H_2O, soot formation (and its effect on the plasma power, albeit relatively small) was visible. This confirms earlier findings in literature regarding the effectiveness of H_2O to counteract soot formation.[22,103,150,151]

Moreover, it should be mentioned that we also observe a difference depending on the SEI. Specifically, we tested the 14–41–45 (CO_2-CH_4-H_2O) mixture at the bottom right corner with the same total input flow rate (3 Ls/min) but a higher plasma power (400 W instead of 300 W). At these conditions, the plasma was significantly more stable. It can be hypothesized that a higher SEI leads to an increased availability of O and OH radicals to remove the (precursor of) the solid carbon, due to a higher CO_2 and H_2O conversion. The latter is indeed the case, as will be discussed in section 5.3.4.

5.3.2 Effect of H_2O input fraction

In section 5.3.1, we showed that adding H_2O to a CO_2-CH_4 mixture improves the overall plasma stability. In this section, we present the effect of H_2O addition on the other performance metrics. Specifically, we compare 28, 36 and 45 % H_2O addition, at a 50/50 CO_2/CH_4 ratio (corresponding to the BRM mixtures of the second column in Table 5). The reactant conversions and product yields are presented in Figure 34 (a), along with the conversion and production rates (b), at three different H_2O input fractions. Energy cost and energy efficiency, as well as syngas ratio, are presented in Figure 35 as a function of H_2O input fraction.

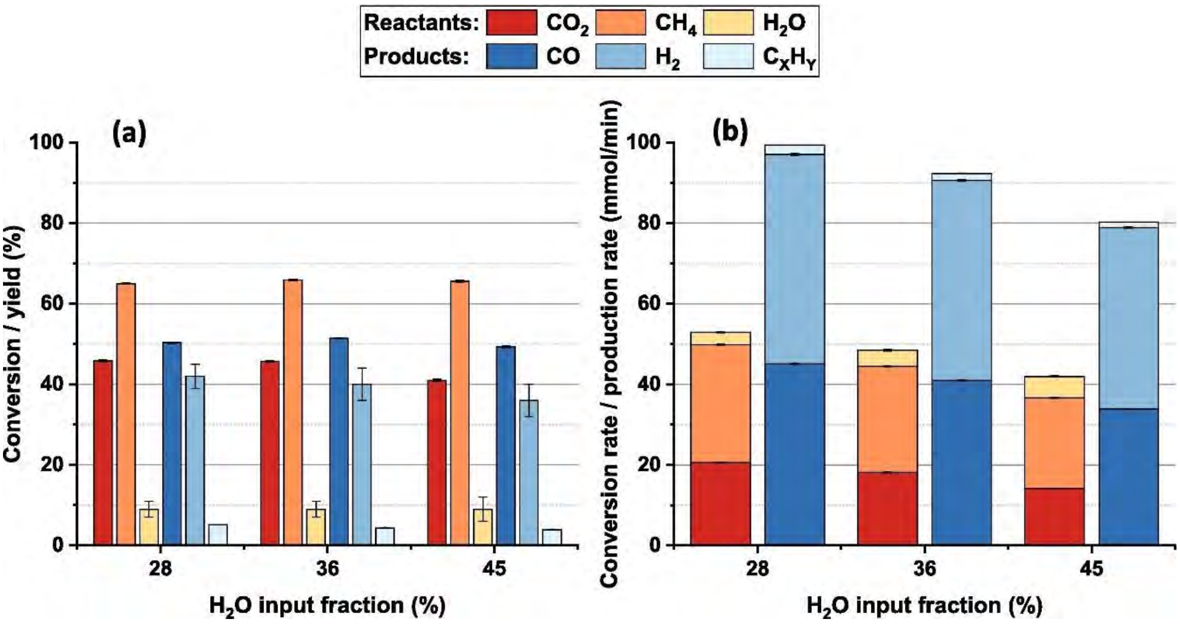

Figure 34: (a) Conversion and yields (%), and (b) conversion and production rates (mmol/min) of the reactants and products, respectively, as a function of the H_2O input fraction (%) at a CO_2/CH_4 ratio of 1. C_XH_Y stands for the combined yields and production rates of the small hydrocarbons detected, consisting of (in decreasing order) C_2H_2, C_2H_4, C_2H_6 and C_3H_8 (i.e. n-propane). The error bars are obtained through linear error propagation, based on the standard deviation of the measured values. In some cases they are too small to be visible.

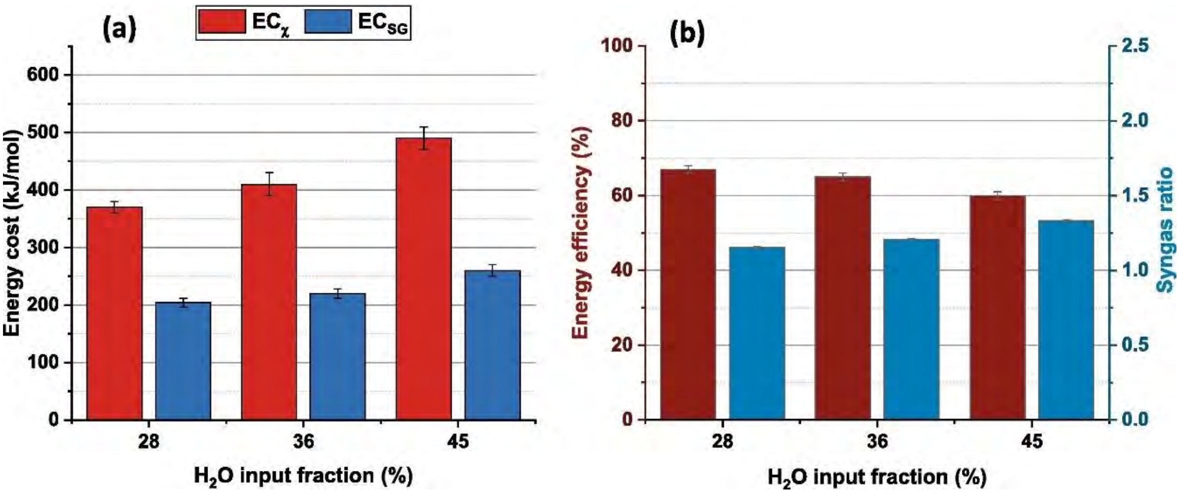

Figure 35: (a) Energy cost (expressed in kJ/mol converted gas, EC_χ, and in kJ/mol syngas formed, EC_{SG}), and (b) energy efficiency (%, left axis) and syngas ratio (right axis) as a function of H_2O input fraction (%) at a CO_2/CH_4 ratio of 1. The error bars are obtained through linear error propagation, based on the standard deviation of the measured values. In some cases they are too small to be visible.

First, note that the error margins for the H_2O conversion (and consequently for the H_2 yield) are somewhat larger relative to the other values, due to the temperature dependence of the H_2O input flow rate. The use of more specialized equipment in the future (such as a

Bronkhorst® controlled evaporator mixer[155]) could solve this issue. In terms of trends, we can observe that increasing the H_2O input fraction has no significant effect on the CH_4 (approx. 66 %) and H_2O (approx. 9 %) conversion, and the CO_2 conversion only slightly decreases, from ca. 46 % to 41 % (Figure 34a). However, the conversion rate (in mmol/min, Figure 34b) decreases for both CO_2 and CH_4, due to the lower flow rate of these components in the feed gas. Specifically, the CH_4 conversion rate drops from ca. 29 to 22 mmol/min. The H_2 production rate also decreases, but not as much, which could mean that simply more H_2 is formed directly from H_2O plasmolysis. However, the CO_2 conversion rate drops from 21 to 14 mmol/min, suggesting that a reaction leading to CO_2 formation may be occurring. Taken together, this suggests that the water–gas shift (WGS) reaction could be taking place (reverse reaction of (R4)). Note that we also observed the WGS reaction in the model for OCRM in section 4.3.4, and other references report this as a common side-reaction of the BRM as well.[104,127,149]

Since adding H_2O negatively affects both conversion and production rates overall, the energy cost rises upon H_2O addition, i.e. from 370 kJ/mol to 490 kJ/mol (for 28 and 45 % H_2O); cf. Figure 35a. To allow a more fair comparison between BRM and DRM (as done in section 5.3.4 below), we also plot the energy cost expressed in kJ/mol syngas (i.e. 1 mole of CO and H_2 combined, with the syngas ratio at the associated condition) produced in Figure 35a, as this is the product shared between both reactions. This value is significantly lower than the energy cost expressed per mole converted reactant, because the number of moles expands during reaction, but the observed trend remains the same. The energy efficiency is also negatively affected upon H_2O addition, with a drop of 7 %, from 67 % to 60 % (Figure 35b). Finally, the syngas ratio rises from ca. 1.15 to 1.33. This is not a consequence of more H_2 produced, but due to a more substantial drop in CO production rate. Furthermore, a ratio of about 1.3 is still far away from the targeted ratio of 2.

Overall, nearly all performance metrics show a negative trend when adding H_2O, so the benefit is limited to plasma stabilization at conditions when otherwise too much soot is produced, i.e. higher CH_4 input fractions, as explained in section 5.3.1. In literature, an increase in the H_2O input fraction or flow rate also does not prove to be beneficial. An overall negative or negligible effect on the conversion is observed by Hrycak et al.[150], Alawi et al.[127], Wang et al.[104] and Xia et al.[103], as well as a decreasing CO yield. The H_2 yield is sometimes reported to increase, in contrast to our work, though the amount of H_2 produced is often seen relative only towards the CH_4 input, neglecting the H_2 that comes from H_2O.[103,127] The same references all report an increasing syngas ratio as well, which is the only positive effect we observed with our data. Most importantly, Hrycak et al.[150] conclude that an increased H_2O input fraction does not lead to an increased H_2 production rate, CH_4 conversion and EC, but that it does allow the use of higher CH_4 input fractions through the suppression of soot formation. Based on the BRM reaction equation (see section 5.1), CH_4 should indeed be further increased, to e.g. afford a syngas ratio closer to 2. Hence, adding H_2O might still be beneficial when simultaneously the CH_4 input fraction is increased and thus, the following section is dedicated to results obtained with the highest H_2O content (45 %) and an increasing CH_4 fraction.

5.3.3 Effect of CO_2/CH_4 ratio

In Figure 36 and Figure 37, we plot the same performance metrics as in section 5.3.2, but comparing four different CO_2/CH_4 ratios at constant H_2O input fraction (45 %, corresponding to the last row in Table 5).

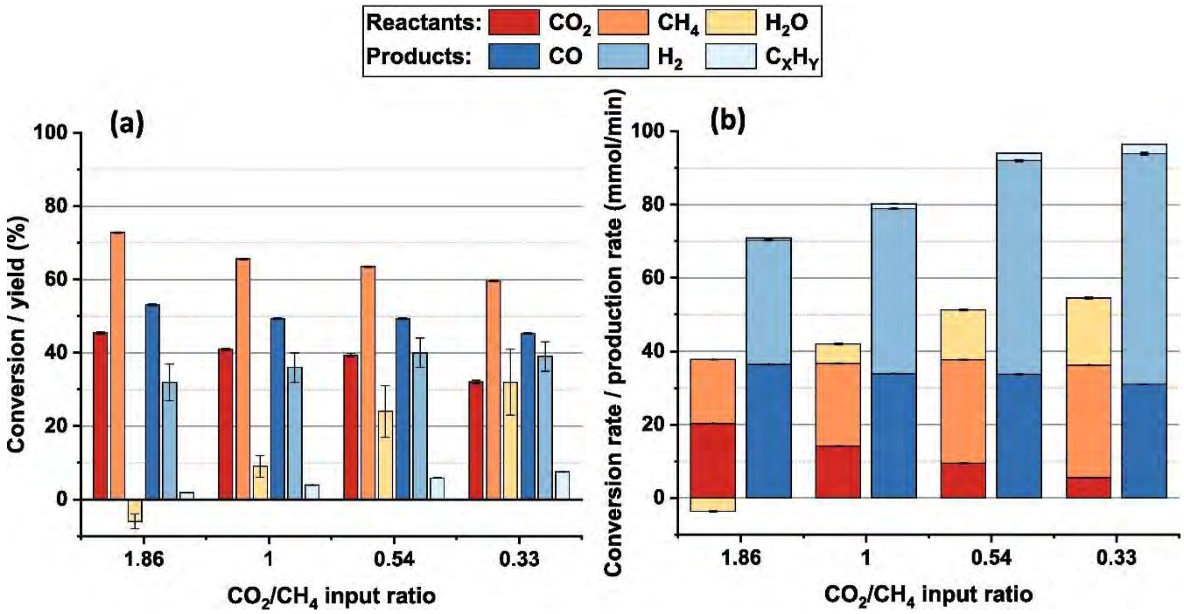

Figure 36: (a) Conversion and yield (%), and (b) conversion and production rate (mmol/min) of the reactants and products, respectively, as a function of the CO_2/CH_4 input ratio at a 45 % H_2O input fraction. C_XH_Y stands for the combined yields and production rates of the small hydrocarbons detected, consisting of (in decreasing order) C_2H_2, C_2H_4, C_2H_6 and C_3H_8 (i.e. n-propane). The error bars are obtained through linear error propagation, based on the standard deviation of the measured values. In some cases they are too small to be visible.

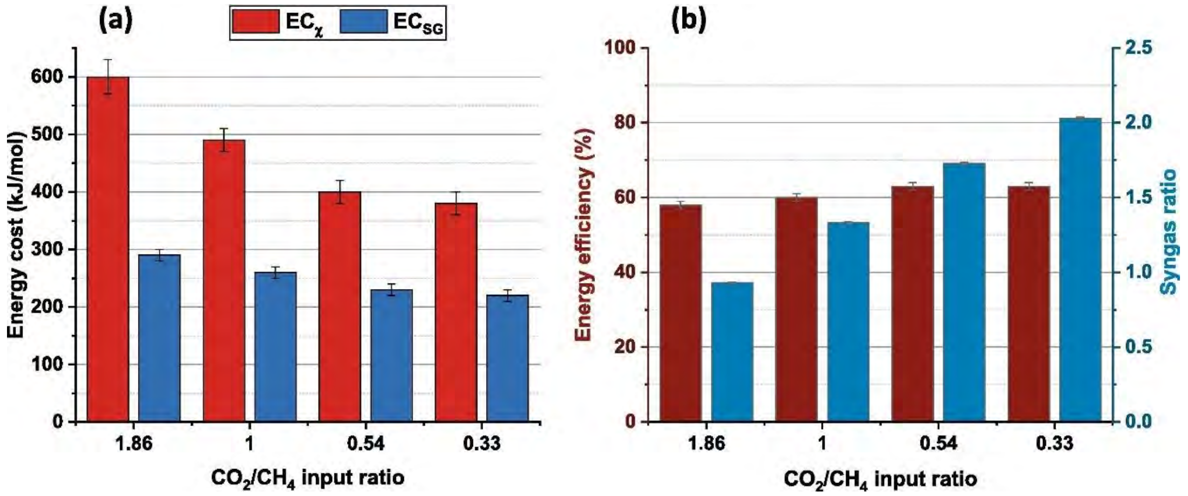

Figure 37: (a) Energy cost (expressed in kJ/mol converted gas, EC_χ, and in kJ/mol syngas formed, EC_{SG}), and (b) energy efficiency (%, left axis) and syngas ratio (right axis) as a function of CO_2/CH_4 input ratio at a 45 % H_2O input fraction. The error bars are obtained through linear error propagation, based on the standard deviation of the measured values. In some cases they are too small to be visible.

Changing the CO_2/CH_4 input ratio towards higher CH_4 amounts is clearly beneficial for the overall conversion rate, which rises with 20.4 mmol/min. Also the H_2O conversion changes drastically, starting with a negative conversion of −6 % (meaning additional H_2O is formed) at 1.86 CO_2/CH_4 ratio, up to a conversion of 32 % at 0.33 CO_2/CH_4 ratio, reaching the same level of conversion as CO_2. At the same time, the CO_2 and CH_4 conversion are both reduced, but as the CH_4 fraction increases from 19 to 41 %, its conversion rate rises significantly by 13.2 mmol/min. The reason for the significant drop in CO_2 conversion rate is because its input fraction is the lowest at the 0.33 CO_2/CH_4 ratio, while simultaneously H_2O makes up 45 % of the input mixture (vs 14 % CO_2). Hence, either SRM is heavily promoted over DRM in this overall BRM reaction process, or the WGS reaction could again take place, explaining the lower CO_2 and higher H_2O conversion.

In terms of yields and production rates, there is a visible decrease for CO and increase for H_2. This is explained by the higher conversion rate of CH_4 and H_2O and the lower CO_2 conversion rate. As a consequence, the syngas ratio rises up to 2.03 (cf. Figure 37b), more than twice compared to the value at 1.86 CO_2/CH_4 input ratio, and reaching the desired target for further downstream production of value-added oxygenates, e.g. methanol. Note that also the C_XH_Y yield and production rate increases at higher CH_4, which is also logical, although not exceeding 7 % and 2.6 mmol/min, respectively.

The energy cost is substantially reduced as well. At 0.33 CO_2/CH_4 input ratio, the energy cost per mole of converted reactants equals 380 kJ/mol, which is 220 kJ/mol lower than at

1.86 CO_2/CH_4 input ratio. Moreover, it drops below the target of 412 kJ/mol (= 4.27 eV/molecule), as set by Snoeckx and Bogaerts for DRM.[12] We observe the same trend for the energy cost expressed per mole syngas, though its drop (approx. 75 kJ/mol) is less spectacular. The energy efficiency improves as well, up to 63 % at 0.33 CO_2/CH_4 input ratio.

Our observations in terms of trends are generally in agreement with literature. Hrycak et al.[150] also reported an improved H_2 production rate and energy cost at a higher CH_4 input fraction. Wang et al.[104] and Xia et al.[103] reported a lower CH_4 conversion and a higher syngas ratio, as in our work. A difference with our work is that they reported a higher CO_2 conversion at a lower CO_2/CH_4 input ratio. However, the large H_2O input fraction in our conditions can be the cause of this different trend, as e.g. Wang et al.[104] did not apply an input fraction above 27 %, and H_2O can compete with CO_2, as explained above.

It is clear that changing the CO_2/CH_4 ratio towards higher CH_4 amounts is beneficial. In fact, the best results are reached for almost all performance metrics (except CO_2 conversion) at the highest CH_4 fraction, and the most important targets (i.e., syngas ratio of 2 and energy cost below 412 kJ/mol) are achieved. The ideal stoichiometric BRM reaction (cf. section 5.1) dictates a 1–3-2 CO_2-CH_4-H_2O mixture as input, while our best results are obtained for this 1–2.9–3.2 ratio. Unfortunately, a drop in H_2O content from 45 to 33 % (as dictated by the optimal stoichiometry), compromised the plasma stability again (see Table 5: conditions in red).

5.3.4 Effect of SEI and comparison with state-of-the-art

As mentioned in section 5.3.1, the plasma stability improved upon increasing SEI. The same applies to (most of) the other performance metrics. Table 6 indeed demonstrates that a higher SEI (due to a higher power of 400 W instead of 300 W, at the same total input flow rate of 3 Ls/min) greatly improves the conversions and product yields, while the energy cost and energy efficiency are quasi the same and the syngas ratio only slightly worse (though 1.94 is still at a sufficiently high level for further methanol synthesis). These general trends are in line with what we observed for DRM in Chapter 3, and are very similar for many plasma reactors described in literature, for both DRM and BRM: higher conversions and yields, but usually at the cost of a higher energy cost and lower energy efficiency.[12,127,131,150–152] It should be noted that we also briefly tested a power of 500 W (and thus an even higher SEI of 240 kJ/mol), but then the reactor would show signs of overheating, hence we did not investigated this further.

Table 6: Comparison of our work (at two different SEI values) with literature, both in the same APGD reactor but without H_2O addition (no BRM), and for BRM in other reactors, for conversion χ (%), product yield Y (%), syngas ratio SR, syngas production rate $\dot{n}_{syngas}^{produced}$ (mmol/min), energy cost EC (kJ/mol) and energy efficiency EE (%). Values with '' were not explicitly reported in the cited references, but could be derived from other reported values in the paper. Values with '**' were explicitly reported, but are recalculated to allow proper comparison with our data. Values that were not reported and could not be derived through other data, are indicated with '/'. Parameters that are not applicable are indicated in grey.*

		SEI (kJ/mol)	Input fraction (%)					χ (%)				Y (%)		SR	$\dot{n}_{syngas}^{produced}$ (mmol/min)	EC (kJ/mol)		EE (%)
			CO_2	CH_4	H_2O	O_2	N_2	CO_2	CH_4	H_2O	Total	CO	H_2			Conv.	Syngas	
BRM, DRM and OCRM in APGD	**BRM**	160	14	41	45			32.1	59.6	32	43	45.3	39	2.03	93.9	380	220	63
		210	14	41	45			49.0	73.9	40	54	59.2	49	1.94	119.1	390	220	62
	DRM	190	65	35				53.9	72.4		61.1	57.3	52	0.64	42.4	320	200	69
	OCRM	127	42.5	42.5		15		49.5	74.4		66.7	58.6	46.5	0.78	39.3	190	143	70
BRM in other reactors	**Hrycak et al.**[150]	95*	27.3*	27.3*	45.3*			63*	74.3	-47*	17*	41*	35*	1.56*	2326	565*	145*	56*
		54*	15.4*	46.2*	38.4*			48*	48.9	-51*	12*	16*	21*	2.80*	2682	445*	168*	42*
	Alawi et al.[127]	280*	10.7*	5.3*	43.3*		40.7*	19.2	82.7	/	/	9.04	14**	5.23	13.5	/	3107*	/
	Wang et al.[104]	75*	40	40	20			22.5	15	/	/	11*	3*	0.35	36.6	/	635*	29*
	Xia et al.[103]	200**	16*	47*	37*			47.5	52.5	/	/	18*	26*	3	10.7	/	447*	/

Table 6 also provides a comparison with (i) some of our results for DRM and OCRM, and (ii) literature values for BRM experiments in other reactor types, i.e., a MW[127,150] and GA[103,104] reactor. Noticeably, when comparing with DRM, the CH_4 conversion and CO and H_2 yields are almost equal. The somewhat higher CO_2 and total conversion than for BRM is due to the H_2O addition, reducing the CO_2 conversion, as observed in section 5.3.2 and 5.3.3. This also explains the better energy cost expressed per mol converted for DRM. However, the energy cost expressed per mol syngas formed is only slightly better for DRM. This indicates that the lower conversion is compensated by a larger selectivity towards syngas with BRM. The most substantial difference lies with the syngas ratio, which is more than three times higher for BRM than for DRM. When aiming at further methanol synthesis, this is a crucial advantage of BRM over DRM.

For OCRM, the SEI was lower than for BRM, yet the conversions and product yields are very much in line (and the total conversion was even higher, due to the more difficult conversion of H_2O, which is absent in OCRM). Consequently, the energy cost is approx. 200 kJ/mol lower for OCRM. This can be explained by the overall reaction enthalpy for OCRM, which is lower than for DRM or BRM, hence, a much lower SEI can give the same level of conversion and syngas yield. However, in case of OCRM, the syngas ratio barely differs from the one obtained by DRM, again demonstrating the advantage of BRM. Note that also the syngas production rate for BRM is higher than for DRM and OCRM, mainly because of the larger total input flow rate in our work (3 Ls/min instead of 1 Ls/min).

BRM has also been investigated recently in other plasma reactors. Hrycak et al.[150] described BRM in a MW plasma, operating at a plasma power of 6.5 kW and flow rates of 50–100 L/min. Due to this large flow rate, the syngas production rate is much higher than in our experiments, but simultaneously, the SEI is much lower. Still, at a SEI of 95 kJ/mol, they reported a CH_4 conversion of 74.3 %, comparable to our data, with a syngas ratio of 1.5 – 2.8. However, based on their data and assuming that H_2O was the only significant component missing to obtain a perfect mass balance, they had a significant H_2O production instead of conversion. In fact, these data imply that the presence of H_2O merely suppressed the soot formation. The latter was also observed at an even lower SEI, for a mixture comparable to our best BRM mixture. In section 5.3.3, we also observed a negative H_2O conversion for one condition, and in general, the H_2O conversion was the lowest of all reactants. This indicates that at even lower SEI, the H_2O conversion drops the most, and can become negative (i.e., net H_2O production). Taking this negative conversion into account, the energy cost expressed per mol converted is of course very high for their conditions (cf. Table 6) and much higher than in our experiments. Yet, when expressing the energy cost per mol syngas formed, its value is lower than our results. This can also be explained by the net H_2O formation, which is an exothermic reaction, hence increasing the temperature of the mixture, similar to the effect we observed for O_2 addition in OCRM.[97]

Alawi et al.[127] used a significantly higher SEI than in our work. Furthermore, while their H_2O input fraction was similar to ours, a large fraction of N_2 was also added. As mentioned previously, the addition of N_2 can lead to a better performance overall, but typically only when its fraction is kept low enough (Van Alphen et al.[99] found an optimum at 20 %, for DRM).[48,96] Additionally, their CH_4 input fraction was the lowest across all references presented in Table 6, while higher amounts of CH_4 generally improve the total conversion and energy cost, as observed in section 5.3.3, and also in Chapter 3. As a result, their syngas-based energy cost was extremely high, even in the order of MJ/mol syngas. The CO_2 conversion and syngas yield were also significantly lower than in our work, despite the much higher SEI. Only the CH_4 conversion exceeds ours, which may be explained by the higher SEI, but also due to its low input fraction and the fact that it is the easiest reactant to convert. This also explains why the authors reached a high syngas ratio (even of 5.23).

Wang et al.[104] used a GA reactor, generating a CO_2-H_2O plasma with CH_4 injected in the afterglow, and at much lower SEI than in our work, hence their results are quite different from ours. In fact, they even obtained a lower CH_4 conversion than CO_2 conversion, attributed to their specific setup, where CH_4 is only injected in the afterglow. This further results in low product yields, a low syngas ratio, a very high syngas-based energy cost and low energy efficiency. It should however be mentioned that they focused on the production of liquid by-products, rather than on obtaining a high syngas ratio.

Finally, Xia et al.[103] described BRM in a GA reactor, with a similar SEI and input mixture as in our work. Their CO_2 conversion was similar as ours, yet their CH_4 conversion was more than 20 % lower, and also the syngas yield was a factor 2–3 lower, with the lowest syngas production rate in Table 6. They reported a higher C_2H_2 than CO selectivity, obviously different from our work. However, exact comparison is difficult, due to the different reactor types. They used a classical GA, and such design suffers from a large fraction of gas not being treated by the plasma.[12] This could perhaps explain the difference with our APGD reactor, where the confinement of the gas prevents this issue.[71]

Overall, our obtained conversions, syngas yield, syngas ratio, energy cost and energy efficiency are among the best values reported in literature thus far for plasma-based BRM. Furthermore, BRM exhibits similar performance in terms of conversion, yield and energy cost as DRM and OCRM (in the same reactor setup), while the syngas ratio is significantly improved up to the desired level of 2, required for further methanol synthesis.

5.4 Conclusion

We demonstrated that BRM in an APGD reactor is beneficial on several fronts. First, compared to DRM, the addition of H_2O seems more successful in counteracting soot formation compared to CO_2, and thus in creating more stable plasma conditions. A mixture of 14–41–45 % (CO_2-CH_4-H_2O) leads to the overall best results in terms of stable plasma and performance metrics. Specifically, at a SEI of 210 kJ/mol, we obtained a CO_2 and CH_4 conversion of 49 % and 74 %, respectively, at an energy cost of 390 kJ/mol converted reactants, or 4.0 eV/molecule, which is below the target defined for plasma-based syngas production to be competitive with other technologies. Moreover, we reached CO and H_2 yields of 59 % and 49 %, and a syngas ratio of 2, which is ideal for further methanol synthesis.

Our results for BRM in an APGD, in terms of conversion and syngas yield, are in line with our previous results for DRM and OCRM in an APGD (see Chapter 3 and Chapter 4), while the energy cost is slightly higher than for OCRM, as the latter could benefit from the presence of O_2 as reactant. However, BRM scores substantially better in terms of syngas ratio, because our obtained value of 2 is three times higher than the values obtained for DRM and OCRM. We also compared our results to other works that investigated plasma-based BRM, and we obtain conversions and syngas yields that are among the best reported, at an energy cost that is lower than most of the values reported in literature, while reaching a syngas ratio ideal for further methanol synthesis.

Based on these results, it would appear that BRM in our cAPGD reactor has the highest potential as CCU technology, combining environmental and economic benefits. However, in order to objectively determine which of the three processes investigated in this thesis performs the best as CCU process, an LCA and TEA of each process has to be carried out and compared with one another, which is discussed next in Chapter 6.

Chapter 6 Techno-economic analysis and life cycle assessment of APGD-based DRM, OCRM and BRM[5]

Abstract

In this chapter, we discuss the environmental performance and economic viability of DRM, OCRM and BRM, based on our data obtained in the cAPGD, presented in Chapter 3, Chapter 4 and Chapter 5, and we compare with current state-of-the-art classical SRM technology. This evaluation was carried out through a TEA and a cradle-to-gate LCA, performed by external collaborators, based on our input data. Among the scenarios analyzed, OCRM demonstrates the most favorable economic performance, leading to an unitary cost of production (UCOP) of 529 $/ton syngas, followed by DRM and BRM. The same order of preferences is achieved when assessing environmental performance based on LCA metrics. Key impact categories identified include freshwater eutrophication (EPw) potential and energy consumption, which are significant contributors to environmental impacts. A study on the transition of energy sources indicates a substantial decrease in global environmental impact in the range of 50 % when shifting from current electricity generation methods to wind energy sources. Circularity indicators lead to a material circularity indicator (MCI) around 0.7 in all scenarios with slight differences, reflecting a medium-high level of circularity. Comparative benchmarking reveals that the technologies evaluated in all three plasma scenarios perform better in environmental metrics across 7 over 9 categories assessed, when compared with current state-of-the-art classical SRM technologies.

---

[5] This chapter is based on:
Techno-Economic and Life Cycle Assessment for Syngas Production Using Sustainable Plasma-Assisted Methane Reforming Technology
M. Escribà-Gelonch*, J. Osorio-Tejada*, L. Yu, B. Wanten, A. Bogaerts, V. Hessel
Energy & Environmental Science, under review (2024)
*Shared first author

6.1 Introduction

To summarize the overall performance in terms of conversion and energy cost for DRM, OCRM and BRM carried out with the cAPGD reactor, we add the best datapoint obtained for each of these reactions to the literature overview figure from section 3.3.3, as presented in Figure 38. Specifically, we obtained a total conversion of 74 % for DRM, 67 % for OCRM and 54 % for BRM. Simultaneously, the energy cost, expressed in eV per converted molecule, was equal to 3.9, 2.0 and 4.0 eV/molecule, respectively. All of these values reach the efficiency target stated by Snoeckx and Bogaerts[12], and thus, one would conclude that all three processes are competitive compared to existing or emerging technologies used for syngas production.

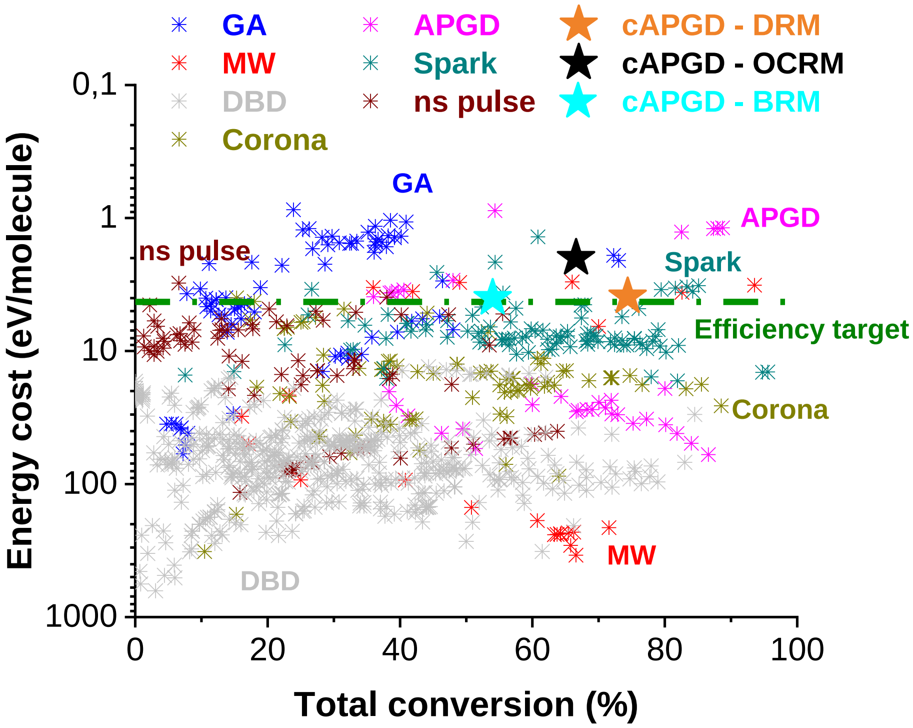

Figure 38: Literature overview figure presented as Figure 14 in section 3.3.3, now updated with our best data point for DRM, OCRM and BRM (represented by the large orange, black and cyan asterisk, respectively).

The literature overview figure from Snoeckx and Bogaerts[12] is indeed an excellent first indication towards the performance of any technology used for DRM (or similar processes like OCRM or BRM that produce syngas) and to compare the performance of different plasma reactor types. However, Snoeckx and Bogaerts[12] correctly stated that for the references included, the efficiency target can drastically change depending on whether syngas or valuable liquid chemicals are the main product. This is equally true for the syngas ratio that is obtained, which is not the same for all data points included in this figure. Furthermore, it remains difficult to assess which of the three processes investigated in this study is performing the best overall. Indeed, the DRM datapoint shows the highest total conversion and just reaches the efficiency target, but the value of the product output is limited due to the low syngas ratio (ca. 0.6). The best OCRM datapoint corresponds to a similar product output and a slightly lower total conversion, but the energy cost is drastically reduced. Finally, the best BRM datapoint has the lowest total conversion and a similar energy cost compared to DRM, but it provides the ideal syngas ratio (ca. 2) for methanol production. Hence, the consequences of all these different aspects towards the environmental impact and competitiveness compared to the state-of-the-art, cannot be fully derived from Figure 38.

Additionally, as there is no 100 % conversion and 100 % selectivity towards syngas reached, any form of these processes on a larger scale will involve product separation and reactant recycling to some extent, leading to an additional amount of energy input required. Simultaneously, the overall power consumed by the entire process is what counts, indicating that also the efficiency of the power delivery system, and not only the plasma-deposited power, needs to be considered. Whether or not 100 % of the energy is coming from renewable electricity or not, will also influence the environmental impact. In order to assess all these aspects, an LCA and TEA is required.

Other examples on recent LCA studies have focused on evaluating the carbon footprint of novel technologies compared to traditional methods for syngas production.[156,157] As an example, Choe et al.[158] examined the potential of emerging solid oxide electrolysis to generate syngas using various renewable energy sources, including hydropower, onshore and offshore wind, solar photovoltaic (PV), bioenergy, and geothermal energy. They concluded that syngas production from onshore wind, offshore wind, solar PV, and geothermal energy effectively offers environmental benefits over syngas produced from fossil fuels. Likewise, Sternberg et al.[159] conducted a comparative study of syngas production methods, comparing DRM and rWGS with conventional SRM, concluding that rWGS (5.8 kg CO_2 eq./kg syngas, 1.9 kg oil eq./kg syngas) and DRM (4.2 kg CO_2 eq./kg syngas, 1.5 kg oil eq./kg syngas) have higher global warming and fossil resource scarcity impacts than conventional SRM (2.5 kg CO_2 eq./kg syngas, 1.2 kg oil eq./kg syngas), primarily due to the high electricity consumption of the proton exchange membrane (PEM) electrolysis unit. In other cases, biochemical approaches have been considered, such as comparing biogas with natural gas reforming[160], assessing the water footprint of biomass chemical looping gasification[161], and comparing thermo- and bio-chemical routes for biowaste gasification.[162]

In contrast, only a few studies have addressed the environmental impact and carbon emission of plasma-assisted SRM via LCA, and almost no studies have been reported on plasma-assisted DRM.[163] In order to address this gap in existing research, we collaborated with external researchers and experts in the field (Marc Escribà-Gelonch and Jose Osorio-Tejada). Specifically, based on our own best lab-scale data combined with simulation data, and after various discussions and a collaborative literature search, they carried out calculations for a TEA and cradle-to-gate LCA. We present the most important results obtained through this TEA and LCA in this Chapter, to conclude our evaluation in this thesis of DRM, OCRM and BRM carried out with the cAPGD.

6.2 Methods

6.2.1 Process description

The process design for DRM (scenario 1) and OCRM (scenario 2) was composed of the APGD plasma-based reaction described in Chapter 3 and Chapter 4, followed by the WGS reaction, gas cleanup and a dual PSA system. The WGS reaction was applied to improve the syngas ratio to a useful ratio of 1, at a temperature of 400 °C and a reaction efficiency of 90 %. After the reaction, the gas mixture was subject to cooling treatment (25 °C) to remove H_2O traces. To achieve high purity of the gas product, dual PSA, as a promising membrane purification method, was used to separate O_2 and recover H_2. In case of BRM (scenario 3), the same process design was used, but without WGS system and the syngas ratio obtained at the end was equal to 2. Figure 39 illustrates the system boundaries and process flow for the three scenarios considered. More details related to the process design conditions are provided as supporting information (see section 8.4.1).

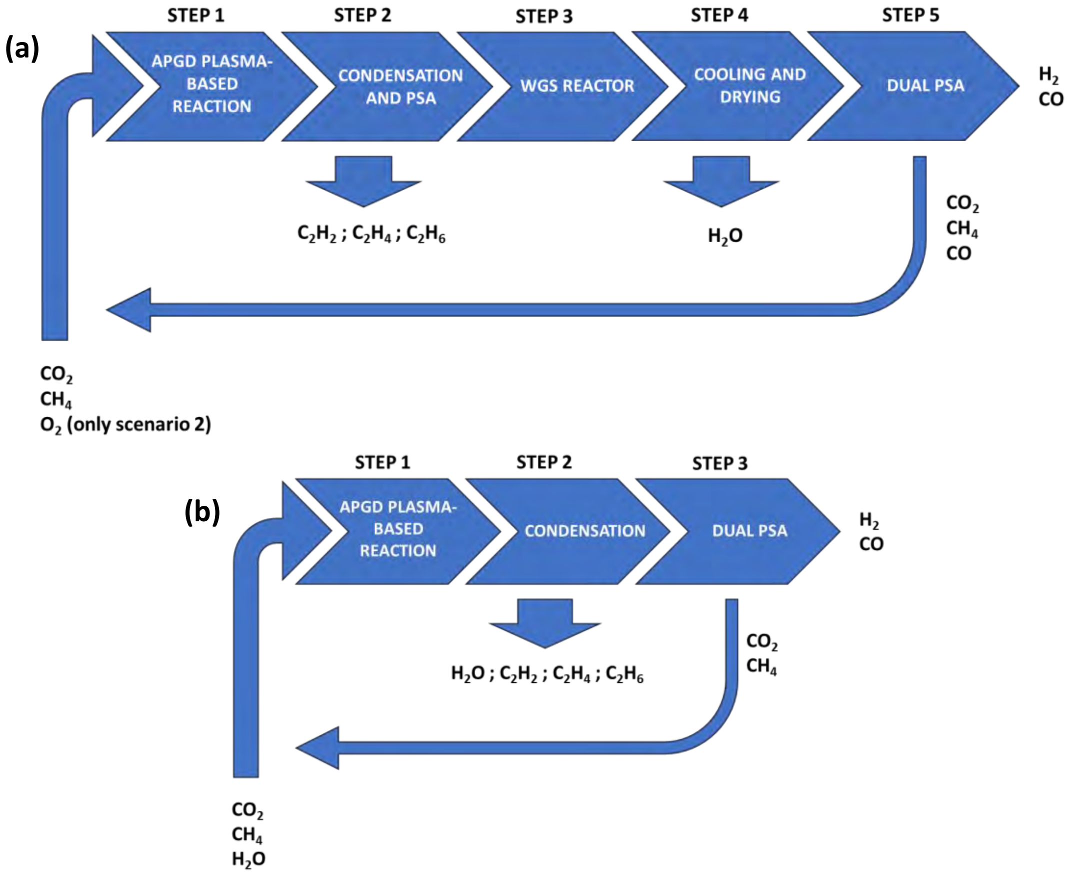

Figure 39: Process scheme for (a) scenarios 1 and 2 and (b) scenario 3.

6.2.2 Life cycle assessment (LCA)

Since a LCA is a thorough and quantitative approach used to evaluate the environmental impacts associated with a process, product, or service[164], conducted in accordance with ISO 14040-44 standards, it involves four essential steps:[165,166] (a) defining the goal, scope and process boundaries, (b) conducting an inventory analysis, (c) performing an impact assessment, and (d) interpreting the results.

6.2.2.1 Goal and scope definition

The goal of this study is to investigate the environmental impact of plasma-based DRM, OCRM and BRM, compared to conventional SRM. This analysis was considered as a cradle-to-gate LCA study, using the data presented in Chapter 3, Chapter 4 and Chapter 5. Its system boundary included the feed input, energy flows into and out of the plasma reactor without transportation and plant construction, and the downstream processes, including gas cleanup, WGS system, cooling and drying, and dual PSA system. Considering the low TRL of the APGD plasma process (laboratory stage, TRL of 3), the energy efficiency and the gas conversion rate (i.e., conversion per unit of time) of the three processes on a larger scale were adapted from estimated data from literature *in lieu* of the actual assessment.[28,72,167] The obtained results of the above-mentioned processes were then benchmarked with the current SRM technology. The process information of SRM technology was obtained from the electrification of the endothermal reactor process described by Cao et al.[168], involving all material input and energy consumption through the process for syngas production.

The functional unit is defined as 1 kg syngas production, and the energy required for the entire process is supplied via electricity from the European mixture standards: renewable energy (43 %), nuclear energy (28 %), solid fuels (19 %), natural gas (6 %) and crude oil (3 %).[169] The key environmental category of interest for this study is global warming potential (GWP) with the unit of kg CO_2-eq. per kg syngas produced.

The assessment within the cradle-to-gate boundary is carried out using the allocation at the point of substitution (APOS) system model. This method aims to evaluate the life cycle impacts from the extraction of raw materials up to the processing of desired products, such as syngas, while also accounting for the generation of unwanted waste pollutants within the industrial gate. The analysis does not include potential aspects of the product distribution, consumption, or disposal.[170] By focusing on the cradle-to-gate boundary, a thorough evaluation and comparison of both current and emerging syngas production systems is addressed.

6.2.2.2 Life cycle inventory

The feed input, product composition, energy consumption and inventory data for DRM, OCRM and BRM, are listed in Table 7 and Table 8.

Table 7: Feed input, product composition and energy consumption of the various steps for the three plasma-based CH_4 reforming processes. Values are rounded to two significant digits.

Information		DRM	OCRM	BRM
Feed input (weight %)	CH_4	28	35	44
	CO_2	72	49	27
	O_2	-	16	-
	H_2O	-	-	29
	CO_2/CH_4 molar ratio	1.8	1.0	0.3
Syngas output (g)	CO	0.6	0.5	1.1
	H_2	0.1	0.1	0.2
	H_2/CO molar ratio	1.0	1.0	1.9
Energy consumption (kWh)	Plasma reaction	3.9×10^{-3}	3.9×10^{-3}	1.1×10^{-2}
	Gas cleanup	9.7×10^{-4}	10.4×10^{-4}	2.6×10^{-3}
	WGS reaction	1.9×10^{-4}	1.8×10^{-4}	-
	Cooling and drying	5.4×10^{-5}	4.6×10^{-5}	-
	Dual PSA system	1.1×10^{-3}	9.9×10^{-4}	2.5×10^{-3}
	Total energy	6.2×10^{-3}	4.6×10^{-3}	16.1×10^{-3}

Table 8: Inventory data of the three plasma-based CH_4 reforming processes compared to classical SRM[159].

Information	DRM	OCRM	BRM	SRM
H_2 production (g)	0.1	0.1	0.2	0.2
Total energy consumption (kWh)	6.2×10^{-3}	4.6×10^{-3}	16.1×10^{-3}	15×10^{-3}
Total energy (kWh/kg H_2)	62	46	81	75

6.2.2.3 Impact assessment

The detailed information of the inventory analysis is discussed in section 6.3. We selected ten impact categories for the LCA analysis, including acidification potential (AP), climate change (GWP), freshwater ecotoxicity (FET), EPw, human toxicity (HT) including carcinogenic (HTc) and non-carcinogenic (HTnc), terrestrial eutrophication (EPt), non-renewable energy resources (cumulative energy demand – fossils; CEDf), material resources (metals/minerals) (cumulative energy demand – materials; CEDm) and photochemical ozone formation (Ph). The projected ecological impact of this research is afforded using EF3.1 environmental impact quantification, which refers to the standardized method developed under the European Commission's Environmental Footprint initiative.[171] Ecoinvent 3.10 is used for impacts comprehensive categorization.

6.2.2.4 Interpretation of the results

During the LCA analysis, data obtained from literature was used with no further accuracy evaluation. All the raw data, such as feed and product gases, were obtained from the experiments described in Chapter 3, Chapter 4 and Chapter 5. However, to investigate the reliability of the LCA results, the uncertainty of analysis-related input flows was evaluated for all three plasma-assisted approaches. This analysis will be discussed and explained in section 6.3. Importantly to note, our LCA studies show that OCRM is the most promising approach for syngas production, compared to DRM, although the environmental impact assessment may not be fully comprehensive. Downstream processes were necessary, including WGS and dual PSA system, that are simultaneously performed after the DRM and OCRM. The reaction efficiencies of all processes were adapted from the literature based on the reaction conditions. The BRM process was designed without WGS system. Although it produced slightly higher climate impact compared to the other two processes, the syngas ratio equal to 2 still offers a way to synthesize major gas-based chemicals, such as methanol.

To guarantee the reliability of the outcomes of this assessment, it is crucial to acknowledge the intrinsic limitations and uncertainties relevant to the available literature sources. In particular, in terms of OCRM and BRM, further research and improvement for the processing data collection based on feed and energy flows can potentially contribute to enhanced accuracy and robustness of the comparison between SRM and plasma-assisted CH_4 reforming technologies.

6.2.3 Circularity of mass flow metrics

A circularity assessment utilizing circular economy metrics is designed to quantify the performance of products by assessing the extent of material and resource usage and reuse until they are fully exhausted. This process also evaluates the reduction of waste generation, aiming to promote a sustainable and regenerative economic system. By measuring aspects such as material efficiency, product lifespan extension and waste minimization, these metrics support innovation by design, identifying opportunities for resource optimization and waste reduction throughout the product life cycle. Integrating these metrics aids in the development of circular economy strategies focused on closed-loop systems, which reduce environmental impacts related to resource extraction and consumption, aligning with global sustainability objectives like the United Nations Sustainable Development Goals. The methodology proposed by the Ellen MacArthur Foundation (EMAF) is widely recognized for this purpose.[172] The calculation procedure includes several indices, converging on the MCI, which quantifies the restorative and regenerative nature of material flows on a scale from 0 (fully linear) to 1 (fully circular). This assessment approach has been applied in previous studies[164,173].

6.2.4 Techno-economic analysis (TEA)

This analysis was performed to estimate the UCOP per ton of syngas in each of the three scenarios. The UCOP was estimated as the sum of the annual operating expenditure (OPEX) and the annualized capital cost (ACC) divided by the annual syngas production.[174] The ACC was calculated based on the total fixed capital expenditure (CAPEX), considering a 20-year lifespan (n) and 10 % interest rate (i), as presented in equations (20) and (21).

$$UCOP = \frac{OPEX + ACC}{annual\ plant\ capacity} \tag{20}$$

$$ACC = \frac{[i(1+i)^n]}{[(1+i)^n - 1]} \cdot CAPEX \tag{21}$$

CAPEX was calculated based on the uninstalled cost (i.e., excl. costs associated to shipment, installation, etc.) of the different equipment from literature specifying a reference capacity and year. Subsequently, the reference costs were scaled up/down to the required size and updated to US$2020 prices based on the chemical engineering plant cost indices (CEPCI), as presented in equation (22). A currency exchange of 1.142 US dollar per euro was used when required.

$$C_B = C_A \left(\frac{S_B}{S_A}\right)^N \cdot \frac{CEPCI_{2020}}{CEPCI_{year}} \tag{22}$$

Here, C_B represents the updated cost of the uninstalled equipment to the required capacity, S_B is the required capacity of the equipment, C_A is the reference cost of the equipment with specific capacity S_A, and N is the scaling exponent indicated for each equipment. For our plants, these scaling exponents mostly were between 0.6 and 0.9. This equipment cost estimation is based on 'the Rule of Six-tenths' approach.[175] The reference capacities, uninstalled costs, year, and scaling exponents are summarized in Table 9.

Table 9: Capacities, installation costs and scaling exponents of the process components.

Equipment	Unit	Reference capacity	Reference uninstalled cost ($)	Year	Scaling exponent	Reference
cAPGD setup	kW	5.6	7 691	2020	0.9	[28] and own data
Fired heater	kW	24 580	8 540 000	2018	0.7	[167,176]
Heat exchanger	kW	59 540	3 000 000	2018	0.62	[167,177]
Cooler	kW	5 720	320 000	2018	0.62	[167,177]
Low temp cooler	kW	5 720	320 000	2018	0.62	[167,177]
Compressor	kW	12 490	5 460 000	2018	0.67	[167,177]
Knockout drum	kg/h	99 795	157 277	2002	0.6	[178]
Cyclone	m^3/s	34.2	3 000 000	2016	0.7	[179]
VPSA O_2 separation	m^3/h	11 900	4 430 000	2020	0.67	[180]
WGS reactor	(H_2+CO) kmol/h	8 819	12 200 000	2002	0.65	[176,179]
PSA syngas separation	m^3/h	1 000	1 998 500	2015	0.67	[181]

Since there are no actual cost estimates for commercial-scale plants using the APGD plasma setup, the reference cost for this plasma section was based on a recent experience, where the start-up company D-CRBN scaled up a GA plasma prototype.[28] This prototype costs around € 2 400 per kW with a capacity of 5.6 kW of plasma power, capable of processing

6.7 ton of CO_2 per year, with future installation plans expected to process 30 000 ton of CO_2 per year.[28,182,183] The lower cost for the APGD plasma was estimated based on our current lab-scale setup, which had a cost of € 17 900 for a theoretical maximum plasma power of 1.5 kW, compared to the lab-scale GA setup, which had a cost of € 24 800 for a maximum plasma power of 1 kW. It is also important to note that about 70 % of the total cost is due to the PSU. Therefore, the setup cost is primarily dictated by the required electric power, rather than the gas flow rate, as is typical for conventional reactors. This also explains the scaling exponent of 0.9 suggested by the manufacturer, which is appropriate for electronic devices, as opposed to the usual 0.6 exponent for reactors scaled up via volume expansion.

In this context, aside from using a different scaling exponent, the upscaling design of the plasma setup is also distinct, consisting of several reactor nodes in parallel instead of a single, large reactor scaled up using traditional methods. The most appropriate method in our case would be internal numbering up.[182,184] This method involves grouping several reactor nodes into a unified reactor body, powered by a single PSU, instead of using one PSU per reactor node (referred to as external numbering up). This method has already been tested by unifying five 1.1 kW reactor nodes in parallel, maintaining similar energy performance as the lab-scale setup.[28]

Regarding the direct and indirect costs of installation of the whole plants, they were calculated through a factorial approach based on the uninstalled cost of equipment and utilizing similar ratio factors to those obtained via modelling in Aspen Plus for a plasma-based plant for nitrogen fixation.[185] Working capital was excluded from the total CAPEX estimation as it is expected to be recouped upon project completion.[186]

For the three analyzed plants, the production capacity of 4 084 kmol/h was defined based on the alternative syngas production plants through rWGS reactors, evaluated by Rezaei and Dzuryk[167], who estimated approximate costs of \$ 460 and \$ 620 per ton of syngas with syngas ratios of 1 and 2, respectively. For syngas with a ratio of 2, the authors used a larger capacity of 22 500 kmol/h to compare the cost with conventional SRM-DRM plants producing syngas at this ratio. Therefore, in case of scenario 3, we also analyzed the syngas production cost considering this larger capacity as a sensitivity analysis.

With a capacity of 4 084 kmol/h and assuming an average of 8 160 productive hours per year, our plants would produce 499 755 ton, 499 562 ton, and 362 622 ton of syngas in scenarios 1, 2, and 3, respectively. The lower production capacity in scenario 3 compared to the other scenarios is due to the higher syngas ratio and the significantly lower molar mass of H_2 compared to CO.

OPEX consists of variable and fixed OPEX. For variable OPEX, we assumed an average electricity cost of \$ 30 per MWh for onsite generation, based on projections for onshore wind energy plants in Northern Europe in 2030.[187] The cost of CO_2 feedstock was set at \$ 40 per ton, reflecting the average cost used in various TEA studies for CO_2 conversion.[182,188–197] The CH_4 feedstock cost was defined at \$ 274 per ton, based on a price of \$ 5.25 per GJ.[167] The costs for high-purity deionized water and oxygen were set at \$ 14 and \$ 120 per ton, respectively.[182,198,199] Cooling water costs were estimated at \$ 0.066 per m³, based on the method by Ulrich and Vasudevan[200], adapted to use electricity instead of natural gas (used to produce electricity onsite) to power the cooling system.

Concerning fixed OPEX, since the different plants with the same capacity have varying levels of complexity, we have set the labor cost as 5 % of the total capital investment[158,201], rather than estimating the number of operators per production capacity. The catalysts used in the WGS reactor are categorized as fixed OPEX because they are replaced every four years.[179,202,203] In this regard, Chiuta et al.[179] estimated that annual maintenance of these low-temperature WGS reactors can be fixed at 10 % of the total capital cost of the reactor, while the annual maintenance for the rest of the plant was fixed at 3 % of the remaining total capital cost. Insurance, taxes, and licensing and permits were set at 1 %, 1 %, and 0.1 % of the total capital investment, respectively.[201]

6.3 Results and discussion

6.3.1 Cost of production

The UCOP of syngas for the plants with a capacity of 4 084 kmol/h in the three scenarios are presented in Figure 40, and are \$ 569, \$ 529 and \$ 644 per tonne syngas in scenario 1, 2, and 3, respectively. The total annual syngas production costs per specific item are provided as supporting information (see section 8.4.2).

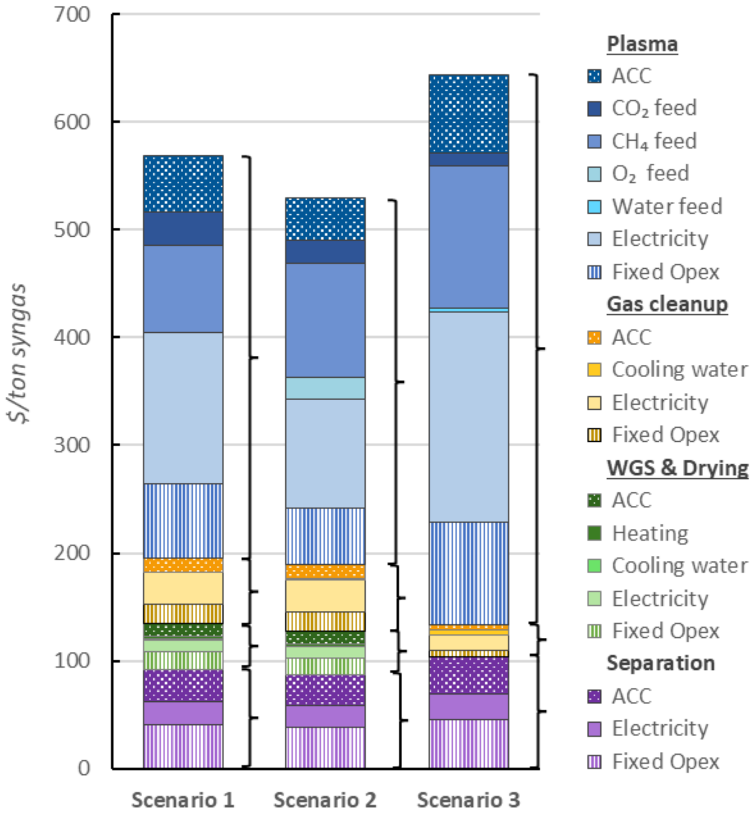

Figure 40: Production costs of syngas with H_2/CO ratios of 1 (Scenarios 1 and 2) and 2 (Scenario 3) in the base cases (4 084 kmol/h). The production costs are presented by section of the plants and their respective CAPEX and OPEX. The ACC are represented by columns with dotted patterns, fixed OPEX by columns with vertical line patterns, and variable OPEX by columns with solid color patterns.

These results show that despite the complexity of the plants in scenarios 1 and 2, the plasma setups contribute the most to both total CAPEX and OPEX. For syngas with a ratio of 1, the plasma-based conversion sections account for over 64 % of the total production cost. For syngas with a ratio of 2, this section's contribution increases to almost 80 % of the total cost. Moreover, despite the utilization of low-cost onsite-generated electricity, the main cost driver in these plasma sections is power consumption, except in scenario 2, where the cost of electricity is similar to the cost of the CH_4 feedstock. Plasma power consumption contributes 30.3 %, 19.1 %, and 24.5 % to the total UCOP of syngas in scenario 1, 2, and 3, respectively.

The high share of plasma electricity costs indicates that the most important strategy to further increase the cost-effectiveness of these alternative plasma-based syngas plants is to improve the energy efficiency of the plasma-based conversion. This is also consistent with the significant share of the plasma sections in the total CAPEX of the plants, as shown in Figure 41. Analyzing the CAPEX shares individually suggests that investing in reactor engineering development to reduce the equipment cost of the plasma setup would be a relevant strategy. However, given the significant share of electricity consumption and the fact that the PSU constitutes most of the CAPEX for the plasma setup, any increase in the reactor's energy efficiency would automatically decrease the power required for the PSU, thereby reducing both the total CAPEX and fixed OPEX, as well as a large part of the variable OPEX.

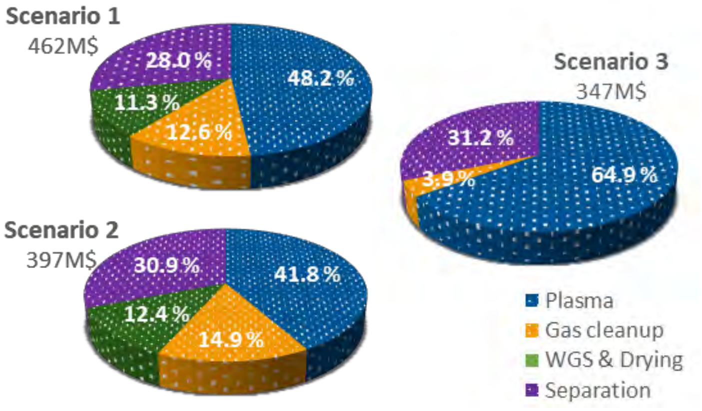

Figure 41: Contribution of the different sections to the capital investment of the plants in the base cases. The values under each scenario represent the total CAPEX (uninstalled equipment cost plus direct and indirect installation costs) in millions of dollars (M$).

The greater relevance of the plasma reactor's energy efficiency compared to electricity, equipment, and main feedstock prices is illustrated in the tornado charts in Figure 42. In this sensitivity analysis, the variation of the UCOP of syngas is evaluated after varying by ± 50 % the values of the plasma power consumption and the items with the highest contributions to the UCOP of syngas in Figure 40. Note that this 50 % variation for a specific parameter is not by definition realistic; it is simply a method to obtain a clear view on the sensitivity of all parameters compared to one another.

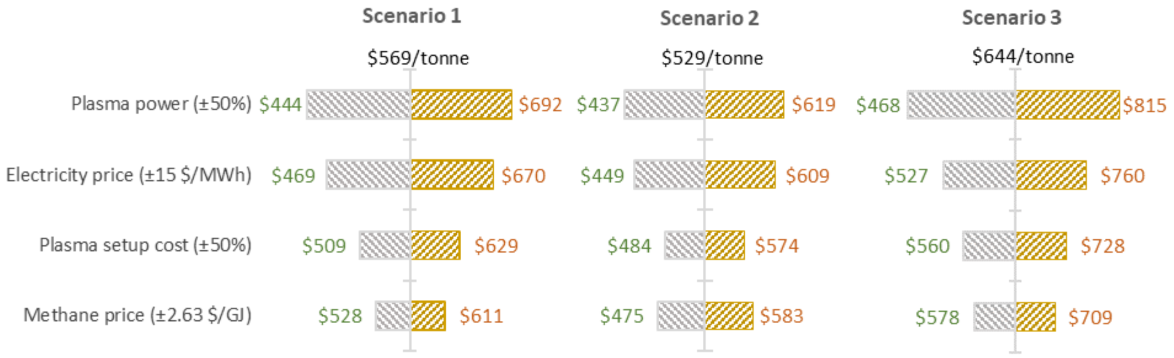

Figure 42: Sensitivity analysis for the UCOP of syngas for each scenario in the base case.

A 50 % variation in plasma power results in a UCOP variation of 22 %, 17 %, and 27 % in scenario 1, 2, and 3, respectively, demonstrating the highest sensitivity in syngas costs to this parameter. Similarly, the impact of other parameters related to plasma power, such as the plasma setup cost and electricity price, is also significant, except in scenario 2, where the CH_4 price contributes notably to the operating expenses. Due to the more balanced cost distribution in this OCRM method, the UCOP of syngas in scenario 2 is less sensitive to variations in the cost of individual parameters compared to the other scenarios.

Nevertheless, despite the demonstrated sensitivity of these syngas plants to variations in energy efficiency (plasma power) and equipment costs for the plasma setup, variations in electricity prices are more likely. Even with on-site renewable energy generation, which is less affected by market dynamics, factors like the intermittency of renewable sources and weather events could necessitate purchasing more expensive electricity from third-party suppliers to maintain assumed yearly productivity.

Additionally, to benchmark our results against previous and future TEA of alternative syngas production plants, it is necessary to present the obtained UCOP using different electricity prices. For example, the referenced syngas costs from rWGS-based plants in section 6.2.4 were calculated using a similar CH_4 price of \$ 5.25/GJ, but with a much higher electricity price of \$ 70/MWh.[167] In those rWGS-based plants, electricity represented the main expense in the syngas production cost structure. Furthermore, in the referenced study, neither installation costs nor fixed OPEX were included in the total annual costs. Therefore, to provide a more transparent benchmark, we have updated the syngas costs reported by Rezaei and Dzuryk[167] by estimating the installation costs and fixed OPEX based on the reported total cost of bare modules and applying the ratio factors used in our study. This results in a UCOP of syngas from rWGS-based plants of \$ 490 and \$ 643 per ton for syngas ratios of 1 and 2, respectively. Therefore, parameter-specific sensitivity analyses for electricity prices for our syngas plants and the reference benchmark for each syngas ratio are presented in Figure 43. For each scenario, a new analysis assuming a 50 % reduction in the required plasma power was included.

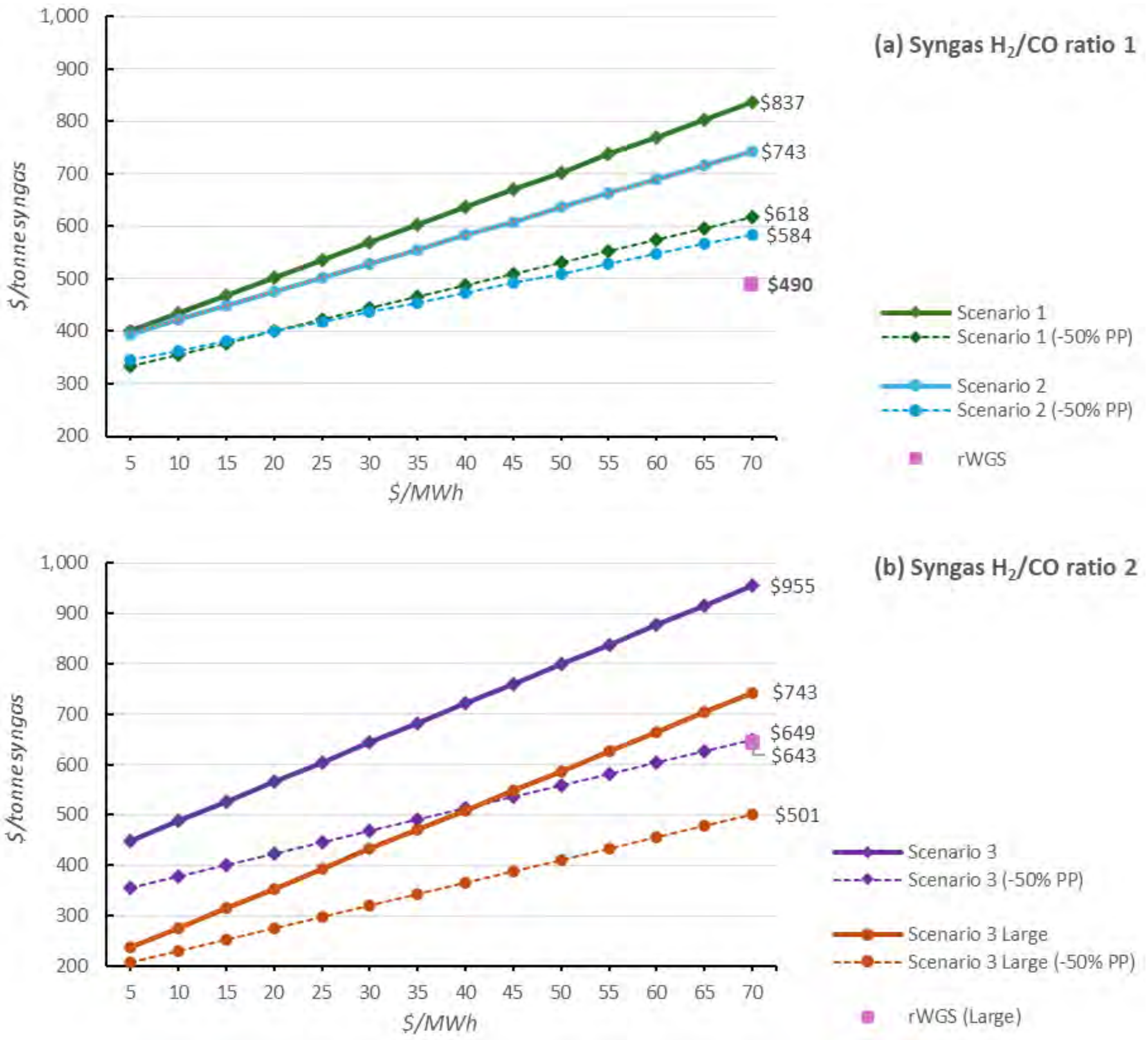

Figure 43: Sensitivity analysis for electricity prices. Chart (a) presents scenarios 1 and 2, along with the benchmark using a rWGS-based plant to produce syngas with a ratio of 1. Chart (b) presents scenario 3 at base scale (4 084 kmol/h), scenario 3 at large scale (22 500 kmol/h), and the benchmark using a rWGS-based plant to produce syngas with a ratio of 2. In both charts, new scenarios assuming a 50 % reduction in plasma power (PP) are shown with dashed lines.

For the production of syngas with a ratio of 1 (Figure 43(a)), the plasma-based plant would have a much higher UCOP than the benchmark when electricity costs $ 70/MWh, even when considering scenarios with a 50 % reduction in plasma power (dashed lines in Figure 43(a)). If plasma power was the only variable parameter, only the plasma-based plant in scenario 2 would match the benchmark, but this would require the reactor to consume less than 19 W, which is one-fifth of the base case plasma power. In contrast, producing syngas with a ratio of 2 in scenario 3 would be more competitive. Specifically, scenario 3 large (using the benchmark scale of 22 500 kmol/h, equivalent to producing 2 million ton of syngas per year), would have a UCOP of $ 432 per tonne of syngas when electricity costs $ 30/MWh. However, when electricity costs $ 70/MWh, scenario 3 large would have a higher UCOP than the benchmark. Nevertheless, in the scenarios assuming half the plasma power consumption (series with dashed lines), both scenarios 3 (base and large) would be competitive. In detail, these reduced power cases for scenario 3 base matched the benchmark with a UCOP of $ 649 per ton, while scenario 3 large had a much lower UCOP of $ 501 per ton. For scenario 3 operating at a large scale, the syngas production cost would match the benchmark if only a 20 % reduction in plasma power consumption were achieved, indicating that in the near future, plasma-based BRM could be competitive against other more mature electric-powered technologies such as rWGS-based plants.

Regarding the competitiveness of these electric-based alternative plants for syngas production compared to conventional fossil-based methods, such as SRM-DRM plants, the plant in scenario 3 would also be attractive. The UCOP of syngas from large SRM-DRM plants is approximately $ 225 per ton, estimated using CH_4 and electricity prices of $ 5.25/GJ and $ 70/MWh, respectively.[167] Since the electricity price is not a major cost component for these plants, their UCOP can be compared with the UCOP obtained in our scenario 3 at the same large scale, using the assumed electricity price of $ 30/MWh, which was estimated at $ 432 and $ 320 per ton of syngas in the base and reduced plasma power cases, respectively, as seen in Figure 43(b) (orange solid and dashed lines). In the reduced plasma power case, the plant would match this UCOP when the electricity price drops to $ 10/MWh. Therefore, given the difficulty of achieving such low electricity prices and halving plasma power consumption, improving the cost-effectiveness of these plants could also be plausible by using a less expensive CH_4 source or optimizing the syngas separation system, which also significantly impacts the plant's cost structure as observed in Figure 41.

6.3.2 Life cycle assessment (LCA)

Table 10 presents the environmental impacts of the plasma-based process for syngas production under investigation, categorized by the defined midpoint impact categories, as also depicted in Figure 44. In all three scenarios, the primary environmental impact is predominantly driven by the energy demands (CEDf), accounting for approximately half of the total impacts. FET contributes significantly to the remaining half. The GWP represents about 2.3 % of the impact, while the remaining 0.04 % is distributed among the other seven categories. In Scenario 3, CEDf contributes the most, accounting for 55 %. In contrast, in Scenario 1, CEDf contributes the least, at 47.7 %, with Scenario 2 falling in between. This distribution of contributions is inversely related to FET (50 and 42 % for scenarios 1 and 3, respectively), as the variation in GWP lies within a narrow range of 2.29 % to 2.45 %. These results confirm the high energy dependency of plasma-mediated technology. In this context, the final mixture is intended for commercial storage, rather than emission and consequently not considered as emissions. Whilst at the inlet of the process in scenario 1, 83 % of the consumed gases are CO_2 and 16 % CH_4, at the outlet the composition shifts significantly, with CO and H_2 comprising 49 % and 51 %, respectively, so that the emissions of CH_4 and CO_2 are reduced to less than 0.2 %. Approximately 10 % of the initial mass is converted into secondary gases, including H_2O vapor, C_2H_2, C_2H_4 and C_2H_6. The latter three gases are condensed during the second gas cleanup step using PSA, while H_2O is removed in the fourth step through cryogenic drying. For the purpose of this study, all of these gases have been considered as by-products, together with 1 % production loses considered along the process, and therefore classified as waste, despite their potential suitability as raw materials for secondary processes. In the dual PSA system, a portion of the flow stream is recycled, containing 0.81 g/min of CO_2, 0.0068 g/min of CH_4, and 0.001 g/min of CO. These components are not regarded as waste because they are reintroduced into the process. In scenario 2, the CO_2 concentration in the inlet is reduced to 67 %, while the CH_4 concentration is increased to 24 %. To achieve the same syngas composition as in scenario 1, an additional 9 % O_2 is required, leaving other emissions below 0.2 %. Scenario 3 involves the addition of 40 % H_2O, resulting in a significant difference compared to the other two scenarios. In this case, CO_2 constitutes only 29 % of the inlet composition, while CH_4 accounts for 31 %. This leads to an immediate increase in the recycling flow stream, with 50 % of the unreacted CO_2, 25 % of the initial CH_4, and 62 % of the H_2O being recycled. Additionally, the introduction of H_2O also leads to increased waste generation. The outlet composition in scenario 3 includes 66 % H_2 and 34 % CO, with CH_4 and CO_2 levels reduced to below 0.2 %.

Table 10: Environmental impact values corresponding to the selected ten categories, applied for each of the three plasma-based scenarios.

Impact category	Units	Scenario 1	Scenario 2	Scenario 3
AP	mol H^+-Eq	1.28×10^{-3}	6.88×10^{-4}	1.76×10^{-3}
GWP	kg CO_2-Eq	2.32×10^{-1}	1.24×10^{-1}	3.10×10^{-1}
FET	CTUe	5.04	2.47	5.31
CEDf	MJ	4.81	2.66	7.06
EPw	kg PO_4-Eq	1.66×10^{-4}	8.83×10^{-5}	2.21×10^{-4}
EPt	mol N-Eq	2.22×10^{-3}	1.16×10^{-3}	2.87×10^{-3}
HTc	CTUh	1.83×10^{-10}	8.79×10^{-11}	1.85×10^{-10}
HTnc	CTUh	5.24×10^{-9}	2.50×10^{-9}	4.89×10^{-9}
CEDm	kg Sb-Eq	1.38×10^{-5}	6.02×10^{-6}	1.04×10^{-5}
Ph	kg NMVOC-.	6.36×10^{-4}	3.46×10^{-4}	8.99×10^{-4}

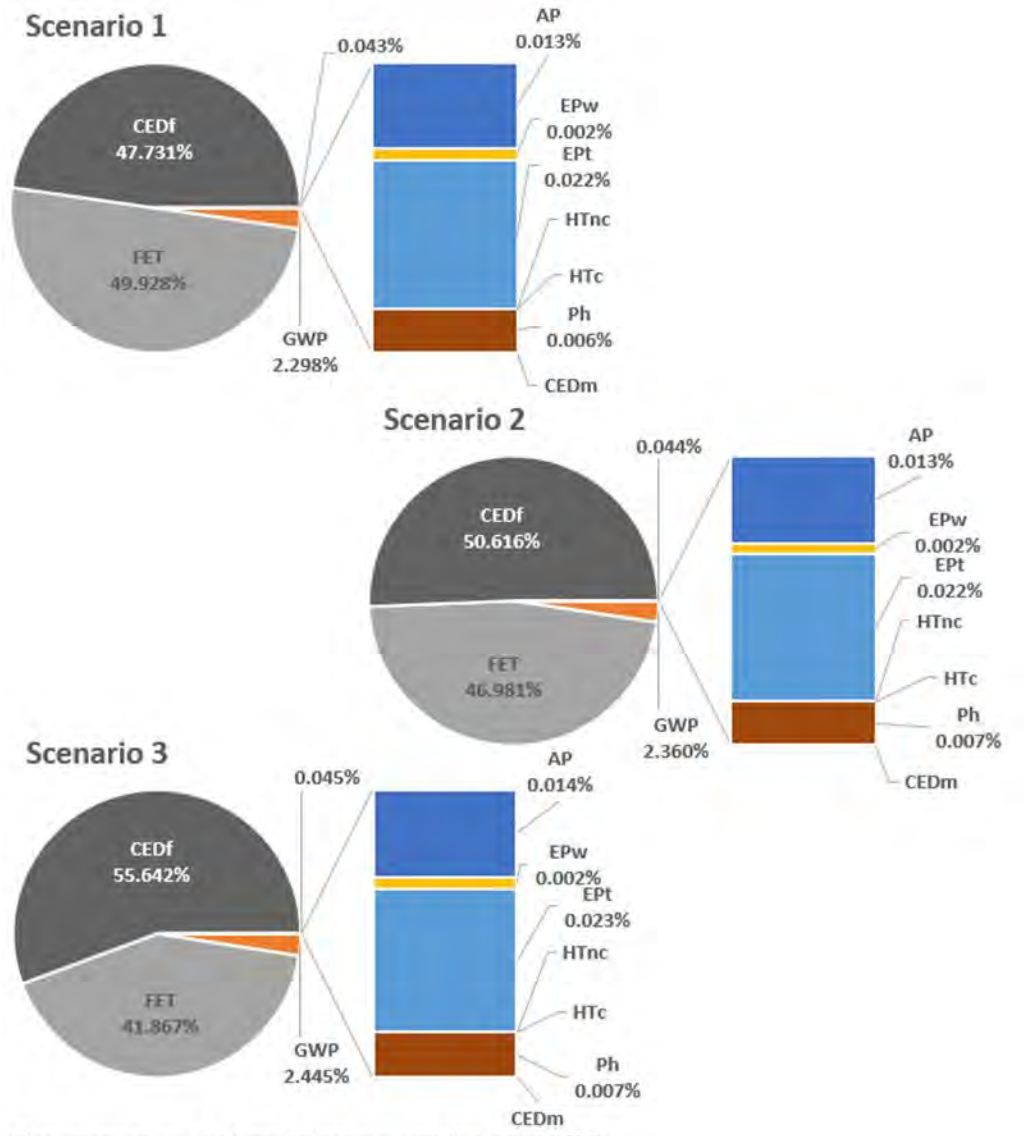

When no percentage is shown it denotes a contribution < 0.001 %

Figure 44: Contribution of the different impact categories to the global impacts according to the defined scenarios.

As denoted in the scenarios assessment, CEDf is the primary impact category in the LCA, and this category is significantly influenced by the source of the energy. For the study presented here, the low-voltage European energy mix was used from the Ecoinvent database to quantify the associated impacts. However, these impacts could be mitigated by adopting an optimal renewable energy mix. In this context, Heide et al.[204] described an optimal mix for a fully renewable energy scenario in Europe, recommending a seasonal mix of 55 % wind and 45 % solar power generation. By considering the ideal scenario of 100 % renewable energy, we can evaluate the decrease on impact categories using data obtained from Ecoinvent, as depicted in Figure 45. Interestingly, the impact categories most significantly affected are those associated with higher environmental impacts for plasma-mediated syngas production. This observation confirms that transitioning from non-renewable to renewable energy sources would substantially reduce environmental impacts of the whole process. Significantly, the categories CEDf and EPw would result in more than an 80 % reduction in impacts, while GWP and EPt would reduce impacts by over 70 % and 65 %, respectively. Together, these four categories account for more than 99 % of the environmental impacts in the global LCA presented in this work. On the other side, the exclusive use of renewable energy sources would result in a modest increase in environmental impacts concerning AP and HTc, although these increases would be less than 1 %.

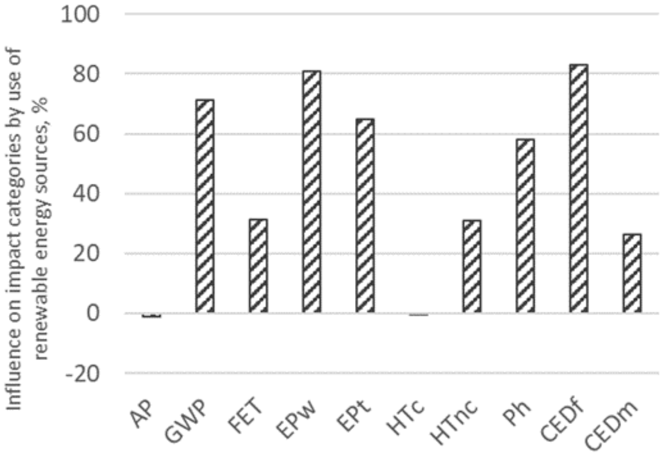

Figure 45: Influence on environmental impact categories in case of the substitution of the current European energy source by a fully optimized renewable energy source.

An internal comparison of the three scenarios evaluated in this study was conducted to identify the most advantageous scenario in terms of environmental impact. Figure 46 and Figure 47 illustrate the comparison between scenarios 2 and 3 relative to scenario 1. The data are normalized to a value of one, where values in the range (0,1) indicate reduced impacts compared to scenario 1, and values greater than one indicate increased impacts. The figures clearly show opposing trends: scenario 2 demonstrates improvements over scenario 1 across all impact categories by approximately 50 %, while scenario 3 exhibits increased environmental impacts in 8 out of 10 categories, with the exceptions being HTnc and CEDm. Key environmental impact categories, such as EPw and GWP, which contribute significantly to the overall environmental footprint of the process, have shown an increase in impacts by approximately 30 %. Additionally, CEDf rises by around 45 %.

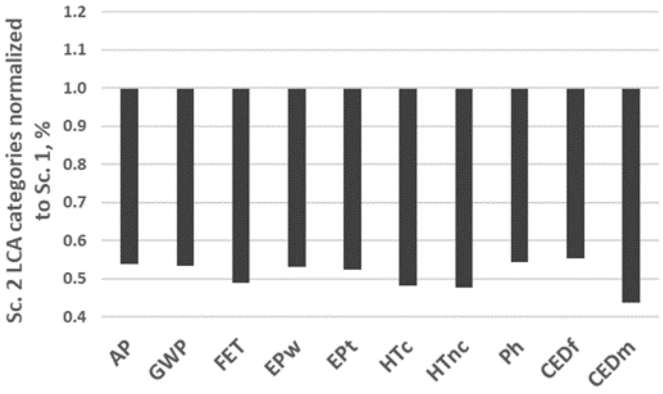

Figure 46: LCA categories for scenario 2 normalized relative to scenario 1.

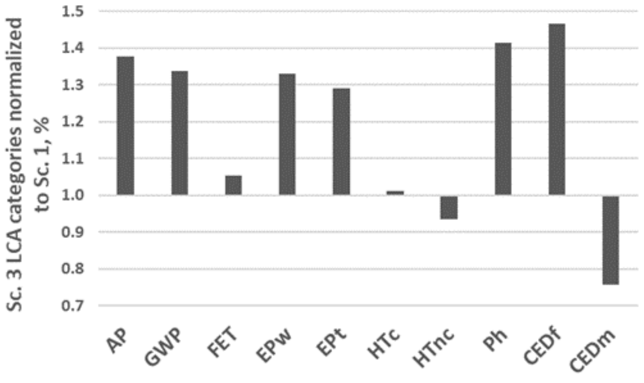

Figure 47: LCA categories for scenario 3 normalized relative to scenario 1.

Based on the environmental impact results, scenario 3 exhibits the highest impacts, whereas scenario 2 has the lowest. This contrast is clearly illustrated in Figure 48, where the environmental impacts of Scenario 3 (the highest) are more than twice in 8 over 10 categories of scenario 2 (the lowest). The significant difference is primarily due to the additional water usage and increased energy requirements associated with scenario 3. Consequently, we conclude that OCRM (scenario 2) is the best choice from an environmental point of view, while BRM (scenario 3) exhibits the highest environmental impacts.

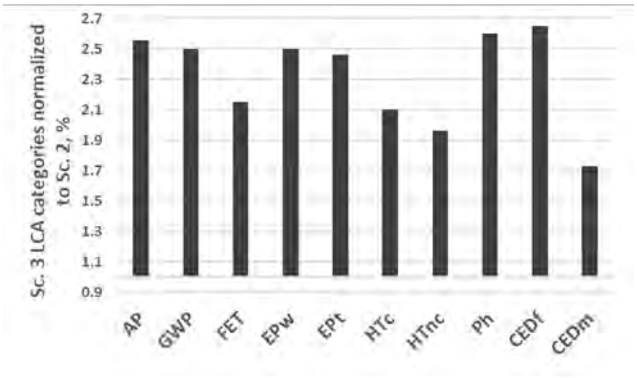

Figure 48: LCA categories for scenario 3 normalized relative to scenario 2.

Following the evaluation of the environmental performance of plasma-based syngas production from CH_4-rich natural gas across three scenarios, i.e., DRM (Scenario 1), OCRM (Scenario 2) and BRM (Scenario 3), we now compare the results with the existing state-of-the-art SRM technology using the cradle-to-gate LCA. For benchmarking our alternatives against the current leading technology, the literature source by Matin et al.[163] was used. In the referenced literature, the authors employed the TRACI methodology to quantify environmental impacts, which offers characterization factors for LCA particularly applicable to processes, products, facilities, companies, and communities. However, this methodology is primarily tailored for use within the United States. In this case, the impact categories are AP (moles H^+-eq), HTc (kg benzene-eq), ecotoxicity (ET– kg 2,4-D-eq), eutrophication (EP – kg N-eq), CEDf (MJ), GWP (kg CO_2-eq), HTnc (kg toluene-eq), ozone depletion potential (OD – kg CFC-11-eq) and respiratory effects (RE – kg PM2.5-eq). Since our initial assessment was conducted using the EF3.1 framework closer and recommended by European institutions, it was necessary to recalculate our data using TRACI to enable meaningful benchmarking. Additionally, the process was scaled to the same functional unit used in this work, and the impact categories of AP, HTc, HTnc, and ET needed to be aligned with the process LCA, so unit conversions were necessary. To this aim we used the factors proposed by Thiel et al.[205], namely: for AP, a characterization factor of 50.79 kg SO_2 equivalent per mole H^+ was applied. The economic input-output LCA (EIO-LCA) method reports HT impacts (both HTc and HTnc) in terms of benzene and toluene equivalent emissions to air. Consequently, TRACI characterization factors of 2.97×10^{-7} CTUh per kg of benzene to air and 5.3×10^{-8} CTUh per kg of toluene to air were utilized, where CTUh represents the cumulative toxicity unit for humans. ET, as reported by EIO-LCA, is expressed as kg 2,4-D (i.e., 2,4-dichlorophenoxyacetic acid) to continental freshwater, and a characterization factor of 8.60×10^{2} CTUe per kg 2,4-D was employed, with CTUe denoting the cumulative toxicity unit for the environment. It is important to note that the EIO-LCA analysis did not account for the fate of chemicals in soil and water concerning HT, nor in air and soil for ET. Matin et al.[163] evaluated the environmental impacts of plasma-based DRM methods (including a DBD, MW and DC-pulsed plasma reactor) relative to traditional thermal SRM by employing eight different allocation scenarios. The corresponding values for these allocations were also included in this study to provide additional comparative sources.

Based on the comparative results of the data gathered from the literature, after scaling and unit homogenization, it is observed that there are substantial differences between the values reported in the literature on one hand, and the results obtained in our study on the other hand. These differences span several orders of magnitude, either in favor or against, as shown in Figure 49. Note that these differences may also stem from variations in allocation methods or differing assumptions made during the process design. The exact values for all impact categories in our study and all literature sources, are provided in section 8.4.3.

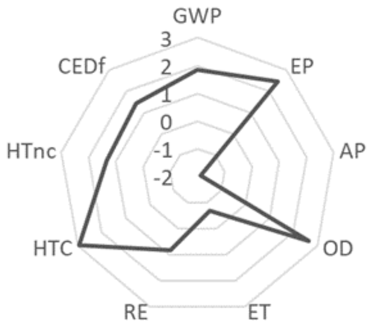

Figure 49: Orders of magnitude differences on environmental impacts between literature references[163] and our work.

Accordingly, values above zero indicate that our process improved the reported outcomes when compared to the literature, whereas values below zero denote our process increased environmental impacts by the same magnitude. As shown, most impact categories benefited from our process, with values exceeding zero in 7 over 9 impact categories assessed. Notably, OD, HTc, and EP demonstrated improvements exceeding 2 orders of magnitude. On the counterpart, AP and ET yielded values below zero, indicating increased environmental impacts from the plasma-based process scenarios presented here. Regarding critical environmental impacts, namely ET and CEDf, the results present opposite conclusions. On one hand, environmental impacts related to energy consumption were reduced by 1.4 orders of magnitude, while on the other hand, our process increased ET by 0.7 orders of magnitude. This increase may be due to secondary compounds generated during the process. Proper capture of these compounds could potentially reduce emissions and thus mitigate ET.

6.3.3 Circularity metrics of the process

This study was performed using the material flow data presented in the process inventories (Table 7 and Table 8), as well as the following assumptions: (i) 1 % losses along the process, (ii) utility factor ($F(X)$) was considered equal to 0.9, as the obtained syngas was considered to have the same purity in all cases and the same lifetime depending on the demand (hence, $L = L_0$ and $U = U_0$), (iii) the recycling efficiency was considered the same in all scenarios and therefore non-significant for benchmarking, and (iv) the unreacted CO_2 and CH_4 are properly separated and recycled to the inlet stream. The calculation of circular indices includes the global mass of inputs (M), including the flow stream coming from the recycling loop (F_R), which at the same time defines the quantity of new raw materials (V). One key circular metric is the waste generations (including unrecoverable mass fraction (W) and waste generated when recycling (W_F)), which are assessed using the EMAF methodology[172], resulting in a linear flow index (LFI). The MCI is directly calculated as a function of LFI, reflecting the process's circularity ranging from 0 (fully linear) to 1 (fully circular), according to equations (23) and (24).

$$MCI_P = 1 - \big(LFI \cdot F(X)\big) \tag{23}$$

$$a) \quad LFI = \frac{V + W}{2M + \frac{W_F}{2}} \quad ; \quad b) \quad F(X) = \frac{0.9}{\left(\frac{L}{L_0}\right) \cdot \left(\frac{U}{U_0}\right)} \tag{24}$$

Table 11: Overall circularity calculations of MCI and other partial indicators according to EMAF methodology, for each scenario.

Symbol	Definition	Scenario 1	Scenario 2	Scenario 3
M	Mass of raw materials	2.51	2.18	2.04
F_R	Fraction of mass from recycled sources	0.53	0.49	0.47
V	Materials not from reuse	1.18	1.11	1.08
W	Mass of unrecoverable waste	0.078	0.076	0.113
W_0	Mass of unrecoverable waste through emissions	0.052	0.050	0.073
W_F	Mass of unrecoverable waste generated when producing recycled feedstock	0.054	0.052	0.079
LFI	Linear Flow Index (material flowing in a linear fashion)	0.250	0.270	0.290
MCI	Material Circularity Indicator	0.775	0.757	0.739

The circularity of the three scenarios is assessed as medium-high, with the first scenario achieving the highest score (0.775) and the third scenario the lowest (0.739). The scenarios exhibit similar circularity in terms of mass flows, as indicated by the narrow range of MCI values, all within 0.036. The comparatively lower circularity of scenario 3 is primarily attributed to a 48 % increase in waste generation and an 11 % reduction in recycling flow streams. Scenario 1, which attains the highest MCI of 0.775, is characterized by a higher recycling rate and moderate waste production relative to the other scenarios.

6.4 Conclusion

This Chapter aims to fill the gap of the lack of information about the environmental impacts associated with the use of the cAPGD for syngas production. Based on our input data (Chapter 3, Chapter 4, Chapter 5), our external collaborators first conducted a comprehensive TEA, encompassing all three scenarios, along with their respective sub-scenarios. This analysis was designed to evaluate varying market price conditions in detail, which were highly influenced by the production scale. Scenario 3, which exhibited the highest UCOP, changed from an initial $ 649, reducing 20 % when operating at large scale, denoting a highly competitive capacity in the near future when compared with electric-powered technologies such as rWGS-based plants. Overall, the production capacity in scenarios 1 and 2 were around 500 kt syngas/year, while scenario 3 exhibited milder productivity 363 kt/year. Nonetheless, under the assumption of production cost in scenario 3, this scenario achieved the highest rank, attaining a score of 644 $/t syngas, which was 13 % and 22 % higher when compared with scenarios 1 and 2, respectively, concluding in a lower productivity at higher costs for scenario 3. Scenario 2 resulted to be the most competitive in terms of high productivity 499.6 kt/year at lower cost, i.e., 529 $/t syngas.

To evaluate the environmental impact of the process, our collaborators performed a prospective cradle-to-gate LCA comparing all three scenarios. The energy expenses (47-55 %) and EP potential (41-49 %) accounted to most of the environmental impacts in all scenarios, with scenario 2 being the most advantageous in an environmental perspective, followed by scenario 1 and scenario 3. Given the energy-intensive nature of plasma-based DRM processes and excluding the use of renewable energy sources, the potential for improving the environmental performance of plasma-based DRM is strongly influenced by the energy consumption per unit mass of syngas produced. In the context of circularity, scenario 1 exhibited the highest MCI value, reaching 0.775. This was followed by scenario 2, which had a slightly lower MCI (0.757), and scenario 3 (0.739), which had the lowest MCI among the three scenarios, due to the lower recycling stream capacity and the higher waste production. Finally, when benchmarking with several other syngas production processes, our process exhibited a better performance in 7 over 9 environmental categories, denoting a significant improvement with respect of the current state-of-the-art classical (non-plasma) SRM technologies and DRM carried out with DBD, MW and pulsed plasma discharges.

Chapter 7 Overall conclusions and outlook

In this thesis, we investigated the performance of a cAPGD reactor towards syngas production by means of experiments, for a variety of conditions. Three processes, i.e., DRM, OCRM and BRM, were tested and evaluated in terms of conversion, energy cost/efficiency, syngas ratio and syngas selectivity/yield, next to overall plasma stability and extent of soot formation. Additionally, the environmental impact and economic potential was investigated.

A general observation is that for every process, the conversion and energy cost in comparison with the state-of-the-art is always among the best values reported. Specifically, for DRM, the highest total conversion obtained was 74 %, at an energy cost of 4.2 eV/molecule. For OCRM, this changed to 67 % at an energy cost of 2.0 eV/molecule. For BRM, the best result obtained was a total conversion of 54 % at an energy cost of 4.0 eV/molecule. The confinement of the plasma partially explains the high conversions compared to other setups, as the fraction of gas that passes the plasma active region is maximized, a high SEI can be applied and the close presence of the ceramic material to the plasma can provide a certain wall stabilization effect, affecting the gas temperature gradient and subsequently the conversion. Moreover, the energy cost values satisfy the target set by Snoeckx and Bogaerts[12], and in addition, at an increased SEI the energy cost does not increase significantly, in contrast to what is observed for many other setups. This indicates that the ceramic tube can hold the majority of the heat, which was a concern previously described by Trenchev et al.[71] regarding CO_2 splitting in a cAPGD.

The limited value of the product output for DRM was the main motivation to investigate the addition of other gases next to CO_2 and CH_4. Indeed, a stable, decent performance was limited due to the negative effect of extensive soot deposition on the reactor's electrodes at increased CH_4 fractions. Therefore, the CH_4 input fraction had to be kept low, resulting in a syngas ratio below 1. Adding O_2 improved this only slightly, with a syngas ratio slightly above 1, while adding H_2O could significantly increase the syngas ratio, eventually leading to a value of 2, ideal for further methanol synthesis. The syngas yield was also similar for the best conditions of all processes, with a CO and H_2 yield close to 60 % and 50 %, respectively.

The solid carbon deposited was analyzed through electron microscopy by a fellow PhD student (Robin De Meyer), and it was found to be turbostratic carbon, based on the observed structure. Impurities, originating from the electrode material, were observed as well, indicating electrode erosion alongside the carbon deposition, and limiting the potential value of this solid material as by-product. For BRM, an increased SEI had a positive effect on the rate of soot formation, which can be attributed to a steeper temperature gradient at higher SEI, limiting the region where species that act as pre-cursor for soot formation (like C_2H_2) are primarily formed. This would be in line with predictions from the multidimensional model developed by my fellow PhD student (Stein Maerivoet; details in Maerivoet et al.[139]) and applied to our OCRM experiments, i.e., that an increasing O_2 fraction leads to a stronger temperature gradient, decreasing the width of the zone where C_XH_Y species are formed and pushing it more towards the sides of the reactor.

Based on a LCA and TEA carried out by our external collaborators (Dr. M. Escribà-Gelonch, Dr. J. Osorio-Tejada, Dr. L. Yu, L. and Prof. Dr. V. Hessel), we could deduce that the OCRM process had the lowest environmental impact and was the most competitive on a small scale. At a large scale, the BRM process has the highest potential to become competitive with other existing technologies leading to syngas with a H_2/CO ratio of 2. However, it also had the highest environmental impact of all three processes. Nevertheless, all processes scored better compared to the current state-of-the-art (non-plasma-based SRM) for the majority of environmental parameters that were evaluated, and have a medium-high circularity.

Further research can be focused on different aspects. For example, testing different ceramic materials to confine the plasma might be a good way to investigate in more detail the effects of the wall on the overall performance. Different thermal properties could influence the heat losses and the overall energy efficiency. In addition, this would also allow to investigate whether or not surface wall reactions take place. For example, MACOR contains a small fraction (ca. 17 %) of MgO, on which CO_2 can easily adsorb[206–209], but it is unclear whether or not this has played a significant role in the chemistry and overall performance. When this material has a high optical transparency (e.g. quartz), OES measurements can be done, which would provide accurate information on the various species and temperature inside the plasma.[210] This would provide vital input to improve the reliability and predictive capability of the fluid dynamics model discussed in Chapter 4. The effect of the increased/decreased discharge length at constant SEI mentioned in Chapter 5 is another aspect that can be investigated further, in combination with modelling and/or OES measurements

From both LCA and TEA, it became very clear that improving the energy efficiency should be the main strategy to make the process more environmentally friendly and more cost-effective. Various ways to achieve this can be considered, but improving the efficiency of the power delivery system is crucial. Fortunately, it is shown that significant improvements are possible when a PSU is specifically designed for a certain reactor and process. For example, Renninger et al.[72] used a power supply with a flyback driver and an inductor with no ballast resistors for an APGD, used for CO_2 conversion. They mentioned that for a scaled up system, the efficiency (in terms of plasma-deposited power relative to supplied power) could be improved up to 80-90 %. O'Modhrain et al.[28] used low-cost PSUs that operate with an efficiency of ca. 80 %, and they stated that this can be improved further over 90 % as well.

Furthermore, improvements in terms of reactor design can also heavily influence the energy efficiency. Indeed, a significant improvement in energy efficiency was observed when moving from a traditional GA to the GAP[12]. In case of the latter, the electrode design was found to have an impact on the energy efficiency as well.[63,211] When investigating three different APGD designs, Trenchev et al.[71] reported relevant differences in energy efficiency (and conversion) between the different configurations. Hence, altering the reactor design and/or materials is definitely important to consider.

However, for every reactor there is a limit on how much the design can be improved.[211] Specifically for the cAPGD, which is already an improved design relative to a more basic APGD, it is more likely that further improvements should be expected rather from the post-plasma region. For example, the development and implementation of catalysts in the post-plasma region (so-called post-plasma catalysis, PPC) may improve the conversion and energy efficiency, and possibly also the selectivity towards the desired products. Even though only long-lived species can interact with the catalyst in case of PPC, the residual (downstream) heat from the plasma is not lost, but can be used for thermal activation of the catalyst, leading to an increased conversion and energy efficiency.[42,125,212,213] Another promising route would be placing a heat exchanger in the plasma afterglow that can recover a fraction of the heat lost, transfer it to the input gas mixture, while simultaneously reducing the electric input power. This concept is already described by Shenoy et al.[214] for syngas production by a GAP reactor, and resulted in energy efficiencies above 95 % accordingly.

Through the combination of all these steps and the insights obtained in this thesis, it is safe to assume that plasma-based syngas production has the potential of a bright future. In this way, a more sustainable chemical industry will no longer be out of reach, enabling mankind to make the necessary transition into a new sustainable era.

Chapter 8 Appendix

8.1 Supporting information Chapter 3

8.1.1 Details on gas and liquid analysis

The equipment used for gas analysis is a Thermo Scientific Trace 1310 GC. The GC contains two separate ovens, one containing the different columns while the other contains all valves and sample loops. The incoming gas flow is sampled at constant pressure in a set of 100 µL sample loops positioned in a valve oven. With helium used as carrier gas, the sample is sent onto two consecutive Rt-Q-BOND columns, which separates the permanent gases H_2, O_2, N_2, CO and CH_4 from CO_2 and lower hydrocarbons (up to C_3), while more polar molecules like H_2O are backflushed. Afterwards the sample passes one molsieve 5A column, which will separate the permanent gases from each other, while CO_2 and hydrocarbons by-pass this column. The sample arrives on a thermal conductivity detector (TCD). Calibration was performed for the gases CO_2, CH_4, N_2, O_2, CO, H_2, C_2H_2, C_2H_4 and C_2H_6.

A liquid sample collected at 25 % CH_4, 20 mA and 1 Ln/min was also analyzed. A Thermo Focus SSL GC with Stabilwax column and FID was used to quantify methanol in the sample. The same sample was also analyzed by means of a Waters alliance 2695 HPLC, containing a Shodex RSpak KC-811 column, PDA (photo-diode array) 2996 detector and RI (refractive index) 2414 detector. Formaldehyde and acetic acid could be detected. For both GC and HPLC analysis, 100 ppm standard solutions in water and an internal standard was used for proper identification and quantification.

As mentioned in section 2.2, the DRM reaction stoichiometry leads to an increase in the overall molar/volumetric flow rate. Furthermore, some products condense and are not present anymore in the GC's sample mixture. These effects influence the species concentrations. In order to obtain the species individual flow rates (instead of the concentrations) and derive several of the performance metrics correctly, the flux ratio needs to be derived. If not taken into account, these effects can lead to significant errors regarding conversion, selectivity, etc.[108,215] Figure 50 shows a schematic representation of the different stages during the measurements that lead to changes in concentration of the components in the output gas mixture.

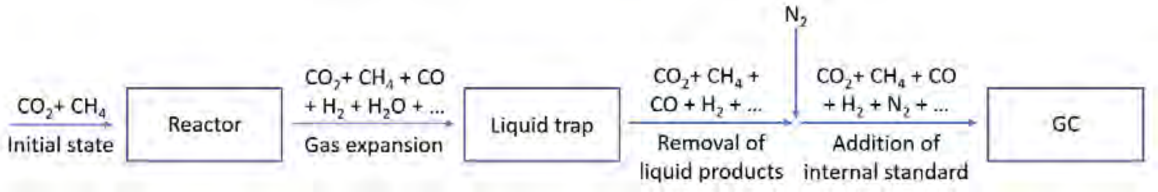

Figure 50: Schematic overview of different steps between the reactor inlet and GC that influence the measured concentrations.

To correct for these effects, N_2 is used as a standard and added to the gas mixture after the reactor outlet. In this way, the flux ratio can be derived as follows:

$$\alpha = \frac{y_{N_2}^{in}}{y_{N_2}^{out}} \tag{25}$$

Together with the measured fractions at the GC, all formulas presented in Chapter 2 can be used.[215]

8.1.2 Additional results for selectivity and yield

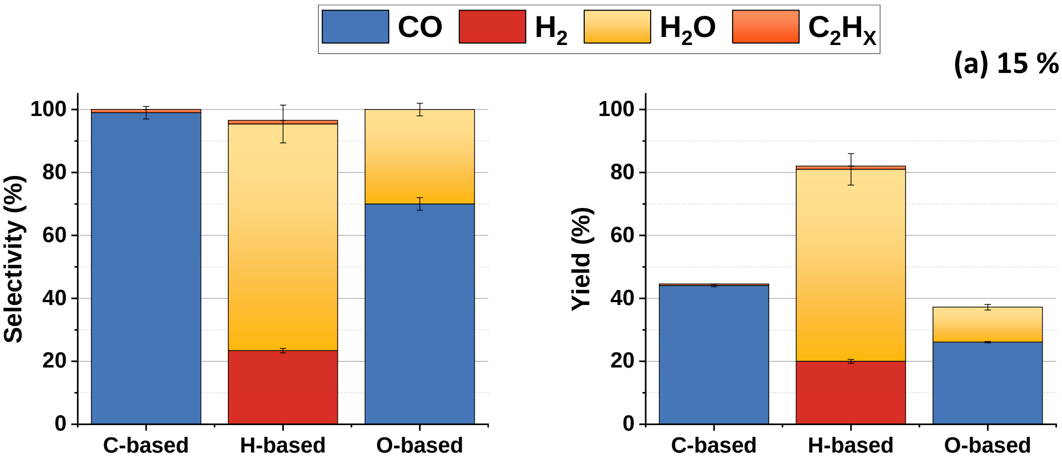

(a) 15 % CH_4

(b) 25 % CH_4

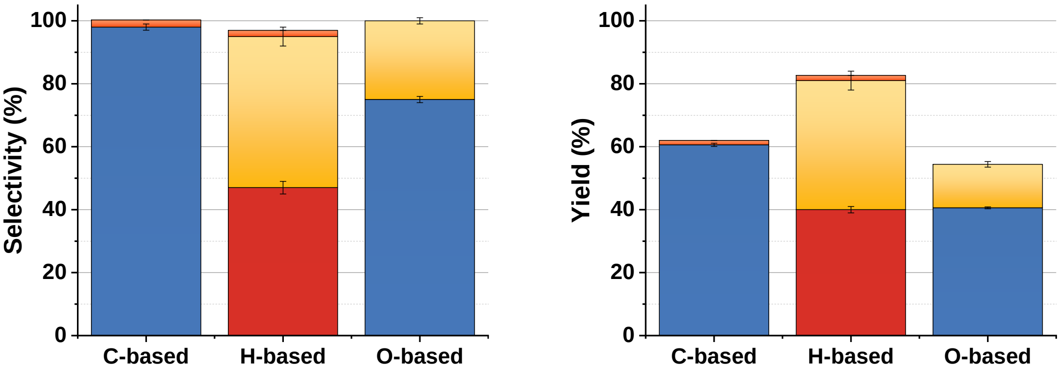

(c) 35 % CH_4

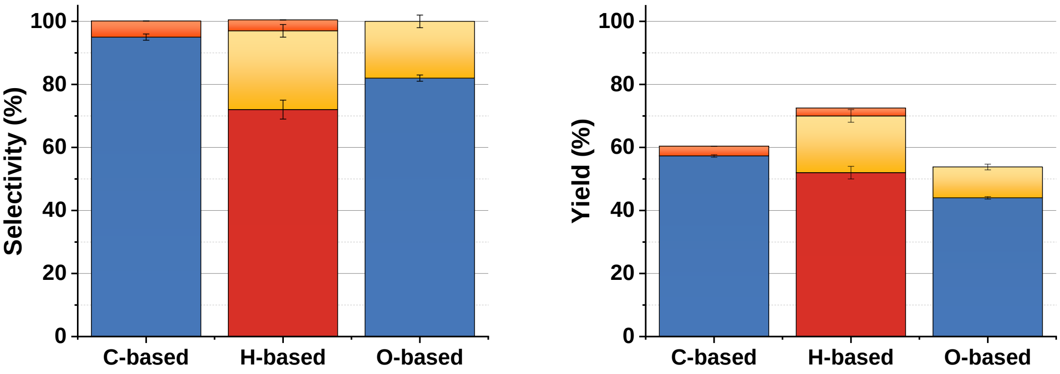

Figure 51: Experimental C-, H- and O-based selectivities (left) and yields (right) for 15 (a), 25 (b) and 35 % (c) CH_4 at 35 mA and 1 Ln/min. C_2H_2, C_2H_4 and C_2H_6 are grouped together as "C_2H_X" but C_2H_2 is the major component (~ 72 (a), 82 (b) and 88 % (c) of the total C_2H_X-fraction). Error bars are added for the experimental results, but are often too small to be visible.

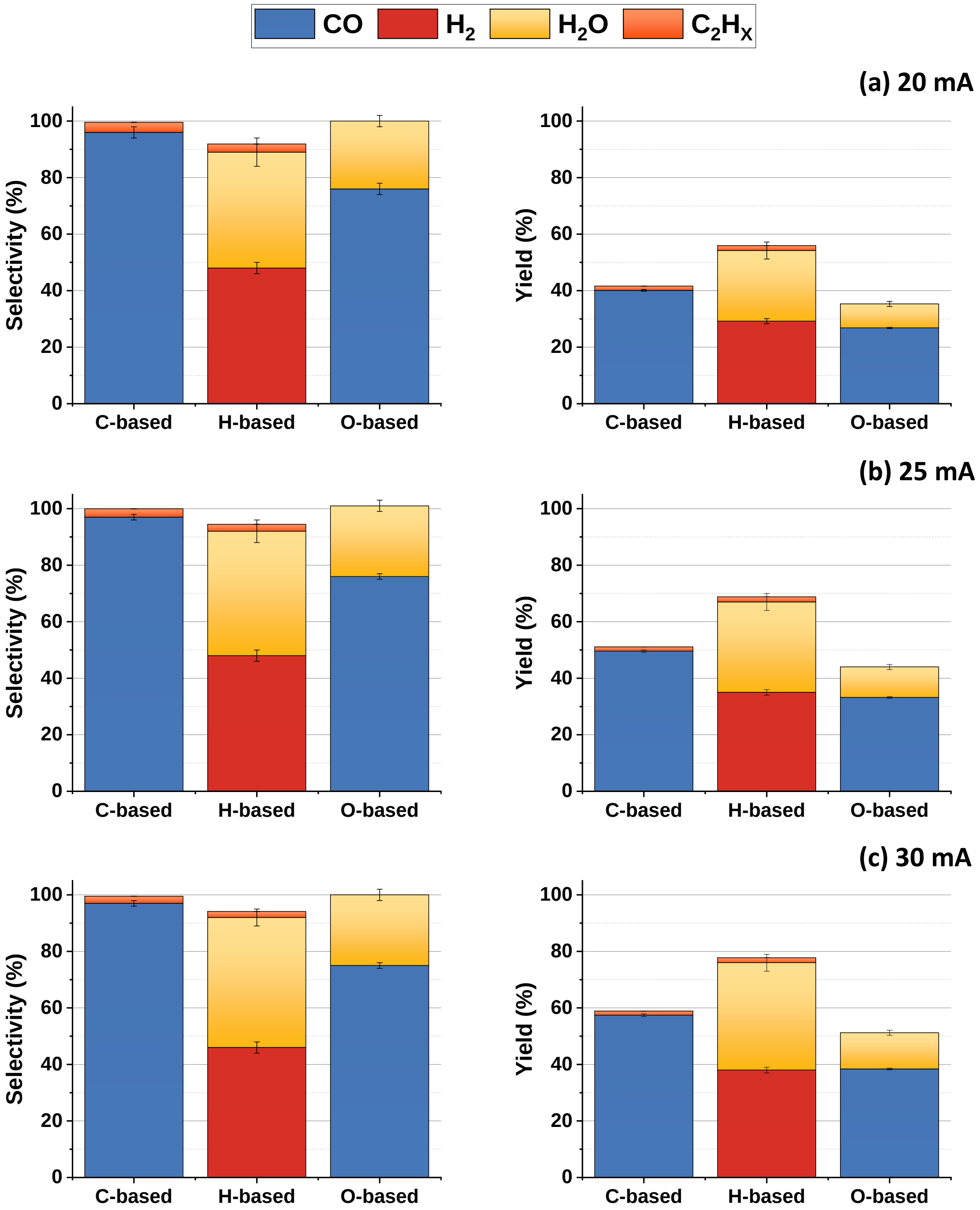

Figure 52: Experimental C-, H- and O-based selectivities (left) and yields (right) for 20 (a), 25 (b) and 30 mA (c) at 25 % CH_4 and 1 Ln/min. C_2H_2, C_2H_4 and C_2H_6 are grouped together as "C_2H_X" but C_2H_2 is the major component (~ 84 (a), 83 (b) and 83 % (c) of the total C_2H_X-fraction). Error bars are added for the experimental results, but are often too small to be visible.

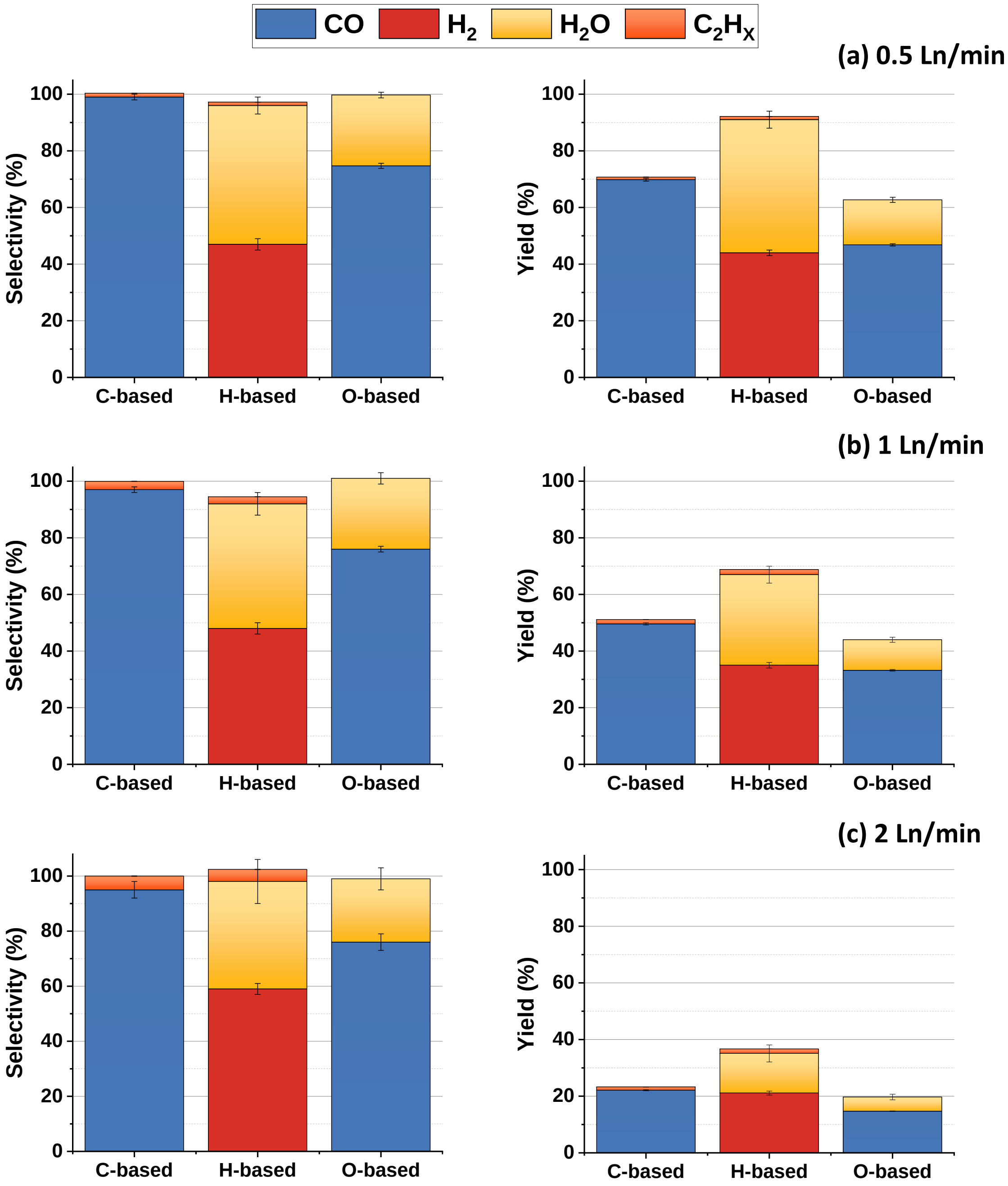

(a) 0.5 Ln/min

(b) 1 Ln/min

(c) 2 Ln/min

Figure 53: Experimental C-, H- and O-based selectivities (left) and yields (right) for 0.5 (a), 1 (b) and 2 Ln/min (c) at 25 % CH_4 and 25 mA. C_2H_2, C_2H_4 and C_2H_6 are grouped together as "C_2H_X" but C_2H_2 is the major component (~ 79 (a), 83 (b) and 76 % (c) of the total C_2H_X-fraction). Error bars are added for the experimental results, but are often too small to be visible.

8.1.3 Deriving the concentration of H_2O

GC- and HPLC-analysis of the liquid fraction collected at 25 % CH_4, 20 mA and 1 Ln/min showed that it mostly consists of water, with formaldehyde, acetic acid and methanol present at levels of 20-200 ppm. Because of the very low concentration of these components, the liquid fraction itself can be approximated as being pure H_2O.

However, we also need to take into account the flux ratio at the time when there was no condensation (i.e., α^{init}, as shown by equation (8)), but also no standard added yet, as this dilutes the output components as well. In that case, equation (8) changes to equation (26):

$$\alpha^{init} = \frac{\alpha^{fin} \cdot (1+\beta) - \beta}{1 - y_{H_2O}^{out}} \tag{26}$$

With the factor β the ratio of the flow rate of the standard relative to the CO_2-CH_4 flow rate at the reactor inlet, which in the case of this work was always kept at 10 %.

Because we cannot measure the fraction of H_2O and the initial flux ratio directly, we have to derive it through the O-balance equation.

$$1 = \frac{\alpha^{fin} \cdot \left(\sum_i \left(\mu_i^O \cdot y_i^{out}\right) + \sum_j \left(\mu_j^O \cdot y_j^{out}\right)\right) + \alpha^{init} \cdot y_{H_2O}^{out}}{\sum_i \left(\mu_i^O \cdot y_i^{in}\right)} \tag{27}$$

In this equation, $\alpha^{init} \cdot y_{H_2O}^{out}$ is the only unknown. This product is then directly used in equation (5) and (6), to obtain the selectivity and yield of H_2O. Because of its derivation through the atom balance, the error margin on each measured concentration is propagated onto this value, explaining the somewhat larger error bars in Figure 16 for these values.

8.2 Supporting information Chapter 4

8.2.1 Details on gas and liquid analysis

We used an Agilent 990 Micro GC for our gas analysis. Only two GC channels are used, each with a column and thermal conductivity detector (TCD): channel 1 and 2. Channel 1 uses a molsieve 5A column and Ar as carrier gas; permanent gases (CO, H_2, O_2, and CH_4), are separated and detected on this channel. Channel 2 uses a PoraPLOT U column and He as carrier gas; it separates CO_2, C_2H_2, C_2H_4 and C_2H_6 from each other and from the permanent gases. Both these channels utilize a CP PoraBOND Q as pre-column.

Before entering a channel, the gas mixture is heated to 70 °C by an electrically heated cable to ensure elimination of any liquid fraction from the GC. Gases with boiling points below 70 °C are caught in the cold trap, to ensure safety of the GC channels. The liquid fraction collected in the cold trap was analysed by a Thermo Focus SSL GC with Stabilwax column and FID. Table 12 shows the concentrations of the main components present (besides H_2O) for each condition. It is clear that the concentrations of the main components, i.e., CH_3OH and CH_3CH_2OH, are at maximum 0.04 % and 0.003 %, respectively. Hence, we can approximate the liquid sample as pure H_2O.

Unfortunately, this means that the APGD appears not suitable to create valuable oxygenated compounds. The model of Maerivoet et al.[139] supports this claim, because it predicts the immediate destruction of these compounds in the modelled plasma chemistry.

Table 12: Liquid analysis results of the cold trap liquid samples, for all conditions investigated.

CO_2-CH_4-O_2 fraction (%-%-%)	CH_3OH (%)	CH_3CH_2OH (%)
65-35-0	0.00	0.000
63-34-3	0.01	0.000
61-33-6	0.02	0.000
59-32-9	0.01	0.000
57-31-12	0.02	0.002
55-30-15	0.01	0.000
49-36-15	0.02	0.002
42.5-42.5-15	0.03	0.003
36-49-15	0.04	0.002

8.2.2 Safety precautions

Working with high voltages, in a CO_2-CH_4-O_2 plasma producing CO, requires some safety precautions, as listed below:

- Figure 54 depicts the explosion limit of a CO_2-CH_4-O_2 gas mixture.[216] We stayed below 15 % O_2 to ensure staying out of any explosion zone. The literature described several plasma reactors operating at higher O_2 fractions, but Figure 54 shows this is dangerous and should be considered carefully.
- Pressure relief valves releasing at 5 bar were also present in the setup to eliminate eventual explosions due to built-up pressure.
- An insulation mat is present next to the high voltage fume hoods to ensure no current can flow through any person towards the ground. The voltages used in this work, in the range of 10 kV, can create sparks up to a few centimeters long, which might be further than expected.

- CO detectors were present at all times during plasma measurements, both on working personnel as well as stationary detectors on the walls.
- All reactors are placed in a fume hood and the power supply can only be activated once the glass window of the fume hood is lowered.
- At all times multiple people were present in the lab, to act in case of emergency.
- A grounding stick was used to ground all remaining charges of all used experimental equipment after each measurement. Charge can accumulate and linger on conductive equipment if it is not in contact with the built-in grounding pin.

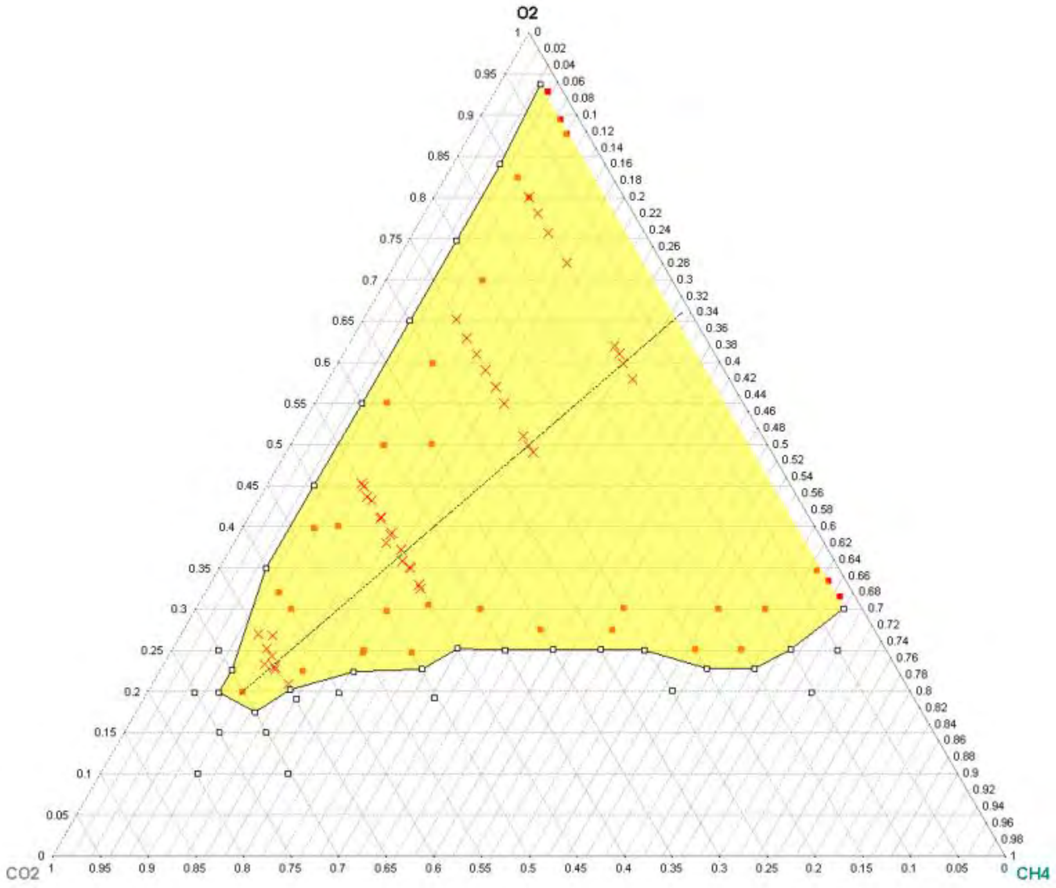

Figure 54: Safe (white) and explosive (yellow) area of any CO_2-CH_4-O_2 mixture.[216]

8.2.3 Syngas energy cost

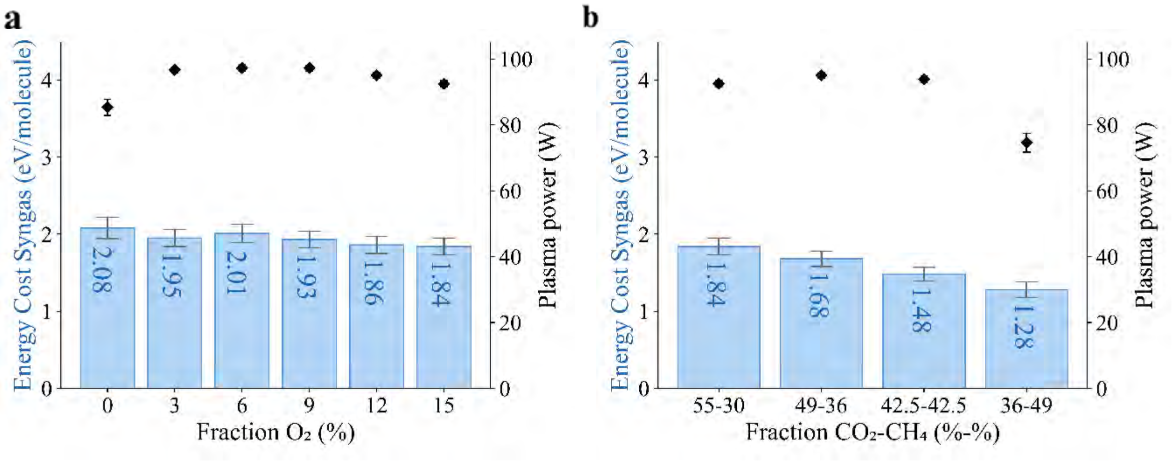

Figure 55: Energy cost of syngas in eV/molecule, as well as plasma power (right y-axis), as a function of O_2 fraction (a, series A), and CO_2-CH_4 fraction (b, series B). Error bars are based on three successive experiments.

8.2.4 Carbon deposit analysis for "without O_2" sample

In section 4.2.3, the analyses of the solid carbon deposits are shown for an experiment with O_2 added. Here, in Figure 56, the same analyses are presented for a sample that was formed in a plasma without O_2 added. Similarly, heavy spherical particles are commonly found on the carbon structures. The EDX analysis reveals a similar stainless steel composition as for the other sample. Further, the TEM analyses yield the same results as for the "with O_2" sample, being a carbon structure consisting of planar carbon, without much additional ordering. Again, this carbon material could be characterized as so-called turbostratic carbon.

Overall, no significant differences were observed between the solid carbon samples formed with and without O_2 added.

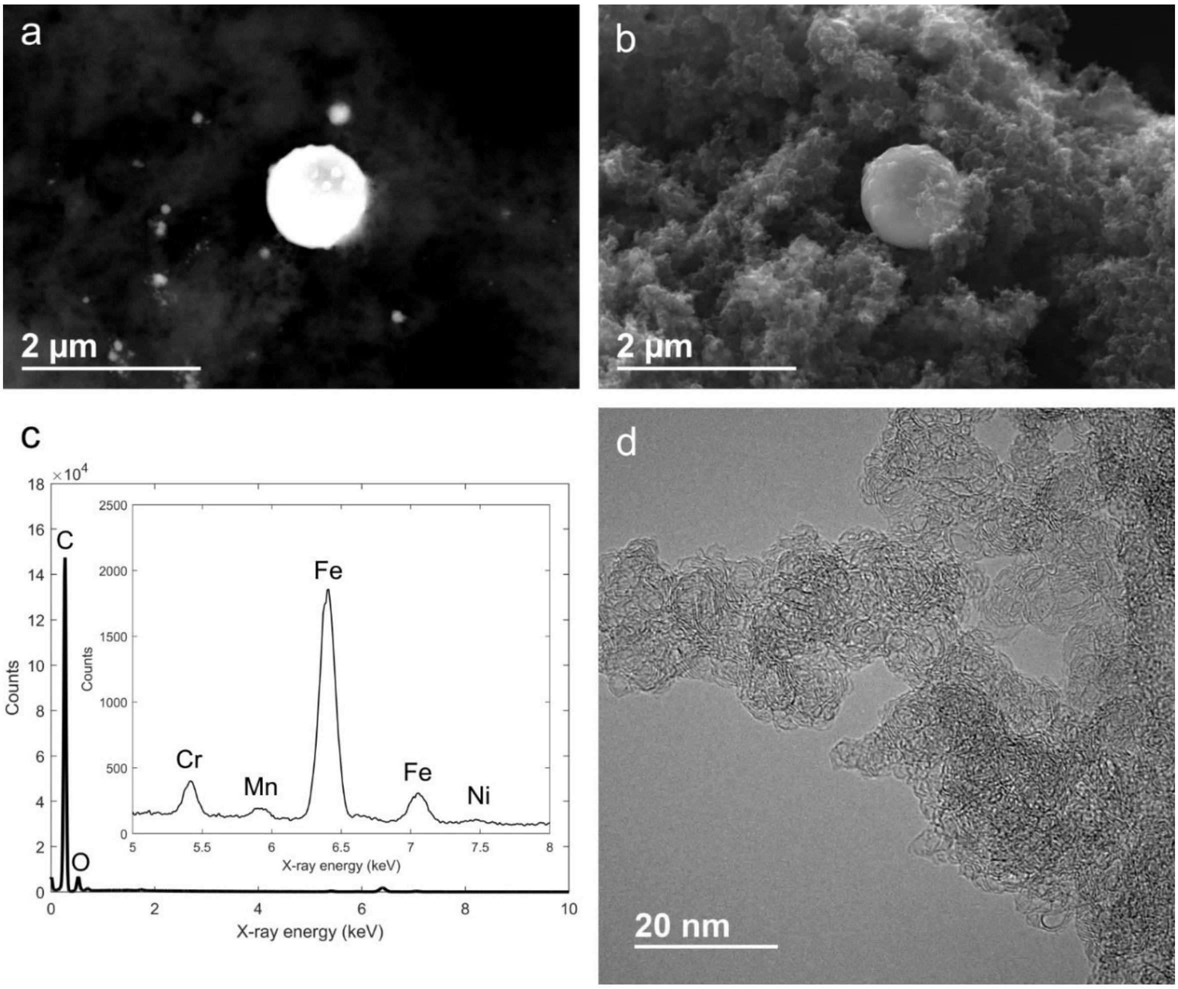

Figure 56: SEM, EDX, and TEM data for the carbon collected at the anode after an experiment without O_2 added with a 65/35/0 ratio. A: BSE SEM image, highlighting a heavy, spherical particle, with smaller heavy particles around. B: SE SEM image of the same area as in A, showing the microscopic structure of the carbon surrounding the heavy spherical particles. The carbon material appears to consist of a large agglomerate of smaller structures. C: EDX spectrum of the heavy particle presented in A, the inset shows the same spectrum but zoomed in on a relevant energy range, proving that the heavy particle is in fact stainless steel (containing Fe, Cr, and small amounts of Ni and Mn). D: Representative BF-TEM image of the carbon material. The material consists of layers of graphene-like carbon that are not structured, indicating the material is not crystalline, but also not fully amorphous.

8.3 Supporting information Chapter 5

8.3.1 H_2O vapor input fraction as function of liquid H_2O temperature

As described in section 5.2.1, dry gas (CO_2 and CH_4) is sent through the H_2O container surrounded by an oil bath, which is heated to a certain temperature. The amount of H_2O vapor carried with the dry gas flow towards the reactor inlet depends on this temperature. Table 13 presents the mass of H_2O vapor per volume dry gas as taken from literature[217], as a function of temperature. The input fraction of H_2O vapor is then derived by converting the mass of H_2O per m^3 dry gas into volume H_2O per volume dry gas, taking into account the molar volume at 1 atm and the corresponding temperature.

Table 13: Mass of H_2O vapor per volume dry gas (kg/m^3), molar volume at 1 atm (L/mol) and H_2O input fraction (%) as function of temperature (°C)

Temperature (°C)	kg H_2O/m^3 dry gas	Molar volume (L/mol) at 1 atm	H_2O input fraction (%)
60	0.13	27.3	16.5
70	0.2	28.2	23.8
80	0.29	29.0	31.8
90	0.42	29.8	41.0
100	0.59	30.6	50.1

As a result, the relation between temperature and H_2O input fraction between 60 and 100 °C can be represented by a 2nd degree equation (with $R^2 = 0.9999$):

$$y_{H_2O}^{input} = 3.3 \cdot 10^{-5} \cdot T^2 + 0.0031 \cdot T - 0.14 \tag{28}$$

This equation is subsequently used to determine the exact H_2O input fraction and flow rate entering the reactor at the conditions under study in our work (see Table 4).

8.3.2 Derivation of species molar output flow rates

As described in the main paper in section 5.2.1, the output gas mixture passes through a cold trap where the liquid fraction is condensed, and the dry gas mixture arrives at the GC for analysis. The molar/volumetric fractions of these components are obtained through calibration prior to the experiments, but the molar flow rates of the individual species cannot be measured. For this reason, the total output molar flow rate needs to be derived, and together with the molar fractions measured at the GC, it leads to the individual species molar flow rates. In our case, the total output flow rate can be derived through assuming a perfect C-balance:[215]

$$1 = \frac{\dot{n}_{tot}^{out} \cdot \left(\sum_i \left(\mu_i^C \cdot y_i^{out}\right) + \sum_j \left(\mu_j^C \cdot y_j^{out}\right)\right)}{\dot{n}_{tot}^{in} \cdot \sum_i \left(\mu_i^C \cdot y_i^{in}\right)} \tag{29}$$

In this equation i and j are representing reactants and products, respectively, and in and out are representing values corresponding to the reactor input or output, respectively. The total molar flow rate is noted as $\dot{n}_{tot}^{in/out}$, fractions measured with the GC are noted as $y_{i/j}^{in/out}$ and $\mu_{i/j}^C$ represents the number of C atoms in one molecule of i or j. As can be seen, when all carbon-containing components present in significant amounts are taken into account in this equation, the only unknown becomes the total molar output flow rate $\dot{n}_{tot}^{out}$.

The soot formed during measurements does not compromise this assumption, since for each condition labeled as green or orange, less than a mg was collected at the end of the measurement, i.e. the actual ‘soot generation rate’ expressed in mmol/min is negligible. Moreover, this approach is validated by comparing with a 500 mL soap film flow meter and stopwatch used with the initial measurements for a varying H_2O input fraction. In Table 14 we present the difference in terms of dry output flow rate and corresponding residence time in the flow meter obtained through the two techniques. As can be seen, the time difference is max. 0.5 s, which is an acceptable deviation given the inevitable human error during measurements with a stopwatch while using the soap film flow meter. These measurements, together with the negligible amount of soot collected, demonstrate that the assumption of a carbon balance equal to 1 is generally acceptable.

Table 14: Comparison of the dry output flow rate and residence time of the output gas in the 500 mL soap film flow meter, derived through the carbon balance and measured with the actual flow meter, at a varying H_2O input fraction (%).

	28 % H_2O input fraction		**36 % H_2O input fraction**		**45 % H_2O input fraction**	
	Based on C-balance	*Based on flow meter*	*Based on C-balance*	*Based on flow meter*	*Based on C-balance*	*Based on flow meter*
Dry output flow rate (Ls/min)	3.358 ± 0.006	3.44 ± 0.05	3.069 ± 0.006	3.07 ± 0.04	2.700 ± 0.006	2.82 ± 0.04
Residence time flow meter (s)	8.93 ± 0.09	8.7 ± 0.2	9.8 ± 0.1	9.8 ± 0.2	11.1 ± 0.1	10.6 ± 0.2

Finally, note that the flow rate of unconverted H_2O at the outlet cannot be obtained through this approach as it does not arrive at the GC. However, in previous work the liquid fraction for DRM[131] and OCRM[97] in an APGD, at a similar SEI, was analyzed and the liquid by-products other than H_2O were negligible. We therefore assume that H_2O can be considered as the only product not detected by the GC, and hence the H_2O output flow rate can be derived from the mass balance equation, where it is the only unknow variable:

$$1 = \frac{\dot{n}_{tot}^{out} \cdot \left(\sum_i (M_i \cdot y_i^{out}) + \sum_j \left(M_j \cdot y_j^{out}\right)\right)}{\dot{n}_{tot}^{in} \cdot \sum_i \left(M_i \cdot y_i^{in}\right)} \tag{30}$$

With $M_{i/j}$ representing the molecular mass of i or j. The molar flow rates of all individual species are then used in the formulas described in section 5.2.2 in the main paper.

8.3.3 Performance metrics at constant power and different current-voltage combinations

A slight decrease in power caused by soot formation can be counteracted by a small increase in either current or inter-electrode distance, which changes the voltage, so that the power goes back to its original level. Changing the inter-electrode distance would change the residence time of the molecules in the plasma. However, this was found not to affect the performance within a sufficiently wide range. At a constant total input flow rate (3 Ls/min), total power (300 W) and gas composition (42-22-36 CO_2-CH_4-H_2O), four different current-voltage combinations were tested, and the performance metrics remained virtually the same, as shown in Table 15. Note that the inter-electrode distance at the highest current (ca. 28 mm) is almost half of the inter-electrode distance at the lowest current (ca. 52 mm), indicating that this is a sufficiently wide range tested, especially to validate only small changes during a regular experiment.

Table 15: Results for performance metrics at same power but different current-voltage combinations, corresponding to different inter-electrode distances.

		40 mA – 11.5 kV	**50 mA – 11 kV**	**60 mA – 11 kV**	**75 mA – 11.5 kV**
Conversion (%)	**CO_2**	46.4	46.9	45.8	47.0
	CH_4	71.0	70.6	68.4	69.6
	H_2O	-13	-14	-14	-15
Yield (%)	**CO**	52.9	52.7	51.3	52.6
	H_2	34	35	33	34
Syngas ratio		0.83	0.83	0.82	0.79
Energy cost (kJ/mol)	**Conversion-based**	450	460	480	460
	Syngas-based	225	226	230	230
Energy efficiency (%)		62	63	61	62

8.4 Supporting information Chapter 6

8.4.1 Details on process design

Table 16: Process design for the APGD-assisted CH_4 reforming process.

Information	Unit	APGD-assisted CH_4 reforming
	APGD plasma reaction:	
Temperature (at reactor outlet)	°C	Sc. 1: 450 Sc. 2: 630 Sc. 3: 500
Electricity (assuming 80 % plug-to-plasma efficiency)	W	Sc. 1: 175 Sc. 2: 118 Sc. 3: 500
Reaction efficiency	%	Sc. 1: 62 Sc. 2: 65 Sc. 3: 57
	Gas cleanup:	
Temperature	°C	-103
Condensation energy	kJ/min	1.9
Coefficient of performance	-	0.5
Cooling for gas flow	kJ/min	2.8
	WGS:	
Temperature	°C	400
Heating for gas mixture	kJ/min	0.7
Reaction efficiency	%	90
Total heating energy	kJ/min	0.8

	Dual PSA system:	
Temperature	°C	25
Reaction efficiency	%	90
Pressure	bar	23

8.4.2 Total annual syngas production costs per item

Table 17: Total annual syngas production costs per item for each scenario in the base case (4 084 kmol/h).

Section	**Item**	**Annual syngas production costs ($)**		
		Scenario 1	**Scenario 2**	**Scenario 3**
Plasma	ACC	26 134 228	19 505 945	26 461 831
	CO_2 feed	15 764 305	10 766 197	4 241 347
	CH_4 feed	40 542 907	52 590 456	47 667 900
	O_2 feed		10 290 098	
	Water feed			1 559 916
	Electricity	69 727 732	50 378 606	70 699 605
	Fixed OPEX	34 602 374	25 894 320	34 468 526
Gas cleanup	ACC	6 831 752	6 933 126	1 601 358
	Cooling water	23 633	398 273	1 605 925
	Electricity	14 463 522	14 800 269	5 281 975

	Fixed OPEX	9 045 411	9 203 789	2 085 889
WGS and drying	ACC	6 110 467	5 809 830	
	Heating	1 097 235	918 455	
	Cooling water	583 754	510 197	
	Electricity	5 278 459	4 917 279	
	Fixed OPEX	8 090 411	7 712 603	
Separation	ACC	15 188 503	14 426 161	12 740 965
	Electricity	10 870 140	10 085 983	8 379 157
	Fixed OPEX	20 109 960	19 150 861	16 596 065
Total ($)		284 464 791	264 292 448	233 390 458
Capacity (tonne syngas/year)		499 755	499 562	362 622
UCOP ($/tonne syngas)		569	529	644

8.4.3 Comparison of obtained LCA values with literature data

Table 18: Benchmarking of LCA values compared with data obtained from Matin et al.[163] *(A-G Different allocations) (Impact categories AP (kg* SO_2*-eq), HTc (CTUh), ET (CTUe), EP (kg N-eq), CEDf (MJ), GWP (kg* CO_2*-eq), HTnc (CTUh), OD (kg CFC-11-eq) and RE (kg PM2.5-eq))*

	Literature reference								**Our work**		
	SRM-A	**SRM-B**	**SRM-C**	**SRM-C-DBD**	**DRM-D**	**DRM-E**	**DRM-F**	**DRM-G**	**Sc. 1**	**Sc. 2**	**Sc. 3**
GWP	8.41	9.60	1.05×10^{1}	1.81×10^{1}	1.46×10^{2}	8.83×10^{1}	2.05×10^{1}	2.39×10^{1}	5.98×10^{-1}	3.18×10^{-1}	8.03×10^{-1}
EP	9.60×10^{-3}	1.10×10^{-2}	1.10×10^{-2}	1.18×10^{-2}	6.42×10^{-2}	3.88×10^{-2}	1.27×10^{-2}	1.29×10^{-2}	7.20×10^{-5}	3.96×10^{-5}	9.77×10^{-5}
AP	3.04×10^{-2}	3.38×10^{-2}	5.90×10^{-2}	3.69×10^{-2}	2.53×10^{-1}	1.52×10^{-1}	4.47×10^{-2}	4.76×10^{-2}	6.40	3.39	8.51
OD	1.88×10^{-6}	2.00×10^{-6}	1.95×10^{-6}	2.03×10^{-6}	2.40×10^{-6}	1.45×10^{-5}	4.50×10^{-6}	4.70×10^{-6}	1.65×10^{-8}	9.69×10^{-9}	2.28×10^{-8}
ET	2.08×10^{1}	2.25×10^{1}	2.23×10^{1}	2.48×10^{1}	1.53×10^{2}	9.21×10^{1}	3.43×10^{1}	3.36×10^{1}	2.74×10^{2}	1.38×10^{2}	3.20×10^{2}
RE	3.95×10^{-3}	4.41×10^{-3}	5.85×10^{-3}	4.70×10^{-3}	2.77×10^{-2}	1.67×10^{-2}	5.66×10^{-3}	5.74×10^{-3}	1.42×10^{-3}	7.55×10^{-4}	1.91×10^{-3}
HTC	1.94×10^{-7}	2.08×10^{-7}	2.10×10^{-7}	2.33×10^{-7}	1.32×10^{-6}	7.93×10^{-7}	3.26×10^{-7}	3.11×10^{-7}	6.79×10^{-10}	3.15×10^{-10}	6.21×10^{-10}
HTnc	9.71×10^{-7}	1.09×10^{-6}	1.24×10^{-6}	1.33×10^{-6}	8.81×10^{-6}	5.31×10^{-6}	1.45×10^{-6}	1.58×10^{-6}	1.59×10^{-7}	7.61×10^{-8}	1.60×10^{-7}
CEDf	3.84×10^{1}	4.04×10^{1}	3.85×10^{1}	3.95×10^{1}	4.37×10^{2}	2.64×10^{2}	8.83×10^{1}	9.00×10^{1}	4.81	2.66	7.06

Bibliography

(1) Kahn, C.; Osborne, K. *World History: Societies of the Past*, Illustrated.; Portage & Main Press, 2005.

(2) Simmons, I. G. *Global Environmental History: 10,000 BC to AD 2000*, Illustrated.; Edinburgh University Press, 2008.

(3) Ledley, T. S.; Sundquist, E. T.; Schwartz, S. E.; Hall, D. K.; Fellows, J. D.; Killeen, T. L. Climate Change and Greenhouse Gases. *Eos, Transactions American Geophysical Union* **1999**, *80* (39), 453–458. https://doi.org/10.1029/99EO00325.

(4) Haines, A. Health Effects of Climate Change. *JAMA* **2004**, *291* (1), 99. https://doi.org/10.1001/jama.291.1.99.

(5) Spigarelli, B. P.; Kawatra, S. K. Opportunities and Challenges in Carbon Dioxide Capture. *Journal of CO2 Utilization* **2013**, *1*, 69–87. https://doi.org/10.1016/J.JCOU.2013.03.002.

(6) Valluri, S.; Claremboux, V.; Kawatra, S. Opportunities and Challenges in CO2 Utilization. *Journal of Environmental Sciences* **2022**, *113*, 322–344. https://doi.org/10.1016/J.JES.2021.05.043.

(7) Jeffry, L.; Ong, M. Y.; Nomanbhay, S.; Mofijur, M.; Mubashir, M.; Show, P. L. Greenhouse Gases Utilization: A Review. *Fuel* **2021**, *301*, 121017. https://doi.org/10.1016/J.FUEL.2021.121017.

(8) The Engineering Toolbox. *Standard State and Enthalpy of Formation, Gibbs Free Energy of Formation, Entropy and Heat Capacity*. https://www.engineeringtoolbox.com/standard-state-enthalpy-formation-definition-value-Gibbs-free-energy-entropy-molar-heat-capacity-d_1978.html (accessed 2024-03-13).

(9) Ritchie, H.; Roser, M.; Rosado, P. *Renewable Energy*. OurWorldInData.org. https://ourworldindata.org/renewable-energy#article-citation (accessed 2024-03-13).

(10) Bogaerts, A.; Neyts, E. C. Plasma Technology: An Emerging Technology for Energy Storage. *ACS Energy Letters*. American Chemical Society April 13, 2018, pp 1013–1027. https://doi.org/10.1021/acsenergylett.8b00184.

(11) Mallapragada, D. S.; Dvorkin, Y.; Modestino, M. A.; Esposito, D. V.; Smith, W. A.; Hodge, B. M.; Harold, M. P.; Donnelly, V. M.; Nuz, A.; Bloomquist, C.; Baker, K.; Grabow, L. C.; Yan, Y.; Rajput, N. N.; Hartman, R. L.; Biddinger, E. J.; Aydil, E. S.; Taylor, A. D. Decarbonization of the Chemical Industry through Electrification: Barriers and Opportunities. *Joule*. Cell Press January 18, 2023, pp 23–41. https://doi.org/10.1016/j.joule.2022.12.008.

(12) Snoeckx, R.; Bogaerts, A. Plasma Technology-a Novel Solution for CO2 Conversion? *Chem Soc Rev* **2017**, *46* (19), 5805–5863. https://doi.org/10.1039/c6cs00066e.

(13) Kitsinelis, S.; Kitsinelis, S. *Light Sources: Basics of Lighting Technologies and Applications*, 2nd ed.; CRC Press, 2015.

(14) Lynn, S. Virtual Metrology for Plasma Etch Processes. **2011**.

(15) Fridman, A. *Plasma Chemistry*; Cambridge University Press, 2008. https://doi.org/10.1017/CBO9780511546075.

(16) Slaets, J.; Loenders, B.; Bogaerts, A. Plasma-Based Dry Reforming of CH4: Plasma Effects vs. Thermal Conversion. *Fuel* **2024**, *360*, 130650. https://doi.org/10.1016/j.fuel.2023.130650.

(17) Kumar, B.; Llorente, M.; Froehlich, J.; Dang, T.; Sathrum, A.; Kubiak, C. P. Photochemical and Photoelectrochemical Reduction of CO $_2$. *Annu Rev Phys Chem* **2012**, *63* (1), 541–569. https://doi.org/10.1146/annurev-physchem-032511-143759.

(18) Madejski, P.; Chmiel, K.; Subramanian, N.; Kuś, T. Methods and Techniques for CO2 Capture: Review of Potential Solutions and Applications in Modern Energy Technologies. *Energies (Basel)* **2022**, *15* (3), 887. https://doi.org/10.3390/en15030887.

(19) Inthawong, S.; Wongkoblap, A.; Intomya, W.; Tangsathitkulchai, C. The Enhancement of CO2 and CH4 Capture on Activated Carbon with Different Degrees of Burn-Off and Surface Chemistry. *Molecules* **2023**, *28* (14), 5433. https://doi.org/10.3390/molecules28145433.

(20) Yu, C.-H.; Huang, C.-H.; Tan, C.-S. A Review of CO2 Capture by Absorption and Adsorption. *Aerosol Air Qual Res* **2012**, *12* (5), 745–769. https://doi.org/10.4209/aaqr.2012.05.0132.

(21) Kougias, P. G.; Angelidaki, I. Biogas and Its Opportunities—A Review. *Front Environ Sci Eng* **2018**, *12* (3), 14. https://doi.org/10.1007/s11783-018-1037-8.

(22) Zhao, X.; Joseph, B.; Kuhn, J.; Ozcan, S. Biogas Reforming to Syngas: A Review. *iScience* **2020**, *23* (5), 101082. https://doi.org/10.1016/j.isci.2020.101082.

(23) Scarlat, N.; Dallemand, J. F.; Fahl, F. Biogas: Developments and Perspectives in Europe. *Renew Energy* **2018**, *129*, 457–472. https://doi.org/10.1016/J.RENENE.2018.03.006.

(24) Girard-Sahun, F.; Biondo, O.; Trenchev, G.; van Rooij, G.; Bogaerts, A. Carbon Bed Post-Plasma to Enhance the CO2 Conversion and Remove O2 from the Product Stream. *Chemical Engineering Journal* **2022**, *442*, 136268. https://doi.org/10.1016/J.CEJ.2022.136268.

(25) Li, Z.; Yang, T.; Yuan, S.; Yin, Y.; Devid, E. J.; Huang, Q.; Auerbach, D.; Kleyn, A. W. Boudouard Reaction Driven by Thermal Plasma for Efficient CO2 Conversion and Energy Storage. *Journal of Energy Chemistry* **2020**, *45*, 128–134. https://doi.org/10.1016/J.JECHEM.2019.10.007.

(26) Chen, G.; Buck, F.; Kistner, I.; Widenmeyer, M.; Schiestel, T.; Schulz, A.; Walker, M.; Weidenkaff, A. A Novel Plasma-Assisted Hollow Fiber Membrane Concept for Efficiently Separating Oxygen from CO in a CO2 Plasma. *Chemical Engineering Journal* **2020**, *392*, 123699. https://doi.org/10.1016/J.CEJ.2019.123699.

(27) Mercer, E. R.; Van Alphen, S.; van Deursen, C. F. A. M.; Righart, T. W. H.; Bongers, W. A.; Snyders, R.; Bogaerts, A.; van de Sanden, M. C. M.; Peeters, F. J. J. Post-Plasma Quenching to Improve Conversion and Energy Efficiency in a CO2 Microwave Plasma. *Fuel* **2023**, *334*, 126734. https://doi.org/10.1016/J.FUEL.2022.126734.

(28) O'Modhrain, C.; Trenchev, G.; Gorbanev, Y.; Bogaerts, A. Upscaling Plasma-Based CO 2 Conversion: Case Study of a Multi-Reactor Gliding Arc Plasmatron . *ACS Engineering Au* **2024**, *4* (3), 333–344. https://doi.org/10.1021/acsengineeringau.3c00067.

(29) Wnukowski, M. Methane Pyrolysis with the Use of Plasma: Review of Plasma Reactors and Process Products. *Energies (Basel)* **2023**, *16* (18), 6441. https://doi.org/10.3390/en16186441.

(30) Daghagheleh, O.; Schenk, J.; Zarl, M. A.; Lehner, M.; Farkas, M.; Zheng, H. Feasibility of a Plasma Furnace for Methane Pyrolysis: Hydrogen and Carbon Production. *Energies (Basel)* **2023**, *17* (1), 167. https://doi.org/10.3390/en17010167.

(31) Ajanovic, A.; Sayer, M.; Haas, R. The Economics and the Environmental Benignity of Different Colors of Hydrogen. *Int J Hydrogen Energy* **2022**, *47* (57), 24136–24154. https://doi.org/10.1016/J.IJHYDENE.2022.02.094.

(32) Dames, E.; Rohani, V.; Fulcheri, L. Plasma Chemistry and Plasma Reactors for Turquoise Hydrogen and Carbon Nanomaterials Production; 2023; pp 253–317. https://doi.org/10.1016/bs.ache.2023.05.001.

(33) Fulcheri, L.; Dames, E.; Rohani, V. Plasma-Based Conversion of Methane into H2 and Carbon Black. *Curr Opin Green Sustain Chem* **2024**, 100973. https://doi.org/10.1016/j.cogsc.2024.100973.

(34) *The Monolith Process*. https://carbonblack.monolith-corp.com/methane-pyrolysis (accessed 2024-10-02).

(35) Scapinello, M.; Delikonstantis, E.; Stefanidis, G. D. The Panorama of Plasma-Assisted Non-Oxidative Methane Reforming. *Chemical Engineering and Processing: Process Intensification* **2017**, *117*, 120–140. https://doi.org/10.1016/J.CEP.2017.03.024.

(36) Biondo, O.; van Deursen, C. F. A. M.; Hughes, A.; van de Steeg, A.; Bongers, W.; van de Sanden, M. C. M.; van Rooij, G.; Bogaerts, A. Avoiding Solid Carbon Deposition in Plasma-Based Dry Reforming of Methane. *Green Chemistry* **2023**, *25* (24), 10485–10497. https://doi.org/10.1039/D3GC03595F.

(37) Kechagiopoulos, P. N.; Rogers, J.; Maitre, P.-A.; McCue, A. J.; Bannerman, M. N. Non-Oxidative Coupling of Methane via Plasma-Catalysis Over M/γ-Al2O3 Catalysts (M = Ni, Fe, Rh, Pt and Pd): Impact of Active Metal and Noble Gas Co-Feeding. *Plasma Chemistry and Plasma Processing* **2024**, *44* (6), 2057–2085. https://doi.org/10.1007/s11090-024-10507-2.

(38) Baig, S.; Sajjadi, B. Non-Thermal Plasma Enhanced Catalytic Conversion of Methane into Value Added Chemicals and Fuels. *Journal of Energy Chemistry* **2024**, *97*, 265–301. https://doi.org/10.1016/J.JECHEM.2024.05.024.

(39) De Felice, G.; Li, S.; Gallucci, F.; Pourali, N.; Rebrov, E. On Design of Plasma Jet Reactor for Non-Oxidative Methane Conversion. *React Chem Eng* **2023**, *8* (5), 1125–1133. https://doi.org/10.1039/d2re00536k.

(40) Cleiren, E.; Heijkers, S.; Ramakers, M.; Bogaerts, A. Dry Reforming of Methane in a Gliding Arc Plasmatron: Towards a Better Understanding of the Plasma Chemistry. *ChemSusChem* **2017**, *10* (20), 4025–4036. https://doi.org/10.1002/cssc.201701274.

(41) Buttler, A.; Spliethoff, H. Current Status of Water Electrolysis for Energy Storage, Grid Balancing and Sector Coupling via Power-to-Gas and Power-to-Liquids: A Review. *Renewable and Sustainable Energy Reviews* **2018**, *82*, 2440–2454. https://doi.org/10.1016/J.RSER.2017.09.003.

(42) Li, K.; Liu, J. L.; Li, X. S.; Lian, H. Y.; Zhu, X.; Bogaerts, A.; Zhu, A. M. Novel Power-to-Syngas Concept for Plasma Catalytic Reforming Coupled with Water Electrolysis. *Chemical Engineering Journal* **2018**, *353*, 297–304. https://doi.org/10.1016/J.CEJ.2018.07.111.

(43) Khoja, A. H.; Tahir, M.; Amin, N. A. S. Recent Developments in Non-Thermal Catalytic DBD Plasma Reactor for Dry Reforming of Methane. *Energy Convers Manag* **2019**, *183*, 529–560. https://doi.org/10.1016/J.ENCONMAN.2018.12.112.

(44) Ghenai, C.; Inayat, A. *Sustainable Alternative Syngas Fuel*; BoD - Books on Demand, 2019.

(45) de Klerk, A. *Fischer-Tropsch Refining*, First edition.; John Wiley & Sons, 2012.

(46) Maitlis, P. M.; Quyoum, R.; Long, H. C.; Turner, M. L. Towards a Chemical Understanding of the Fischer–Tropsch Reaction: Alkene Formation. *Appl Catal A Gen* **1999**, *186* (1–2), 363–374. https://doi.org/10.1016/S0926-860X(99)00155-6.

(47) Davis, B. H. Fischer–Tropsch Synthesis: Reaction Mechanisms for Iron Catalysts. *Catal Today* **2009**, *141* (1–2), 25–33. https://doi.org/10.1016/J.CATTOD.2008.03.005.

(48) Spath, P. L.; Dayton, D. C. *Preliminary Screening -- Technical and Economic Assessment of Synthesis Gas to Fuels and Chemicals with Emphasis on the Potential*

for Biomass-Derived Syngas; Golden, CO (United States), 2003. https://doi.org/10.2172/15006100.

(49) Chun, D. H.; Park, J. C.; Hong, S. Y.; Lim, J. T.; Kim, C. S.; Lee, H. T.; Yang, J. Il; Hong, S.; Jung, H. Highly Selective Iron-Based Fischer–Tropsch Catalysts Activated by CO2-Containing Syngas. *J Catal* **2014**, *317*, 135–143. https://doi.org/10.1016/J.JCAT.2014.06.014.

(50) Lu, W.; Cao, Q.; Xu, B.; Adidharma, H.; Gasem, K.; Argyle, M.; Zhang, F.; Zhang, Y.; Fan, M. A New Approach of Reduction of Carbon Dioxide Emission and Optimal Use of Carbon and Hydrogen Content for the Desired Syngas Production from Coal. *J Clean Prod* **2020**, *265*, 121786. https://doi.org/10.1016/J.JCLEPRO.2020.121786.

(51) Slaets, J.; Aghaei, M.; Ceulemans, S.; Van Alphen, S.; Bogaerts, A. CO_2 and CH_4 Conversion in “Real” Gas Mixtures in a Gliding Arc Plasmatron: How Do N_2 and O_2 Affect the Performance? *Green Chemistry* **2020**, *22* (4), 1366–1377. https://doi.org/10.1039/C9GC03743H.

(52) Hannula, I.; Kaisalo, N.; Simell, P. Preparation of Synthesis Gas from CO2 for Fischer–Tropsch Synthesis—Comparison of Alternative Process Configurations. *C (Basel)* **2020**, *6* (3), 55. https://doi.org/10.3390/c6030055.

(53) Bozzano, G.; Manenti, F. Efficient Methanol Synthesis: Perspectives, Technologies and Optimization Strategies. *Prog Energy Combust Sci* **2016**, *56*, 71–105. https://doi.org/10.1016/J.PECS.2016.06.001.

(54) Dalena, F.; Senatore, A.; Marino, A.; Gordano, A.; Basile, M.; Basile, A. Methanol Production and Applications: An Overview. *Methanol: Science and Engineering* **2018**, 3–28. https://doi.org/10.1016/B978-0-444-63903-5.00001-7.

(55) Iaquaniello, G.; Centi, G.; Salladini, A.; Palo, E. Waste as a Source of Carbon for Methanol Production. *Methanol: Science and Engineering* **2018**, 95–111. https://doi.org/10.1016/B978-0-444-63903-5.00004-2.

(56) Svanberg, M.; Ellis, J.; Lundgren, J.; Landälv, I. Renewable Methanol as a Fuel for the Shipping Industry. *Renewable and Sustainable Energy Reviews* **2018**, *94*, 1217–1228. https://doi.org/10.1016/J.RSER.2018.06.058.

(57) Olah, G. A. Beyond Oil and Gas: The Methanol Economy. *Angewandte Chemie International Edition* **2005**, *44* (18), 2636–2639. https://doi.org/10.1002/anie.200462121.

(58) The methanol institute. *Methanol price and supply/demand*. https://www.methanol.org/methanol-price-supply-demand/ (accessed 2024-08-08).

(59) Magaldi, B. V.; Pessoa, R. S.; Cesare, M. P.; Ribeiro, A. A.; Martins, C. A.; Sobrinho, A. S. da S. Control and Data Acquisition System to Study Dielectric Breakdown in Low-Pressure DC Plasma Reactor with Parallels Electrodes. *Revista Brasileira de Aplicações de Vácuo* **2022**, *40* (1). https://doi.org/10.17563/rbav.v40.1216.

(60) Anders, A. Glows, Arcs, Ohmic Discharges: An Electrode-Centered Review on Discharge Modes and the Transitions between Them. *Appl Phys Rev* **2024**, *11* (3), 031310. https://doi.org/10.1063/5.0205274.

(61) Thanompongchart, P.; Khongkrapan, P.; Tippayawong, N. Partial Oxidation Reforming of Simulated Biogas in Gliding Arc Discharge System. *Periodica Polytechnica Chemical Engineering* **2014**, *58* (1), 31. https://doi.org/10.3311/PPch.2114.

(62) Liu, J. L.; Park, H. W.; Chung, W. J.; Ahn, W. S.; Park, D. W. Simulated Biogas Oxidative Reforming in AC-Pulsed Gliding Arc Discharge. *Chemical Engineering Journal* **2016**, *285*, 243–251. https://doi.org/10.1016/J.CEJ.2015.09.100.

(63) Ramakers, M.; Trenchev, G.; Heijkers, S.; Wang, W.; Bogaerts, A. Gliding Arc Plasmatron: Providing an Alternative Method for Carbon Dioxide Conversion. *ChemSusChem* **2017**, *10* (12), 2642–2652. https://doi.org/10.1002/cssc.201700589.

(64) Zhang, H.; Li, L.; Li, X.; Wang, W.; Yan, J.; Tu, X. Warm Plasma Activation of CO2 in a Rotating Gliding Arc Discharge Reactor. *Journal of CO2 Utilization* **2018**, *27*, 472–479. https://doi.org/10.1016/J.JCOU.2018.08.020.

(65) Trenchev, G.; Kolev, St.; Wang, W.; Ramakers, M.; Bogaerts, A. CO $_2$ Conversion in a Gliding Arc Plasmatron: Multidimensional Modeling for Improved Efficiency. *The Journal of Physical Chemistry C* **2017**, *121* (44), 24470–24479. https://doi.org/10.1021/acs.jpcc.7b08511.

(66) Allah, Z. A.; Whitehead, J. C. Plasma-Catalytic Dry Reforming of Methane in an Atmospheric Pressure AC Gliding Arc Discharge. *Catal Today* **2015**, *256* (P1), 76–79. https://doi.org/10.1016/J.CATTOD.2015.03.040.

(67) Van Alphen, S.; Ahmadi Eshtehardi, H.; O'Modhrain, C.; Bogaerts, J.; Van Poyer, H.; Creel, J.; Delplancke, M. P.; Snyders, R.; Bogaerts, A. Effusion Nozzle for Energy-

Efficient NOx Production in a Rotating Gliding Arc Plasma Reactor. *Chemical Engineering Journal* **2022**, *443*, 136529. https://doi.org/10.1016/J.CEJ.2022.136529.

(68) Li, L.; Zhang, H.; Li, X.; Kong, X.; Xu, R.; Tay, K.; Tu, X. Plasma-Assisted CO2 Conversion in a Gliding Arc Discharge: Improving Performance by Optimizing the Reactor Design. *Journal of CO2 Utilization* **2019**, *29*, 296–303. https://doi.org/10.1016/J.JCOU.2018.12.019.

(69) Lu, N.; Sun, D.; Xia, Y.; Shang, K.; Wang, B.; Jiang, N.; Li, J.; Wu, Y. Dry Reforming of CH4CO2 in AC Rotating Gliding Arc Discharge: Effect of Electrode Structure and Gas Parameters. *Int J Hydrogen Energy* **2018**, *43* (29), 13098–13109. https://doi.org/10.1016/J.IJHYDENE.2018.05.053.

(70) Trenchev, G.; Bogaerts, A. Dual-Vortex Plasmatron: A Novel Plasma Source for CO2 Conversion. *Journal of CO2 Utilization* **2020**, *39*, 101152. https://doi.org/10.1016/J.JCOU.2020.03.002.

(71) Trenchev, G.; Nikiforov, A.; Wang, W.; Kolev, St.; Bogaerts, A. Atmospheric Pressure Glow Discharge for CO2 Conversion: Model-Based Exploration of the Optimum Reactor Configuration. *Chemical Engineering Journal* **2019**, *362*, 830–841. https://doi.org/10.1016/j.cej.2019.01.091.

(72) Renninger, S.; Lambarth, M.; Birke, K. P. High Efficiency CO2-Splitting in Atmospheric Pressure Glow Discharge. *Journal of CO2 Utilization* **2020**, *42*, 101322. https://doi.org/10.1016/j.jcou.2020.101322.

(73) Deng, X. L.; Nikiforov, A. Yu.; Vanraes, P.; Leys, Ch. Direct Current Plasma Jet at Atmospheric Pressure Operating in Nitrogen and Air. *J Appl Phys* **2013**, *113* (2). https://doi.org/10.1063/1.4774328.

(74) Li, D.; Li, X.; Bai, M.; Tao, X.; Shang, S.; Dai, X.; Yin, Y. CO2 Reforming of CH4 by Atmospheric Pressure Glow Discharge Plasma: A High Conversion Ability☆. *Int J Hydrogen Energy* **2009**, *34* (1), 308–313. https://doi.org/10.1016/j.ijhydene.2008.10.053.

(75) Xiang Li; Xumei Tao; Yongxiang Yin. An Atmospheric-Pressure Glow-Discharge Plasma Jet and Its Application. *IEEE Transactions on Plasma Science* **2009**, *37* (6), 759–763. https://doi.org/10.1109/TPS.2009.2016968.

(76) Wei, D.; Hui, Y.; Qi, C.; Yongxiang, Y.; Xiaoyan, D. Methane Conversion to C $_2$ Hydrocarbons by Abnormal Glow Discharge at Atmospheric Pressure. *Plasma Science and Technology* **2005**, *7* (6), 3132–3134. https://doi.org/10.1088/1009-0630/7/6/013.

(77) Qi, C.; Wei, D.; Xumei, T.; Hui, Y.; Xiaoyan, D.; Yongxiang, Y. CO $_2$ Reforming of CH $_4$ by Atmospheric Pressure Abnormal Glow Plasma. *Plasma Science and Technology* **2006**, *8* (2), 181–184. https://doi.org/10.1088/1009-0630/8/2/12.

(78) Akishev, Y.; Grushin, M.; Karalnik, V.; Petryakov, A.; Trushkin, N. On Basic Processes Sustaining Constricted Glow Discharge in Longitudinal N $_2$ Flow at Atmospheric Pressure. *J Phys D Appl Phys* **2010**, *43* (21), 215202. https://doi.org/10.1088/0022-3727/43/21/215202.

(79) Staack, D.; Farouk, B.; Gutsol, A.; Fridman, A. Characterization of a Dc Atmospheric Pressure Normal Glow Discharge. *Plasma Sources Sci Technol* **2005**, *14* (4), 700–711. https://doi.org/10.1088/0963-0252/14/4/009.

(80) Bruggeman, P.; Brandenburg, R. Atmospheric Pressure Discharge Filaments and Microplasmas: Physics, Chemistry and Diagnostics. *J Phys D Appl Phys* **2013**, *46* (46), 464001. https://doi.org/10.1088/0022-3727/46/46/464001.

(81) Raja, B.; Sarathi, R.; Vinu, R. Development of a Swirl-Induced Rotating Glow Discharge Reactor for CO $_2$ Conversion: Fluid Dynamics and Discharge Dynamics Studies. *Energy Technology* **2020**, *8* (12). https://doi.org/10.1002/ente.202000535.

(82) Gielniak, B.; Fiedler, T.; Broekaert, J. A. C. Study of a New Direct Current Atmospheric Pressure Glow Discharge in Helium. *Spectrochim Acta Part B At Spectrosc* **2011**, *66* (1), 21–27. https://doi.org/10.1016/j.sab.2010.11.013.

(83) Wu, P.; Li, X.; Ullah, N.; Li, Z. Synergistic Effect of Catalyst and Plasma on CO2 Decomposition in a Dielectric Barrier Discharge Plasma Reactor. *Molecular Catalysis* **2021**, *499*, 111304. https://doi.org/10.1016/J.MCAT.2020.111304.

(84) Andersen, J. A.; Christensen, J. M.; Østberg, M.; Bogaerts, A.; Jensen, A. D. Plasma-Catalytic Dry Reforming of Methane: Screening of Catalytic Materials in a Coaxial Packed-Bed DBD Reactor. *Chemical Engineering Journal* **2020**, *397*, 125519. https://doi.org/10.1016/J.CEJ.2020.125519.

(85) Wang, Q.; Shi, H.; Yan, B.; Jin, Y.; Cheng, Y. Steam Enhanced Carbon Dioxide Reforming of Methane in DBD Plasma Reactor. *Int J Hydrogen Energy* **2011**, *36* (14), 8301–8306. https://doi.org/10.1016/j.ijhydene.2011.04.084.

(86) Chang, J.-S.; Lawless, P. A.; Yamamoto, T. *Corona Discharge Processes*; 1991; Vol. 19.

(87) Xu, W.; Li, M.-W.; Xu, G.-H.; Tian, Y.-L. Decomposition of CO $_2$ Using DC Corona Discharge at Atmospheric Pressure. *Jpn J Appl Phys* **2004**, *43* (12), 8310–8311. https://doi.org/10.1143/JJAP.43.8310.

(88) Zhu, B.; Li, X. S.; Liu, J. L.; Zhu, A. M. Optimized Mixed Reforming of Biogas with O2 Addition in Spark-Discharge Plasma. *Int J Hydrogen Energy* **2012**, *37* (22), 16916–16924. https://doi.org/10.1016/J.IJHYDENE.2012.08.091.

(89) Chung, W. C.; Chang, M. B. Dry Reforming of Methane by Combined Spark Discharge with a Ferroelectric. *Energy Convers Manag* **2016**, *124*, 305–314. https://doi.org/10.1016/J.ENCONMAN.2016.07.023.

(90) Lašič Jurković, D.; Liu, J. L.; Pohar, A.; Likozar, B. Methane Dry Reforming over Ni/Al2O3 Catalyst in Spark Plasma Reactor: Linking Computational Fluid Dynamics (CFD) with Reaction Kinetic Modelling. *Catal Today* **2021**, *362*, 11–21. https://doi.org/10.1016/J.CATTOD.2020.05.028.

(91) Montesano, C.; Faedda, M.; Martini, L. M.; Dilecce, G.; Tosi, P. CH4 Reforming with CO2 in a Nanosecond Pulsed Discharge. The Importance of the Pulse Sequence. *Journal of CO2 Utilization* **2021**, *49*, 101556. https://doi.org/10.1016/J.JCOU.2021.101556.

(92) Morais, E.; Delikonstantis, E.; Scapinello, M.; Smith, G.; Stefanidis, G. D.; Bogaerts, A. Methane Coupling in Nanosecond Pulsed Plasmas: Correlation between Temperature and Pressure and Effects on Product Selectivity. *Chemical Engineering Journal* **2023**, *462*, 142227. https://doi.org/10.1016/J.CEJ.2023.142227.

(93) de la Fuente, J. F.; Moreno, S. H.; Stankiewicz, A. I.; Stefanidis, G. D. Reduction of CO2 with Hydrogen in a Non-Equilibrium Microwave Plasma Reactor. *Int J Hydrogen Energy* **2016**, *41* (46), 21067–21077. https://doi.org/10.1016/J.IJHYDENE.2016.08.032.

(94) Zhang, F.; Zhang, X.; Song, Z.; Li, X.; Zhao, X.; Sun, J.; Mao, Y.; Wang, X.; Wang, W. Promotion of Microwave Discharge over Carbon Catalysts for CO2 Reforming of

CH4 to Syngas. *Fuel* **2023**, *331*, 125914. https://doi.org/10.1016/J.FUEL.2022.125914.

(95) Sun, H.; Lee, J.; Bak, M. S. Experiments and Modeling of Atmospheric Pressure Microwave Plasma Reforming of a Methane-Carbon Dioxide Mixture. *Journal of CO2 Utilization* **2021**, *46*, 101464. https://doi.org/10.1016/J.JCOU.2021.101464.

(96) Wiegers, K.; Schulz, A.; Walker, M.; Tovar, G. E. M. Determination of the Conversion and Efficiency for CO $_2$ in an Atmospheric Pressure Microwave Plasma Torch . *Chemie Ingenieur Technik* **2022**, *94* (3), 299–308. https://doi.org/10.1002/cite.202100149.

(97) Maerivoet, S.; Wanten, B.; De Meyer, R.; Van Hove, M.; Van Alphen, S.; Bogaerts, A. Effect of O $_2$ on Plasma-Based Dry Reforming of Methane: Revealing the Optimal Gas Composition via Experiments and Modeling of an Atmospheric Pressure Glow Discharge. *ACS Sustain Chem Eng* **2024**, *12* (30), 11419–11434. https://doi.org/10.1021/acssuschemeng.4c04283.

(98) Kelly, S.; Mercer, E.; De Meyer, R.; Ciocarlan, R. G.; Bals, S.; Bogaerts, A. Microwave Plasma-Based Dry Reforming of Methane: Reaction Performance and Carbon Formation. *Journal of CO2 Utilization* **2023**, *75*, 102564. https://doi.org/10.1016/J.JCOU.2023.102564.

(99) Van Alphen, S.; Slaets, J.; Ceulemans, S.; Aghaei, M.; Snyders, R.; Bogaerts, A. Effect of N2 on CO2-CH4 Conversion in a Gliding Arc Plasmatron: Can This Major Component in Industrial Emissions Improve the Energy Efficiency? *Journal of CO2 Utilization* **2021**, *54*, 101767. https://doi.org/10.1016/J.JCOU.2021.101767.

(100) Wang, Y.; Gu, M.; Zhu, Y.; Cao, L.; Zhu, B.; Wu, J.; Lin, Y.; Huang, X. A Review of the Effects of Hydrogen, Carbon Dioxide, and Water Vapor Addition on Soot Formation in Hydrocarbon Flames. *Int J Hydrogen Energy* **2021**, *46* (61), 31400–31427. https://doi.org/10.1016/J.IJHYDENE.2021.07.011.

(101) Liu, J.; Zhu, X.; Li, X.; Li, K.; Shi, C.; Zhu, A. Effect of O2/CH4 Ratio on the Optimal Specific-Energy-Input (SEI) for Oxidative Reforming of Biogas in a Plasma-Shade Reactor. *Journal of Energy Chemistry* **2013**, *22* (5), 681–684. https://doi.org/10.1016/S2095-4956(13)60090-X.

(102) Roth, P.; Brandt, O.; Von Gersum, S. High Temperature Oxidation of Suspended Soot Particles Verified by CO and CO2 Measurements. *Symposium (International)*

on Combustion **1991**, *23* (1), 1485–1491. https://doi.org/10.1016/S0082-0784(06)80417-0.

(103) Xia, Y.; Lu, N.; Li, J.; Jiang, N.; Shang, K.; Wu, Y. Combined Steam and CO2 Reforming of CH4 for Syngas Production in a Gliding Arc Discharge Plasma. *Journal of CO2 Utilization* **2020**, *37*, 248–259. https://doi.org/10.1016/J.JCOU.2019.12.016.

(104) Wang, K.; Zhang, H.; J, A.; Rao, L.; Lin, X.; Wan, J.; Long, Y.; Gao, M.; Wang, W.; Tu, X.; Li, X.; Huang, Q. Bi-Reforming of Methane in a Carbon Deposit-Free Plasmatron with High Operational Adaptability. *Fuel Processing Technology* **2023**, *248*, 107826. https://doi.org/10.1016/J.FUPROC.2023.107826.

(105) Shaharuddin, S.; Abdul Maulud, K. N.; Syed Abdul Rahman, S. A. F.; Che Ani, A. I.; Pradhan, B. The Role of IoT Sensor in Smart Building Context for Indoor Fire Hazard Scenario: A Systematic Review of Interdisciplinary Articles. *Internet of Things* **2023**, *22*, 100803. https://doi.org/10.1016/J.IOT.2023.100803.

(106) Li, D.; Liu, S. Drinking Water Detection. *Water Quality Monitoring and Management* **2019**, 251–267. https://doi.org/10.1016/B978-0-12-811330-1.00010-7.

(107) Li, D.; Liu, S. Groundwater Quality Detection. *Water Quality Monitoring and Management* **2019**, 269–302. https://doi.org/10.1016/B978-0-12-811330-1.00011-9.

(108) Pinhão, N.; Moura, A.; Branco, J. B.; Neves, J. Influence of Gas Expansion on Process Parameters in Non-Thermal Plasma Plug-Flow Reactors: A Study Applied to Dry Reforming of Methane. *Int J Hydrogen Energy* **2016**, *41* (22), 9245–9255. https://doi.org/10.1016/j.ijhydene.2016.04.148.

(109) Mass Flow online. *What do ln/min, ls/min, slm and sccm stand for?* https://www.massflow-online.com/frequently-asked-questions/general/what-do-ln-min,-is-min,-slm-and-sccm-stand-for/?srsltid=AfmBOoooUOr6brhnWF3G718xlO20uKtWVQ-CoRS2r4XQhMuY3HzIeUm9 (accessed 2024-10-03).

(110) Kathiraser, Y.; Oemar, U.; Saw, E. T.; Li, Z.; Kawi, S. Kinetic and Mechanistic Aspects for CO2 Reforming of Methane over Ni Based Catalysts. *Chemical Engineering Journal* **2015**, *278*, 62–78. https://doi.org/10.1016/j.cej.2014.11.143.

(111) Zhou, L. M.; Xue, B.; Kogelschatz, U.; Eliasson, B. Nonequilibrium Plasma Reforming of Greenhouse Gases to Synthesis Gas. *Energy & Fuels* **1998**, *12* (6), 1191–1199. https://doi.org/10.1021/ef980044h.

(112) Mehariya, S.; Iovine, A.; Casella, P.; Musmarra, D.; Figoli, A.; Marino, T.; Sharma, N.; Molino, A. Fischer–Tropsch Synthesis of Syngas to Liquid Hydrocarbons. *Lignocellulosic Biomass to Liquid Biofuels* **2020**, 217–248. https://doi.org/10.1016/B978-0-12-815936-1.00007-1.

(113) Zhang, H.; Sun, Z.; Hu, Y. H. Steam Reforming of Methane: Current States of Catalyst Design and Process Upgrading. *Renewable and Sustainable Energy Reviews* **2021**, *149*, 111330. https://doi.org/10.1016/J.RSER.2021.111330.

(114) Abiev, R. Sh.; Sladkovskiy, D. A.; Semikin, K. V.; Murzin, D. Yu.; Rebrov, E. V. Non-Thermal Plasma for Process and Energy Intensification in Dry Reforming of Methane. *Catalysts* **2020**, *10* (11), 1358. https://doi.org/10.3390/catal10111358.

(115) Huang, A.; Xia, G.; Wang, J.; Suib, S. L.; Hayashi, Y.; Matsumoto, H. CO2 Reforming of CH4 by Atmospheric Pressure Ac Discharge Plasmas. *J Catal* **2000**, *189* (2), 349–359. https://doi.org/10.1006/JCAT.1999.2684.

(116) Yang, Y. Methane Conversion and Reforming by Nonthermal Plasma on Pins. *Ind Eng Chem Res* **2002**, *41* (24), 5918–5926. https://doi.org/10.1021/ie0202322.

(117) Kashiwagura, N.; Akita, M.; Kamioka, H. Ultrasonic Study of Machinable Ceramic over Temperature Range from Room Temperature to 1000°C. *Jpn J Appl Phys* **2005**, *44* (6S), 4339. https://doi.org/10.1143/JJAP.44.4339.

(118) Taylor, J. R. *An Introduction to Error Analysis: The Study of Uncertainties in Physical Measurements*, 2nd ed.; University Science Books, 1997.

(119) Lebigot, E. *Uncertainties: a Python package for calculations with uncertainties*. https://pythonhosted.org/uncertainties/ (accessed 2024-12-01).

(120) Octopart. *Datasheet for L225J100KE Ohmite Chassis Mount Resistors*. https://octopart.com/datasheet/l225j100ke-ohmite-128124 (accessed 2024-12-03).

(121) Dinh, D. K.; Trenchev, G.; Lee, D. H.; Bogaerts, A. Arc Plasma Reactor Modification for Enhancing Performance of Dry Reforming of Methane. *Journal of CO2 Utilization* **2020**, *42*, 101352. https://doi.org/10.1016/J.JCOU.2020.101352.

(122) Jahn, R. G.; Lyman, F. A. Physics of Electric Propulsion. *J Appl Mech* **1969**, *36* (3), 655–655. https://doi.org/10.1115/1.3564751.

(123) Mancinelli, B.; Prevosto, L.; Chamorro, J. C.; Minotti, F. O.; Kelly, H. Modelling of the Plasma–Sheath Boundary Region in Wall-Stabilized Arc Plasmas: Unipolar Discharge Properties. *Plasma Chemistry and Plasma Processing* **2018**, *38* (1), 147–176. https://doi.org/10.1007/s11090-017-9859-x.

(124) Li, K.; Liu, J. L.; Li, X. S.; Zhu, X.; Zhu, A. M. Warm Plasma Catalytic Reforming of Biogas in a Heat-Insulated Reactor: Dramatic Energy Efficiency and Catalyst Auto-Reduction. *Chemical Engineering Journal* **2016**, *288*, 671–679. https://doi.org/10.1016/J.CEJ.2015.12.036.

(125) Li, K.; Liu, J. L.; Li, X. S.; Zhu, X. B.; Zhu, A. M. Post-Plasma Catalytic Oxidative CO2 Reforming of Methane over Ni-Based Catalysts. *Catal Today* **2015**, *256* (P1), 96–101. https://doi.org/10.1016/J.CATTOD.2015.03.013.

(126) Chun, S. M.; Hong, Y. C.; Choi, D. H. Reforming of Methane to Syngas in a Microwave Plasma Torch at Atmospheric Pressure. *Journal of CO2 Utilization* **2017**, *19*, 221–229. https://doi.org/10.1016/J.JCOU.2017.03.016.

(127) Majd Alawi, N.; Hung Pham, G.; Barifcani, A.; Hoang Nguyen, M.; Liu, S. Syngas Formation by Dry and Steam Reforming of Methane Using Microwave Plasma Technology. *IOP Conf Ser Mater Sci Eng* **2019**, *579* (1), 012022. https://doi.org/10.1088/1757-899X/579/1/012022.

(128) Snoeckx, R.; Wang, W.; Zhang, X.; Cha, M. S.; Bogaerts, A. Plasma-Based Multi-Reforming for Gas-To-Liquid: Tuning the Plasma Chemistry towards Methanol. *Sci Rep* **2018**, *8* (1), 15929. https://doi.org/10.1038/s41598-018-34359-x.

(129) Krawczyk, K.; Młotek, M.; Ulejczyk, B.; Schmidt-Szałowski, K. Methane Conversion with Carbon Dioxide in Plasma-Catalytic System. *Fuel* **2014**, *117* (PART A), 608–617. https://doi.org/10.1016/J.FUEL.2013.08.068.

(130) The Engineering ToolBox. *Solubility of Gases in Water vs. Temperature*. https://www.engineeringtoolbox.com/gases-solubility-water-d_1148.html (accessed 2024-11-27).

(131) Wanten, B.; Maerivoet, S.; Vantomme, C.; Slaets, J.; Trenchev, G.; Bogaerts, A. Dry Reforming of Methane in an Atmospheric Pressure Glow Discharge: Confining the

Plasma to Expand the Performance. *Journal of CO2 Utilization* **2022**, *56*, 101869. https://doi.org/10.1016/J.JCOU.2021.101869.

(132) Joo, O.-S.; Jung, K.-D.; Moon, I.; Rozovskii, A. Ya.; Lin, G. I.; Han, S.-H.; Uhm, S.-J. Carbon Dioxide Hydrogenation To Form Methanol via a Reverse-Water-Gas-Shift Reaction (the CAMERE Process). *Ind Eng Chem Res* **1999**, *38* (5), 1808–1812. https://doi.org/10.1021/ie9806848.

(133) Kassel, L. S. THE THERMAL DECOMPOSITION OF METHANE ^{1}. *J Am Chem Soc* **1932**, *54* (10), 3949–3961. https://doi.org/10.1021/ja01349a019.

(134) Gautier, M.; Rohani, V.; Fulcheri, L. Direct Decarbonization of Methane by Thermal Plasma for the Production of Hydrogen and High Value-Added Carbon Black. *Int J Hydrogen Energy* **2017**, *42* (47), 28140–28156. https://doi.org/10.1016/J.IJHYDENE.2017.09.021.

(135) Fedotov, A. Conversion of Methane and Carbon Dioxide on Porous Catalytic Membranes, Institut National Polytechnique de Lorraine, 2009.

(136) Szyk, B.; Czernia, D. *Enthalpy Calculator*. https://www.omnicalculator.com/physics/enthalpy (accessed 2024-09-10).

(137) Foo, S. Y.; Cheng, C. K.; Nguyen, T.-H.; Adesina, A. A. Oxidative CO $_2$ Reforming of Methane on Alumina-Supported Co−Ni Catalyst. *Ind Eng Chem Res* **2010**, *49* (21), 10450–10458. https://doi.org/10.1021/ie100460g.

(138) Martínez-Sánchez, B.; Quílez-Bermejo, J.; Cazorla-Amorós, D.; Morallón, E. Electrocatalysis with Metal-Free Carbon-Based Catalysts. *Carbon-Based Metal Free Catalysts: Preparation, Structural and Morphological Property and Application* **2022**, 213–244. https://doi.org/10.1016/B978-0-323-88515-7.00007-9.

(139) Maerivoet, S.; Tsonev, I.; Slaets, J.; Reniers, F.; Bogaerts, A. Coupled Multi-Dimensional Modelling of Warm Plasmas: Application and Validation for an Atmospheric Pressure Glow Discharge in CO2/CH4/O2. *Chemical Engineering Journal* **2024**, *492*, 152006. https://doi.org/10.1016/J.CEJ.2024.152006.

(140) Long, X.; Zhang, S.; Shao, C.; Wang, B.; Wang, Y. Effects of Heat-Treatment on the Microstructure, Electromagnetic Wave Absorbing Properties, and Mechanical Properties of SiCN Fibers. *Front Mater* **2020**, *7*. https://doi.org/10.3389/fmats.2020.563891.

(141) Kowalewski, E.; Zienkiewicz-Machnik, M.; Lisovytskiy, D.; Nikiforov, K.; Matus, K.; Śrębowata, A.; Sá, J. Turbostratic Carbon Supported Palladium as an Efficient Catalyst for Reductive Purification of Water from Trichloroethylene. *AIMS Mater Sci* **2017**, *4* (6), 1276–1288. https://doi.org/10.3934/matersci.2017.6.1276.

(142) Zhu, X.; Li, K.; Liu, J. L.; Li, X. S.; Zhu, A. M. Effect of CO2/CH4 Ratio on Biogas Reforming with Added O2 through an Unique Spark-Shade Plasma. *Int J Hydrogen Energy* **2014**, *39* (25), 13902–13908. https://doi.org/10.1016/J.IJHYDENE.2014.01.040.

(143) Meng, G.; Xia, L.; Cheng, Y.; Yin, Z. AC-Driven Atmospheric Pressure Glow Discharge Co-Improves Conversion and Energy Efficiency of CO2 Splitting. *Journal of CO2 Utilization* **2023**, *70*, 102447. https://doi.org/10.1016/J.JCOU.2023.102447.

(144) Abdo, Y.; Rohani, V.; Cauneau, F.; Fulcheri, L. New Perspectives on the Dynamics of AC and DC Plasma Arcs Exposed to Cross-Fields. *J Phys D Appl Phys* **2017**, *50* (6), 065203. https://doi.org/10.1088/1361-6463/aa540e.

(145) Biswas, A. N.; Winter, L. R.; Loenders, B.; Xie, Z.; Bogaerts, A.; Chen, J. G. Oxygenate Production from Plasma-Activated Reaction of CO_2 and Ethane. *ACS Energy Lett* **2022**, *7* (1), 236–241. https://doi.org/10.1021/acsenergylett.1c02355.

(146) Kumar, N.; Shojaee, M.; Spivey, J. J. Catalytic Bi-Reforming of Methane: From Greenhouse Gases to Syngas. *Curr Opin Chem Eng* **2015**, *9*, 8–15. https://doi.org/10.1016/J.COCHE.2015.07.003.

(147) Farooqi, A. S.; Abdullah, B.; Ayodele, B. V.; Ishtiaq, U.; Marias, F.; Nemitallah, M. A.; Ali, B. Catalytic Bi-Reforming of Methane as a Potential Source of Hydrogen Rich Syngas: Promotional Effect of Strontium on the Catalytic Performance of Ni/MgO-ZrO2. *Energy Conversion and Management: X* **2024**, *22*, 100567. https://doi.org/10.1016/J.ECMX.2024.100567.

(148) Ibrahim, I. H.; Shafiqah, M.-N. N.; Rosli, S. N. A.; Mohamed, H.; Panpranot, J.; Cuong Nguyen, V.; Abidin, S. Z. Optimization of Syngas Production via Methane Bi-Reforming Using CeO2 Promoted Cu/MnO2 Catalyst. *Chemical Engineering Research and Design* **2024**, *206*, 62–78. https://doi.org/10.1016/J.CHERD.2024.04.039.

(149) Mohanty, U. S.; Ali, M.; Azhar, M. R.; Al-Yaseri, A.; Keshavarz, A.; Iglauer, S. Current Advances in Syngas (CO + H2) Production through Bi-Reforming of Methane Using

Various Catalysts: A Review. *Int J Hydrogen Energy* **2021**, *46* (65), 32809–32845. https://doi.org/10.1016/J.IJHYDENE.2021.07.097.

(150) Hrycak, B.; Mizeraczyk, J.; Czylkowski, D.; Dors, M.; Budnarowska, M.; Jasiński, M. Hydrogen Production by the Steam Reforming of Synthetic Biogas in Atmospheric-Pressure Microwave (915 MHz) Plasma. *Sci Rep* **2023**, *13* (1), 1–15. https://doi.org/10.1038/s41598-023-29433-y.

(151) Czylkowski, D.; Hrycak, B.; Jasiński, M.; Dors, M.; Mizeraczyk, J. Microwave Plasma-Based Method of Hydrogen Production via Combined Steam Reforming of Methane. *Energy* **2016**, *113* (2016), 653–661. https://doi.org/10.1016/j.energy.2016.07.088.

(152) Ni, G.; Lan, Y.; Cheng, C.; Meng, Y.; Wang, X. Reforming of Methane and Carbon Dioxide by DC Water Plasma at Atmospheric Pressure. *Int J Hydrogen Energy* **2011**, *36* (20), 12869–12876. https://doi.org/10.1016/j.ijhydene.2011.07.063.

(153) Le, H.; Hoang, T.; Mallinson, R.; Lobban, L. Methane Using AC Discharge. *147* (ID), 175–180.

(154) *T.E. Toolbox, Gases - Gross and Net Heat Values*. https://www.engineeringtoolbox.com/gross-net-heating-values-d_420.html (accessed 2024-02-12).

(155) Bronkhorst. *VAPOUR Flow Control Solutions*. https://www.bronkhorst.com/int/products/vapour-flow/ (accessed 2024-12-03).

(156) Ai, L.; Ng, S.; Ong, W. A Prospective Life Cycle Assessment of Electrochemical CO $_2$ Reduction to Selective Formic Acid and Ethylene. *ChemSusChem* **2022**, *15* (19). https://doi.org/10.1002/cssc.202200857.

(157) Ling, G. Z. S.; Foo, J. J.; Tan, X.-Q.; Ong, W.-J. Transition into Net-Zero Carbon Community from Fossil Fuels: Life Cycle Assessment of Light-Driven CO $_2$ Conversion to Methanol Using Graphitic Carbon Nitride. *ACS Sustain Chem Eng* **2023**, *11* (14), 5547–5558. https://doi.org/10.1021/acssuschemeng.2c07375.

(158) Choe, C.; Cheon, S.; Gu, J.; Lim, H. Critical Aspect of Renewable Syngas Production for Power-to-Fuel via Solid Oxide Electrolysis: Integrative Assessment for Potential Renewable Energy Source. *Renewable and Sustainable Energy Reviews* **2022**, *161*, 112398. https://doi.org/10.1016/J.RSER.2022.112398.

(159) Sternberg, A.; Bardow, A. Life Cycle Assessment of Power-to-Gas: Syngas vs Methane. *ACS Sustain Chem Eng* **2016**, *4* (8), 4156–4165. https://doi.org/10.1021/acssuschemeng.6b00644.

(160) Puig-Gamero, M.; Parascanu, M. M.; Sánchez, P.; Sanchez-Silva, L. Olive Pomace versus Natural Gas for Methanol Production: A Life Cycle Assessment. *Environmental Science and Pollution Research* **2021**, *28* (23), 30335–30350. https://doi.org/10.1007/s11356-021-12710-6.

(161) Li, G.; Ma, S.; Liu, F.; Zhou, X.; Wang, K.; Zhang, Y. Life Cycle Water Footprint Assessment of Syngas Production from Biomass Chemical Looping Gasification. *Bioresour Technol* **2021**, *342*, 125940. https://doi.org/10.1016/j.biortech.2021.125940.

(162) Ardolino, F.; Arena, U. Biowaste-to-Biomethane: An LCA Study on Biogas and Syngas Roads. *Waste Management* **2019**, *87*, 441–453. https://doi.org/10.1016/j.wasman.2019.02.030.

(163) Matin, N. S.; Flanagan, W. P. Environmental Performance of Nonthermal Plasma Dry and Conventional Steam Reforming of Methane for Hydrogen Production: Application of Life Cycle Assessment Methodology. *Int J Hydrogen Energy* **2024**, *49*, 1405–1413. https://doi.org/10.1016/j.ijhydene.2023.10.106.

(164) Escribà-Gelonch, M.; Bricout, J.; Hessel, V. Circular Economy Metrics for the Photo-High-p,T Continuous Multistep Synthesis of Vitamin D $_3$. *ACS Sustain Chem Eng* **2021**, *9* (4), 1867–1879. https://doi.org/10.1021/acssuschemeng.0c08330.

(165) *ISO14040: Environmental Management — Life Cycle Assessment — Principles and Framework*; 2006.

(166) *ISO14044: Environmental Management — Life Cycle Assessment — Requirements and Guidelines*; 2006.

(167) Rezaei, E.; Dzuryk, S. Techno-Economic Comparison of Reverse Water Gas Shift Reaction to Steam and Dry Methane Reforming Reactions for Syngas Production. *Chemical Engineering Research and Design* **2019**, *144*, 354–369. https://doi.org/10.1016/j.cherd.2019.02.005.

(168) Cao, G.; Handler, R. M.; Luyben, W. L.; Xiao, Y.; Chen, C.-H.; Baltrusaitis, J. CO2 Conversion to Syngas via Electrification of Endothermal Reactors: Process Design

and Environmental Impact Analysis. *Energy Convers Manag* **2022**, *265*, 115763. https://doi.org/10.1016/j.enconman.2022.115763.

(169) Eurostat. *Shedding light on energy in Europe*. https://ec.europa.eu/eurostat/web/interactive-publications/energy-2024#about-publication (accessed 2024-09-26).

(170) Schrijvers, D. L.; Loubet, P.; Sonnemann, G. An Axiomatic Method for Goal-Dependent Allocation in Life Cycle Assessment. *Int J Life Cycle Assess* **2021**, *26* (6), 1223–1235. https://doi.org/10.1007/s11367-021-01932-y.

(171) *European platform on LCA | EPLCA*. https://eplca.jrc.ec.europa.eu/LCDN/developerEF.html (accessed 2024-09-26).

(172) MacArthur, E. Towards the Circular Economy. *J Ind Ecol* **2013**, *2* (1), 23–44.

(173) Escribà-Gelonch, M.; Butler, G. D.; Goswami, A.; Tran, N. N.; Hessel, V. Definition of Agronomic Circular Economy Metrics and Use for Assessment for a Nanofertilizer Case Study. *Plant Physiology and Biochemistry* **2023**, *196*, 917–924. https://doi.org/10.1016/j.plaphy.2023.02.042.

(174) Towler, G.; Sinnott, R. Economic Evaluation of Projects. In *Chemical Engineering Design*; Elsevier, 2013; pp 389–429. https://doi.org/10.1016/B978-0-08-096659-5.00009-2.

(175) Williams Jr., R. "Six-Tenths Factor" Aids in Approximating Costs. *Chemical Engineering* **1947**, *54*, 124–125.

(176) Hamelinck, C. N.; Faaij, A. P. C.; den Uil, H.; Boerrigter, H. Production of FT Transportation Fuels from Biomass; Technical Options, Process Analysis and Optimisation, and Development Potential. *Energy* **2004**, *29* (11), 1743–1771. https://doi.org/10.1016/J.ENERGY.2004.01.002.

(177) Whitesides, R. W. Process Equipment Cost Estimating by Ratio and Proportion. *PDH online Course*. PDH Center: Meadow Estates Drive 2020.

(178) Spath, P.; Aden, A.; Eggeman, T.; Ringer, M.; Wallace, B.; Jechura, J. *Biomass to Hydrogen Production Detailed Design and Economics Utilizing the Battelle Columbus Laboratory Indirectly-Heated Gasifier*; 2005.

(179) Chiuta, S.; Engelbrecht, N.; Human, G.; Bessarabov, D. G. Techno-Economic Assessment of Power-to-Methane and Power-to-Syngas Business Models for Sustainable Carbon Dioxide Utilization in Coal-to-Liquid Facilities. *Journal of CO2 Utilization* **2016**, *16*, 399–411. https://doi.org/10.1016/J.JCOU.2016.10.001.

(180) Luberti, M.; Ahn, H. Design of an Industrial Multi-Bed (V)PSA Unit for Argon Concentration. *Sep Purif Technol* **2021**, *261*, 118254. https://doi.org/10.1016/J.SEPPUR.2020.118254.

(181) Paturska, A.; Repele, M.; Bazbauers, G. Economic Assessment of Biomethane Supply System Based on Natural Gas Infrastructure. *Energy Procedia* **2015**, *72*, 71–78. https://doi.org/10.1016/J.EGYPRO.2015.06.011.

(182) Osorio-Tejada, J.; Escriba-Gelonch, M.; Vertongen, R.; Bogaerts, A.; Hessel, V. CO_2 Conversion to CO *via* Plasma and Electrolysis: A Techno-Economic and Energy Cost Analysis. *Energy Environ Sci* **2024**, *17* (16), 5833–5853. https://doi.org/10.1039/D4EE00164H.

(183) *Our Technology | D-CRBN*. https://d-crbn.com/our-technology/ (accessed 2024-09-26).

(184) Yamamoto, A.; Mori, S.; Suzuki, M. Scale-up or Numbering-up of a Micro Plasma Reactor for the Carbon Dioxide Decomposition. *Thin Solid Films* **2007**, *515* (9), 4296–4300. https://doi.org/10.1016/J.TSF.2006.02.058.

(185) Anastasopoulou, A.; Keijzer, R.; Butala, S.; Lang, J.; Van Rooij, G.; Hessel, V. Eco-Efficiency Analysis of Plasma-Assisted Nitrogen Fixation. *J Phys D Appl Phys* **2020**, *53* (23), 234001. https://doi.org/10.1088/1361-6463/ab71a8.

(186) Peters, M. S.; Timmerhaus, K. D.; West, R. E. *Plant Design and Economics for Chemical Engineers*, 5th ed.; McGraw-Hill Education: New York, 2003.

(187) Fasihi, M.; Breyer, C. Global Production Potential of Green Methanol Based on Variable Renewable Electricity. *Energy Environ Sci* **2024**, *17* (10), 3503–3522. https://doi.org/10.1039/D3EE02951D.

(188) Yue, P.; Fu, Q.; Li, J.; Zhu, X.; Liao, Q. Comparative Life Cycle and Economic Assessments of Various Value-Added Chemicals' Production *via* Electrochemical CO_2 Reduction. *Green Chemistry* **2022**, *24* (7), 2927–2936. https://doi.org/10.1039/D1GC04270J.

(189) Huang, Z.; Grim, R. G.; Schaidle, J. A.; Tao, L. The Economic Outlook for Converting CO_2 and Electrons to Molecules. *Energy Environ Sci* **2021**, *14* (7), 3664–3678. https://doi.org/10.1039/D0EE03525D.

(190) Bushuyev, O. S.; De Luna, P.; Dinh, C. T.; Tao, L.; Saur, G.; van de Lagemaat, J.; Kelley, S. O.; Sargent, E. H. What Should We Make with CO2 and How Can We Make It? *Joule* **2018**, *2* (5), 825–832. https://doi.org/10.1016/J.JOULE.2017.09.003.

(191) Jouny, M.; Hutchings, G. S.; Jiao, F. Carbon Monoxide Electroreduction as an Emerging Platform for Carbon Utilization. *Nat Catal* **2019**, *2* (12), 1062–1070. https://doi.org/10.1038/s41929-019-0388-2.

(192) Kibria, M. G.; Edwards, J. P.; Gabardo, C. M.; Dinh, C.; Seifitokaldani, A.; Sinton, D.; Sargent, E. H. Electrochemical CO_2 Reduction into Chemical Feedstocks: From Mechanistic Electrocatalysis Models to System Design. *Advanced Materials* **2019**, *31* (31). https://doi.org/10.1002/adma.201807166.

(193) Lee, J.; Lee, W.; Ryu, K. H.; Park, J.; Lee, H.; Lee, J. H.; Park, K. T. Catholyte-Free Electroreduction of CO_2 for Sustainable Production of CO: Concept, Process Development, Techno-Economic Analysis, and CO_2 Reduction Assessment. *Green Chemistry* **2021**, *23* (6), 2397–2410. https://doi.org/10.1039/D0GC02969F.

(194) Li, W.; Feaster, J. T.; Akhade, S. A.; Davis, J. T.; Wong, A. A.; Beck, V. A.; Varley, J. B.; Hawks, S. A.; Stadermann, M.; Hahn, C.; Aines, R. D.; Duoss, E. B.; Baker, S. E. Comparative Techno-Economic and Life Cycle Analysis of Water Oxidation and Hydrogen Oxidation at the Anode in a CO_2 Electrolysis to Ethylene System. *ACS Sustain Chem Eng* **2021**, *9* (44), 14678–14689. https://doi.org/10.1021/acssuschemeng.1c01846.

(195) Orella, M. J.; Brown, S. M.; Leonard, M. E.; Román-Leshkov, Y.; Brushett, F. R. A General Technoeconomic Model for Evaluating Emerging Electrolytic Processes. *Energy Technology* **2020**, *8* (11). https://doi.org/10.1002/ente.201900994.

(196) Ramdin, M.; De Mot, B.; Morrison, A. R. T.; Breugelmans, T.; van den Broeke, L. J. P.; Trusler, J. P. M.; Kortlever, R.; de Jong, W.; Moultos, O. A.; Xiao, P.; Webley, P. A.; Vlugt, T. J. H. Electroreduction of CO_2/CO to C_2 Products: Process Modeling, Downstream Separation, System Integration, and Economic Analysis. *Ind Eng Chem Res* **2021**, *60* (49), 17862–17880. https://doi.org/10.1021/acs.iecr.1c03592.

(197) Verma, S.; Kim, B.; Jhong, H. "Molly"; Ma, S.; Kenis, P. J. A. A Gross-Margin Model for Defining Technoeconomic Benchmarks in the Electroreduction of CO $_2$. *ChemSusChem* **2016**, *9* (15), 1972–1979. https://doi.org/10.1002/cssc.201600394.

(198) Kuckshinrichs, W.; Ketelaer, T.; Koj, J. C. Economic Analysis of Improved Alkaline Water Electrolysis. *Front Energy Res* **2017**, *5*. https://doi.org/10.3389/fenrg.2017.00001.

(199) Šulc, R.; Ditl, P. A Technical and Economic Evaluation of Two Different Oxygen Sources for a Small Oxy-Combustion Unit. *J Clean Prod* **2021**, *309*, 127427. https://doi.org/10.1016/J.JCLEPRO.2021.127427.

(200) Ulrich, G. D.; Vasudevan, P. T. How to Estimate Utility Costs. *Chem Eng* **2006**, *113* (4), 66–69.

(201) Nguyen, T.; Abdin, Z.; Holm, T.; Mérida, W. Grid-Connected Hydrogen Production via Large-Scale Water Electrolysis. *Energy Convers Manag* **2019**, *200*, 112108. https://doi.org/10.1016/j.enconman.2019.112108.

(202) Giuliano, A.; Freda, C.; Catizzone, E. Techno-Economic Assessment of Bio-Syngas Production for Methanol Synthesis: A Focus on the Water–Gas Shift and Carbon Capture Sections. *Bioengineering* **2020**, *7* (3), 70. https://doi.org/10.3390/bioengineering7030070.

(203) Rosner, F.; Chen, Q.; Rao, A.; Samuelsen, S. Thermo-Economic Analyses of Isothermal Water Gas Shift Reactor Integrations into IGCC Power Plant. *Appl Energy* **2020**, *277*, 115500. https://doi.org/10.1016/J.APENERGY.2020.115500.

(204) Heide, D.; von Bremen, L.; Greiner, M.; Hoffmann, C.; Speckmann, M.; Bofinger, S. Seasonal Optimal Mix of Wind and Solar Power in a Future, Highly Renewable Europe. *Renew Energy* **2010**, *35* (11), 2483–2489. https://doi.org/10.1016/j.renene.2010.03.012.

(205) Thiel, C. L.; Eckelman, M.; Guido, R.; Huddleston, M.; Landis, A. E.; Sherman, J.; Shrake, S. O.; Copley-Woods, N.; Bilec, M. M. Environmental Impacts of Surgical Procedures: Life Cycle Assessment of Hysterectomy in the United States. *Environ Sci Technol* **2015**, *49* (3), 1779–1786. https://doi.org/10.1021/es504719g.

(206) *MACOR® - Morgan Technical Ceramics*. https://www.morgantechnicalceramics.com/en-gb/materials/macor/ (accessed 2024-12-01).

(207) Ruhaimi, A. H.; Aziz, M. A. A.; Jalil, A. A. Magnesium Oxide-Based Adsorbents for Carbon Dioxide Capture: Current Progress and Future Opportunities. *Journal of CO2 Utilization* **2021**, *43*, 101357. https://doi.org/10.1016/J.JCOU.2020.101357.

(208) Kim, B. J.; Park, H. R.; Lee, Y. L.; Ahn, S. Y.; Kim, K. J.; Hong, G. R.; Roh, H. S. Customized Ni-MgO-ZrO2 Catalysts for the Dry Reforming of Methane Using Coke Oven Gas: Optimizing the MgO Content. *Journal of CO2 Utilization* **2023**, *68*, 102379. https://doi.org/10.1016/J.JCOU.2022.102379.

(209) Meshkani, F.; Rezaei, M.; Andache, M. Investigation of the Catalytic Performance of Ni/MgO Catalysts in Partial Oxidation, Dry Reforming and Combined Reforming of Methane. *Journal of Industrial and Engineering Chemistry* **2014**, *20* (4), 1251–1260. https://doi.org/10.1016/J.JIEC.2013.06.052.

(210) Alves Junior, C.; Galvão, N. K. M.; Gregory, A.; Henrion, G.; Belmonte, T. OES during Reforming of Methane by Microwave Plasma at Atmospheric Pressure. *J Anal At Spectrom* **2009**, *24* (10), 1459. https://doi.org/10.1039/b905323a.

(211) Vertongen, R.; Bogaerts, A. How Important Is Reactor Design for CO2 Conversion in Warm Plasmas? *Journal of CO2 Utilization* **2023**, *72*. https://doi.org/10.1016/j.jcou.2023.102510.

(212) Bogaerts, A.; Tu, X.; Whitehead, J. C.; Centi, G.; Lefferts, L.; Guaitella, O.; Azzolina-Jury, F.; Kim, H.-H.; Murphy, A. B.; Schneider, W. F.; Nozaki, T.; Hicks, J. C.; Rousseau, A.; Thevenet, F.; Khacef, A.; Carreon, M. The 2020 Plasma Catalysis Roadmap. *J Phys D Appl Phys* **2020**, *53* (44), 443001. https://doi.org/10.1088/1361-6463/ab9048.

(213) Long, H.; Shang, S.; Tao, X.; Yin, Y.; Dai, X. CO2 Reforming of CH4 by Combination of Cold Plasma Jet and Ni/γ-Al2O3 Catalyst. *Int J Hydrogen Energy* **2008**, *33* (20), 5510–5515. https://doi.org/10.1016/J.IJHYDENE.2008.05.026.

(214) Shenoy, S. B.; Rabinovich, A.; Fridman, A.; Pearlman, H. Process Optimization of Methane Reforming to Syngas Using Gliding Arc Plasmatron. *Plasma Processes and Polymers* **2019**, *16* (4). https://doi.org/10.1002/ppap.201800159.

(215) Wanten, B.; Vertongen, R.; De Meyer, R.; Bogaerts, A. Plasma-Based CO2 Conversion: How to Correctly Analyze the Performance? *Journal of Energy Chemistry* **2023**, *86*, 180–196. https://doi.org/10.1016/J.JECHEM.2023.07.005.

(216) Janes, A.; Chaineaux, J.; Marlair, G.; Carson, D.; Benaissa, W.; Tribouilloy, B. *Experimental Study of CH4/O2/CO2 Mixtures Flammability Experimental Study of CH 4 /O 2 /CO 2 Mixtures Flammability*; 2011. https://hal-ineris.archives-ouvertes.fr/ineris-00976228.

(217) Engineering ToolBox. *Saturation pressure of water vapor in moist air vs. temperature*. https://www.engineeringtoolbox.com/water-vapor-saturation-pressure-air-d_689.html (accessed 2024-02-23).

Academic curriculum vitae

General information

Name: Bart Wanten

Date and place of birth: January 25, 1997 at Wilrijk, Belgium

Education:

- 2020-present: PhD student, University of Antwerp
- 2018-2020: Master in Chemistry, University of Antwerp
- 2015-2018: Bachelor in Chemistry, University of Antwerp

Publications linked to this doctoral thesis

As first author

Dry Reforming of Methane in an Atmospheric Pressure Glow Discharge: Confining the Plasma to Expand the Performance.
Wanten, B.; Maerivoet, S.; Vantomme, C.; Slaets, J.; Trenchev, G.; Bogaerts, A.
Journal of CO2 Utilization 2022, 56, 101869.
https://doi.org/10.1016/J.JCOU.2021.101869

Plasma-Based CO_2 Conversion: How to Correctly Analyze the Performance?
Wanten, B.*; Vertongen, R.*; De Meyer, R.; Bogaerts, A.
Journal of Energy Chemistry 2023, 86, 180–196.
https://doi.org/10.1016/J.JECHEM.2023.07.005
*Shared first author

Effect of O_2 on Plasma-Based Dry Reforming of Methane: Revealing the Optimal Gas Composition via Experiments and Modeling of an Atmospheric Pressure Glow Discharge.
Maerivoet, S.*; Wanten, B.*; De Meyer, R.; Van Hove, M.; Van Alphen, S.; Bogaerts, A.
ACS Sustain Chem Eng 2024, 12 (30), 11419–11434.
https://doi.org/10.1021/acssuschemeng.4c04283
*Shared first author

Plasma-Based Conversion of CO_2 and CH_4 into Syngas: A Dive into the Effect of Adding Water.
Wanten, B.; Gorbanev, Y.; Bogaerts, A.
Fuel 2024, 374, 132355.
https://doi.org/10.1016/j.fuel.2024.132355.

As co-author

Techno-economic and Life Cycle Assessment for Syngas Production Using Sustainable Plasma-Assisted Methane Reforming Technology
Escribà-Gelonch, M.*; Osorio-Tejada, J.*; Yu, L.; Wanten, B.; Bogaerts, A.; Hessel, V.
Energy & Environmental Science 2024, under review
*Shared first author

Other publications

The role of CH_4 in plasma-assisted CO_2 and CH_4 conversion in a rotating gliding arc plasma: Insights revealed by experiments and modeling
Van Alphen, S.*; Wanten, B.*; Girard-Sahun, F.*; Slaets, J.*; Creel, J.; Aghaei, M.; Bogaerts, A.
ACS Sustain Chem Eng 2024, 12 (42), 15715-15728
https://doi.org/10.1021/acssuschemeng.4c06627
*Shared first author

Conference/workshop contributions

ERC SCOPE project meeting, online (Teams), July 6th 2021. Oral presentation: "Combined CO_2 and CH_4 conversion in atmospheric pressure glow discharge: experiments + modelling"

CAPTURE Science Talks, online (Teams), May 6th 2022. Oral presentation: "Confining the plasma to expand the performance: CO_2 and CH_4 conversion in an atmospheric pressure glow discharge"

5th International Symposium on Plasmas for Catalysis and Energy Materials (ISPCEM), Liverpool (UK), July 4th 2022. Oral presentation: "CO_2 and CH_4 conversion in a confined atmospheric pressure glow discharge".

2nd International Conference on Unconventional Catalysis, Reactors and Applications (UCRA), Leamington Spa (UK), September 21-23 2022. Oral presentation: “Oxy-CO_2 reforming of methane in an atmospheric pressure glow discharge”.

Thesis supervision

Bachelor thesis

Dry Reforming of Methane met een Atmospheric Pressure Glow Discharge reactor: op weg naar een klimaatneutrale industrie
Vantomme, Christine
2020-2021

Effect van O_2 op het dry reforming of methane proces in een atmospheric pressure glow discharge - Gecombineerde experimentele en computationele studie
Van Hove, Morgane
2021-2022

Dry reforming of methane in een nieuwe confined atmospheric pressure glow discharge: Effect van een variërende kathode-anode afstand op de reactieprestaties
Vandenbroucke, Amira
2022-2023

Master thesis

Effect of O_2 on Dry Reforming of Methane in a Confined Atmospheric Pressure Glow Discharge - Searching a path to a better syngas ratio via experiments and modelling
Maerivoet, Stein
2021-2022